



UNIVERSITÄT ZU LÜBECK

From the Institute of Physics
of the University of Lübeck
Director: Prof. Dr. Christian Hübner

Investigation of protein dynamics under high hydrostatic pressure using nsFRET-FCS

Dissertation
for Fulfillment of
Requirements
for the Doctoral Degree
of the University of Lübeck

from the Department of Natural Sciences

Submitted by
Kim Colin Reiter
from Lübeck

Lübeck 2024

First referee: Prof. Dr. Christian Hübner

Second referee: Prof. Dr. Thomas Gutschmann

Date of oral examination: 27.10.2025

Approved for printing. Lübeck, 28.10.2025

Abstract

A central question in structural biology concerns the speed of protein folding and the associated speed limit. According to Kramers' theory, this limit for fast-folding proteins is determined by the diffusive motion of the polypeptide chains [1–3]. Therefore, the study of unfolded proteins, as well as intrinsically disordered proteins (IDPs), is of great importance, as the unfolded state forms the starting point of the folding reaction. By combining Förster resonance energy transfer (FRET) and nanosecond fluorescence correlation spectroscopy (nsFCS), proteins can be studied at the single-molecule level. nsFRET-FCS experiments not only provide information about individual protein populations but also allow for the investigation of chain dynamics in unfolded proteins or IDPs. While the influence of temperature and chemical denaturants has already been well-studied, the influence of hydrostatic pressure, e.g., via the hydration shell around the protein, on chain dynamics remains unknown.

The aim of this work is to conduct nsFRET-FCS experiments under high pressure. For this, the experimental setup for high-pressure experiments developed by Sven Schneider [4,5] was extensively modified to create the technical prerequisites for the temporal analysis of fluorescence signals down to the sub-nanosecond range. A new, dead-time-free measuring electronics system and two additional detectors were integrated into the experimental setup. The functionality of the modified experimental setup and the developed LabVIEW VI was verified through fluorescence measurements of freely diffusing fluorophores. Additionally, the reliability and reproducibility of spectroscopic experiments were improved by optimizing the sample connection technique to the experimental setup. The new sample stage allowed for more precise and safe adjustment of the capillary position, reducing potential damage. This is because the height of the capillary above the objective can be continuously adjusted with the new holder. Furthermore, the lateral position can be adjusted without shifting the two capillary ends relative to each other, thereby reducing the risk of damage. For optimal alignment of the capillary over the objective, the capillary can be rotated with the new setup without significantly changing its lateral position.

To evaluate the experimental setup, initial coverslip measurements were made at ambient pressure. Due to their stability, DNA samples served as negative controls and showed no chain movements in the correlation functions. For the detection of chain dynamics, chemically denatured cold shock protein CspA and the native unfolded IDP prothymosin alpha (ProT α), which has been shown to exhibit chain movements in the time range of less than 100 ns [6,7], were used. Chain dynamics are also expected for denatured CspA, as it is comparable in structure and composition to cold shock protein CspTM, for which dynamics have already been experimentally demonstrated [8].

In the first successful nsFRET-FCS experiments under high pressure, DNA hybrids were used as negative controls, as well as the IDP prothymosin alpha. The DNA

experiments showed no significant changes under pressure, ensuring that potential pressure artifacts could be excluded from the measurements of the IDP. The analysis of the ProT α experiments indicates a pressure-induced expansion of the polypeptide chain, which is qualitatively reflected in the time constants of the fluorescence antibunching of the donor fluorophore. Consistent with this is the apparently shortened reconfiguration time of the chain with increasing pressure. Reduced internal friction leads to a more flexible chain and, thus, a shorter reconfiguration time.

The experiments demonstrate that nsFRET-FCS measurements under high hydrostatic pressure with a sufficiently high signal-to-noise ratio (SNR) are possible with the experimental setup, even though the SNR is lower than under standard conditions with coverslips. Fluorescence fluctuations can still be analyzed over the entire time range, from fluorescence antibunching (sub-ns) to diffusion (ms) through the focus.

Zusammenfassung

Eine zentrale Fragestellung der Strukturbiologie betrifft die Geschwindigkeit der Proteinfaltung und das damit verbundene Geschwindigkeitslimit. Nach Kramers Theorie wird dieses Limit bei schnell faltenden Proteinen durch die diffusive Bewegung der Polypeptidketten bestimmt [1–3]. Daher ist die Untersuchung entfalteter Proteine, aber auch intrinsisch ungefalteter Proteine (IDPs) von großer Bedeutung, da der ungefaltete Zustand den Ausgangspunkt der Faltungsreaktion bildet. Mittels der Kombination des Förster-Resonanz-Energie-Transfers (FRET) und der Nanosekunden-Fluoreszenz-Korrelations-Spektroskopie (nsFCS) können Proteine auf Einzelmolekülebene untersucht werden. nsFRET-FCS-Experimente liefern dabei nicht nur Informationen über einzelne Proteinpopulationen, sondern erlauben es gleichzeitig Kettendynamiken entfalteter Proteine bzw. IDPs zu untersuchen. Während der Einfluss der Temperatur und von chemischen Denaturierungsmitteln bereits gut erforscht ist, ist der Einfluss des hydrostatischen Drucks, z.B. über die Hydrathülle um das Protein auf die Kettendynamik noch unbekannt.

Ziel dieser Arbeit ist die Realisierung von nsFRET-FCS Experimenten unter hohem Druck. Dazu wurde der von Sven Schneider entwickelte Versuchsaufbau für Hochdruck-Experimente [4, 5] weiter modifiziert, um die technischen Voraussetzungen für die zeitliche Analyse des Fluoreszenzsignals bis in den sub-ns Bereich zu schaffen. Dafür wurden eine neue, totzeitfreie Messelektronik sowie zwei zusätzliche Detektoren in den Versuchsaufbau integriert. Die Funktionsfähigkeit des modifizierten Versuchsaufbaus und der entwickelten LabVIEW VI wurde durch Fluoreszenzmessungen frei diffundierender Fluorophore verifiziert. Zudem wurde die Zuverlässigkeit und Reproduzierbarkeit spektroskopischer Untersuchungen durch eine Verbesserung der Probenanschlusstechnik an den Versuchsaufbau optimiert. Der neue Probenstisch ermöglichte dabei eine präzisere und risikoärmere Justierung der Kapillarenposition, wodurch Beschädigungen reduziert werden. Das ist darauf zurückzuführen, dass die Höhe der Kapillare über dem Objektiv mit der neuen Halterung stufenlos justiert werden kann. Des Weiteren kann die laterale Position eingestellt werden, ohne die beiden Kapillarenden relativ zueinander zu verschieben und damit potentiell zu beschädigen. Für eine ideale Ausrichtung der Kapillare über dem Objektiv kann die Kapillare mit dem neuen Aufbau rotiert werden, ohne, dass sich ihre laterale Position signifikant ändert.

Zur Evaluation des Versuchsaufbaus wurden zunächst Deckglasmessungen bei Umgebungsdruck durchgeführt. DNA-Proben dienen aufgrund ihrer Stabilität als Negativkontrollen und zeigen keine Kettenbewegungen in den Korrelationen. Für den Nachweis von Kettendynamiken wurden das chemisch denaturierte Kälteschockprotein CspA und das nativ entfaltete IDP Prothymosin Alpha ($\text{ProT}\alpha$) verwendet, welches Kettenbewegungen im Zeitbereich von unter 100 ns aufweist [6, 7]. Auch

für das denaturierte CspA ist Kettendynamik zu erwarten, da es strukturell mit dem Kälteschockprotein CspTM sehr ähnlich ist, für das bereits Dynamiken experimentell nachgewiesen wurden [8].

In den ersten erfolgreichen nsFRET-FCS-Experimenten unter hohem Druck wurden DNA-Hybride als Negativkontrolle sowie das IDP Prothymosin Alpha verwendet. Die DNA Experimente zeigen dabei keine signifikanten Änderungen unter Druck, sodass potentielle Druckartefakte auch bei den Messungen des IDPs ausgeschlossen werden können. Die Analyse der Prothymosin-Alpha-Experimente deutet auf eine druckinduzierte Expansion der Polypeptidkette hin, was sich qualitativ in den Zeitkonstanten des Fluoreszenz-Antibunching des Donorfluorophors widerspiegelt. In Übereinstimmung damit ist die mit steigendem Druck scheinbar verkürzte Rekonfigurationszeit der Kette. Eine verringerte interne Reibung führt zu einer flexibleren Kette und damit kürzeren Rekonfigurationszeit.

Die Experimente zeigen, dass mit dem experimentellen Aufbau nsFRET-FCS Messungen unter hohem hydrostatischen Druck mit einem ausreichend hohen Signal-zu-Rausch-Verhältnis (SNR) möglich sind, auch wenn dieses geringer ist als bei Standardbedingungen mit Deckgläsern. Fluoreszenzfluktuationen können dennoch über den gesamten Zeitbereich analysiert werden, der von Fluoreszenz-Antibunching (sub-ns) bis hin zur Diffusion (ms) durch den Fokus reicht.

Contents

1	Introduction	1
2	Fundamentals	5
2.1	Photoluminescence	5
2.1.1	Franck-Condon principle and Stoke's shift	10
2.1.2	Fluorescence lifetime	13
2.1.3	Fluorescence quantum yield	15
2.1.4	Fluorescence quenching	15
2.1.5	Fluorescence and pressure	18
2.2	Confocal microscopy	19
2.2.1	Excitation	21
2.2.2	Detection	23
2.2.3	Observation Volume	23
2.2.4	Resolution	24
2.3	Single molecule spectroscopy	28
2.3.1	Signal-to-noise ratio	29
2.4	Förster resonance energy transfer	31
2.4.1	Overlap integral	35
2.4.2	Orientation factor	36
2.4.3	Single molecule FRET	37
2.5	Fluorescence correlation spectroscopy	39
2.5.1	Brownian motion	41
2.5.2	Internal two-state dynamics	43
2.5.3	nsFCS	45
2.6	FRET-FCS	47
2.7	Proteins	47
2.7.1	Protein structures	48
2.7.2	Intrinsically disordered proteins	51
2.7.3	Folding	54
2.7.4	Denaturation	55
2.7.5	Denatured state	56
2.7.6	Folding kinetics	57
2.7.7	Speed limit of protein folding	58

3	Material and Methods	61
3.1	Experimental setup	61
3.1.1	Four detector configuration	63
3.2	Pressure setup	64
3.2.1	Fused silica capillary	66
3.2.2	Capillary preparation and handling	67
3.2.3	Optical multi layer	69
3.2.4	Capillary PMMA multi layer	71
3.2.5	Reuse of pressure plugs	72
3.3	Counting electronics	73
3.3.1	Routed TCSPC	73
3.3.2	Parallel time tagger	73
3.4	Pressure capillary sample stage	76
3.5	Samples and buffer	79
3.5.1	Fluorophores	79
3.5.2	Fluorescent microspheres	81
3.5.3	DNA samples	81
3.5.4	Cold shock protein CspA	84
3.5.5	Prothymosin alpha	84
3.5.6	Buffers	85
3.6	LabVIEW and data editing	86
3.6.1	Overflows	89
3.6.2	Synchronization with the laser pulse	90
3.7	Data processing	91
3.7.1	FCS	91
3.7.2	Effective triplet transition rate and molecular brightness	94
3.7.3	FRET	95
4	GPX-TDC implementation and experimental setup improvements	97
4.1	Implementation of GPX-TDC	97
4.1.1	FCS benchmarks	98
4.1.2	Antibunching of free diffusing AF488	103
4.1.3	Time differences between detection channels	105
4.2	Avalanche photodiodes	108
4.3	Experimental setup and capillary handling improvements	110
4.3.1	Immersion water protection	110
4.3.2	Sample stage	114
4.3.3	Capillary preparation	115
4.4	Capillary PMMA multi layer	116
4.4.1	Fluorescent microspheres as a test system	116
4.4.2	Alexa Fluor 488	121
4.4.3	Cross section images	122
4.4.4	Discussion	123

4.5	Influence of the microscope objective correction collar	124
4.5.1	Bare square capillary	124
4.5.2	Optical multi layer	126
4.6	Focus position within the sample volume of the capillary	127
5	nsFRET-FCS	131
5.1	Ambient pressure	131
5.1.1	3/4-stranded DNA hybrids	131
5.1.2	DNA hairpin	135
5.1.3	Cold shock protein CspA	137
5.1.4	Prothymosin alpha	141
5.2	High-pressure experiments	149
5.2.1	3-stranded DNA hybrid	149
5.2.2	Prothymosin alpha	152
6	Conclusion, summary and outlook	163
6.1	GPX-TDC implementation and experimental setup improvements . .	163
6.2	nsFRET-FCS	166
6.3	Conclusion and outlook	169
	Appendix	171
A.1	FCS benchmarks	171
A.2	Igor Pro procedures	173
A.2.1	Editing of raw data and time correction	173
A.2.2	Filtered nsFRET-FCS analysis	174
A.3	Focus position within the capillary	175
A.4	Prothymosin alpha	176
A.4.1	Interval analysis of prothymosin alpha	176
A.4.2	Influence of the measurement duration for prothymosin alpha	178
	List of Figures	181
	List of Tables	187
	References	187

Chapter 1

Introduction

The central paradigm of structural biology states that the folded, native three-dimensional structure of a protein is directly responsible for its function [9]. This paradigm is supported by the models of Pauling and Fischer [10, 11]. It raises a very fundamental question: how do proteins achieve their native state? The basis for the answer to the question is Anfinsen's work in the 1960s, particularly with experiments on the enzyme bovine pancreatic ribonuclease (RNase A). These studies proved that proteins can fold reversibly, suggesting that the information for folding must be encoded in the amino acid sequence [12–14]. Nonetheless, Anfinsen's results could not explain the high speed of the folding process. If a protein were to randomly sample all possible configurations, the process would take longer than the age of the universe [15]. This is known as the Levinthal paradox [15–17]. New calculations, which incorporated a slight energy bias, reduced the timescale to a few seconds [18].

A crucial and essential question arising from this is the speed at which proteins can fold and the resulting speed limit of protein folding. The investigation of fast-folding proteins, which exhibit two-state kinetics, provides an opportunity to gain insight into the entire folding process and mechanism [1, 19–22]. In this case, according to Kramer's theory [2, 3], the speed limit is constrained by intrachain diffusion, which becomes the dominant factor [23, 24]. Furthermore, proteins that fold in the shortest possible time frame are suitable for comparing experimental results with computationally intensive simulations [1, 25–29]. Hence, the analysis of the unfolded polypeptide chain is of significant interest. The dynamics of the chain determine the timeframe in which distinct residues along the amino acid sequence can approach each other and enable interactions between them [30]. Additionally, the denatured state serves as the starting point for the protein folding process [30–32]. In this context, proteins of interest include intrinsically disordered proteins (IDPs). Due to the observation of IDPs the central paradigm has been challenged in recent years as more and more proteins have been discovered to possess either highly flexible, unstructured regions [33–35] or being completely unfolded [36, 37]. Despite their unstructured conformation, IDPs are functional [38–40]. Since experiments with unfolded proteins often involve chemical denaturants, IDPs offer a promising opportunity to investigate polypeptide chain dynamics under physiological conditions.

Single-molecule fluorescence spectroscopy is a well-suited method to examine such dynamics [30, 31] and was first conducted at room temperature by Shera et al. in 1990 [41]. One of the significant strengths of single-molecule spectroscopic methods is overcoming ensemble averaging and analyzing conformational heterogeneities and their dynamics [42–44]. One of these methods is Förster resonance energy transfer (FRET) at the single molecule (sm) level. FRET is a strongly distance dependent process where an excited fluorophore, called donor, transfers its energy non-radiatively to another fluorophore called acceptor [45–47]. The discovery of FRET dates back to 1948 and Theodor Förster [48], but Stryer and Haugland recognized that the distance dependence of FRET can be utilized for distance determinations in the nanometer range [49]. First experiments at the single molecule level (smFRET) were realized by Ha et al. in 1996 [50]. A major advantage and strength of smFRET experiments is the ability to distinguish and separately analyze different populations, such as folded and unfolded proteins [51, 52]. Consequently, populations with a low contribution to the overall signal can still be investigated, which would otherwise be dominated by the signal of other populations [53]. Single-molecule FRET has been extensively used to study various biological systems, including DNA [54, 55], RNA [56–59], DNA-protein interactions [60], conformational changes of proteins [61, 62], and protein-protein interactions [63]. In particular, protein unfolding due to temperature [64], chemical denaturants [51, 52, 65], and most recently, due to pressure has been analyzed [4, 5]. By combining FRET with FCS, molecular dynamics in the microsecond range can be examined [66–70].

An excellent complement to FRET is fluorescence correlation spectroscopy (FCS). First introduced in 1970, FCS allows for the investigation of biological and biophysical processes leading to fluctuations in the fluorescence signal [45, 46, 71–73]. By accessing a broad time range from diffusion in the millisecond to second time regime to fluorescence antibunching in the nanosecond range, nanosecond FCS (nsFCS) in combination with FRET (nsFRET-FCS) is a useful tool, which offers a versatile approach for analyzing chain dynamics of unfolded proteins and IDPs [31, 53, 74, 75].

This method is based on the analysis of fluctuations in the donor-acceptor distance due to the diffusion of the unfolded polypeptide chain, leading to fluctuations in the fluorescence signal [53]. These fluctuations result in a characteristic anti-correlation in the cross-correlation functions of both fluorophores and a correlated signal in the respective auto-correlation functions, allowing for the determination of the relaxation time as a shared fit parameter in a global fit of all correlation functions [7, 31, 66, 76–78]. Several studies using nsFRET-FCS have been conducted with unfolded proteins and IDPs. Nettels et al. probed the dynamics of the unfolded cold shock protein CspTM, a small β -barrel protein, exhibiting two-state kinetics [79]. Like mentioned above, for small two-state folders, the pre-exponential factor of folding is in approximation solely dependent on the diffusion of the polypeptide chain. Thus, a limit for the folding time of the protein could be estimated based on the determined reconfiguration time. Furthermore, the study showed the strength of

single molecule analysis with an individual distance and correlation analysis of the unfolded population. Other investigations, for example, analyzed the viscosity dependent dynamics of chain movements and internal friction processes [7,8,78]. These studies indicate that chain dynamics of intrinsically disordered proteins (IDPs) and unfolded proteins can be well elucidated within the framework of simple polymer models such as the Rouse or Zimm model [80]. Consequently, the strong agreement between theoretical polymer concepts and experimental observations is an important basis for the physical understanding of the structural and dynamic behavior of IDPs and unfolded proteins [53].

In contrast to temperature changes or chemical denaturants, high pressure single molecule nsFRET-FCS experiments examining their influence on the behavior of unfolded polypeptide chains have not been performed yet.

Experiments on protein denaturation using high pressure trace back to the pioneering work of Bridgman, who in 1914 described the coagulation of egg white under pressure [81]. However, the first fluorescence measurements under high pressure were demonstrated in 1981 by Paladini et al., showing the pressure-induced dissociation of Enolase [82]. Nonetheless, the experimental setup and the characteristics of the pressure cell were not suitable for single molecule experiments. The realization of high pressure fluorescence measurements at single molecule concentration was first presented by Gratton et al. [83]. The used pressure cell was a cylindrical fused silica capillary with an outer diameter of 360 μm and an inner diameter of 50 μm . The thin wall thickness of the capillary makes it suitable for the use with microscope objectives with high numerical aperture and small working distance. Tekmen and Müller utilized the same pressure cell for fluorescence correlation spectroscopy (FCS) measurements and reported a pressure resistance of at least 4 kbar for the round capillary [84]. They also tested a fused silica capillary with a square cross section as an alternative to the cylindrical shape, which leads to severe aberrations. But the square capillary showed a significant reduced pressure stability of about 2 kbar, as reported by Schneider [5]. Nevertheless, a recent study by Sung and Nesbitt reported a pressure stability of the square capillary of up to nearly 5 kbar without any signs of fracturing, achieved by an improved sealing procedure for the capillary end [85]. To reduce aberrations when using fused silica capillaries, Schneider developed an assembly consisting of the capillary, an index-matching gel and a fused silica coverslip [4, 5]. Although this new arrangement does not match the imaging properties of a standard borosilicate coverslip, improved results can be achieved compared to using a bare capillary.

However, like mentioned above, despite the realization of single molecule high pressure fluorescence experiments and the recent studies of protein unfolding due to pressure [4, 5] and of effects of high pressure on DNA and RNA [85–88], nsFRET-FCS experiments under high pressure have not been carried out until present. The distinct unfolding mechanism induced by pressure compared to temperature or chemical denaturants could provide additional insights into the folding process, as different perturbation effects on the energy landscape are observed [89]. Pressure also influences the kinetics of folding and unfolding and has the potential to stabilize folding

intermediates [90, 91]. Therefore, the analysis of dynamics and chain movements of unfolded proteins and IDPs under high pressure conditions using nsFRET-FCS is of great interest, as the unfolded chain represents the starting point of the folding reaction, and its dynamics represent a limit for the speed of protein folding. Additionally, potential influences of folding intermediates or transition states on chain movements could be investigated.

Consequently, the aim of this work was to further extend the experimental setup developed by Schneider [4] to enable single molecule nsFRET-FCS measurements under high hydrostatic pressure. Additionally, the reliability of high pressure measurements and the entire handling process of the capillary were to be improved to streamline the execution of experiments using high pressure. For this purpose, the experimental setup was initially equipped with improved measurement electronics without technical dead time limitations. Furthermore, the connection procedure of the fused silica capillary to the experimental setup and the alignment for measurements were simplified using a completely newly developed sample stage.

After the evaluation of the new sample stage and the implementation of the new measurement electronics, nsFRET-FCS measurements were made. First, nsFRET-FCS measurements at ambient pressure were performed with DNA samples, serving as a reference for potential pressure artifacts and dynamics. Further nsFRET-FCS experiments were performed with GdmCl denatured cold shock protein CspA and the IDP prothymosin alpha (ProT α). Finally, single molecule high pressure nsFRET-FCS experiments were made, with DNA as a reference and ProT α as a model system for unfolded proteins.

Chapter 2

Fundamentals

2.1 Photoluminescence

Photoluminescence is one kind of luminescence and describes the emission of light by a substance that is in an electronically excited state due to the absorption of photons [46,47]. It is further divided into fluorescence and phosphorescence depending on the electronic state from which the photon emission occurs. Organic compounds with the ability to fluoresce are called fluorophores. In the following, the photophysical properties of fluorophores suitable for single molecule studies will be outlined. As photophysical dynamics can occur on similar time scales as protein chain dynamics, there will be an emphasis on this dynamics. On the other hand, the photophysical dynamics can also be used to quantitatively characterize the instrument.

Excluding radicals, electrons occupying the ground state of organic fluorophores are always paired [46, 92]. For solely paired electrons with opposite spin and a magnetic spin quantum number m_s of $\frac{1}{2}$ and $-\frac{1}{2}$, respectively, the total spin quantum number

$$S = \sum m_s \quad (2.1)$$

equals zero, which results in a multiplicity M of one:

$$M = 2S + 1. \quad (2.2)$$

States with a multiplicity of one are called singlet states. By absorbing photons of a suitable wavelength, an electron of the singlet ground state S_0 of a fluorophore can be promoted to an excited singlet state S_n ($n = 1, 2, 3, \dots$). Requirement for this is that the energy of the absorbed photon E_{ph} is at least as large as the energy gap between S_1 and S_0 . The energy of the photon is given by

$$E_{\text{ph}} = h\nu_{\text{ph}} = \frac{hc}{\lambda_{\text{ph}}}, \quad (2.3)$$

where h is Planck's constant, c the speed of light, ν_{ph} the frequency and λ_{ph} the wavelength of the photon. The excitation rate k_{ex} is given by the intensity of the

absorbed light I , the energy of the photon E_{ph} and the absorption cross section σ of the fluorophore [93]:

$$k_{\text{ex}} = \frac{I\sigma}{E_{\text{ph}}}, \quad (2.4)$$

with

$$\sigma = \frac{\ln(10)}{N_{\text{A}}} \varepsilon, \quad (2.5)$$

where ε is the molar absorption coefficient and N_{A} is the Avogadro constant. With the photon flux

$$\phi_{\text{ex}} = \frac{I}{h\nu} \quad (2.6)$$

Eq. 2.4 becomes

$$k_{\text{ex}} = \phi_{\text{ex}}\sigma. \quad (2.7)$$

The absorbed energy brings the fluorophore to the vibrational ground state or a higher vibrational level of an excited singlet state (see subsection 2.1.1), usually S_1 or S_2 [45,46]. Following excitation to S_1 , the excited fluorophore drops to the lowest vibrational state of S_1 by vibrational relaxation, caused by collision with solvent molecules. If the excitation goes to a state $S_{n>1}$, the fluorophore reaches the lowest vibrational state of the respective electronic state by vibrational relaxation, following internal conversion (IC) to a higher vibrational state of the next lower electronically excited state S_{n-1} . Internal conversion refers to a non-radiative, isoenergetic transition between two electronic states of equal multiplicity [47]. This process repeats itself in every electronic state until the lowest vibrational level of S_1 is reached.

From S_1 , there are several depopulation pathways to the electronic ground state S_0 . Once again, a non-radiative transition via internal conversion is possible, followed by vibrational relaxation to the lowest vibrational level of S_0 . Due to the larger energy gap between S_1 and S_0 than between two neighbouring electronically excited singlet states, internal conversion is less efficient [46,47]. The here most relevant transition to return to the ground state is via the emission of a fluorescence photon, where the fluorophore may also decay to a higher vibrational level of S_0 [45]. The wavelength of the fluorescence photon

$$\lambda_{\text{f}} = \frac{hc}{\Delta E} \quad (2.8)$$

results from the energy gap ΔE of the two states involved.

Tab. 2.1: Overview of possible depopulation pathways of excited fluorophores. S_n and T_n represent singlet and triplet states, respectively, whereas ν symbolizes their vibrational levels [46].

Description	Transition type	Transition time in s
Singlet-singlet absorption	$S_0 \rightarrow S_n$	$\leq 10^{-15}$
Internal conversion	$S_n \rightarrow S_1, T_n \rightarrow T_1$	$10^{-10} - 10^{-14}$
Vibrational relaxation	$S_1 \rightarrow S_0$	$10^{-6} - 10^{-7}$
	$S_{1,\nu=n} \rightarrow S_{1,\nu=0}$	$10^{-10} - 10^{-12}$
	$S_{0,\nu=n} \rightarrow S_{0,\nu=0}$	10^{-12}
Fluorescence emission	$S_1 \rightarrow S_0$	$10^{-7} - 10^{-9}$
Intersystem crossing	$S_n \rightarrow T_n, T_n \rightarrow S_n$	$10^{-5} - 10^{-8}$
Phosphorescence	$T_1 \rightarrow S_0$	$10^{-3} - 10^2$

Since vibrational relaxation and internal conversion occur on a picosecond timescale and the average lifetime of fluorophores is in the nanosecond range, fluorescence emission occurs always from the lowest vibrational level of S_1 (see Tab. 2.1). This is known as Kasha’s rule [45, 46], which states the effect that the wavelength of fluorescence photons is usually independent of the excitation wavelength.

Intersystem crossing (ISC) to the triplet state T_1 represents another depopulation pathway. This transition is associated with a spin flip of the excited electron and is actually spin forbidden, but possible due to spin-orbit coupling [46]. According to Eq. 2.1, the spin change leads to a total spin quantum number of one and therefore a multiplicity of three (see Eq. 2.2), which is why these states are called triplet states [45–47]. In principle, ISC is an inefficient process in most organic fluorophores, because of weak spin orbit coupling, despite the fact that triplet states have lower energy than their corresponding singlet states [46, 94]. After the transition to an excited vibrational level of T_1 , vibrational relaxation leads to a decay to the lowest vibrational level of T_1 . In order to return from T_1 to the singlet ground state S_0 , a change of electron spin and thus the multiplicity is necessary, again. This makes the lifetime of T_1 , with times of up to 100 s, long in comparison to the average fluorescence lifetime (see subsection 2.1.2) of 10^{-7} s – 10^{-9} s (see Tab. 2.1). One way to return to the ground state is the emission of a phosphorescence photon, followed by vibrational relaxation to the lowest level of S_0 . Due to the lower energy of T_1 in comparison to S_1 , in general phosphorescence photons have a longer wavelength than fluorescence photons. Given the long lifetime of the state, non-radiative internal conversion with subsequent vibrational relaxation is more likely to happen, than the emission of a phosphorescence photon [45–47]. The specified transitions between the several electronic and vibrational singlet and triplet states are illustrated in a Jablonski diagram [95] in Fig. 2.1. The characteristic times of the transitions are listed in Tab. 2.1.

By only considering the electronic ground state S_0 and the first excited singlet state and triplet state S_1 and T_1 , respectively, and neglecting coherent terms, the popu-

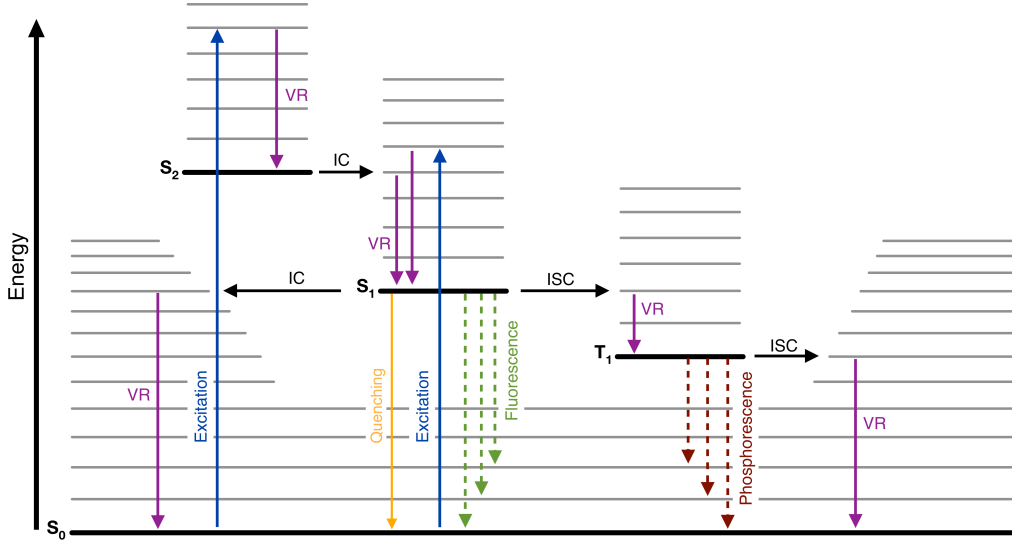


Fig. 2.1: Jablonski diagram showing possible excitation and depopulation pathways within a fluorophore. Thick black lines represent electronic states of fluorophores, both singlet and triplet states, respectively (S_n , T_n). Thinner grey lines are the associated vibrational states of the respective electronic state. Dashed arrows showing radiative decays of fluorescence (green) and phosphorescence (dark red), whereas non-radiative transitions are shown as solid arrows, with blue for excitation, purple for vibrational relaxations (VR) and black for internal conversion (IC) as well as intersystem crossing (ISC).

lation of these states can be described by the following rate equations [96,97]:

$$[\dot{S}_0] = -k_{\text{ex}}[S_0] + k_f[S_1] + k_{\text{IC}}[S_1] + k_{\text{rISC}}[T_1], \quad (2.9a)$$

$$[\dot{S}_1] = k_{\text{ex}}[S_0] - k_f[S_1] - k_{\text{IC}}[S_1] - k_{\text{ISC}}[S_1], \quad (2.9b)$$

$$[\dot{T}_1] = k_{\text{ISC}}[S_1] - k_{\text{rISC}}[T_1]. \quad (2.9c)$$

In Eq. 2.9a to Eq. 2.9c, $[S_0]$, $[S_1]$ and $[T_1]$ denote the population of the respective state, and k_{ex} , k_f , k_{IC} , k_{ISC} and k_{rISC} are the corresponding transition rates for absorption, fluorescence emission, internal conversion, intersystem crossing and reverse intersystem crossing. For stationary conditions, the emission rate R is given by [96]

$$R = [S_1]k_f = \frac{k_f}{1 + \frac{k_{\text{ISC}}}{k_{\text{rISC}}} + \frac{k_f + k_{\text{IC}} + k_{\text{ISC}}}{k_{\text{ex}}}}. \quad (2.10)$$

Assuming an infinitely high excitation rate k_{ex} , the emission rate R becomes

$$\lim_{k_{\text{ex}} \rightarrow \infty} R = R_{\infty} = \frac{k_f}{1 + \frac{k_{\text{ISC}}}{k_{\text{rISC}}}}. \quad (2.11)$$

R can then be expressed by

$$R = R_\infty \frac{1}{1 + \frac{k_{\text{sat}}}{k_{\text{ex}}}}, \quad (2.12)$$

with the saturation rate

$$k_{\text{sat}} = \frac{(k_{\text{IC}} + k_{\text{ISC}} + k_{\text{f}}) k_{\text{rISC}}}{k_{\text{ISC}} + k_{\text{rISC}}}. \quad (2.13)$$

The saturation of the fluorescence emission at high laser excitation powers is shown in Fig. 2.16. Like the fluorescence emission, the triplet state T_1 can be saturated as well. Since the rate of intersystem crossing k_{ISC} is much lower than the fluorescence emission rate k_{f} , the triplet state can be saturated with less laser power. Due to this, the triplet state saturation can be used to quantify the excitation quality of a microscope, with the effective transition rate to the triplet state $k_{\text{ISC}}^{\text{eff}}$, which is given by [93, 97]

$$k_{\text{ISC}}^{\text{eff}} = \frac{k_{\text{ex}}}{k_{\text{ex}} + k_{\text{f}}} k_{\text{ISC}}. \quad (2.14)$$

The triplet rate k_{T} is given by

$$k_{\text{T}} = k_{\text{ISC}}^{\text{eff}} + k_{\text{rISC}}. \quad (2.15)$$

With Eq. 2.15, it follows for the triplet relaxation time τ_{T}

$$\tau_{\text{T}} = \frac{1}{k_{\text{ISC}}^{\text{eff}} + k_{\text{rISC}}}. \quad (2.16)$$

The fraction of fluorophores in the triplet state \bar{T} is given by

$$\frac{\bar{T}}{1 - \bar{T}} = \frac{k_{\text{ISC}}^{\text{eff}}}{k_{\text{rISC}}}. \quad (2.17)$$

It follows

$$k_{\text{ISC}}^{\text{eff}} = \frac{\bar{T}}{\tau_{\text{T}}}, \quad (2.18)$$

showing that the effective intersystem crossing rate is directly accessible with a FCS experiment (see section 2.5). The triplet state is called saturated, if $k_{\text{ISC}}^{\text{eff}}$ equals

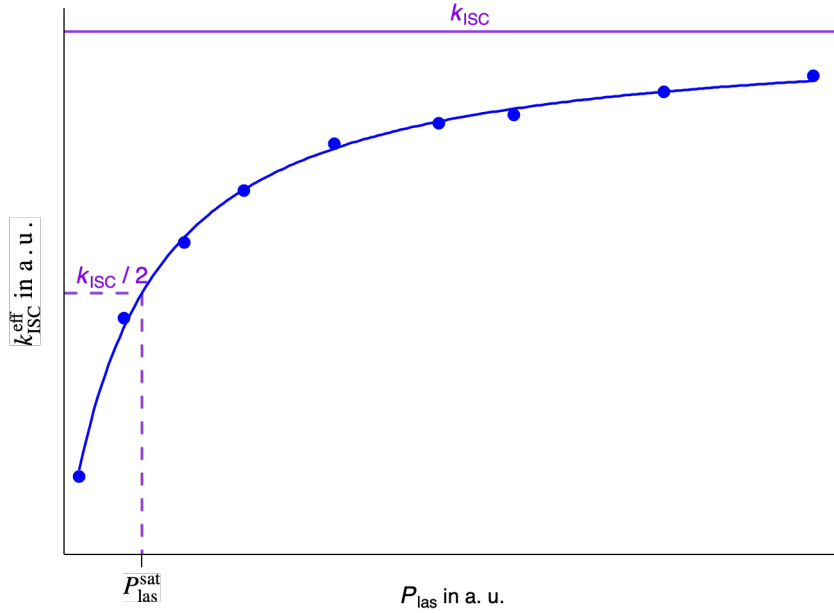


Fig. 2.2: Effective intersystem crossing rate $k_{\text{ISC}}^{\text{eff}}$ in dependence on the laser power P_{las} . The laser power $P_{\text{las}}^{\text{sat}}$ required to saturate the triplet state can be determined with multiple FCS experiments at different excitation powers. For each laser power, $k_{\text{ISC}}^{\text{eff}}$ is calculated with Eq. 2.18 (blue dots). Finally, $P_{\text{las}}^{\text{sat}}$ is determined by a fit according to Eq. 2.19 (blue line).

$k_{\text{ISC}}/2$. Therefore, the laser power necessary to saturate the triplet state, the saturation power $P_{\text{las}}^{\text{sat}}$, can be determined by measuring the effective intersystem crossing rate at different laser powers P_{las} and a fit according to

$$k_{\text{ISC}}^{\text{eff}}(P_{\text{las}}) = \frac{k_{\text{ISC}}}{1 + \frac{P_{\text{las}}^{\text{sat}}}{P_{\text{las}}}}. \quad (2.19)$$

This is shown in Fig. 2.2. A lower saturation power indicates a higher photon flux density and thus more efficient excitation of the fluorophores, which might be due to a smaller focal volume (see subsection 2.2.3). For this reason, saturation measurements of the triplet state can be utilized to evaluate and compare different optical setups or excitation paths of a setup.

2.1.1 Franck-Condon principle and Stoke's shift

The probability of electronic transitions within a molecule can be described by the Franck-Condon principle. According to this principle, the transition of an electron to an excited state occurs nearly without a change in the nuclear coordinates of the molecule, because the transitions occur on a timescale of about 10^{-15} s,

while characteristic times for vibrational motions are in the picosecond regime (see Tab. 2.1) [46, 94, 98].

This is due to the fact that the mass of an electron is roughly 1870 times smaller than the mass of the nucleotides [46, 98]. Fig. 2.3 illustrates the Franck-Condon principle with potential energy curves expressed by Morse functions representing two electronic states of a molecule with their various vibrational states, dependent on the nuclear coordinates. The upper potential is shifted to a greater equilibrium bond length due to more antibonding character of electronically excited states [98, 99]. For organic fluorophores in the visible range, characterized by delocalized π -electron systems, this shift is rather small. At room temperature the fluorophore usually exists at the lowest vibrational level of the electronic ground state S_0 [46]. Since the transition to the electronically excited state S_1 is much faster than the movement of the nuclei, the transition occurs without a change in the nuclear coordinates of the molecule. Therefore, the excitation process is illustrated with a vertical arrow and this transition is called a vertical transition. The probability of a transition to a certain vibrational level is given by the Franck-Condon factor. The Franck-Condon factor,

$$\chi_{\text{FC}} = |\langle \chi_f | \chi_i \rangle|^2, \quad (2.20)$$

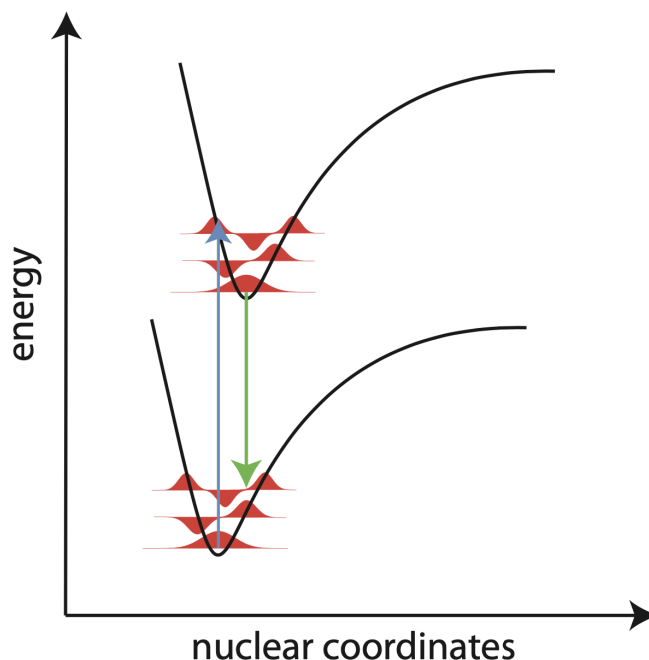


Fig. 2.3: Illustration of the Franck-Condon principle [5]. Solid black lines are two electronic states represented by Morse functions. Each state contains multiple vibrational states (red). After excitation (blue arrow) the fluorophore is most likely excited to a state, where the wave functions of the initial and excited state have the largest overlap. The same holds for the return to the ground state (green arrow).

is the square of the overlap integral of the vibrational (nuclear) wave functions of the initial χ_i and final state χ_f . This means that a transition is most likely to happen to an excited state, which vibrational wave function has the largest overlap with the vibrational wave function of the initial state [98]. Following excitation, the fluorophore rapidly decays to the lowest vibrational level of the electronically excited state [46]. Like described in section 2.1, the rapid decay to the lowest vibrational state in combination with a comparatively long lifetime of S_1 is the reason for Kasha's rule that fluorescence emission will occur from the vibrational ground state of S_1 [45, 100]. Since the Franck-Condon principle applies to both, absorption and emission (see Fig. 2.3), most dyes show a mirror symmetry of the $S_0 \rightarrow S_1$ absorption and emission [45, 46]. As a result of the energy losses due to vibrational relaxations in both, the electronically excited state as well as the electronic ground state, the wavelength of fluorescence photons is larger than the wavelength of the absorbed photons. This phenomenon is called Stokes shift (see Fig. 2.4). The Stokes shift is defined as the energy difference $\Delta\bar{\nu}_s$ between the maximum of the first absorption band $\bar{\nu}_a^{\max}$ and the maximum of the fluorescence spectrum $\bar{\nu}_f^{\max}$, given in wavenumbers [47, 101]

$$\Delta\bar{\nu}_s := \bar{\nu}_a^{\max} - \bar{\nu}_f^{\max} \quad (2.21)$$

or wavelengths of maximum absorption λ_a^{\max} and fluorescence emission λ_f^{\max}

$$\Delta\lambda_s = \lambda_f^{\max} - \lambda_a^{\max}. \quad (2.22)$$

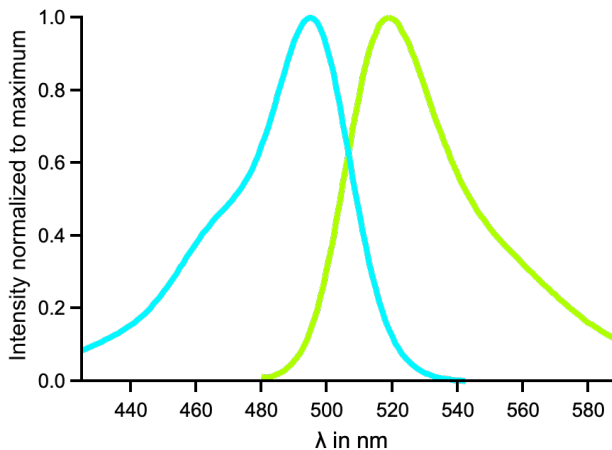


Fig. 2.4: Illustration of the Stokes shift of the fluorophore Alexa Fluor 488. The Stokes shift represents the shift between the maximum of the absorption (cyan) and emission spectrum (green). The small shoulder visible in the absorption spectrum corresponds to the $S_0 \rightarrow S_2$ transition, being less intense due to a smaller Franck-Condon factor.

In solution, solvent relaxation is the most important mechanism leading to the Stokes shift.

2.1.2 Fluorescence lifetime

One important characteristic of fluorophores is the fluorescence lifetime τ_f . It describes the average time the molecule stays in the excited state prior to fluorescence emission [45, 46]. It is given by

$$\tau_f = \frac{1}{k_f + k_{nr}}, \quad (2.23)$$

where k_f describes the rate of fluorescence emission. The rate k_{nr} consists of the rates of all processes that can cause a non-radiative depopulation of the first excited singlet state S_1 . These include on the one hand intersystem crossing (ISC) and internal conversion (IC), discussed in section 2.1, with their respective rates k_{ISC} and k_{IC} , and on the other hand possible quenching processes explained in subsection 2.1.4, with the quenching rate k_q . Consequently, the rate of the non-radiative processes k_{nr} is the sum of all individual rates:

$$k_{nr} = k_{ISC} + k_{IC} + k_q. \quad (2.24)$$

For commonly used fluorophores, the lifetimes are usually in the range of nanoseconds. When k_{nr} equals zero and there are thus no non-radiative processes, one gets the natural lifetime τ_n , sometimes also called radiative lifetime

$$\tau_n = \frac{1}{k_f}. \quad (2.25)$$

Since the fluorescence lifetime τ_f indicates the average lifetime that a dye spends in the excited state S_1 , one can consider an ensemble of fluorophores. After excitation with an infinitely small pulse (δ -pulse), a certain number of fluorophores is in the excited state S_1 . The number of excited molecules then decreases with the rate

$$\frac{d[S_1]}{dt} = -\frac{1}{\tau_f}[S_1], \quad (2.26)$$

where $[S_1]$ is the concentration of excited fluorophores in S_1 . Integration from $t = 0$ to t gives the exponential decay

$$[S_1](t) = [S_1]_0 e^{-\frac{t}{\tau_f}}, \quad (2.27)$$

where $[S_1]_0$ describes the concentration of fluorophores in the excited state direct after the excitation with the δ -pulse. As the intensity of fluorescence is proportional to the number of excited fluorophores, the fluorescence lifetime is the time, where the intensity of fluorescence emission dropped to approximately 37% of the initial emission intensity at $t = 0$ (see Fig. 2.5a). This simple relation only holds for one existing fluorescence lifetime in the sample. For a mixture of fluorophores or the case of dynamic quenching for a portion of the fluorophores, one has to consider a multi-exponential decay (see Fig. 2.5b):

$$I(t) = \sum_{i=1}^n \alpha_i e^{-\frac{t}{\tau_i}} \quad (2.28)$$

with the condition

$$\sum_{i=1}^n \alpha_i = 1. \quad (2.29)$$

In the equations above, $I(t)$ is the fluorescence intensity at time t , τ_i the various fluorescence lifetimes and α_i the respective relative amplitudes of these lifetimes [46].

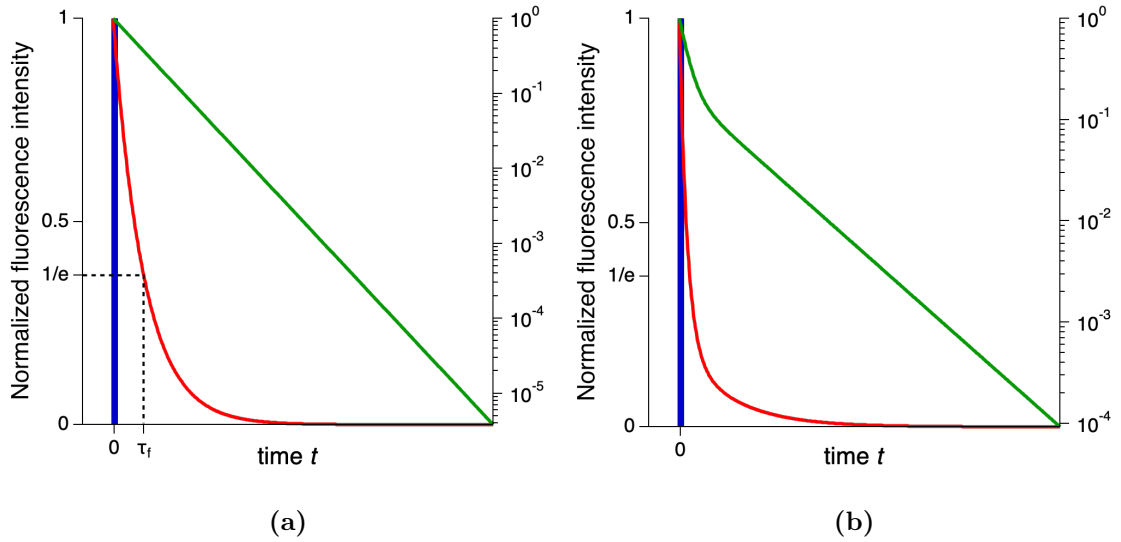


Fig. 2.5: Exponential decay of the fluorescence intensity (red) after excitation with a δ -pulse (blue) at time $t = 0$. The green curves show the logarithmic representation of fluorescence intensity. (a) In the simplest case, the decrease of fluorescence intensity can be described with a single exponential decay (Eq. 2.27). (b) For more complex decays a multi-exponential model has to be used to describe the fluorescence decay properly (Eq. 2.28).

2.1.3 Fluorescence quantum yield

Another attribute that plays an important role in the selection of dyes for fluorescence spectroscopic applications is the fluorescence quantum yield Φ_f . It is a measure of the efficiency of a fluorophore and is determined by the ratio of all emitted photons to all absorbed fluorescence photons:

$$\Phi_f = \frac{\text{number of emitted photons}}{\text{number of absorbed photons}} = \frac{k_f}{k_{\text{ex}}}. \quad (2.30)$$

In Eq. 2.30, k_{ex} describes the rate of absorbed photons and k_f the rate of emitted fluorescence photons, respectively. Since there are multiple non-radiative depopulation pathways, it is possible to express the fluorescence quantum yield with both, the rates of the non-radiative processes k_{nr} and the rate of fluorescence k_f :

$$\Phi_f = \frac{k_f}{k_f + k_{\text{nr}}}. \quad (2.31)$$

By using Eq. 2.23 and Eq. 2.25, the fluorescence quantum yield can be expressed in terms of the fluorescence lifetime and natural fluorescence lifetime τ_n with

$$\Phi_f = \frac{\tau_f}{\tau_n}. \quad (2.32)$$

2.1.4 Fluorescence quenching

Like described in subsection 2.1.2, the non-radiative depopulation rate of the excited state k_{nr} contains the rate of fluorescence quenching k_q . Fluorescence quenching is a term for processes, where interactions between fluorophores and other molecules lead to a reduction of the fluorescence intensity. The reduction of fluorescence intensity is described by the Stern-Volmer equation [46, 47]

$$\frac{I_0}{I} = 1 + K_{\text{SV}}[Q], \quad (2.33)$$

where I_0 and I are the fluorescence intensities without and with quenching, respectively. K_{SV} denotes the Stern-Volmer quenching constant and $[Q]$ the concentration of the quenching molecules. This relationship is shown in Fig. 2.6. Depending on the quenching mechanism one distinguishes between static and dynamic quenching [45, 47].

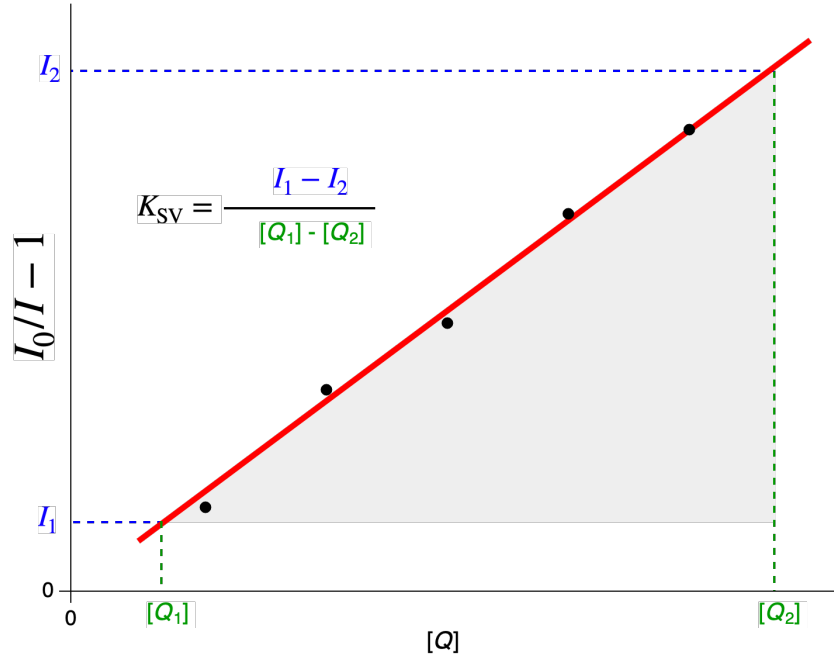


Fig. 2.6: Illustration of the Stern-Volmer relation, with the fluorescence intensity $I_0/I - 1$ in dependence on the concentration of quenching molecules $[Q]$. If the fluorescence intensity I is measured for different $[Q]$ (black dots), the Stern-Volmer constant K_{SV} can be determined by the slope of a linear regression (red). I_0 is the fluorescence intensity for $[Q] = 0$.

Static quenching

In the case of static quenching, complexes form between fluorophores and quencher molecules. These complexes are non fluorescent and lead to an immediate return to the ground state upon excitation, without emission of fluorescence photons. The Stern-Volmer constant for static quenching K_{SV}^{st} is then just the equilibrium constant according to the law of mass action:

$$K_{SV}^{st} = \frac{[FQ]}{[F][Q]}, \quad (2.34)$$

where $[FQ]$ is the concentration of the formed complex and $[F]$ and $[Q]$ are the concentrations of the uncomplexed fluorophore and the quencher molecule, respectively [45]. In a mixture of fluorophores and quencher molecules, the observed fluorescence lifetime and quantum yield of the fluorophores remain unchanged, because the photo physical properties of the photon emitting molecules are not affected (see Fig. 2.7a).

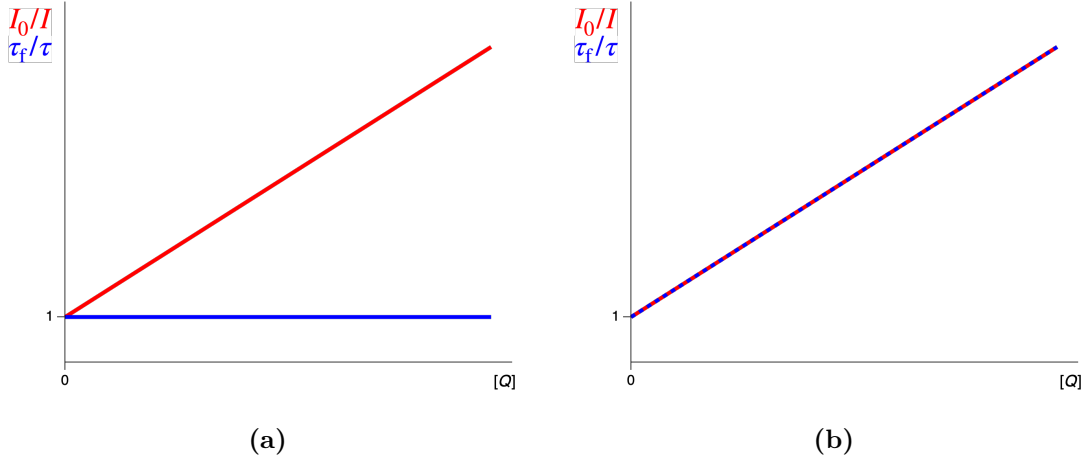


Fig. 2.7: Dependence of the fluorescence intensity I and lifetime τ_f on the concentration of quencher molecules $[Q]$ for (a) static (b) and dynamic quenching.

Dynamic quenching

In contrast to static quenching, dynamic quenching does not lead to formation of non-fluorescent complexes. Dynamic quenching occurs, when an excited fluorophore returns to the ground state without the emission of a photon due to the contact with a quencher [45, 102]. Referring to the underlying mechanism, dynamic quenching is also called collisional quenching [45]. The Stern-Volmer constant of dynamic quenching

$$K_{\text{SV}}^{\text{dyn}} = \tau_q K_{\text{Q}} \quad (2.35)$$

is the product of the fluorescence lifetime in absence of quenching molecules

$$\tau_q = \frac{1}{k_f + k_{\text{ISC}} + k_{\text{IC}}} \quad (2.36)$$

and the bimolecular quenching constant

$$K_{\text{Q}} = \frac{1}{[Q]} \left(\frac{1}{\tau_f} - \frac{1}{\tau_q} \right) \quad (2.37)$$

Dynamic quenching is an additional possibility to depopulate the excited state with the corresponding quenching rate

$$k_q = K_{\text{SV}}^{\text{dyn}} [Q] = \tau_q K_{\text{Q}} \quad (2.38)$$

Therefore, according to Eq. 2.23 and Eq. 2.31, this additional rate results in a reduced fluorescence lifetime and quantum yield. This is illustrated in Fig. 2.7b. Förster resonance energy transfer (FRET) (see section 2.4) can also be regarded as a dynamic quenching process, however, not mediated by collisions but by non-radiative excitation transfer.

2.1.5 Fluorescence and pressure

There are several parameters in spectroscopic experiments that can influence the fluorescence characteristics of the dyes attached to the molecules being investigated. One of these parameters, which is highly relevant for the present thesis, is pressure, which can influence the fluorescence lifetime of the fluorophores. This dependence between high pressures with up to several thousand bar and the fluorescence lifetime can be described by a relatively simple model [84]. Like described in subsection 2.1.2, the lifetime of a fluorophore can be expressed with the radiative and non-radiative decay rates. Therefore, for a certain pressure p , the lifetime is given by

$$\tau_f(p) = \frac{1}{k_{nr}(p) + k_f(p)}. \quad (2.39)$$

By using fluorophores with a high fluorescence quantum yield ($\Phi_f > 0.9$), the approximation of $\Phi_f \approx 1$ is assumed and the corresponding lifetime is dominated by the rate of fluorescence k_f [84]:

$$\tau_f(p) \stackrel{\Phi_f \approx 1}{\cong} \tau_n(p) = \frac{1}{k_f(p)}. \quad (2.40)$$

According to the Strickler-Berg equation, the rate of fluorescence emission is given by [96, 103]

$$k_f = \frac{1}{\tau_n} = 2.88 \cdot 10^{-9} n^2 \frac{\int F(\bar{\nu}) d\bar{\nu}}{\int F(\bar{\nu}) d\bar{\nu} / \bar{\nu}^3} \int \frac{\varepsilon(\bar{\nu})}{\bar{\nu}} d\bar{\nu}, \quad (2.41)$$

where F describes the intensity of fluorescence emission, $\bar{\nu}$ the wavenumber in cm^{-1} , ε the absorption coefficient of the dye and n the refractive index. As the refractive index of water changes with pressure, one can describe the pressure dependence of fluorescence emission in the simplest model by the change of the refractive index of the solvent [84, 104]:

$$k_f(p) = \frac{n^2(p)}{n^2(1 \text{ bar})} k_f(1 \text{ bar}). \quad (2.42)$$

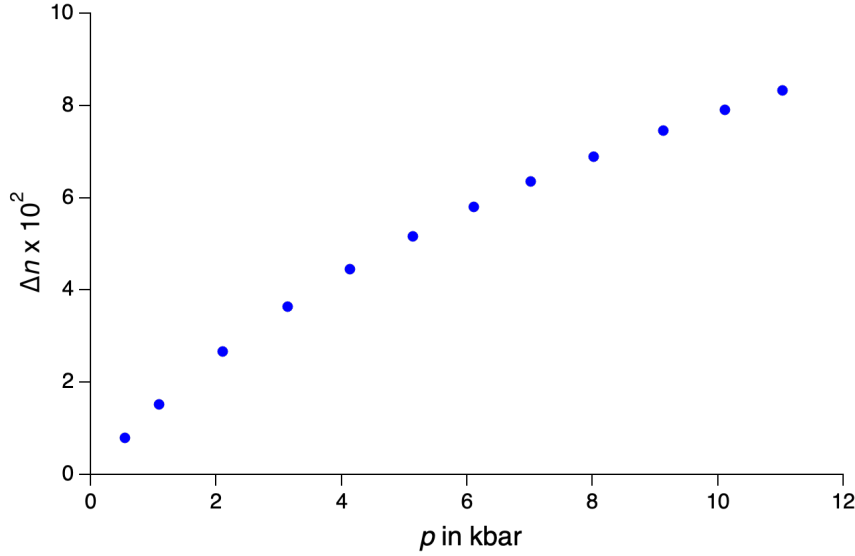


Fig. 2.8: Changes of the refractive index Δn of water with increasing pressure p at a wavelength λ of 546.1 nm. Data taken from [105].

With Eq. 2.40, one can rewrite Eq. 2.42 to

$$\tau_f(p) = \frac{n^2(1 \text{ bar})}{n^2(p)} \tau_f(1 \text{ bar}) \quad (2.43)$$

to obtain the pressure dependence of the fluorescence lifetime. The pressure dependence of the refractive index of water was studied by Vedam and Limsuwan and is shown in Fig. 2.8.

2.2 Confocal microscopy

Confocal microscopy was developed in the 1950s by Marvin Minsky as a postdoctoral student at Harvard University [106–108]. His goal was the investigation or rather imaging of neural networks of brain tissue in vivo [108]. The basic idea of this microscopy technique is the suppression of out of focus light, originating from within the sample, by using two pinholes, one in the excitation path and one in the detection path of the microscope [109]. This is shown in Fig. 2.9 with a schematic of Minsky’s confocal microscope. The first pinhole is placed in front of the lamp and generates a point light source, which is focussed into the sample via an objective lens and creates a small excitation volume. Light passing through the sample, or originating from within the sample, is collected in the same point and focussed on a second pinhole, which is positioned in front of the detector. This pinhole ensures that out

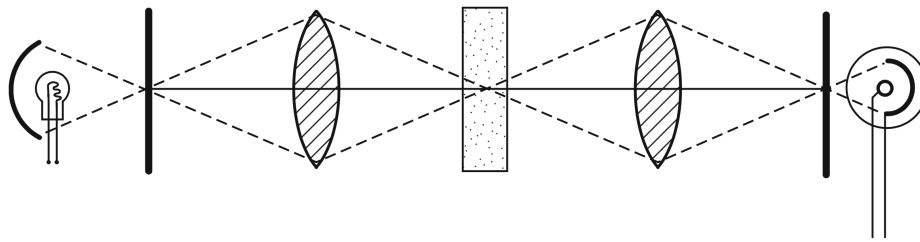


Fig. 2.9: Illustration of a simple confocal microscope invented by Marvin Minsky in the 1950s [106].

of focus light is mostly suppressed and light originating from the focal plane is mostly detected. Because the excitation pinhole and the detection pinhole share the same foci in the sample they are called confocal to each other, thus the term confocal microscopy. Nowadays, confocal microscopes are mainly used for fluorescence and are based on epi-illumination and with a laser as the light source (see Fig. 2.10) [109,110]. The laser light passes a pinhole and is reflected by a dichroic mirror to the objective, which focusses the laser light into the sample. The emitted fluorescence photons are collected by the same objective and directed to the dichroic mirror. Due to the Stokes shift and thus longer wavelength of the fluorescence photons in comparison to the wavelength of the laser (see subsection 2.1.1), they pass the mirror and are focussed onto the detection pinhole, which is placed in front of the detector [108, 111]. A consequence of the punctual illumination and detection is, that the entire sample must be scanned to acquire an image, since only the signal

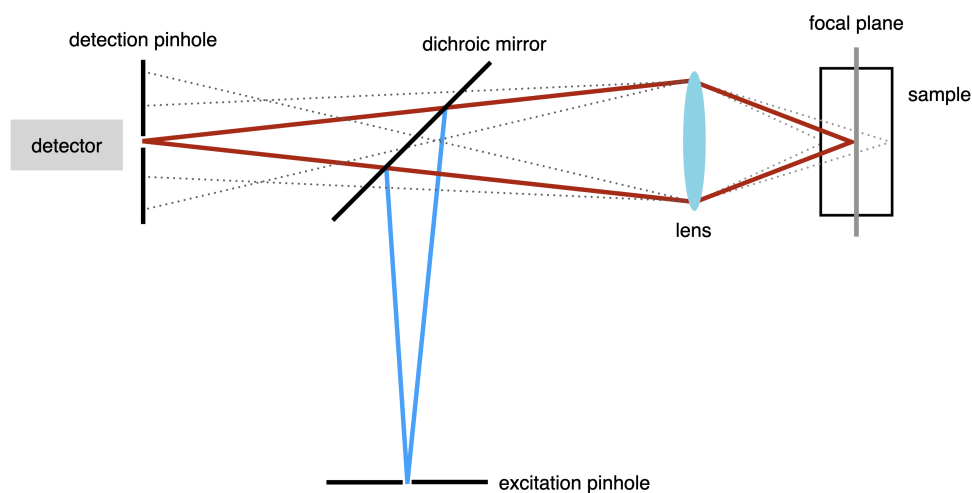


Fig. 2.10: Illustration of an epi-illumination confocal microscope. The light of a point light source is focussed into the sample. The light originating from the focal plane (red) is focussed onto a detection pinhole, before being detected. Light, which is emitted from below or above the focal plane is mostly blocked by the detection pinhole and not reaching the detector (dashed lines).

from a small section can be detected at once. Basically, there are two different approaches for scanning. Either the laser focus is fixed and the sample is moved by a piezo-driven scanning stage or the laser beam is moved over the sample with a galvanometer mirror scanner [96, 108]. The confocal principle can also be applied in parallel with many pinholes and a camera as the detector, which is the principle behind spinning-disc confocal scan units, similar to Minsky's original idea [112, 113]. For single molecule methods, the background suppression of the confocal principle is the most important advantage over conventional epi-fluorescence microscopy.

2.2.1 Excitation

As described in section 2.2, a laser is typically used to excite the fluorophores in a confocal microscope. The radial intensity distribution of a laser in the mode TEM₀₀ is described by the Gaussian function expressed with

$$I_{\text{las}}(r) = I_{\text{las},0} e^{-\frac{2r^2}{w^2}}, \quad (2.44)$$

with the laser intensity I_{las} at a certain distance r to the optical axis. The beam radius w denotes the distance to the optical axis, where the maximum intensity $I_{\text{las},0}$ dropped to $1/e^2$ [114–116]. Along the optical axis, the intensity of a focused laser beam is Lorentzian [73]. Therefore, the whole intensity profile of the laser beam can be written as

$$I_{\text{las}}(r, z) = I_{\text{las},0}(z) e^{-\frac{2r^2}{w(z)^2}} \quad (2.45)$$

with

$$I_{\text{las},0}(z) = \frac{2P_{\text{las}}}{\pi w^2(z)}. \quad (2.46)$$

The radius of the laser beam along the optical axis $w(z)$ is given by

$$w^2(z) = w_0^2 + z^2 \tan^2 \delta \quad (2.47)$$

with

$$w_0 = \frac{\lambda}{n\pi \tan \delta}. \quad (2.48)$$

In the equations above, z is the position along the optical axis, with the beam waist radius w_0 , positioned at $z = 0$. P_{las} is the laser power, n the refractive index of the sample, λ the wavelength and δ the angle of the focussed laser beam [73, 115, 117]. With the Rayleigh length z_r given by

$$z_r = \frac{\pi w_0^2 n}{\lambda}, \quad (2.49)$$

the dependence of the beam radius can be expressed as

$$w(z) = w_0 \sqrt{1 + \left(\frac{z}{z_r}\right)^2}. \quad (2.50)$$

Thus, the Rayleigh length marks the position along the optical axis, at which the beam radius $w(z)$ expanded to $\sqrt{2}w_0$, due to which it is called focal length or confocal parameter [115]. For distances with $z \gg z_r$, the beam radius increases approximately linearly with z [115, 117]:

$$w(z) = w_0 \frac{z}{z_r}, \quad (2.51)$$

which leads to

$$\delta = \lim_{z \rightarrow \infty} \frac{w(z)}{z} = \frac{\lambda}{\pi w_0 n}. \quad (2.52)$$

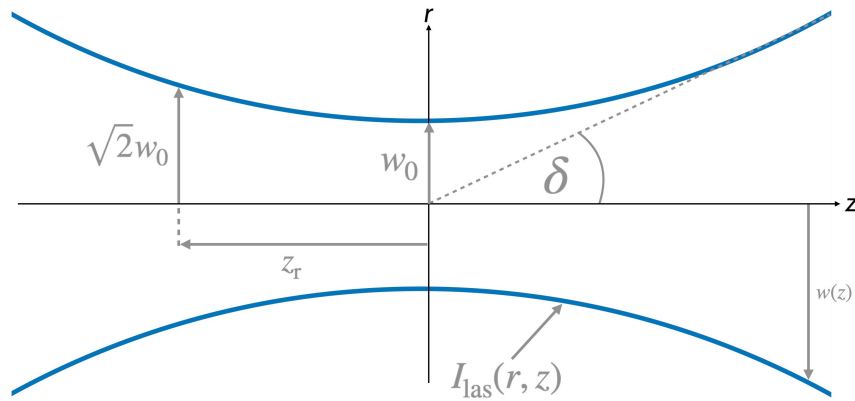


Fig. 2.11: Illustration of a Gaussian beam with the change of its beam radius w along the optical axis z . The beam radius is defined in such a way that it marks the distance to the optical axis, where the intensity has dropped to $I(0, z)/e^2$ (blue). w_0 is the beam waist radius at $z = 0$, which increases to $\sqrt{2}w_0$ at a distance of the Rayleigh length z_r . For $z \gg z_r$, the beam radius increases linearly with the angle δ .

For illustration purposes, Fig. 2.11 shows the propagation of a Gaussian beam with the discussed parameters used in Eq. 2.44 to Eq. 2.52.

2.2.2 Detection

The detection of a confocal setup can be described by the collection efficiency function $\text{CEF}(r, z)$ [45]. It takes the effect of the pinhole in the image plane of the microscope into account and determines the fraction of light emitted at point (r, z) in the sample passing the detection pinhole [73, 118]. The $\text{CEF}(r, z)$ is given by

$$\text{CEF}(r, z) = \frac{1}{\Delta} T_{\text{ph}}(r) \text{PSF}(r, r', z) dr, \quad (2.53)$$

where the $\text{PSF}(r, r', z)$ is the point spread function (PSF), describing the image of light emitted at point (r, z) in the sample space [73, 118]. $T_{\text{ph}}(r)$ is the transmission function of the pinhole and given by the disk function [73]

$$T_{\text{ph}}(r) = \text{circ}\left(\frac{r}{s_0}\right) \equiv \begin{cases} 1 & \text{if } |r| \leq s_0 \\ 0 & \text{if } |r| > s_0 \end{cases}, \quad (2.54)$$

where r is the projection of the radial coordinate to the image plane and s_0 represents the radius of the pinhole projected into the sample plane. Δ is a normalization factor given by

$$\Delta = \int \text{circ}\left(\frac{r}{s_0}\right) \text{PSF}(r, 0, 0) dr. \quad (2.55)$$

2.2.3 Observation Volume

The effective observation volume of a confocal microscope is described by the molecule detection efficiency (MDE). It takes the excitation characteristics of a focussed Gaussian laser beam (see subsection 2.2.1) into account and considers the detection efficiency of the confocal setup, including the influence of the detection pinhole (see subsection 2.2.2) as well. Therefore, the MDE can be written as the product of the $\text{CEF}(r, z)$ and the intensity distribution of the laser beam [45, 73]:

$$\text{MDE}(r, z) = I_{\text{las}}(r, z) \text{CEF}(r, z). \quad (2.56)$$

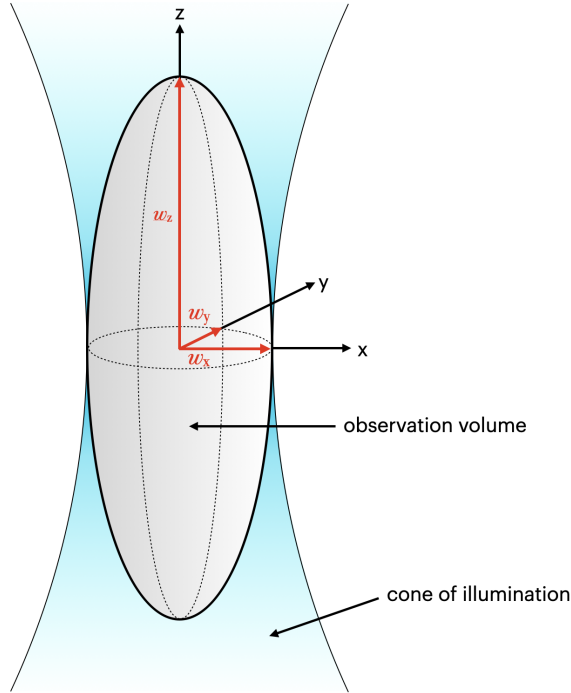


Fig. 2.12: The observation volume in confocal microscopy is often approximated with a three-dimensional Gaussian, with the axial radius w_z and lateral radius w_{xy} .

In confocal microscopy, the brightness profile of the MDE is usually approximated with a three-dimensional Gaussian (see Fig. 2.12) [119]. This leads to

$$\text{MDE}(r, z) = I_0 e^{-\frac{2r^2}{w_0^2}} e^{-\frac{z^2}{z_0^2}}, \quad (2.57)$$

with the radii in the radial and axial direction, denoted with w_0 and z_0 , respectively. They mark the distance at which the maximum laser intensity I_0 has dropped to $1/e^2$.

2.2.4 Resolution

In conventional light microscopy as well as in confocal microscopy the resolution is limited by diffraction. Thus, even an infinitely small point is not imaged as an infinitely small point in the image plane, like in geometrical optics, but as a diffraction image [120]. The size and shape of the diffraction pattern is described by the point spread function (PSF). For a circular aperture the diffraction image is described by the Fraunhofer diffraction at a circular aperture [114, 120]. The PSF can be expressed by using reduced variables

$$\zeta(z) = \frac{2\pi}{n\lambda} \text{NA}^2 z \quad (2.58)$$

and

$$\rho(r) = \frac{2\pi}{\lambda} \text{NA} r \quad (2.59)$$

for the description of the PSF along the optical axis z or transverse to the optical axis r , respectively [116,120]. In Eq. 2.58 and Eq. 2.59, NA is the numerical aperture of the objective, which is given by

$$\text{NA} = n \cdot \sin \alpha, \quad (2.60)$$

where n is the refractive index of the medium and α is the half angle of the aperture. At the focal plane $\zeta = 0$, the PSF is rotationally symmetric and given by

$$\text{PSF}(0, \rho) = \frac{2J_1^2(\rho)}{\rho^2}, \quad (2.61)$$

with the first-order Bessel function J_1 [114, 116]. The resulting diffraction pattern, called Airy Pattern, is shown in Fig. 2.13. The central maximum of this pattern is called Airy disk. Both are named after the astronomer Sir George Bidell [114]. Along the optical axis at $\rho = 0$ the PSF yields

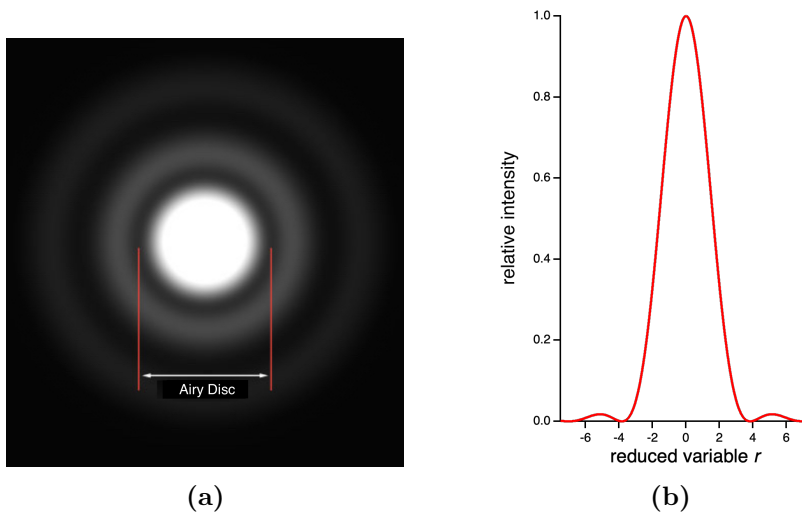


Fig. 2.13: (a) Fraunhofer diffraction pattern of a circular aperture [117] and (b) its radial intensity distribution. The central maximum of the pattern is called an Airy disk.

$$\text{PSF}(\zeta, 0) = \left(\frac{\sin(\zeta/4)}{\zeta/4} \right)^2. \quad (2.62)$$

The resolution of an optical system depends on how far apart two points in the object plane have to be, in order to still be able to differentiate their point spread functions in the image plane. According to the Rayleigh criterion, two equally bright spots can be resolved, if the center of one Airy disk lies in the first minimum of the other Airy pattern [111, 114, 116]. This is illustrated in Fig. 2.14. Therefore, the radius of the Airy disk r_{Airy} is given by the first zero of the Bessel function $J_1(\rho) = 0$, which is at $\rho \approx 3.83$. With Eq. 2.59 one gets

$$r_{\text{Airy}} = \frac{0.61\lambda}{\text{NA}} \quad (2.63)$$

for the radius of the Airy disk for wide field microscopy [114]. The axial resolution along the optical axis is lower than the radial resolution. The minimum distance which is distinguishable in the axial direction is given by [111, 120]

$$z = \frac{2\lambda n}{\text{NA}^2}. \quad (2.64)$$

In the case of confocal microscopy the PSF_{conf} is the product of both PSFs, of excitation (PSF_{exc}) and detection (PSF_{det}):

$$\text{PSF}_{\text{conf}} = \text{PSF}_{\text{exc}} \times \text{PSF}_{\text{det}}. \quad (2.65)$$

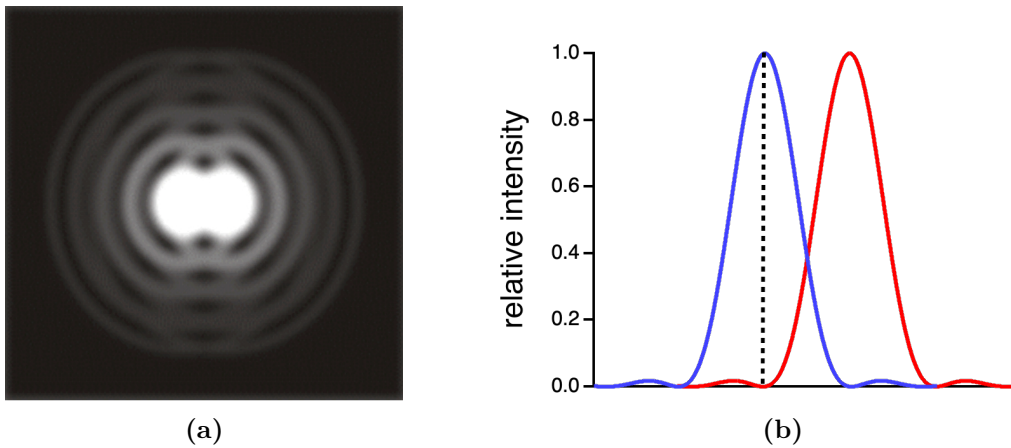


Fig. 2.14: (a) Diffraction pattern of two light sources at a distance according to the Rayleigh criterion [117]. (b) shows a graph of the corresponding intensity distributions. The distance is the radius of the Airy disk. The maximum of one Airy disk has the position of the first minimum of the other Airy pattern.

This leads to an improved resolution in the radial as well as axial direction, due to a sharper-peaked PSF in the confocal case, in contrast to wide field illumination (see Fig. 2.15). The resolvable distances for confocal optics are given in Eq. 2.66 for the lateral direction and in Eq. 2.67 for the axial direction, respectively:

$$r_{\text{conf}} = \frac{0.61 \lambda}{\sqrt{2} \text{NA}}, \quad (2.66)$$

$$z_{\text{conf}} = \frac{1.5\lambda n}{\text{NA}^2}. \quad (2.67)$$

Notably, Fig. 2.15 shows the suppression of the side peaks of the PSFs. The consequence is a reduction of background light from bright objects [116]. It has to be noted that the expressions from Eq. 2.66 and Eq. 2.67 are only valid for an infinitely small pinhole. Since one could detect no photons with an infinitely small pinhole, one has to choose the size of the pinhole in compromise between resolution and signal strength. In many cases a pinhole diameter equal to the diameter of the Airy disk is used, which transmits approximately 80 % of the light originating at the focal plane with a resolution gain of about 10 % [111, 121]. In single molecule applications, however, the detection efficiency is of utmost importance. Therefore, the pinhole is chosen in such a way that the transmission is close to unity.

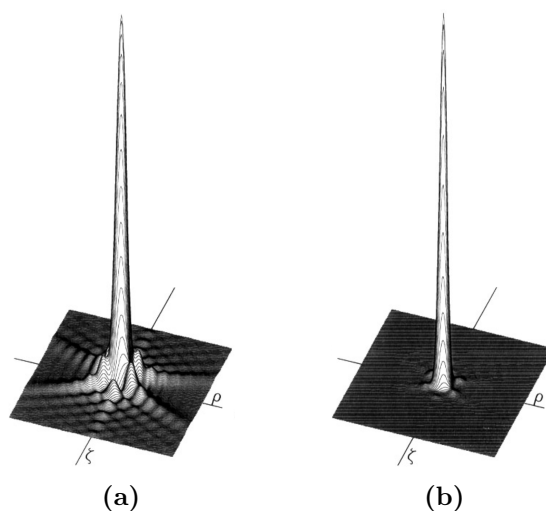


Fig. 2.15: PSFs of a (a) conventional and (b) confocal microscope as a function of the reduced variables ζ (Eq. 2.58) and ρ (Eq. 2.59). Image taken from [116].

2.3 Single molecule spectroscopy

In 1976, Hirschfeld reported experiments with single molecule sensitivity by investigating individual antibody molecules [122]. However, these antibodies were labeled with about 80-100 fluorophores [122, 123]. In 1989, Moerner and Kador demonstrated with their experiments the optical detection and spectroscopy of a single fluorophore molecule (sm) in a solid at low temperatures [42, 124, 125]. One year later, Orrit and Bernard measured the fluorescence signal of single fluorophores [125, 126]. Since then, the use of single molecule spectroscopic methods has rapidly grown [123]. Briefly after these first experiments at low temperatures, sm-experiments at room temperature were realized [41, 127, 128]. Due to the improvement of confocal microscopes in the late 1980s and early 1990s and their capability to perform sm-experiments, the field of single molecule spectroscopy experienced another boost. The strong interest in the fields of chemistry, physics and biophysics and the further improvement of the procedures and techniques is the reason why there are numerous single molecule methods available and used today [125].

One of these methods is fluorescence correlation spectroscopy (FCS), which investigates the time dependent fluctuations of fluorophores (see section 2.5). Another example is single molecule Förster resonance energy transfer (smFRET), discussed in section 2.4. Both, FCS and FRET experiments were carried out within the scope of this work. The motivation to study single molecules is founded in the inherent heterogeneity of biological macromolecules [71]. These characteristics of individual molecules are lost in experiments of molecule ensembles, since all properties are being averaged. For this reason single molecule studies are of great interest and provide the highest level of sensitivity [123]. The investigation of single molecules ensures that only one configuration can be assumed at any given time. This allows for the analysis of multiple folding states of a protein and eventually the study of rare and short lived intermediate states not visible in the ensemble regime [71]. One can, e.g., study kinetic pathways between multiple internal states of a molecule or binding rates [42, 129]. This monitoring of kinetic pathways can be achieved without the need for synchronization, necessary in ensemble experiments [45, 123]. The time range of dynamics accessible in experiments with freely diffusing molecules is defined by the time they spend in the focal volume. All dynamics on a timescale larger than their diffusion time can not be determined. According to the ergodic principle, the ensemble average of a physical quantity at a given time should give the same information like the time average over the same quantity for one specific particle. It follows that without artifacts, a single molecule experiment should additionally provide the information an ensemble experiment gives [71, 102]. In order to perform single molecule experiments successfully, two prerequisites must be met. First, one has to ensure that only one molecule is probed at a given time. Second, a high signal-to-noise ratio is needed (see subsection 2.3.1). Therefore, for experiments of freely diffusing molecules at room temperature, a confocal microscope can be used to satisfy these conditions (see section 2.2). It enables a small observation volume

Tab. 2.2: Probabilities p of having a number of n fluorophores in the focal volume, when the average number of fluorophores in the focal volume is $\langle N \rangle$. Values calculated using Eq. 2.68.

$\langle N \rangle$	$p(n = 0)$	$p(n = 1)$	$p(n > 1)$
1.00	0.368	0.368	0.264
0.50	0.607	0.303	0.090
0.10	0.905	0.090	0.005
0.05	0.951	0.048	0.001

down to 10^{-15} l and a high suppression of background signals. To assure that only signals of a single molecule are detected at a time, a highly diluted sample is mandatory [45, 71]. Due to the underlying Poisson statistics, the probability for a certain number of fluorophores in the focal volume n can be determined by using

$$P(n, \langle N \rangle) = \frac{\langle N \rangle^n}{n!} e^{-\langle N \rangle}, \quad (2.68)$$

with $\langle N \rangle$ being the average number of fluorophores in the focal volume during the experiment [45]. Tab. 2.2 shows example values for the probability of having no, one or more than one fluorophore in the focal volume at a time for multiple values of $\langle N \rangle$. It follows that a low sample concentration associated with a low $\langle N \rangle$ can lead to negligibly small probabilities for having more than one fluorophore in the focus at the same time. Nevertheless, already at $\langle N \rangle = 0.5$, it is most likely to have no fluorophore in the focal volume. Since the probability is further growing with decreasing sample concentration, it is not practical to make the concentration too low, due to a prolonged measurement time.

Rather than analyze freely diffusing molecules, there is the possibility to immobilize the molecules of interest. To this end, they can be, e.g., immobilized in a gel, in liposomes or even directly tethered to the coverslip via hydrogen bonds. However, these methods will not be discussed in detail, as they were not being used in this thesis.

2.3.1 Signal-to-noise ratio

One of the most important requirements for single molecule fluorescence measurements is a high signal-to-noise ratio (SNR). It describes the ratio between the signal, for example the fluorescence emission, and noise [96, 111]:

$$\text{SNR} = \frac{\text{fluorescence signal}}{\text{noise}}. \quad (2.69)$$

Typically, the fluorescence signal in single molecule experiments is the number of detected photons in a given time interval [96]. Since this number of emitted and detected fluorescence photons obeys a Poisson distribution with an average number of detected photons $\langle N \rangle$, the standard deviation $\Delta\langle N \rangle$ of this distribution is given by

$$\Delta\langle N \rangle = \sqrt{\langle N \rangle}. \quad (2.70)$$

Thus, random fluctuations of the fluorescence signal itself, the number of photons, lead to noise, which is called shot noise [111]. Furthermore, background signals are contributing to the total number of detected photons as well. This background originates from laser excitation and induced elastic Rayleigh and inelastic Raman scattering and is linearly dependent on the laser intensity [96]. Another contribution is the dark count rate of the detector, which is independent from the laser excitation power and therefore a constant in the signal. Taking the sources of noise into account, the SNR can be expressed by

$$\text{SNR} = \frac{\eta_{\text{det}} R}{\sqrt{\eta_{\text{det}} R + C_{\text{b}} I_{\text{las}} + N_{\text{d}}}} \sqrt{T_{\text{int}}}, \quad (2.71)$$

with the detection efficiency of the detector η_{det} , the emission rate of fluorescence R , the laser intensity I_{las} , the dark count rate of the detector N_{det} and the integration time T_{int} . C_{b} is the constant of proportionality between laser intensity and laser-induced background photon rate (see Fig. 2.16).

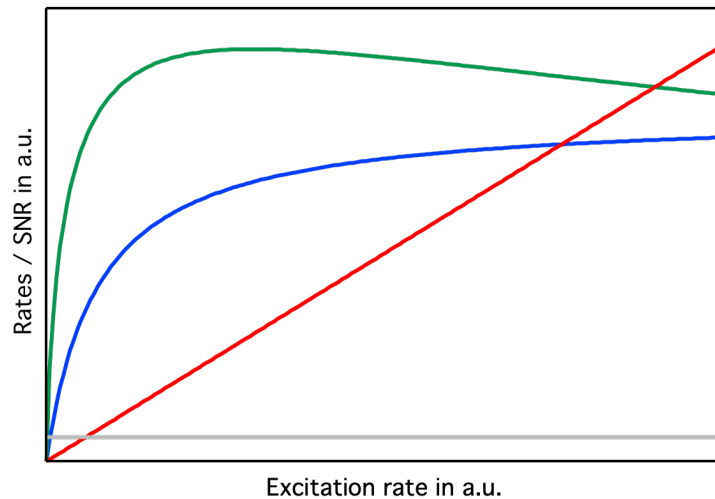


Fig. 2.16: Signal-to-noise ratio (SNR) as a function of the laser excitation rate according to Eq. 2.71. Besides the SNR (green), the fluorescence intensity of a single molecule (blue), laser-induced background (red) and the dark count rate of the detector (gray) are illustrated as well. Image taken and modified from [96].

Although, the laser intensity where the SNR is at maximum seems to be the natural choice, the experiments are typically run at laser intensities close to the maximum as an increase of the laser intensity does not lead to a significant increase of the SNR, but to an increase of the photobleaching probability.

2.4 Förster resonance energy transfer

Förster resonance energy transfer (FRET) refers to a non-radiative energy transfer between two fluorophores called donor and acceptor [45–47]. After the absorption of a photon, the excited donor can transfer its energy to the acceptor via dipole-dipole interactions. As a result of this process, the acceptor is excited from the ground state to an excited singlet state and the donor returns to the ground state without the emission of a photon. This is illustrated in Fig. 2.17 in a simplified Jablonski diagram. The first theoretical description of FRET was made by Theodor Förster in 1948 for chemical identical donor and acceptor fluorophores, named homo transfer [48]. Then, in 1967, Stryer and Haugland showed for chemical distinct fluorophores (hetero transfer) that the strong distance dependence of the transfer makes it suitable for distance determinations in the range of a few nanometers [49]. Thus, by labeling molecules, proteins or specific domains of proteins with donor and acceptor fluorophores, one can investigate inter- and intramolecular distances or distance changes. The rate of the energy transfer k_T is derived from Fermi’s golden rule [130] and can be formulated as follows:

$$k_T = \frac{1}{r_{da}^6} \frac{\Phi_d}{\tau_d} \frac{\kappa^2 9000 \ln(10)}{128\pi^5 n^4 N_A} J. \quad (2.72)$$

In this equation, r_{da} refers to the distance between the donor and acceptor fluorophore. Φ_d and τ_d are the fluorescence quantum yield and fluorescence lifetime of the donor fluorophore without the existence of an acceptor fluorophore, hence without FRET. The orientation factor κ^2 accounts for the relative orientation between donor and acceptor (see subsection 2.4.2). N_A and n are the Avogadro constant and the refractive index of the solvent, respectively. Lastly, J represents the overlap integral between the emission spectrum of the donor and the absorption spectrum of the acceptor fluorophore (see subsection 2.4.1). A characteristic quantity of FRET is the Förster radius R_0 , which specifies the distance of donor and acceptor, at which the rate of the energy transfer equals the sum of all other possible relaxation rates of the excited donor. Therefore,

$$k_T = \frac{1}{\tau_d} \quad (2.73)$$

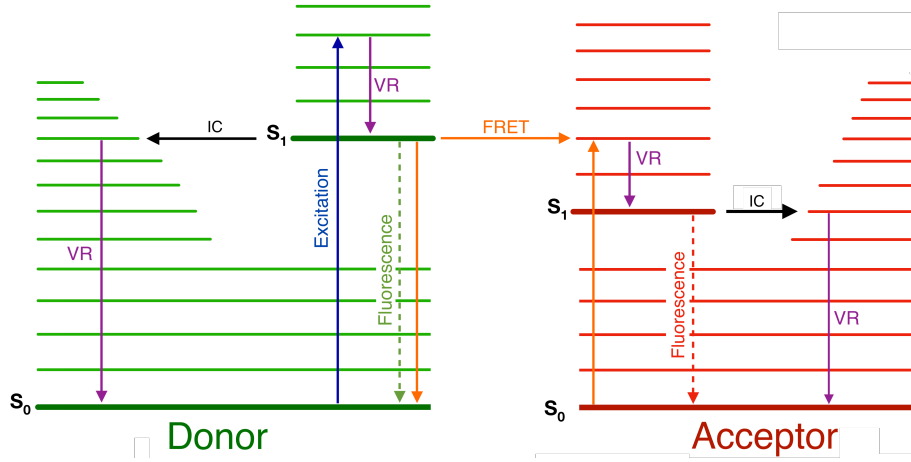


Fig. 2.17: Simplified Jablonski diagram to illustrate FRET. Shown are two singlet states S_0 and S_1 from both, the donor and acceptor fluorophore. Thick lines represent electronic and thinner lines vibrational states. Possible excitation and depopulation pathways are discussed in section 2.1. FRET provides an additional depopulation pathway for the donor, which can transfer its energy in a non-radiative manner to the acceptor (\rightarrow), followed by a non-radiative transition to its ground state (\downarrow). The acceptor is excited to a higher electronic state (\uparrow) and can emit a fluorescence photon of its own. VR: vibrational relaxation, IC: internal conversion.

applies and Eq. 2.72 yields

$$R_0 = \sqrt[6]{\frac{\kappa^2 \Phi_d 9000 \ln(10)}{128 \pi^5 n^4 N_A}} J. \quad (2.74)$$

For common fluorophores, the Förster radius is in the range of approximately 15 Å to 60 Å [47]. Substituting Eq. 2.74 in Eq. 2.72 gives

$$k_T = \frac{1}{\tau_d} \left(\frac{R_0}{r_{da}} \right)^6 \quad (2.75)$$

for the transfer rate k_T . As it is not trivial to experimentally access the transfer rate, one usually determines the transfer efficiency. The transfer efficiency of the process E_T is defined as the ratio of the number of energy transfers to the acceptor to the number of total absorbed photons of the donor fluorophore [131]:

$$E_T := \frac{\text{number of energy transfers}}{\text{number of absorbed photons}}. \quad (2.76)$$

By using the rates of the underlying radiative and non-radiative processes, the transfer efficiency can be expressed with

$$E_T = \frac{k_T}{k_T + k_{\text{ISC}} + k_{\text{IC}} + k_q + k_f} = \frac{k_T}{k_T + \tau_d^{-1}}. \quad (2.77)$$

On the other hand, by using Eq. 2.75, the transfer efficiency can be related to the distance of the fluorophores and the Förster radius:

$$E_T = \frac{R_0^6}{R_0^6 + r_{\text{da}}^6} = \frac{1}{1 + r_{\text{da}}^6/R_0^6}. \quad (2.78)$$

This equation shows that the Förster radius of a donor acceptor pair corresponds to their distance where the FRET efficiency is 0.5. Eq. 2.78 highlights the strong distance dependence of FRET due to the underlying dipole-dipole interactions and thus dependence on the inverse sixth power of the distance between the fluorophores. Substantiating the reference to a spectroscopic ruler, this distance dependence is shown in Fig. 2.18 for multiple ratios of the donor acceptor distance and the Förster radius.

To obtain the efficiency of the transfer experimentally, there are several possibilities. The most common approach is based on the determination of fluorescence intensities of the donor emission I_d and acceptor emission I_a , respectively:

$$E_T = \frac{I_a}{I_a + I_d}. \quad (2.79)$$

As mentioned above, in single molecule experiments, photons are counted instead of intensities measured. Since the fluorescence intensity is proportional to the number of emitted and thus detected photons of the donor and the acceptor, Eq. 2.79 still holds for the number of detected donor and acceptor photons, F_d and F_a and is mostly used in single molecule FRET experiments (see subsection 2.4.3):

$$E_T = \frac{F_a}{F_a + F_d}. \quad (2.80)$$

Both equations, Eq. 2.79 and Eq. 2.80, are only valid for fluorescence quantum yields and detection efficiencies of the detectors of one. Since this is not the case for real experiments, one can account for this deviation with the correction factor

$$\gamma_{\text{cor}}^{\text{FRET}} = \frac{\Phi_a \eta_a}{\Phi_d \eta_d}, \quad (2.81)$$

which includes the quantum yields of the acceptor and donor dyes (Φ_a, Φ_d) and their detection efficiencies with the detection system being used (η_a, η_d) [46]. With the correction factor from Eq. 2.81, the transfer efficiency results in

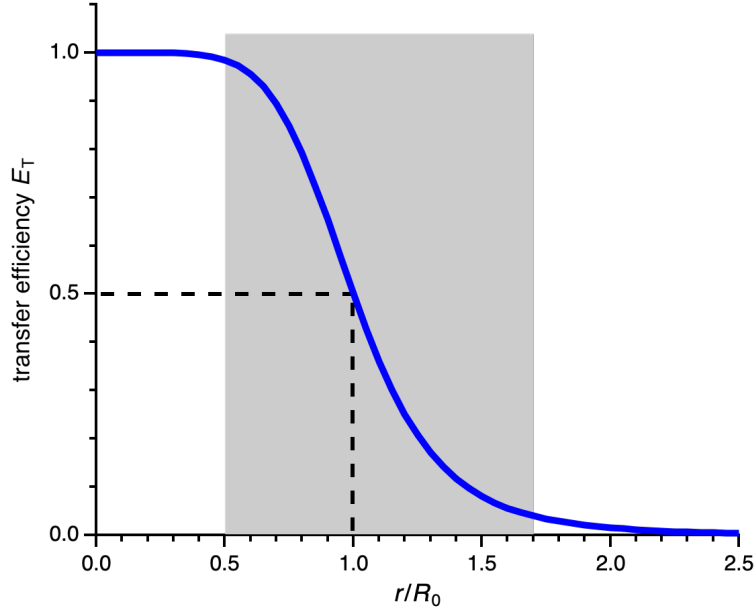


Fig. 2.18: Transfer efficiency E_T as a function of the donor acceptor distance expressed as the ratio of fluorophore distance r_{da} and their respective Förster radius R_0 . It marks the distance, where $E_T = 0.5$. Since small changes in the fluorophore distance have highest effects between $\approx 0.5 R_0$ and $1.7 R_0$ (gray area), that range is favorable for FRET experiments.

$$E_T = \frac{F_a}{F_a + \gamma_{\text{cor}}^{\text{FRET}} F_d}. \quad (2.82)$$

FRET can be considered as a dynamic quenching process (see subsection 2.1.4) that lowers the fluorescence emission of the donor in the presence of the acceptor. By determining the number of emitted donor photons in a certain time interval with and without the existence of the acceptor, denoted with F_d^a and with F_d , respectively, E_T can be expressed as

$$E_T = 1 - \frac{F_d^a}{F_d}. \quad (2.83)$$

Since dynamic quenching processes reduce the fluorescence lifetime as well, one can obtain the FRET efficiency via the fluorescence lifetime of the donor with τ_d^a and τ_d without the presence of the acceptor dye:

$$E_T = 1 - \frac{\tau_d^a}{\tau_d}. \quad (2.84)$$

From the experimentally determined FRET efficiency, eventually the donor and acceptor distance r_{da} can be calculated with

$$r_{\text{da}} = R_0 \sqrt[6]{\frac{1 - E_{\text{T}}}{E_{\text{T}}}}. \quad (2.85)$$

Depending on the type of experiment and the sample to be analyzed, it is important to choose suitable fluorophores. Besides their fluorescence characteristics like the fluorescence lifetime, quantum yield as well as their absorption and emission characteristics, one has to take their Förster radius into account, which is an important quantity for donor acceptor pairs. For distance measurements, the optimal choice for the Förster radius would be in the centre of the donor acceptor distance range. This is evident by looking at Fig. 2.18, again. For distances of donor and acceptor in a range of approximately $0.5R_0 < r_{\text{da}} < 1.7R_0$, small changes in their distance have a significant effect on the transfer efficiency, whereas distance changes outside this interval lead to almost no measurable changes.

2.4.1 Overlap integral

One requirement for the energy transfer is the spectral overlap between the donor and acceptor fluorophore reflecting the resonance condition. More precisely, there has to be an overlap between the emission spectrum of the donor and the excitation spectrum of the acceptor. This is shown in Fig. 2.19. The overlap integral is given by

$$J = \int_0^{\infty} I_{\text{d}}(\lambda) \varepsilon_{\text{a}}(\lambda) \lambda^4 d\lambda \quad (2.86)$$

with the normalized donor fluorescence spectrum

$$\int_0^{\infty} I_{\text{d}}(\lambda) d\lambda = 1, \quad (2.87)$$

where I_{d} is the intensity of the donor, λ the wavelength and $\varepsilon_{\text{a}}(\lambda)$ the extinction spectrum of the acceptor. The overlap integral is shown in Fig. 2.19 as well.

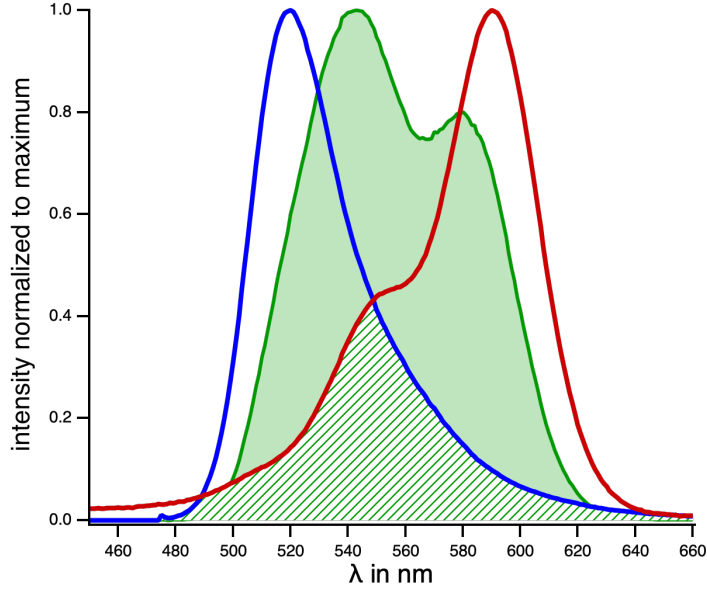


Fig. 2.19: Overlap integral (green) and spectral overlap (green lines) between Alexa Fluor 488 and Alexa Fluor 594 as an example. The spectral overlap between the emission spectrum of the donor (blue) and the absorption spectrum of the acceptor (red) is a prerequisite for FRET. The overlap integral results according to Eq. 2.86.

2.4.2 Orientation factor

Another factor, which influences the FRET efficiency is the relative orientation and location of the transition dipoles of the donor and acceptor fluorophores to each other. This is accounted by the orientation factor κ^2 (Eq. 2.72) according to [45,47]

$$\kappa^2 = (\cos \theta_t - 3 \cos \theta_d \cos \theta_a)^2 \quad (2.88)$$

or

$$\kappa^2 = (\sin \theta_d \sin \theta_a \cos \phi - 2 \cos \theta_d \cos \theta_a)^2, \quad (2.89)$$

respectively. The different angles are illustrated in Fig. 2.20, where θ_t denotes the angle between the transition moments of donor and acceptor. The angles θ_a and θ_d are the angles between the connection vector \mathbf{r} and the transition dipole of acceptor and donor, respectively. ϕ is the angle between the planes of the dipoles [45, 47, 131]. It follows that depending on the orientation, κ^2 takes values between 0 for perpendicular and 4 for collinear transition dipoles. For experiments, where the fluorophores can rotate freely in solution one assumes the isotropic dynamic average with a value of $\kappa^2 = \frac{2}{3}$. This dynamic average is valid if the rotational correlation

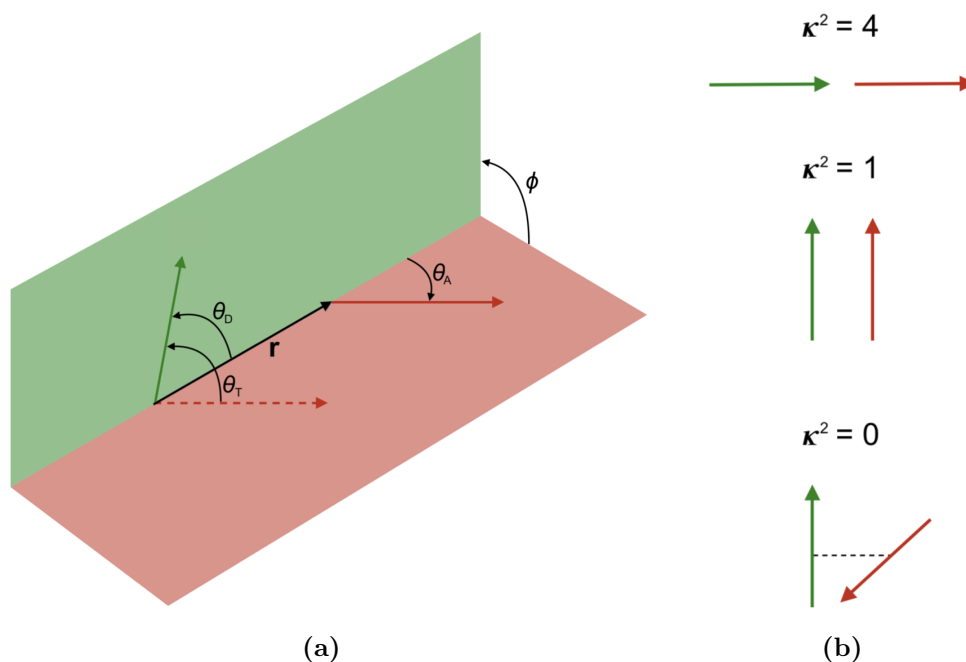


Fig. 2.20: (a) shows the relative orientation of the transition dipoles of the donor (green arrow) and acceptor (red arrow) to each other. The green and red areas represent the dipole planes of donor (green) and acceptor (red). θ_t denotes the angle between the transition dipoles of donor and acceptor and θ_d and θ_a are the angles between these transition dipoles and the separation vector \mathbf{r} . ϕ is the angle between the planes of the dipoles. (b) Specific orientations, where κ^2 yields 4, 1 or 0.

time is much faster than the fluorescence lifetime of the donor [47]. It has to be emphasized that the FRET shortened fluorescence lifetime of the donor has to be considered here.

2.4.3 Single molecule FRET

Single molecule FRET (smFRET) is a powerful and versatile tool to investigate conformational states of (bio-)macro molecules in the process of protein folding and unfolding. As described in section 2.3, single molecule techniques enable the investigation of one molecule at a time, rather than collecting the signal of a whole molecule ensemble at once. This is illustrated in Fig. 2.21 for FRET experiments. In the case of smFRET one can distinguish different folding states with varying transfer efficiencies in one measurement. By using a confocal microscope (see section 2.2) in conjunction with a highly diluted sample, it is assured that only single labelled molecules are detected. According to Poissonian statistics, this implies that most of the time the detection volume is empty (see Tab. 2.2). When proteins diffuse into the observation volume, the attached donor fluorophore is excited with subsequent fluorescence emission of either the donor or the acceptor (see section 2.4). Due to

the low sample concentration the transient intensities in smFRET experiments fluctuate

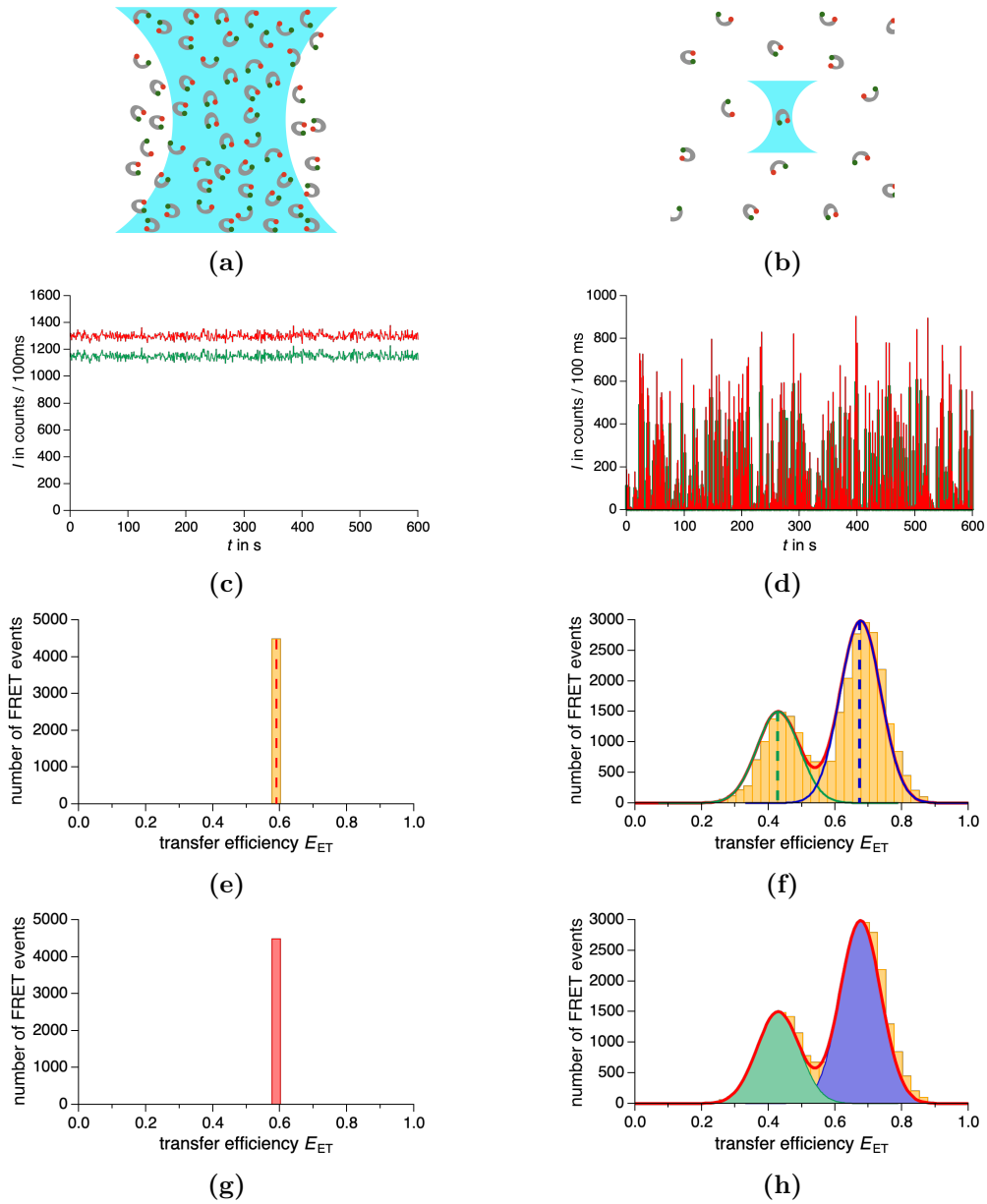


Fig. 2.21: Comparison of ensemble FRET (left) and smFRET (right). (a) Ensemble FRET observes many sample molecules at once. (b) Due to a reduced sample concentration as well as focal volume in smFRET, there is a low probability to observe more than one sample molecule at a time. (c) and (d) show the number of detected fluorescence photons in time bins of 100 ms for the donor (green) and acceptor (red). (e) and (f) show the respective transfer efficiency histograms. Since all histograms in smFRET experiments are broadened due to shot noise, peaks are fitted with a Gaussian (solid lines), to obtain each transfer efficiency (dashed lines). (g) and (h) show the fractions of the efficiency peaks.

tuates between background and bursts of fluorescence photons as the proteins enter and leave the focal volume (see Fig. 2.21d). In comparison, the fluorescence emission of ensemble FRET (enFRET) shows a relatively constant signal in both, the donor and acceptor channel as there are many proteins within the observation volume at any time (see Fig. 2.21c). As a consequence, only a mean transfer efficiency of all proteins can be determined (see Fig. 2.21e). Using smFRET on the other hand, one can distinguish and resolve multiple FRET states (see Fig. 2.21f) [51, 52]. This is done by either analyze each burst individually or by dividing the time trace of the experiment in time bins of appropriate length, e.g. 1 ms. Fluorescence bursts are assigned if the sum of the donor and acceptor signals exceeds a certain threshold $T_{\text{sum}}^{\text{da}}$. For the bursts, the FRET efficiency is calculated, using Eq. 2.79 or Eq. 2.82. Subsequently, the transfer efficiencies are summed up in a transfer efficiency histogram.

Fig. 2.21f shows another characteristic of the detected FRET efficiencies. Even when all proteins would have an identical donor acceptor distance and thus the same FRET efficiency, the histogram is broadened. This is due to shot noise of the measured fluorescence signal (see subsection 2.3.1). Therefore, for a certain conformation having a specific donor-acceptor distance a Gaussian-shaped peak appears in the FRET efficiency histogram, which is fitted with a Gaussian fit function to obtain the mean FRET efficiency of the broadened peak.

2.5 Fluorescence correlation spectroscopy

Fluorescence correlation spectroscopy (FCS) is a method based on the analysis of time-dependent fluctuations of the fluorescence intensity from a small observation volume and was first introduced in the early 1970s [45, 46, 71–73]. The fundamental principle is based on the fact that certain physical processes are causing these intensity fluctuations, which are then analyzed in such a way that the corresponding parameters of those processes can be determined [46]. Potential reasons for the fluctuations are for example diffusion, photo physical processes like transitions to the triplet state or interactions of different molecules. In principle, every process that leads to fluorescence fluctuations on a characteristic timescale can be investigated, given a measurement duration significantly longer than the fluctuation time scale. The observation volume in FCS experiments is usually realized by a confocal setup (see section 2.2) with a focussed laser beam for excitation [45–47]. With a sufficiently low sample concentration, the signal of few or even single molecules are detected at a certain time (see section 2.3). The fluctuations of the fluorescence intensity $\delta I(t)$ are described by the deviation of the fluorescence intensity signal $I(t)$ from the mean fluorescence intensity $\langle I(t) \rangle$ [132]:

$$\delta I(t) = I(t) - \langle I(t) \rangle, \quad (2.90)$$

$$\langle I(t) \rangle = \frac{1}{T} \int_0^T I(t) dt. \quad (2.91)$$

Accordingly, using low concentrations will result in larger fluorescence fluctuations, when molecules are diffusing through the focal volume for example (see Fig. 2.22). Basis of the analysis of these fluctuations is the auto-correlation function of the measured signal

$$G(\tau) = \frac{1}{T} \int_0^T I(t)I(t + \tau) dt = \langle I(t)I(t + \tau) \rangle \quad (2.92)$$

with the delay or lag time τ . The auto-correlation function describes the self-similarity of the measured signal and is a measure of probability to detect a photon at time $t + \tau$, if a photon has already been detected at time t . Typically, the auto-correlation function is normalized by the square of the average intensity [45, 47]:

$$G(\tau) = \frac{\langle I(t)I(t + \tau) \rangle}{\langle I(t) \rangle^2}. \quad (2.93)$$

Inserting Eq. 2.90 yields

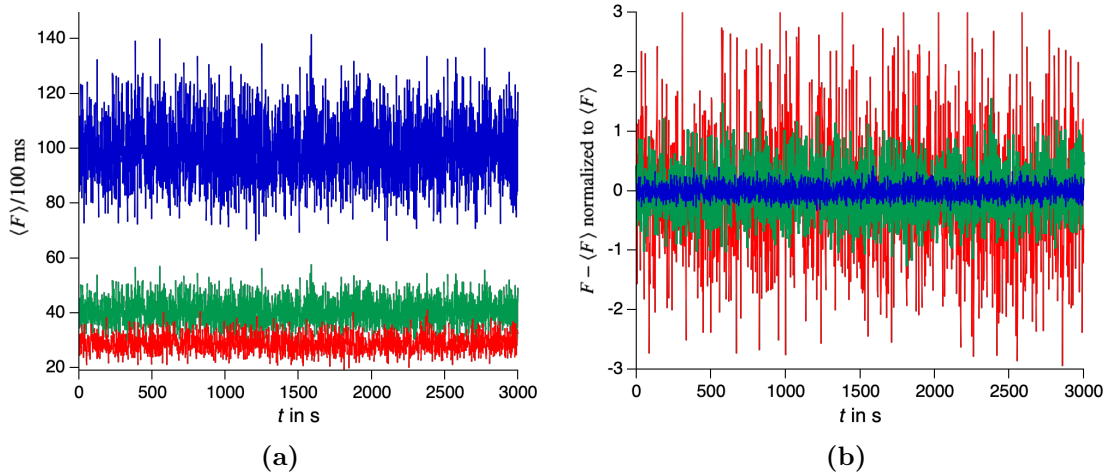


Fig. 2.22: Effect of different sample concentrations on the fluorescence fluctuations. (a) shows absolute fluorescence intensity traces for three different sample concentrations (blue > green > red). (b) shows the fluctuations of the traces from (a) around their mean fluorescence count rate $\langle F \rangle$, demonstrating that the relative fluctuations of the signal are larger for lower concentrations.

$$G(\tau) = 1 + \frac{\langle \delta I(t) \delta I(t + \tau) \rangle}{\langle I \rangle^2}. \quad (2.94)$$

In order to determine the parameters of the underlying processes the experimentally obtained auto-correlation function of the signal is fitted to a theoretical model, which is able to take these processes into account (see subsection 2.5.1 and subsection 2.5.2).

2.5.1 Brownian motion

The Brownian motion of fluorophores or molecules with attached fluorophores, will lead to changes in the distribution of the fluorophores within the observation volume. These fluctuations of the local fluorophore concentration at point \vec{r} at a certain time t in the sample can be described by $\delta C(\vec{r}, t)$. The excitation of the fluorophores and the detection of their emitted photons depend on their position within the observation volume. Excitation und detection efficiencies are combined to the molecule detection efficiency $\text{MDE}(\vec{r})$ (see section 2.2). As a result, the fluctuations of the fluorescence intensity can be expressed as

$$\delta I(t) = \int_V \text{MDE}(\vec{r}) \delta C(\vec{r}, t) dV, \quad (2.95)$$

where V is the observed volume [45, 123]. Are diffusion processes the only cause leading to concentration and thus fluorescence fluctuations, the concentration correlation function for three dimensional diffusion is given by [45]

$$\langle \delta C(r, 0) \delta C(r', \tau) \rangle = \langle C \rangle \frac{1}{(4\pi D\tau)^{\frac{3}{2}}} e^{-\frac{(r-r')^2}{4D\tau}}, \quad (2.96)$$

where r is the position at $t = 0$, r' is the position at lag time τ and D is the diffusion coefficient. The MDE of a confocal setup is often approximated with a three dimensional Gaussian (see Eq. 2.56 and Fig. 2.12). Using Eq. 2.96 and the Gaussian profile (Eq. 2.56) results in [123]

$$1 + \frac{1}{\langle N \rangle} = G_{\text{Dif}}(0) \left(1 + \frac{4D\tau}{w_{xy}^2} \right)^{-1} \left(1 + \frac{4D\tau}{w_z^2} \right)^{-\frac{1}{2}} \quad (2.97)$$

with the average number of molecules in the focal volume $\langle N \rangle$ and the axial and lateral radii of the Gaussian observation volume, denoted by w_{xy} and w_z , respectively. It is convenient to combine both radii to an aspect ratio of

$$S_{\text{ar}} = \frac{w_{xy}}{w_z}. \quad (2.98)$$

The diffusion time τ_{Dif} is related to the diffusion coefficient and the lateral radius as:

$$\tau_{\text{Dif}} = \frac{w_{xy}^2}{4D} \quad (2.99)$$

and is the time, at which the amplitude of the correlation function dropped to half of the start value (see Fig. 2.23). By inserting Eq. 2.98 and Eq. 2.99 in Eq. 2.97, the auto-correlation function results in

$$G_{\text{Dif}}(\tau) = 1 + \frac{1}{\langle N \rangle} \left(1 + \frac{\tau}{\tau_{\text{Dif}}} \right)^{-1} \left(1 + S_{\text{ar}}^2 \frac{\tau}{\tau_{\text{Dif}}} \right)^{-\frac{1}{2}}. \quad (2.100)$$

The amplitude of the correlation function for a lag time of $\tau = 0$

$$G(0) = 1 + \frac{1}{\langle N \rangle} \quad (2.101)$$

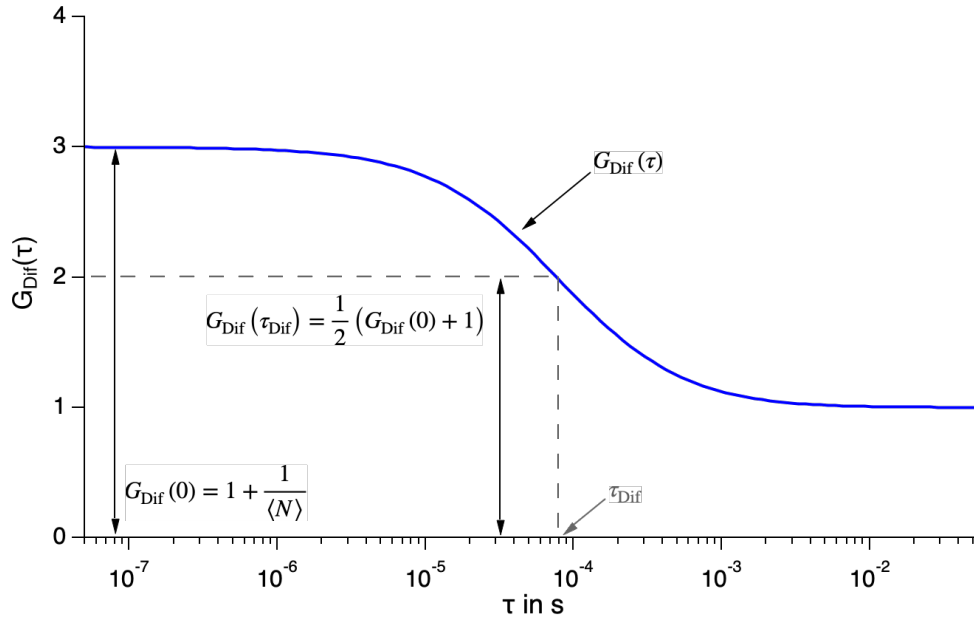


Fig. 2.23: Example of an auto-correlation curve $G_{\text{Dif}}(\tau)$ as a function of lag-time τ (blue). The average number of fluorescence molecules in the focal volume $\langle N \rangle$ can be determined via the amplitude at $G_{\text{Dif}}(0)$. The diffusion time τ_{Dif} marks the time, where the correlation function dropped to $\frac{1}{2} (G_{\text{Dif}}(0) + 1)$.

is solely dependent on the average number of molecules in the focal volume (see Fig. 2.23). If the focal volume V_f is known, one can use

$$\langle C \rangle = \frac{\langle N \rangle}{V_f} \quad (2.102)$$

to calculate the mean of the concentration $\langle C \rangle$.

2.5.2 Internal two-state dynamics

In addition to diffusion of the fluorophores in and out of the focal volume, other processes can lead to fluctuations of the fluorescence intensity as well. One example of such a process is the transition of the fluorophores to the triplet state. They can not emit fluorescence photons from that state and therefore appear dark for a characteristic time [45]. This leads to additional fluctuations, such that Eq. 2.100 is no longer sufficient to describe the experimentally obtained correlation curve. The model has to be extended to take transition to the triplet state into account as well. Usually, triplet dynamics of commonly used fluorophores are faster than their diffusion time [45,123]. In this case, the correlation function can be factorized as a product of the diffusion auto-correlation function $G_{\text{Dif}}(\tau)$ (Eq. 2.100) and an additional term describing the triplet dynamics $G_{\text{T}}(\tau)$ [123,133]:

$$G_{\text{Dif,T}}(\tau) = G_{\text{Dif}}(\tau)G_{\text{T}}(\tau). \quad (2.103)$$

This approximation only holds for processes that are on a different timescale than the diffusion of the molecules and in addition do not alter the diffusion coefficient itself. Triplet dynamics can be described by an exponential term [45,133]

$$G_{\text{T}}(\tau) = \left[1 + A_{\text{T}} e^{-\frac{\tau}{\tau_{\text{T}}}} \right], \quad (2.104)$$

where A_{T} is the triplet amplitude

$$A_{\text{T}} = \frac{\bar{T}}{1 - \bar{T}} \quad (2.105)$$

with the fraction of molecules in the triplet state \bar{T} [134,135]. τ_{T} is the relaxation time due to triplet cycling. Both, A_{T} and τ_{T} can be described with the rates of the transitions involved (see Fig. 2.24):

$$\tau_{\text{T}} = \frac{1}{k_{\text{rISC}}} + \frac{k_{\text{ex}} + k_{\text{f}}}{k_{\text{ex}}k_{\text{ISC}}}, \quad (2.106)$$

$$A_T = \frac{\bar{T}}{1 - \bar{T}} = \frac{k_{\text{ex}} k_{\text{ISC}}}{k_{\text{ex}}(k_{\text{ISC}} + k_{\text{rISC}}) + k_{\text{rISC}}(k_{\text{ISC}} + k_{\text{f}})}. \quad (2.107)$$

Insertion of Eq. 2.100 and Eq. 2.104 in Eq. 2.103 gives

$$G_{\text{Dif,T}}(\tau) = 1 + \frac{1}{\langle N \rangle} \overbrace{\left(1 + \frac{\tau}{\tau_{\text{Dif}}}\right)^{-1}}^{\text{Brownian motion}} \overbrace{\left(1 + S_{\text{ar}}^2 \frac{\tau}{\tau_{\text{Dif}}}\right)^{-\frac{1}{2}} \left[1 + A_T e^{-\frac{\tau}{\tau_T}}\right]}^{\text{Triplet blinking}}. \quad (2.108)$$

Fig. 2.25 illustrates the effect on the correlation curve due to triplet dynamics, which lead to an additional exponential increase at lag times shorter than the characteristic diffusion time. Despite transitions to the triplet state, other processes like chemical reactions or conformational changes can lead to fluctuations of the fluorescence emission as well and could be described with an additional exponential term like in Eq. 2.104. If several of these processes are present, each two-state process will cause an own exponential increase of the correlation curve and can be taken into account by adding an exponential term like Eq. 2.104 to Eq. 2.108. This simple treatment, however, only holds if additional processes have clearly separated characteristic relaxation times. Otherwise the signals overlap and more complex theory is needed [45].

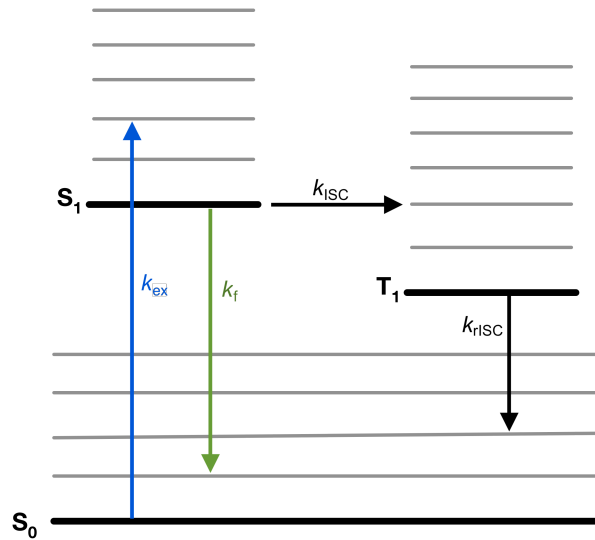


Fig. 2.24: Simplified Jablonski diagram, showing the rates used to describe the singlet-triplet relaxation time τ_T (Eq. 2.106) and triplet amplitude A_T (Eq. 2.107).

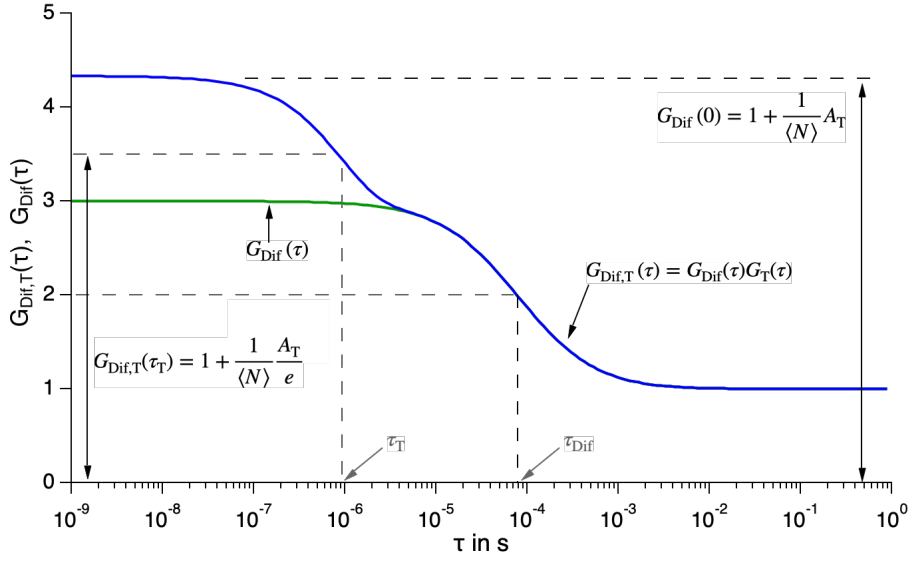


Fig. 2.25: Correlation function with triplet blinking (blue). If fluorescence fluctuations are not solely caused by Brownian motion (green), but faster processes like triplet blinking as well, the correlation function is given by the product of the correlation functions of diffusion $G_{\text{Dif}}(\tau)$ (Eq. 2.100) and triplet blinking $G_{\text{T}}(\tau)$ (Eq. 2.104): $G(\tau) = G_{\text{Dif,T}}(\tau) = G_{\text{Dif}}(\tau) G_{\text{T}}(\tau)$.

2.5.3 nsFCS

In subsection 2.5.2, the effects on the correlation curve due to processes faster than the diffusion of the molecules are discussed. When treating dynamics leading to fluctuations in the nanosecond time regime, the term nanosecond fluorescence correlation spectroscopy or nsFCS is used. For example, nsFCS enables the investigation of chain dynamics and chain reconfiguration times for unfolded or intrinsically unfolded proteins (IDPs) with characteristic reconfiguration times of ≈ 10 ns – 200 ns for 30- to 100-residue chain segments [7, 8, 53, 77–79, 136]. As described before, processes which lead to blinking on a characteristic timescale besides diffusion result in an additional increase and exponential term in the correlation curve [74]. In Eq. 2.109, chain dynamics (CD) are considered exemplarily with A_{CD} for the amplitude and τ_{CD} for their reconfiguration time. With further decreasing lag times τ another phenomenon is visible, which is called fluorescence antibunching (AB). The correlation curve begins to drop in a range of a few nanoseconds. When a fluorophore is excited, it needs a certain amount of time to return to the singlet ground state. Only then it is able to be excited again [45, 137–140]. Due to this, there is always some time delay between two emitted fluorescence photons of the same fluorophore. To account for

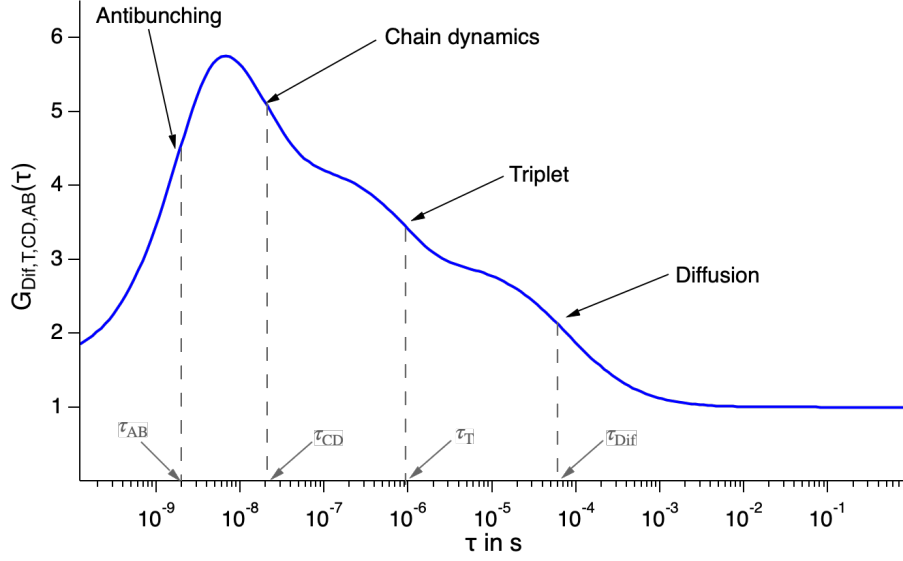


Fig. 2.26: Exemplarily correlation function of a nsFCS measurement (blue). Diffusion processes, triplet and chain dynamics as well as fluorescence antibunching are causing fluorescence fluctuations, at a characteristic time, denoted with τ_{Dif} , τ_{T} , τ_{CD} and τ_{AB} , respectively.

antibunching in the correlation function, another exponential term is added, but with a negative amplitude, where τ_{AB} is the characteristic antibunching time constant and A_{AB} is the amplitude of the fluorescence antibunching term, respectively. Fig. 2.26 shows a correlation curve with all described processes.

$$\begin{aligned}
 G_{\text{Dif,T,CD,AB}}(\tau) = & 1 + \frac{1}{\langle N \rangle} \overbrace{\left(1 + \frac{\tau}{\tau_{\text{Dif}}}\right)^{-1} \left(1 + S_{\text{ar}}^2 \frac{\tau}{\tau_{\text{Dif}}}\right)^{-\frac{1}{2}} \dots}^{\text{Brownian motion}} \\
 & \dots \underbrace{\left[1 + A_{\text{T}} e^{-\frac{\tau}{\tau_{\text{T}}}}\right]}_{\text{Triplet blinking}} \underbrace{\left[1 + A_{\text{CD}} e^{-\frac{\tau}{\tau_{\text{CD}}}}\right]}_{\text{Chain dynamics}} \underbrace{\left[1 - A_{\text{AB}} e^{-\frac{\tau}{\tau_{\text{AB}}}}\right]}_{\text{Antibunching}}.
 \end{aligned} \tag{2.109}$$

2.6 FRET-FCS

As introduced in section 2.4 and section 2.5, FRET and FCS are both spectroscopic methods to analyze inter- and intramolecular dynamics, distances or distance changes, also on a single molecule level. By combining fluorescence resonance energy transfer with fluorescence correlation spectroscopy to FRET-FCS measurements, one is capable of investigating intramolecular dynamics of proteins on the microsecond timescale [66–70]. In addition to the analysis of the auto-correlation functions of the donor and acceptor channel, the cross-correlation functions of both channels are additionally calculated and analyzed. Based on Eq. 2.94, the resulting correlation curve can be described by

$$G_{ij}(\tau) = 1 + \frac{\langle \delta I_i(t) \delta I_j(t + \tau) \rangle}{\langle I_i \rangle \langle I_j \rangle}, \quad (2.110)$$

where the indices i, j represent two different detection channels for the donor and acceptor, respectively. For a typical FRET-FCS experiment it follows that at least four different correlations can be analyzed, two auto-correlation functions for $i = j$ and two cross-correlation functions $G_{ij}(\tau)$, $G_{ji}(\tau)$ with $i \neq j$, respectively. Due to potentially present intermolecular dynamics, the resulting fluctuations are expected to lead to an additional decay component in the auto-correlations and a rise component in the cross-correlations [66, 68]. Furthermore, when combining FRET with nsFCS, it is possible to characterize chain dynamics and chain reconfiguration times of unfolded proteins or intrinsically disordered proteins (IDPs) [7, 30]. Because the underlying dynamics of the processes involved are the same for both, cross- and auto-correlation functions, the relaxation time of the processes can be determined by a global fit based on Eq. 2.109 for example, with the relaxation time of the chain dynamics τ_{CD} as a shared parameter, since it is the same for all correlation functions (see subsection 3.7.1) [53, 77]. For the early steps of protein folding processes τ_{CD} can be used for an estimate of the minimum folding time of a protein since the pre-exponential factor of protein folding (see Eq. 2.120) is solely dependent on the reconfiguration time of a polypeptide chain for small proteins with downhill folding characteristics (see subsection 2.7.6) [1, 79, 141].

2.7 Proteins

Proteins are complex macromolecules, which consist of chains of 20 different proteinogenic amino acids [142]. Proteins are key players in almost all biological processes, like for example in the catalysis of metabolic processes, gene expression, cellular communication or molecular recognition [143–145].

2.7.1 Protein structures

The structure of proteins can be divided into four main levels. These are called primary, secondary, tertiary and quaternary structures and will be briefly described in the following paragraphs.

Primary structure

The primary structure of proteins describes the lowest structural level and represents the specific linear sequence of the amino acids. The general structure of amino acids is shown in Fig. 2.27 and an example of a primary structure is given in Fig. 2.28. Amino acids contain a central carbon atom, which is called α -carbon C_α . Attached to this carbon atom are an amino group, a hydrogen atom, a carboxyl group and a characteristic side chain R . Since, without the exception of proline, the only part that varies between different amino acids is the side chain, it is convenient to divide amino acids into two parts. One part is called the backbone and includes all non side chain atoms of the respective amino acid, thus the hydrogen atom, the amino group and the carboxyl group. This backbone is identical among all amino acids whereas the second part, the side chain is what varies between amino acids [143]. The individual amino acids in a protein are connected by peptide bonds where the carboxyl group of one amino acid is linked with the amino group of the next amino acid [142]. A series of amino acids linked by peptide bonds form a polypeptide chain, the individual amino acids of which are called residues. The peptide bond is partially a double bond, so that OCNH are in a plane. Only the single bonds at the C_α can rotate, characterized by the dihedral angles. The primary structure is unique for every protein and essential, since it determines the final structure of the protein and thus the function as well [12, 143]. A polypeptide chain is charged due to their

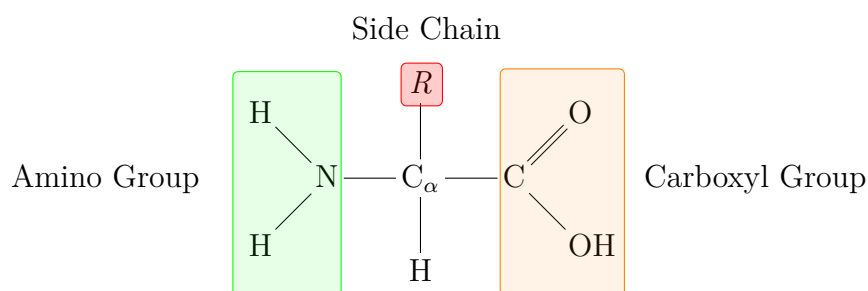


Fig. 2.27: Basic structure of all amino acids with proline as an exception, where the nitrogen atom of the amino group and the C_α are involved in a hetero cycle. The central carbon atom C_α is bonded to a hydrogen atom, a carboxyl group (orange), an amino group (green) and a characteristic side chain (red), which is different for all amino acids.

```
1 MRGK VKWF DSKK GYGF ITKD EGGD VVHV WSAI EMEG FKTL KEGQ
45 VVEF EIQE GKKG PQAA HVKV VE
```

Fig. 2.28: Primary structure or amino acid sequence of the cold shock protein from the hyperthermophilic bacterium *Thermotoga Maritima* [146,147].

different ends with an amino group on one side and a carboxyl group on the other side, respectively. Additionally, the charged side chains contribute to the charge distribution within the chain. This distribution can lead to regions of localized positive or negative charges. The sum of all positive and negative charges along the chain results in the net charge of the chain, which is strongly pH-dependent. The end with the amino group is by convention taken as the start of the amino acid sequence [144].

Secondary structure

The secondary structure of proteins refers to local, regular, simple arrangements of amino acids within the polypeptide chain. The most common secondary structure elements are alpha-helices and beta-sheets, both of which play important roles in determining the overall three-dimensional shape and function of a protein. Both, alpha-helices and beta-sheets are formed by hydrogen bonds between the CO- and NH- groups of the backbone. Both elements are illustrated in Fig. 2.29.

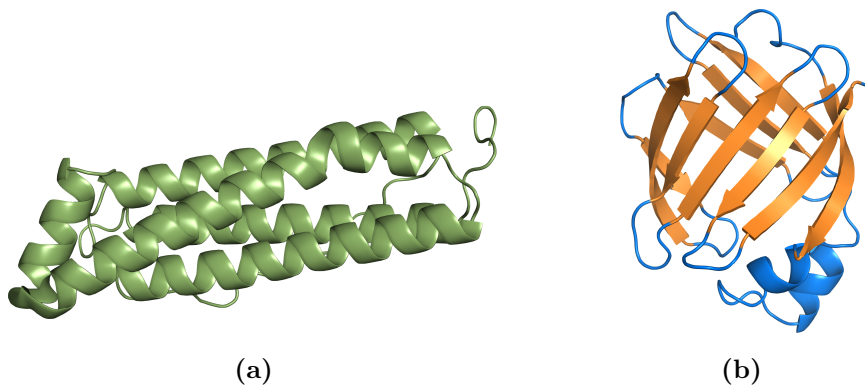


Fig. 2.29: Secondary structure elements of proteins with (a) alpha-helices and (b) beta sheets [144].

Tertiary structure

The tertiary structure of a protein refers to its overall three-dimensional shape [144]. It is determined by interactions between its secondary structure elements and the

rest of the polypeptide chain, as well as by non-covalent interactions such as hydrophobic forces, ionic bonds, and hydrogen bonds. According to the central dogma of structural biology the three-dimensional structure is prerequisite to the protein's function [143,144]. It determines the spatial relationships between the various functional regions, such as active sites and binding sites. Fig. 2.30 shows the solution NMR structure of the cold shock protein of the hyperthermophilic bacterium *Thermotoga Maritima* [147,148].

Anomalous tertiary structures, e.g. amyloids, can lead to protein malfunction and disease due to transitions of alpha helices to beta sheets. This leads to misfolding and an abnormal tertiary structure of the protein, which additionally alters the quaternary structure since it promotes protein aggregation.

However, proteins that are naturally disordered or have disordered regions, called intrinsically disordered proteins (IDPs) (see subsection 2.7.2) are an exception to the paradigm mentioned above.

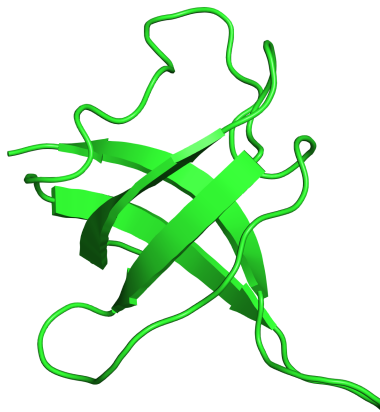


Fig. 2.30: Structure of the cold shock protein *Thermotoga Maritima* as an example of a tertiary structure of a protein [147,148].

Quaternary structure

The quaternary structure of proteins represents the highest structural level and defines the spatial arrangement and interaction between multiple polypeptide chains. Many proteins consist of multiple polypeptide chains, called subunits [143,144]. If these subunits are identical, they are homomers, and when they are different, heteromers. The quaternary structure is essential for the protein's overall function and can greatly influence its biological activity [149]. The simplest case of a quaternary structure of a protein is a dimer consisting of two subunits, shown in Fig. 2.31 with the Cro-protein. Another example is the hetero-tetramer hemoglobin with four non-identical subunits. The driving force of the quaternary structure formation is the hydrophobic effect [150]. The structure itself is primarily stabilized by non-covalent

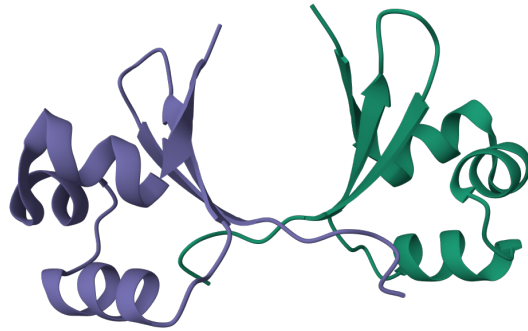


Fig. 2.31: Cro-protein as an example of a homodimer consisting of two identical subunits shown in purple and green, respectively [144,151].

interactions, which allow a dynamic equilibrium between different states of the same protein.

2.7.2 Intrinsically disordered proteins

Intrinsically disordered proteins (IDPs) are proteins that lack a stable, defined three-dimensional structure under physiological conditions and do not adopt a fixed conformation [143]. This structural flexibility is a defining characteristic. Most IDPs contain highly flexible, unstructured regions known as intrinsically disordered regions (IDRs) that can vary in size [33–35]. Some IDPs are even entirely unstructured [36,152–155]. Fig. 2.32 shows the sequence [156–158] and AlphaFold structure prediction of the sperm histone protein from the organism *Gallus gallus* [159–161] as an example of an entirely unstructured IDP. Despite the correlation between protein structure and its function [143], many IDPs serve an important role in a variety of biological processes and facilitate them due to their lack of structural constraints [153,154] including movement to narrow pores [162] or alternative splicing [163]. They also play a role in the regulation of gene expression, cellular signal transduction, protein phosphorylation and protein-protein interactions [36,37,164]. IDPs show a variety of complexes due to interactions with other proteins [165]. IDPs can adopt well-defined three-dimensional structures upon binding to their targets, while, in other complexes, specific protein regions retain their disordered nature [166,167]. Binding to macromolecular binding partners can lead to a gain of structure or, on the contrary, structured domains can become IDPs, e.g. [168]. IDPs, which have a significant net charge, are typically more expanded with the degree of extension depending on the magnitude of the net charge [154,169,170]. Bioinformatic methods suggest a correlation between the occurrence of IDPs in the genome of an organism and its complexity [173]. For mammals it is estimated that approximately 50% of the proteins contain long disordered regions [143,174], which are about 75% of all signaling proteins [175]. For human protein coding genes the

```

1 MARYR RSRTR SRSPR SRRRR RRSGR RRSR RRRRY GSARR SRRSV
46 GGRRR RYGSR RRRRR RY

```

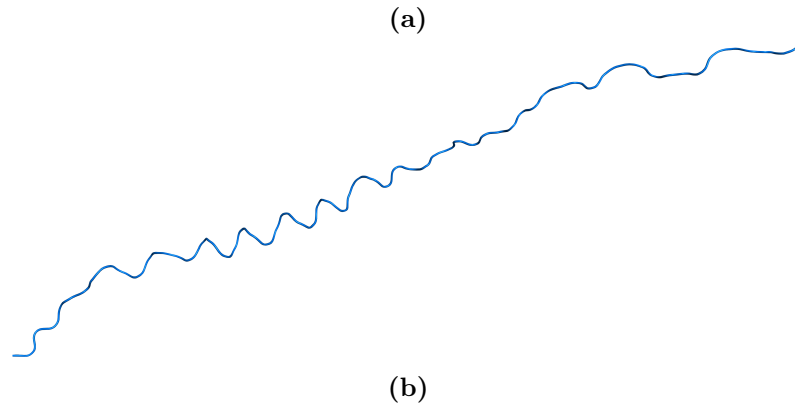


Fig. 2.32: (a) Sequence of the sperm histone protein [156, 157] and (b) the corresponding AlphaFold structure prediction [159–161] as an example of an intrinsically disordered protein without a native three-dimensional structure.

fraction of proteins containing disordered regions with a length of at least 30 amino acids is approximately 44 % [174, 176]. About 5 % of all proteins are predicted to be completely disordered, with a fraction of disordered residues of over 95 % [177, 178]. These numbers show the importance of IDPs and proteins with IDRs and the significance of further investigating their roles and functions. The growing interest in IDPs is evident by looking at the number of publications, related to them on both, PubMed [171] and Google Scholar [172] (see Fig. 2.33).

Despite their importance, the study of IDPs has been challenging due to their lack of a well-defined structure. However, recent advances in computational and experimental techniques have led to an increased understanding of these proteins and their functions. Single molecule fluorescence resonance energy transfer (smFRET)

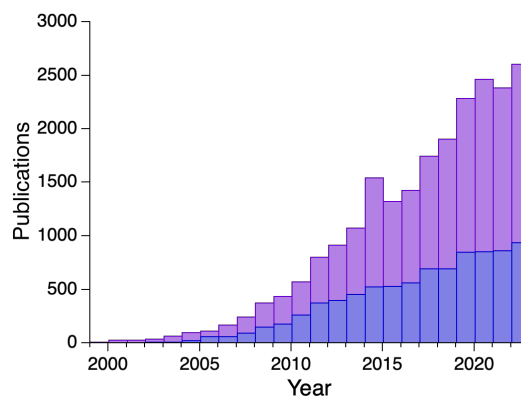


Fig. 2.33: Number of new publications related to intrinsically disordered proteins (IDPs) with numbers obtained from PubMed (blue) and Google Scholar (purple) and the use of the search phrase "intrinsically disordered proteins" [171, 172].

in combination with nanosecond fluorescence correlation spectroscopy (nsFCS) for example is a versatile experimental technique to investigate global chain dynamics of unfolded proteins or IDPs [53, 74, 75, 79]. These long range chain dynamics have a characteristic reconfiguration time, which corresponds to the relaxation time of the distance correlation function of two residues of a polymer [152]. Furthermore, one can examine multiple different states of IDPs in an unbound ensemble or folding intermediates during binding of IDPs to other proteins.

The concepts of polymer physics are a useful and powerful tool for the interpretation of the results of experiments with IDPs and describe their behavior [32, 53, 179–182]. Simple polymer models like the Gaussian chain [52, 76, 170, 183], an excluded volume chain [184, 185] or a worm-like chain [170, 186, 187] can be used to analyze underlying chain statistics and obtained distance distributions. In addition, the development and optimization of force fields for atomistic molecular dynamic simulations of intrinsically disordered proteins [188–193] enable to complement the experimental data [6, 7, 77, 194, 195] and potentially access deviations from the chosen polymer models as well [53, 181, 186].

Prothymosin alpha

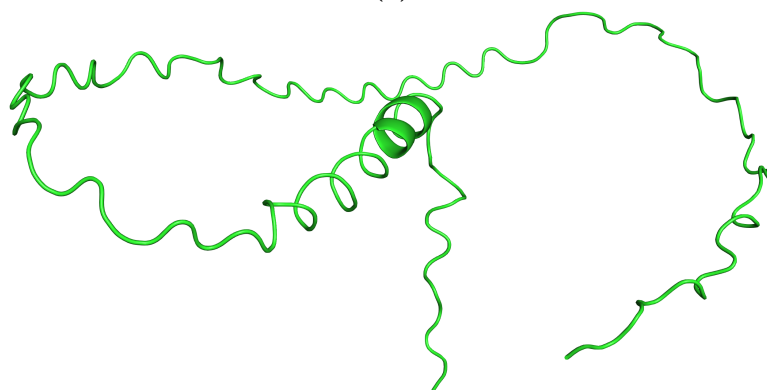
Prothymosin alpha (ProT α) is an intrinsically disordered protein (IDP). It was discovered in 1984 and its sequence consists of 111 amino acids [197–200]. The sequence is shown in Fig. 2.34 alongside its AlphaFold structure prediction [160, 161].

```

1  SDAAV DTSSE ITTKD LKEKK EVVEE AENGR DAPAN GNAEN EENGE
46 QEADN EVDEE EEEGG EEEEE EEEGD GEEED GDEDE EAESA TGKRA
91 AEDDE DDDVD TKKQK TDEDD

```

(a)



(b)

Fig. 2.34: (a) Sequence of the protein prothymosin alpha [156, 157] and (b) the corresponding AlphaFold structure prediction [159–161, 196].

ProT α is entirely unstructured without any regular secondary structure [201] and an IDP with one of the largest identified fraction of charged amino acids [170]. It is highly negatively charged, with a net charge $z = -44$. Therefore, it is comparatively expanded [6, 170, 202, 203]. Despite lacking a distinct folded structure and regular secondary structure it performs an essential role in many biological processes [6, 170, 204]. For example it is involved in chromatin remodeling [205] or cellular proliferation and oncogenesis [206]. Furthermore, it binds to the intrinsically disordered protein H1 with high affinity, proven in vivo [207] and in vitro [208], respectively. It acts as a linker histone chaperone, which increases the H1 mobility in the nucleus [207], but maintain their structural disorder, long-range flexibility, and highly dynamic nature entirely [6].

2.7.3 Folding

The basis for the present understanding of the protein folding process dates back to Anfinsen [9]. With experiments of the enzyme bovine pancreatic ribonuclease (RNase A), which disintegrates single-stranded RNA, Anfinsen and his laboratory discovered that proteins are capable of folding reversibly. All required information must be contained in the amino acid sequence to form the correct four out of 105 possible disulfide bonds [12–14]. Consequently, the structure of the native state is essentially dependent on the amino acid sequence and not on the folding process itself [13, 143]. Anfinsen proposed the *thermodynamic hypothesis*, which states that the three-dimensional structure of the native state of a protein in its normal physiological milieu is the state with the lowest Gibbs free energy [12, 13, 40]. However, the *thermodynamic hypothesis* alone could not explain the speed and efficiency of protein folding. If a protein had to randomly sample all possible unfolded conformations until the native one is found, the folding time would be longer than the life of the universe [9, 15, 16], known as the Levinthal Paradox [15–17]. Therefore, a reasoned conclusion from Levinthal’s calculation was the existence of intermediate states and pathways [17, 209, 210]. Studies in the 1980s showed that the folding process involves the formation of residue-residue interactions as well as compact secondary structures, which limits the number of available configurations for the protein during folding [211, 212]. In 1992, Levinthal’s calculation was repeated with an included small energy bias as the driving force for folding, which reduced the duration of the search process to a few seconds [9, 18]. The energy landscapes according to the Levinthal paradox and pathway solution are illustrated in Fig. 2.35a and Fig. 2.35b, respectively. However, this raised the question of whether the folding process is under thermodynamic or kinetic control [9, 213]. Both approaches can be integrated within the widely accepted energy landscape model [19, 214–217], with its theory based on an energetic bias towards the native state [9, 218]. The folding process is described as an energy-entropy funnel, where each point on the surface represents

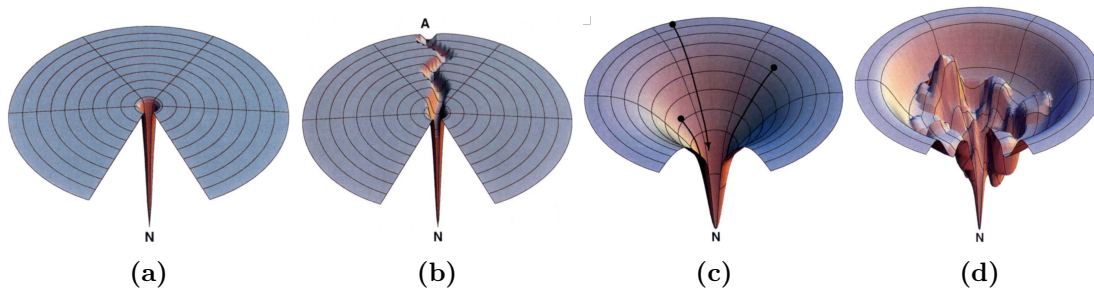


Fig. 2.35: Visualization of different energy landscape concepts with **N** and **A** denoting the native and denatured confirmation, respectively: (a) Levinthal landscape, (b) landscape with pathway solution, (c) idealized funnel landscape and (d) rugged energy landscape with hills, traps and energy barriers [16, 209].

the Gibbs energy of one protein conformation [143]. Hills and valleys within the energy landscape account for energetically unfavored or more favored conformations, respectively (see Fig. 2.35d) [16, 209]. The protein folding process can be described as a downhill process on the energy landscape with multiple possible parallel pathways [209]. Along the path to the native state, various conformational states, e.g., molten globule, transition state, and intermediates, can be occupied [9, 16].

2.7.4 Denaturation

Proteins can be unfolded or denatured in multiple ways. Unfolding leads to the loss of the three-dimensional structure of their native state, which is essential for their function. The most commonly used methods for denaturation include the addition of chemical denaturants, changes in temperature or pH or high pressure [219]. In the following, denaturation due to chemical denaturants as well as unfolding under pressure is briefly discussed.

Urea and Guanidinium chloride Urea and Guanidinium chloride (GdmCl) are the most commonly used denaturants to unfold proteins. Both have low molecular weights and are highly soluble in water [9, 220]. They destabilize the native state by altering the solvation properties of the protein [219]. By forming hydrogen bonds with the protein backbone and weakening hydrophobic interactions in the core, native contacts are disrupted, favoring more extended conformations [220, 221]. Weakening the hydrophobic effect promotes unfolding since it is responsible for protein stability [143]. One challenge in analyzing protein unfolding with chemical denaturants is that the thermodynamic parameters are influenced as well, which shifts the chemical potential of the proteins [222].

Pressure The response of a system to changes in temperature or pressure is determined by Le Chatelier’s principle [89,223]. Consequently, an increase in pressure biases the accessible states towards those with a smaller volume [9]. If the volume of a denatured state of a protein is smaller than the volume of its native state, an increase in pressure leads to unfolding. The total volume of a protein in solution is additive and given by [222–224]:

$$V_{\text{total}} = V_{\text{atoms}} + V_{\text{cavities}} + V_{\text{hydration}}. \quad (2.111)$$

The volume difference ΔV_{total} is due to the difference in volume between the denatured V_{D} and native state V_{N} :

$$V_{\text{total}} = V_{\text{D}} - V_{\text{N}} = \overset{0}{\cancel{\Delta V_{\text{atoms}}}} + \Delta V_{\text{cavities}} + \Delta V_{\text{hydration}}. \quad (2.112)$$

$\Delta V_{\text{hydration}}$ describes the volume change of the hydration shell, and $\Delta V_{\text{cavities}}$ the volume change of the cavities. Since the volume of the atoms is not affected by pressure, ΔV_{atoms} does not contribute to the volume change upon unfolding. With increasing pressure, the hydration shell increases as well due to the more solvent-exposed amino acid residues. However, this effect is more than balanced by the negative contribution from the disruption of electrostatic and hydrophobic interactions [222]. The most significant negative contribution to volume change during protein unfolding comes from the elimination of internal cavities within the folded protein structure [89,225], even though the change is comparatively small, about 1 % of the total volume of the protein [226]. In contrast, a correlation between protein size and volume change could not be observed [227]. Since voids within proteins are not evenly distributed, proteins of the same or similar size and structure can exhibit distinct volumetric properties [89]. However, a recent study on the role of bound water indicates that for smaller peptides like Trp-cage, the solvent accessibility upon unfolding and subsequent increase of bound water molecules might be the major contributor for pressure denaturation [228].

2.7.5 Denatured state

The denatured state of proteins does not correspond to a certain structure but rather an ensemble of different structures. These states have all similar energy and are in rapid equilibrium with each other [32,209,219,229]. The unfolded state is as important as the native state since the denatured state builds the starting point of the protein folding reaction [31,32] (see subsection 2.7.3). Additionally, the stability of a protein arises from the difference in free energy between the native and denatured state, respectively. Furthermore, the denatured and native states are in dynamic equilibrium in vivo [230–232], and some proteins undergo a transition to an unfolded or partially unfolded configuration to cross lipid bilayers [233–235]. However,

a challenge in studying denatured proteins is that they typically exist in the native state under physiological conditions. Therefore, studies are often conducted under non-physiological conditions, e.g. high chemical denaturant concentrations. Hence, intrinsically disordered proteins (IDPs) (see subsection 2.7.2) provide a promising complement for studying the dynamics of unfolded polypeptide chains since they exist in an unfolded state even under physiological conditions. Experiments under high pressure can also provide a different insight since pressure is assumed to have a weaker effect on the unfolded state [225,236]. Like IDPs, denatured proteins can be described and analyzed using the framework of polymer physics in order to support the analysis and understanding of experimental observations [53].

2.7.6 Folding kinetics

In the simplest case protein folding and unfolding can be described by a two-state model [229,237,238]. Even though two-state kinetics could be observed for many small proteins without detectable intermediates [237], two-state behavior does not prove that no intermediates are present [219]. However, two-state folding kinetics are a good start for the basic principles of protein folding. For a protein that populates either the unfolded state U or the native state N, the process can be described by



where k_f and k_u are the rates for folding and unfolding, respectively, combined to the apparent or observed rate [9]

$$k_{\text{app}} = k_{\text{obs}} = k_f + k_u. \quad (2.114)$$

The equilibrium constant for folding K_{eq} is given by

$$K_{\text{eq}} = \frac{[N]_{\text{eq}}}{[U]_{\text{eq}}} = \frac{k_f}{k_u}, \quad (2.115)$$

with the concentration of proteins in the native [N] and unfolded state [U], leading to

$$k_f [U]_{\text{eq}} = k_u [N]_{\text{eq}}. \quad (2.116)$$

The free energy for folding ΔG^* is connected with the equilibrium constant by [9,142]

$$\Delta G^* = -RT \ln(K_{\text{eq}}) = -RT \ln \left(\frac{[N]_{\text{eq}}}{[U]_{\text{eq}}} \right) = -RT \ln \left(\frac{k_f}{k_u} \right). \quad (2.117)$$

2.7.7 Speed limit of protein folding

A crucial aspect in studying protein folding and unfolding processes is the speed at which they occur and determining a speed limit for protein folding. The investigation of fast folding proteins has the advantage that the outcome of experiments can be directly compared with the results of computer simulations [25–29]. Another aspect is that at the speed limit no transition states are present and energy barriers are very small or non-existent. This kind of folding process is known as ‘downhill folding’ and provides an opportunity to gain more information about the entire folding process for fast folding proteins [1, 19–22]. Small proteins with fewer than 100 residues often exhibit two-state folding kinetics (see subsection 2.7.6), where no intermediates can be observed. Accordingly, they are either in the folded or unfolded state and are suitable candidates for fast folding kinetics [1, 237].

A theoretical approach for estimating the speed limit of protein folding is Kramer’s theory, which is based on Brownian motion and the overcoming of energy barriers by thermal fluctuations. Dynamics are described as a one-dimensional diffusion process along a reaction coordinate [1, 2]. The folding time τ_{folding} according to Kramer’s theory is given by [2, 3, 21, 239]

$$\tau_{\text{folding}} = \frac{1}{k_{\text{folding}}} = \tau_0 e^{\left(\frac{\Delta G^*}{k_B T}\right)} \quad (2.118)$$

with the pre-exponential factor

$$\tau_0 = \frac{2\pi k_B T}{D_{\text{max}} \omega^* \omega_u}. \quad (2.119)$$

In Eq. 2.118 and Eq. 2.119, k_{folding} is the folding rate, ΔG^* is the free activation energy barrier height, D_{max} the diffusion coefficient at the barrier top and ω_u and ω^* are frequencies which characterize the curvatures of the free energy surface at the bottom of the unfolded well and at the top of the free energy barrier, respectively (see Fig. 2.36). With the simplified assumptions of a similar diffusion coefficient and curvature of the unfolded well and on top of the barrier, τ_0 can be approximated by

$$\tau_0 \approx 2\pi\tau_{\text{CD}}, \quad (2.120)$$

where the reconfiguration time of the chain τ_{CD} within the unfolded state is directly related to the inverse attempt frequency [1, 79]. Consequently, the pre-exponential factor in the absence of a free energy barrier approximates the speed limit of protein folding [1, 79, 141]. It follows that in the absence of a thermodynamic barrier, the folding speed is limited by intrachain diffusion [23]. Therefore, the contact formation of two residues, which are distant along the amino acid sequence of the polypeptide

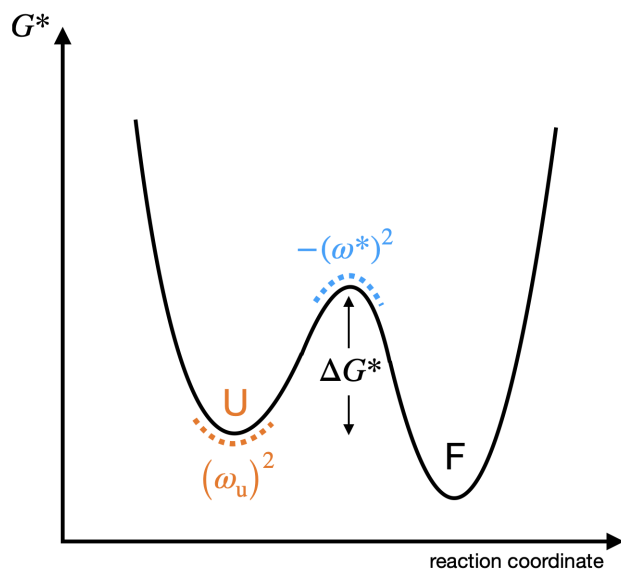


Fig. 2.36: Free energy surface of protein folding. According to Kramer protein folding can be described as a diffusion process on a one dimensional surface along a reaction coordinate. G^* is the free energy, ΔG^* the free energy barrier height and $(\omega_u)^2$ and $(\omega^*)^2$ describe the curvatures at the bottom of the unfolded and at the top of the barrier, respectively. U and F represent the unfolded and folded state.

chain, is assumed to be an important and elementary step in the protein folding process of many proteins, especially in the early steps of folding [240–244]. As an increasing number of proteins are found to fold within the microsecond time range, interest in their study continues to grow. Since the free energy barrier in this time range is expected to be low or non-existent, diffusive chain dynamics are the dominant factor [24]. Since in this case, the pre-exponential factor τ_0 is approximated by Eq. 2.120, single molecule nsFRET-FCS measurements are a promising measurement technique (see section 2.6). The reconfiguration time is obtained from the correlation analysis of donor-acceptor fluorescence fluctuations and gives a lower limit to the folding time. An example is the work of Nettels et al. with their investigation of the cold shock protein CspTM [79]. The determined reconfiguration time of the unfolded CspTM of $\tau_{CD} = 65$ ns sets a limit of the folding time of $\tau_{\text{folding}} \geq 0.4 \mu\text{s}$. The denaturation of proteins due to high hydrostatic pressures in nsFRET-FCS experiments can give an additional inside to other techniques like temperature or chemical denaturation. All methods have a different perturbation mechanism leading to different effects on the folding landscape [89]. Unfolding by pressure leads to proteins with characteristics of a molten globule state, which are regarded as a folding intermediate [222,245]. The increased roughness of the energy landscape due to pressure leads to an increased folding time. [90,91]. With the potential of stabilizing folding intermediates, measurements with high pressures have the potential to enable the investigation of their dynamics and characteristics as well [91].

Chapter 3

Material and Methods

3.1 Experimental setup

The experimental setup, which is used to perform FRET and FCS measurements, is a custom built confocal microscope as illustrated in Fig. 3.1. For the excitation of the sample, three continuous wave (cw) lasers with different excitation wavelengths are available. The lasers have excitation wavelengths of 488 nm (PC13589, Spectra Physic Cyan), 588 nm (Sapphire, Coherent) and 640 nm (OBIS LX, Coherent). The 640 nm OBIS laser is a diode laser that can be digitally modulated with a bandwidth of up to 150 MHz (2 ns rise/fall time), controlled by TTL pulses. This modulation is not possible for the 488 nm and 588 nm solid state lasers. Therefore, an acousto-optical modulator was used, which can be controlled by TTL pulses as well. The repetition rate of the laser pulses is controlled via the signal applied either to the laser controller or the controller of the acousto-optical modulator, respectively. The laser power is adjusted by blocking the laser beams partially with a sphere at the tip of a threaded screw. All lasers are combined with a long pass beam splitter (570DCXR, Chroma[®]), where the alignment was enabled by mirrors with small apertures for guiding. Subsequently, the lasers are coupled into a single mode fiber (SMC-469, Schäfter und Kirchhoff GmbH). The polarization of the light exiting the birefringent fiber is controlled with a quarter and a half waveplate (Melles Griot), respectively, in the laser beam before coupling into the fiber. The divergent light exiting the fiber is collimated by an achromatic microscope objective (Uplan-Apo 4x 0.16, Olympus) to a parallel beam. The width of the laser beam can be adjusted by an aperture placed next to the objective in the parallel beam path. Next, the light is reflected by a dichroic mirror and propagates through a system of two telecentric lenses (200 mm tube lens, Nikon). A removable pinhole with a diameter of 50 μm is placed in their shared focal point. Via a mirror, the light is reflected upwards to the microscope objective (CFI Plan Apochromat 60x 1.2 WI, Nikon), which works with water immersion and has a numerical aperture of $\text{NA} = 1.2$. To adapt to varying thicknesses of coverslips, the objective has a correction collar to properly adjust the objective for borosilicate coverslips with thicknesses between 130 μm and 190 μm .

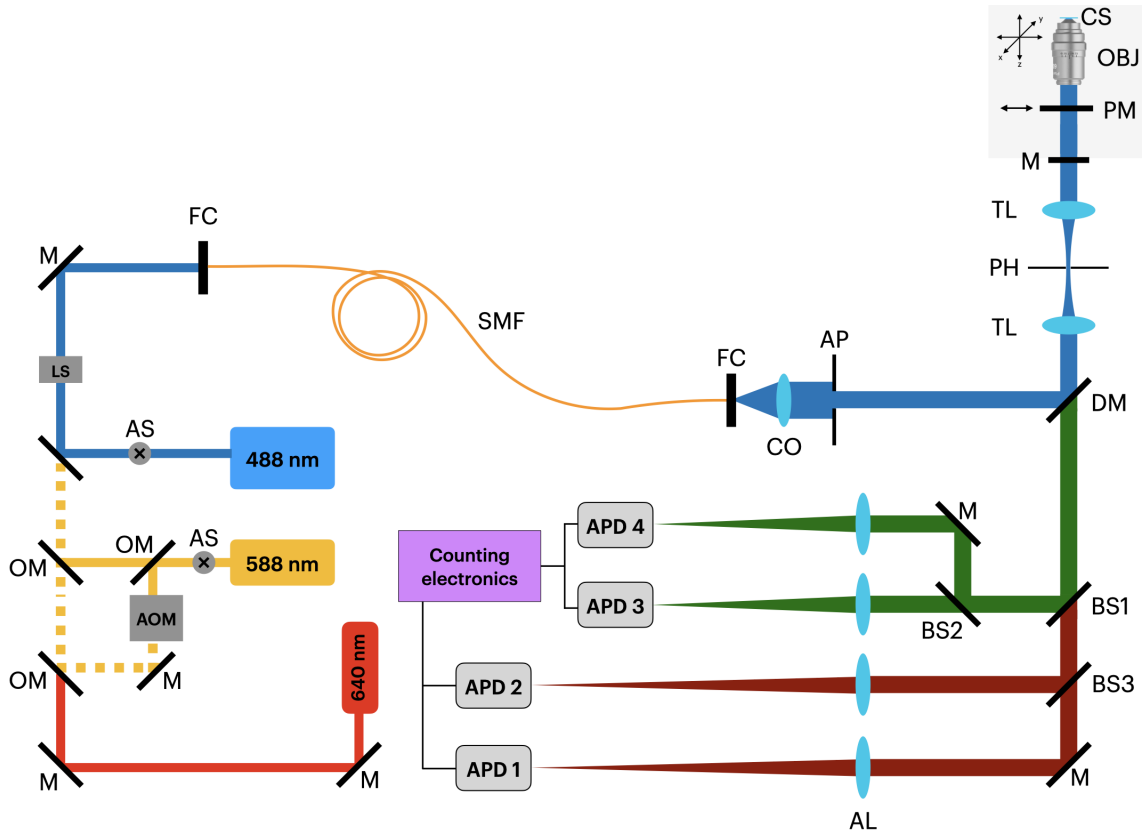


Fig. 3.1: Scheme of the confocal setup used for FCS and FRET experiments. M: mirror, OM: optional mirror with magnetic mount, AOM: acousto-optical modulator, AS: adjustment screw, LS: laser shutter, FC: fiber coupling, SMF: single mode fiber, CO: collimation objective, AP: aperture, DM: dichroic mirror, TL: telecentric lens system, PH: pinhole, PM: power meter, OBJ: objective, CS: coverslip, BS1-3: beam splitter position 1-3, AL: achromatic lenses, APD1-4: avalanche photo diodes 1-4, 488 nm/588 nm/640 nm: laser sources with their emission wavelengths.

Above the objective is the sample stage, where the coverslip or capillary containing the sample is placed for the experiments.

Pressure measurements can be realized by connecting the capillary to a high-pressure screw piston pump (37-5.75-60, PTG pressure technology) (see section 3.2). Piezo actuators (P-733.2CL, $\Delta x = 0.3$ nm, Physik-Instrumente) enable a lateral positioning of the sample stage in a range of $(100 \times 100) \mu\text{m}^2$. For focussing, the microscope objective is placed on a piezo actuator (PiFoc P-721.CLQ, $\Delta x = 0.7$ nm, Physik-Instrumente), enabling the movement within a range of $100 \mu\text{m}$ along the optical axis of the microscope. To measure the laser power, a power meter can be flipped into the beam path directly in front of the back aperture of the objective. Emitted fluorescence is collected with the same objective and follows the beam path in reverse order until it reaches the dichroic mirror, where it gets transmitted due to its longer wavelength with respect to the excitation wavelength. The further exact arrange-

ment of the detection path of the microscope depends on the specific experiment and related requirements. Using four detectors, there are in principle three positions, where light can be split, named BS1, BS2 and BS3 in Fig. 3.1. For FRET experiments for example, a dichroic beam splitter is placed at position 1 (BS1), which reflects the fluorescence photons of the donor and transmits the photons of the acceptor. Subsequently, the donor as well as the acceptor photons each are split by a 50/50 beam splitter (BS2 and BS3). Finally, all photons are focussed onto avalanche photo diodes (APDs), two for the donor channel (SPCM-AQRH-14, PerkinElmer Optoelectronics) and two for the acceptor channel (C11202-100, Hamamatsu). The signal of the APDs is fed either to newly implemented single-photon counting electronics (USB2.0TDC CS, TP: 01-04-82, Surface Concept) or to a TCSPC module (Timeharp200 (Picoquant) and SPC-134 TCSPC (Becker & Hickl GmbH)) to record the arrival times of the detected photons. The properties of both single-photon counting electronics are discussed in section 3.3. The piezo actuators and the laser shutter are controlled using a custom written LabVIEW virtual instrument (VI) [246, 247]. This VI enables lateral scans perpendicular to the optical axis or axial scans along the optical axis of the sample within an area of $100 \mu\text{m}^2$. Furthermore, the APDs can be gated to start a measurement. The recorded photons are shown as a time trace containing the number of photons per 100 ms time bins, which can be used to adjust the achromatic lenses in front of the detectors. The real-time control of the components, e.g. piezo actuators, laser shutter and start/stop of a data acquisition of the PerkinElmer detectors, is performed by an ADwin Gold real time data acquisition system (Jäger Computergesteuerte Messtechnik GmbH).

3.1.1 Four detector configuration

As described in section 3.1, the experimental setup is equipped with a total of four APDs in order to be able to record all required correlations in nsFCS-FRET measurements at once and to overcome afterpulsing and dead time limitations (see subsection 3.3.2). The previous detection path of the microscope consisted of two SPCM-AQR-14 APDs from PerkinElmer Optoelectronics. This model features a high detection efficiency with a peak sensitivity of about 70 % at a wavelength of 650 nm (see Fig. 3.2). Further properties are a dark count rate of about 100 counts per second (cps), a dead time of 50 ns and an active circular detection area with a diameter of $175 \mu\text{m}$ [248]. To extend the detection capabilities of the setup, two single photon counting modules (SPCM) CS11202-100 from Hamamatsu were added. Their characteristic properties as provided by the manufacturer are a low dark count rate of typically 30 cps, a dead time of 30 ns, and a photosensitive area with a diameter of $100 \mu\text{m}$ [249]. The peak sensitivity is about 70 % as well, but at a shorter wavelength of 450 nm (see Fig. 3.2), better matching the donor emission. Inspecting the spectra in Fig. 3.2, it becomes obvious that the efficiency spectrum of the PerkinElmer APD is much broader than for the Hamamatsu APD. In order to account for the different sizes of the active areas of both detector models, achromatic

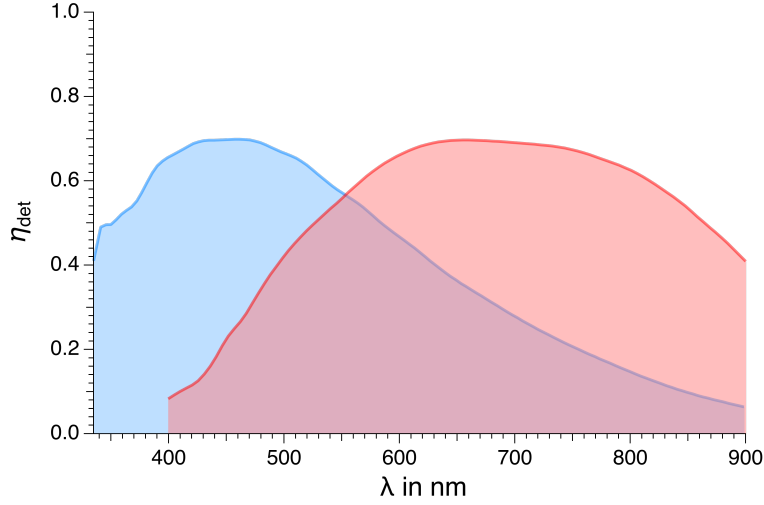


Fig. 3.2: Detection efficiencies η_{det} as a function of the wavelength λ of both APD types, PerkinElmer SPCM-AQR-14 (red) and Hamamatsu C11202-100 (blue). The peak detection efficiencies are at wavelengths of approximately 450 nm and 650 nm, respectively.

lenses with different focal lengths are used. The size of the pinhole imaged onto the detector $d_{\text{PH,APD}}$ can be calculated using

$$d_{\text{PH,APD}} = d_{\text{PH}} \frac{f_{\text{al}}}{f_{\text{tl}}}, \quad (3.1)$$

where d_{PH} is the actual diameter of the pinhole and f_{al} and f_{tl} are the focal lengths of the achromatic lens and tube lens, respectively. With a pinhole diameter of $50 \mu\text{m}$, $f_{\text{tl}} = 200 \text{ mm}$ and $f_{\text{al}} = 500 \text{ mm}$ for the PerkinElmer APDs, it follows a $d_{\text{PH,APD}}$ of $125 \mu\text{m}$. With respect to the diameter of the active area of $175 \mu\text{m}$, the ratio of the imaged pinhole and the active area is ≈ 0.71 . The focal length of the achromatic lens in front of the Hamamatsu APDs was chosen in such a way, that a similar ratio between the imaged pinhole and the size of the active area is achieved, accommodating the smaller active area of the APD. The focal length necessary to obtain the same ratio as with the PerkinElmer APDs is given by approximately 285.6 mm . Thus a focal length of 300 mm was chosen for the achromatic lenses in front of the Hamamatsu APDs, leading to a fill factor of 0.75 .

3.2 Pressure setup

The high-pressure setup was first implemented in the confocal microscope by Sven Schneider in order to be able to perform high-pressure fluorescence spectroscopic experiments [5]. The general arrangement is shown in Fig. 3.3. It consists of a high-pressure screw piston pump (37-5.75-60, PTG pressure technology), which can

generate hydrostatic pressures of up to 4 kbar. The pump is connected to a manometer (0 – 4 kbar, \varnothing 100 mm, PTG pressure technology) and a liquid reservoir through a system of tubes and valves. The manometer enables the monitoring of the applied hydrostatic pressure, generated by the pump, while the liquid reservoir contains the pressuring liquid, which is water for the experiments performed in the context of this thesis. At a third connection, a 50 cm long tube leads to the optical table of the microscope. The sample containing capillary (see subsection 3.2.1) is connected at the other end of this tube and is placed above the objective. This is realized by glueing the capillary in a custom made pressure plug. Subsequently, the pressure plug with the capillary is inserted into a gland, which is screwed to the pump. A more detailed description of the whole procedure and necessary steps for a pressure experiment is given in subsection 3.2.2.

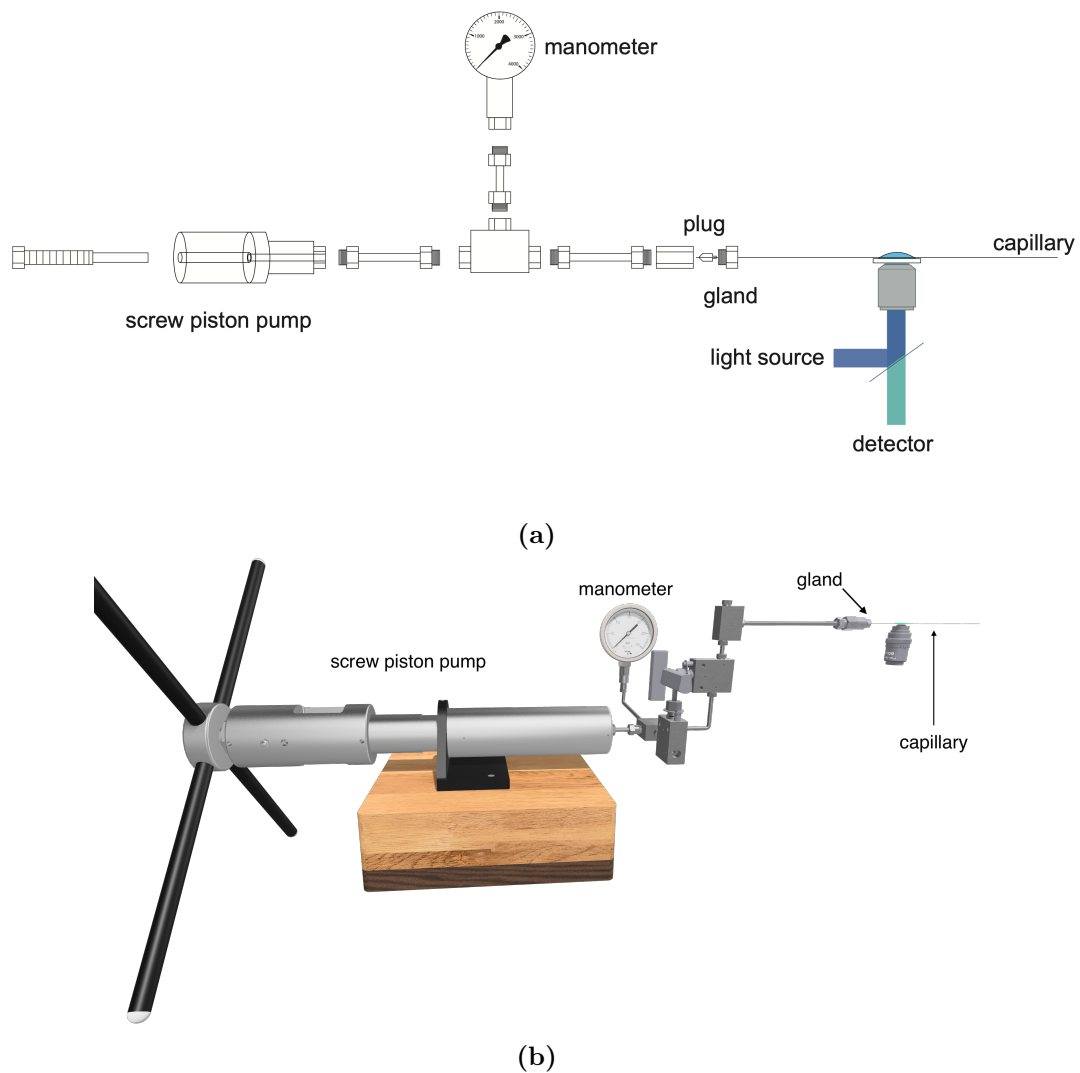


Fig. 3.3: (a) Schematic drawing [5] and (b) 3D rendering of the high-pressure setup.

3.2.1 Fused silica capillary

The used pressure cell is a fused silica capillary (WWP050375, Polymicro Technologies) with a square cross section (see Fig. 3.4). The capillary has an inner diameter of $(50 \pm 5) \mu\text{m}$, an outer glass diameter of $(300 \pm 15) \mu\text{m}$ and a polyimide coating of $\approx 30 \mu\text{m}$ [250]. Fig. 3.4 shows the cross section of the capillary. The refractive index of fused silica has a value of $n_{\text{fs}} \approx 1.46$ (see Fig. 3.5) [251]. The capillary has a length of several meters and is stored on a spool. In order to use it as a sample container for fluorescence spectroscopic measurements, a piece with a length of several centimeters is cut off and further prepared (see subsection 3.2.2).

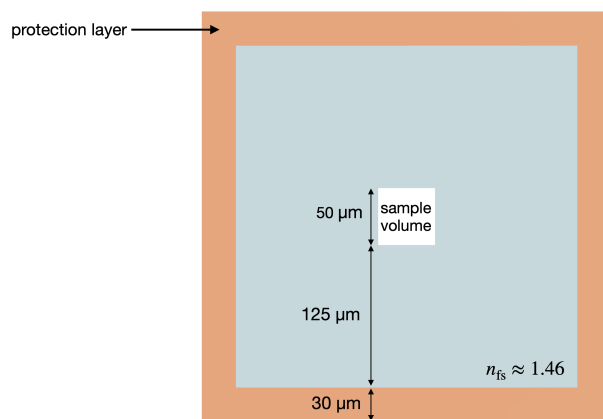


Fig. 3.4: Schematic cross section of the fused silica capillary with a polyimide protection layer (to scale).

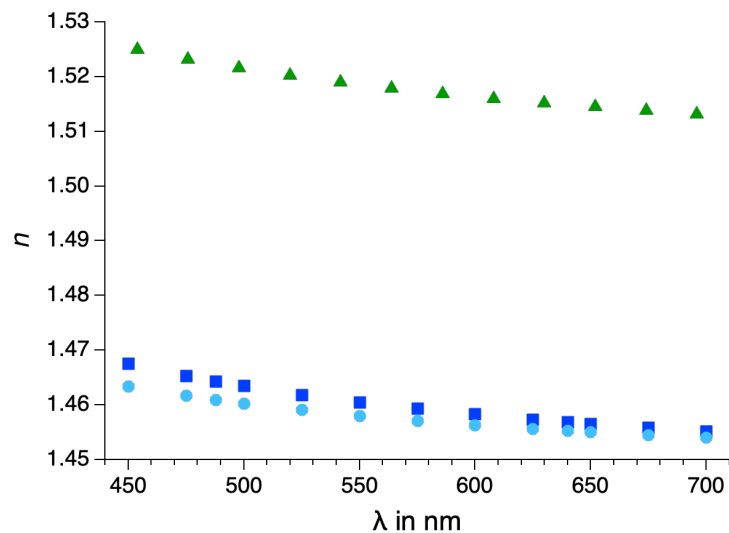


Fig. 3.5: Refractive index n of a fused silica matching liquid (blue squares) (see subsection 3.2.3), fused silica (cyan circles) and borosilicate glass (green triangles).

3.2.2 Capillary preparation and handling

As already mentioned in section 3.2, various steps are necessary to perform a high-pressure experiment using the fused silica capillary. The following steps are based on the capillary handling protocol described in [5, 83, 84] with some modifications enabling more reproducible conditions. First, an approximately 15 cm long piece of the capillary is cut from the spool and cleaned with acetone. The two component epoxy resin (301-2, EPO-TEK) adhesive is prepared as well. 100 parts of component A and 35 parts of component B of the epoxy resin are mixed in an Eppendorf tube, which equals 2.85 g and 1.00 g for component A and B, respectively. It is important to take caution while mixing to prevent air entrapment. Next, the mixture is centrifuged for one minute at 13000 revolutions per minute (rpm) to remove air bubbles. In order to glue the capillary into the pressure plug, the plug is placed in a capillary holder. Then the capillary is inserted in such a way that it protrudes about 1 cm at the top. The adhesive is applied by first dipping a single-use injection cannula (Sterican 0.40 x 20 mm BL/LB, Braun) into the reaction tube containing the adhesive. The droplet on the cannula is wiped off onto the protruding end of the capillary, allowing the droplet to subsequently flow along the capillary into the pressure plug. This process is repeated until the pressure plug is filled. Slight axial and angular motion of the capillary improves the distribution of the adhesive in the pressure plug. A uniform distribution is necessary to achieve a high pressure resistance of the adhesion. Next, the capillary is placed in the oven for 3.5 h - 4 h at a temperature of 80°C to cure the epoxy resin. In the next step, about 2 cm of the polyimide protection layer is removed with a propane flame to form an observation window, which can be positioned above the objective. Additionally, an approximately 1 cm long area is removed at the end of the capillary. Afterwards, the observation window is cleaned with acetone and the end of the capillary with a dry tissue, respectively. The prepared capillary is dipped with its end into the sample

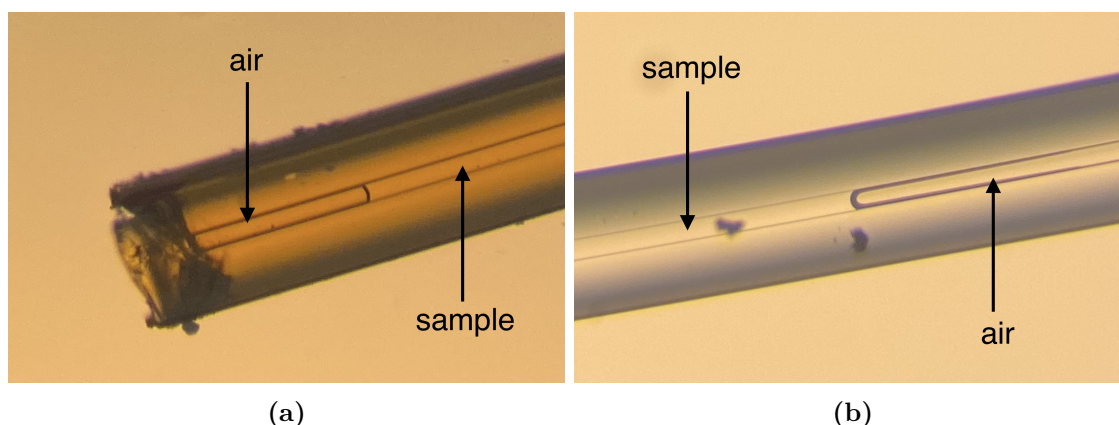


Fig. 3.6: Pictures of a fused silica capillary. The capillary is placed under a microscope to check the filling level of the sample solution. Two menisci should be visible, (a) one at the tip and (b) one in the rear of the capillary.

solution. Capillary forces soak the sample solution into the capillary. As a next step, the capillary is placed in a holder (see Fig. 4.16) and under a microscope to check the filling in order to ensure that the capillary is sufficiently filled with the sample solution (see Fig. 3.6). Two menisci should be identifiable. A propane-oxygen flame, capable of melting fused silica, is used to seal the capillary at the end. The other

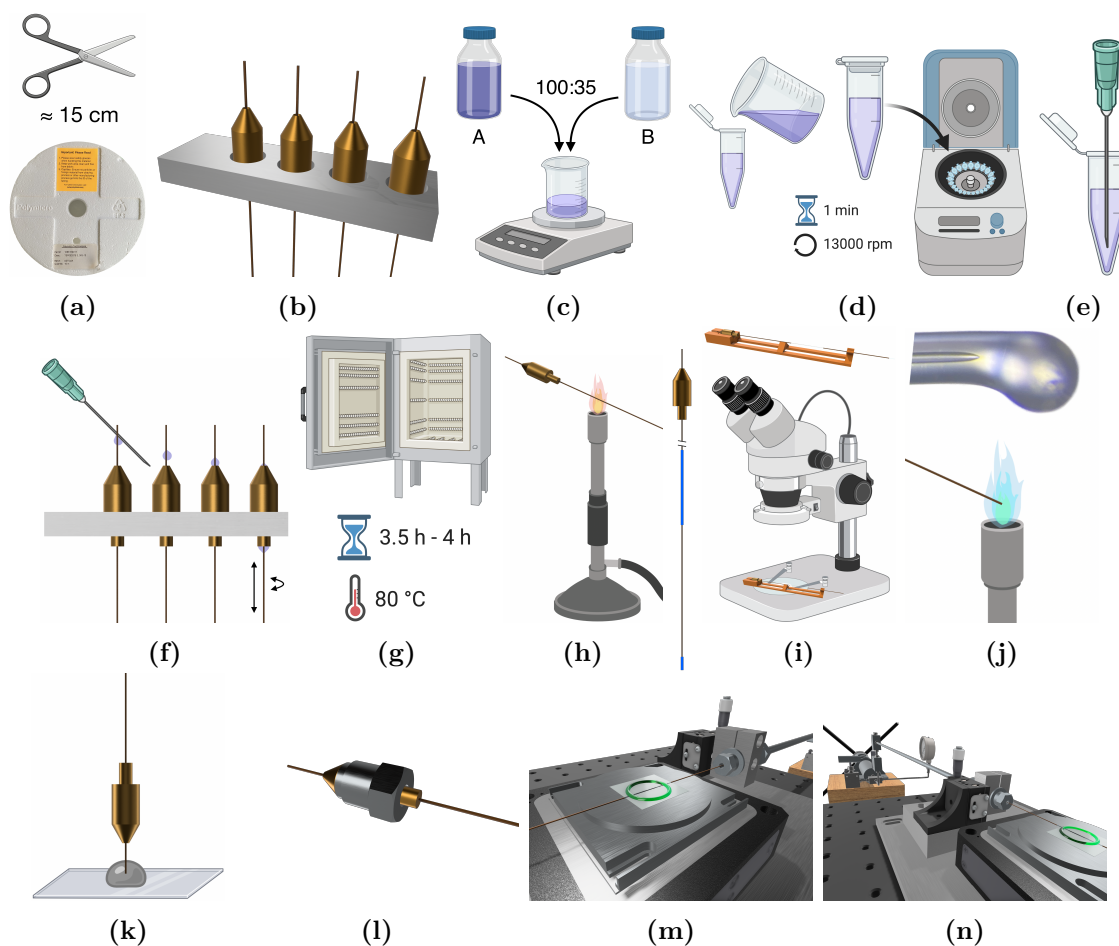


Fig. 3.7: Capillary preparation and handling protocol. (a) A piece of ≈ 15 cm is cut from the spool, (b) inserted in the pressure plug and put onto the capillary holder. (c) The two component adhesive is mixed in a 100:35 ratio and (d) centrifuged for a minute at 13000 rpm. (e,f) A cannula is inserted in the tube and the adhesive is applied by wiping it off onto the protruding end of the capillary. Additionally, repeated slight axial and angular motion ensures a uniform distribution. (g) To cure the adhesive it is baked for ≈ 4 h at 80°C . (h) In the next step, an ≈ 2 cm wide optical window is created by burning of the protection layer. The protection layer at the tip is removed as well (blue lines). Subsequently, the window and the tip are cleaned. After inserting the sample solution by capillary forces, (i) the filling level is checked with a microscope. (j) The capillary is sealed with a propane-oxygen flame. (k) The other end is dipped into silicon oil. (l) Finally, the capillary is inserted into the pressure gland and (m,n) connected to the screw piston pump [252].

end is dipped into silicon oil (Silicone oil M3, 3 cSt, ROTH) in order to prevent a mixture of the hydraulic water and the sample solution. Finally, the pressure plug with the capillary is inserted into the pressure gland which is then connected with the screw piston pump. The entire capillary preparation and handling protocol is illustrated in Fig. 3.7.

3.2.3 Optical multi layer

A major disadvantage of using capillaries made of fused silica is that microscope objectives, such as the one in the experimental setup, are usually designed for coverslips made of borosilicate glass. The lower refractive index of fused silica with $n_{fs} \approx 1.46$ in contrast to borosilicate glass with $n_{bk7} \approx 1.53$ (see Fig. 3.5) results in optical aberrations and thus in a reduced signal-to-noise ratio in single molecule fluorescence detection. Moreover, the light enters the sample volume through the side walls of the capillaries, which leads to even more pronounced aberrations (see Fig. 3.8). However, it is possible to reduce such aberrations by increasing the apparent thickness of the capillary wall [4,5]. The optimal thickness of a fused silica coverslip t_{opt} for different angles of incidence α , when the objective is corrected for a borosilicate coverslip with a thickness of t_{bk7} , can be calculated with

$$t_{opt} = t_{bs} + t_{bs} \cos(\alpha) \cos(\zeta) \frac{\tan(\zeta) - \tan(\xi)}{\sin(\alpha - \zeta)}, \quad (3.2)$$

$$\zeta = \arcsin\left(\frac{n_1}{n_2} \sin(\alpha)\right), \quad (3.3)$$

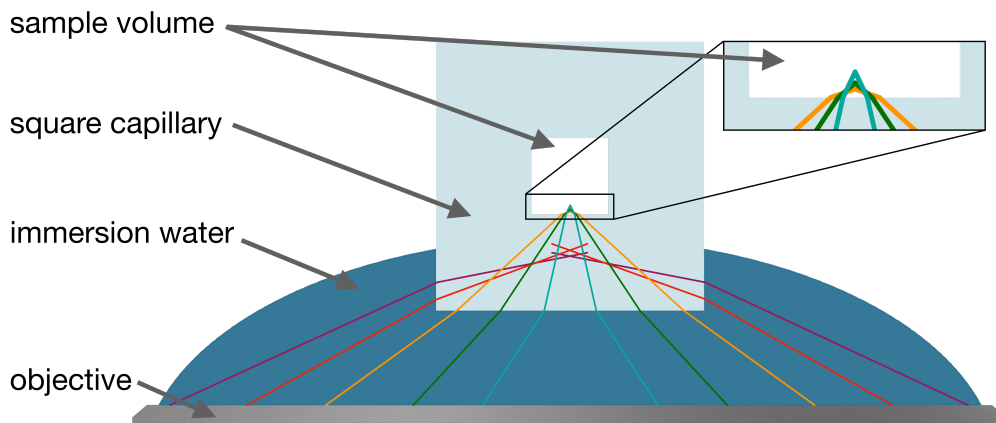


Fig. 3.8: Schematic optical paths when focusing into the square capillary made of fused silica using water immersion. The index mismatch and reduced wall thickness lead to aberrations. Due to light entering the capillary to its side walls, the effective NA of the objective is reduced since these rays are not reaching the sample volume.

$$\xi = \arcsin\left(\frac{n_1}{n_3} \sin(\alpha)\right), \quad (3.4)$$

with the condition

$$n_1 < n_2, n_3,$$

where n_1 is the refractive index of water $n_w \approx 1.33$, n_2 the refractive index of fused silica $n_{fs} \approx 1.46$ and n_3 the refractive index of borosilicate $n_{bk7} \approx 1.52$ [4, 5]. The dependence is additionally illustrated in Fig. 3.9. However, Eq. 3.2 - Eq. 3.4 and Fig. 3.9 show that it is not possible to correct for all angles of incidence α with the same thickness of a fused silica coverslip. In order to preserve a high effective numerical aperture of the objective, being the determinant of the light collection efficiency, it is preferable to get an optimal correction of the highest angle of incidence, which is $\alpha_{\max} \approx 64.6^\circ$ for a NA of 1.2. Based on Fig. 3.9, it can be inferred, that the ideal thickness of a fused silica coverslip is within the range of approximately $160 \mu\text{m}$ to $240 \mu\text{m}$ for the correction of the highest angle of incidence. Given the wall thickness of the capillary itself of $125 \mu\text{m}$ (see Fig. 3.4), a $\approx 35 \mu\text{m} - 115 \mu\text{m}$ thick fused silica coverslip is required with the respective correction collar setting of the objective to correct the beam path of the highest angle. Since fused silica coverslips are brittle, it is advisable to choose a rather thick coverslip. Therefore, and due to their availability, $100 \mu\text{m}$ thick coverslips are used (Hellma Optik GmbH Jena), leading to an

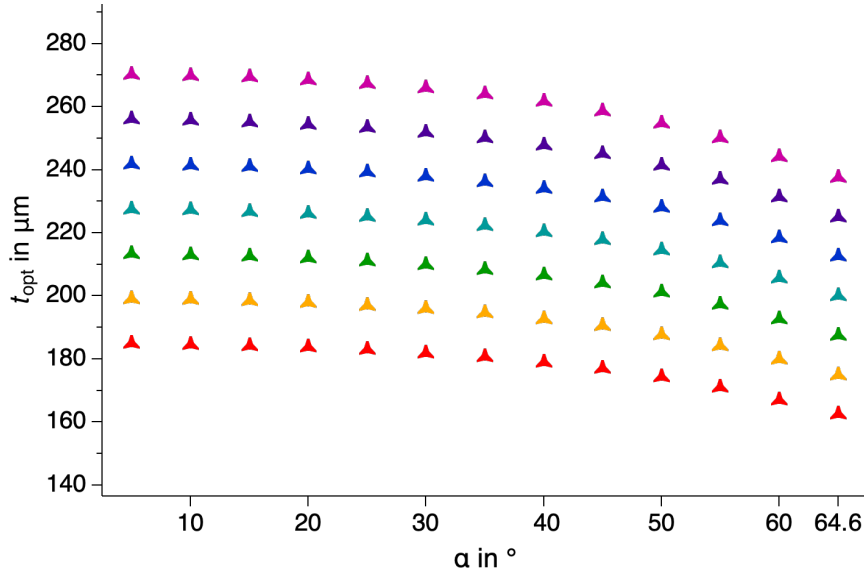


Fig. 3.9: Dependence of the optimal thickness t_{opt} of a fused silica coverslip on the angle of incidence α of an objective corrected for borosilicate coverslips with a thickness of $130 \mu\text{m}$, $140 \mu\text{m}$, $150 \mu\text{m}$, $160 \mu\text{m}$, $170 \mu\text{m}$, $180 \mu\text{m}$ and $190 \mu\text{m}$ (from bottom up).

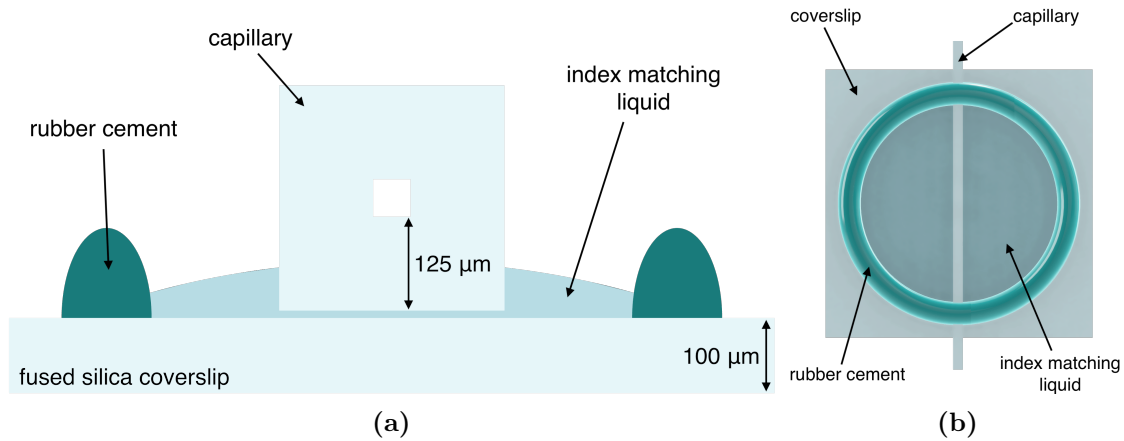


Fig. 3.10: Schematic drawing (not to scale) of the optical multi layer (OML). It consists of a square fused silica capillary positioned on top of a fused silica coverslip. A circle of rubber cement serves as a barrier for an index matching liquid, placed between the capillary and coverslip to prevent severe aberrations. This arrangement results in an effective fused silica glass thickness of $\approx 225 \mu\text{m}$. (a) side and (b) top view of the OML.

effective glass thickness of $225 \mu\text{m}$. To prevent the light passing interfaces between media with differing refractive indices, an optical gel (Fused Silica Matching Liquid Code 50350, Cargille Laboratories) is used, which has almost the same refractive index as fused silica [253]. Thus, there is no refraction of light between the fused silica coverslip and the capillary. The optical gel is held in place by a circle of rubber cement (Fixogum, Marabu) on top of the capillary and coverslip. The rubber cement also serves the purpose of fixing the capillary. The described assembly of this optical multi layer (OML) is shown in Fig. 3.10.

3.2.4 Capillary PMMA multi layer

The optical multi layer (see subsection 3.2.3) reduces aberrations in contrast to the bare capillary. However, a major disadvantage of using these fused silica coverslips is that they are very fragile and very expensive as well. Therefore, as an alternative, the fused silica coverslip was replaced by a PMMA film (LS496283 S J P, GoodFellow). The PMMA film has a refractive index of $n_{\text{PMMA}} \approx 1.49$ and a thickness of $50 \mu\text{m}$. Since a $100 \mu\text{m}$ thick PMMA film was not at hand, two layers of the film were stacked on top of each other to mimic a PMMA film thickness of $100 \mu\text{m}$ and an overall thickness of $225 \mu\text{m}$. In order to prevent optical transitions from the PMMA film to air, a thin film of water was put between both layers of PMMA. Water was

chosen here for simplicity of handling.

3.2.5 Reuse of pressure plugs

Up to present, it was intended that the pressure plugs into which the capillaries are glued prior to the connection to the screw piston pump are used just once. Since it is not practical to have to machine a new pressure plug for each experiment using high pressure, a procedure for the reuse of the pressure plugs has been established. First of all the used pressure plugs with the capillaries are put into an oven for about 3 hours at 400 °C to disintegrate the epoxy resin adhesive. Afterwards, the capillaries can be removed from the plug. Next, the pressure plugs are cleaned with a copper brass cleaning paste (Kupfer-Messing-Bronze, Elsterglanz). In the following step, the plugs are washed with water. In order to clean the inside of the pressure plugs as well small syringes (Injekt®-F, Braun) are used. They are used with cannulas (Sterican 0.40 x 20 mm BL/LB, Braun), which have a diameter of just 0.40 mm and are therefore thin enough to get inside the plugs clearance hole with a minimal diameter of 0.50 mm. The inside of the plugs is then cleaned by flushing it several times with water and a parallel movement of the cannula inside the clearance hole. Finally, the pressure plugs are air-dried before reuse for a new experiment. The individual steps are illustrated in Fig. 3.11.

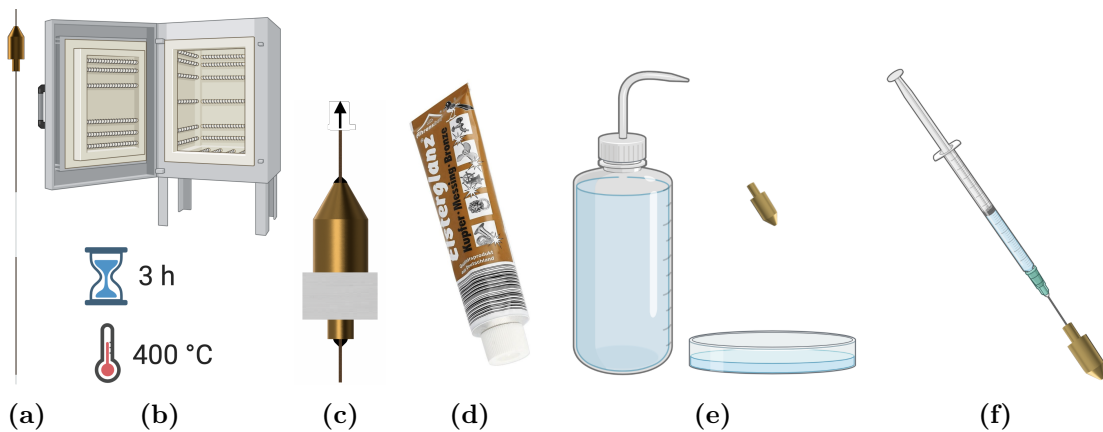


Fig. 3.11: Procedure for the reuse of pressure plugs. After an experiment (a) the used capillary is (b) heated for about 3 h at 400 °C to disintegrate the adhesive. (c) Afterwards the capillary can be removed from the plug. (d) Then it is cleaned with a cooper brass cleaning paste and (e) next with water. (f) In order to clean the inner channel of the capillary, a cannula is used to flush the interior several times. Finally, the pressure plug air dries before it is usable for another experiment.

3.3 Counting electronics

3.3.1 Routed TCSPC

Two already implemented counting electronics useable for experiments are the time correlated single photon counting (TCSPC) boards Timeharp200 [254] from Picoquant and SPC-134 TCSPC from Becker & Hickl GmbH. Both feature classical TCSPC electronics (TDC and TAC based), leading to a characteristic dead time after receiving a photon signal from a detector. The dead time is the time the electronic needs to process an applied signal before it is ready to process the following one. In the case of photon detection it implies that the detected arrival times of two photons have a minimum time difference of the dead time, assuming the dead time is the limiting factor. The dead times of both TCSPC modules are about 350 ns for the Timeharp200 [255] and 100 ns for the SPC-134 [256]. Since the signals of all detectors are sharing the timing electronics through a router, this also applies to signals from different detectors. As a consequence, no photon correlations on timescales shorter than the dead time are available, as can be seen in Fig. 3.12.

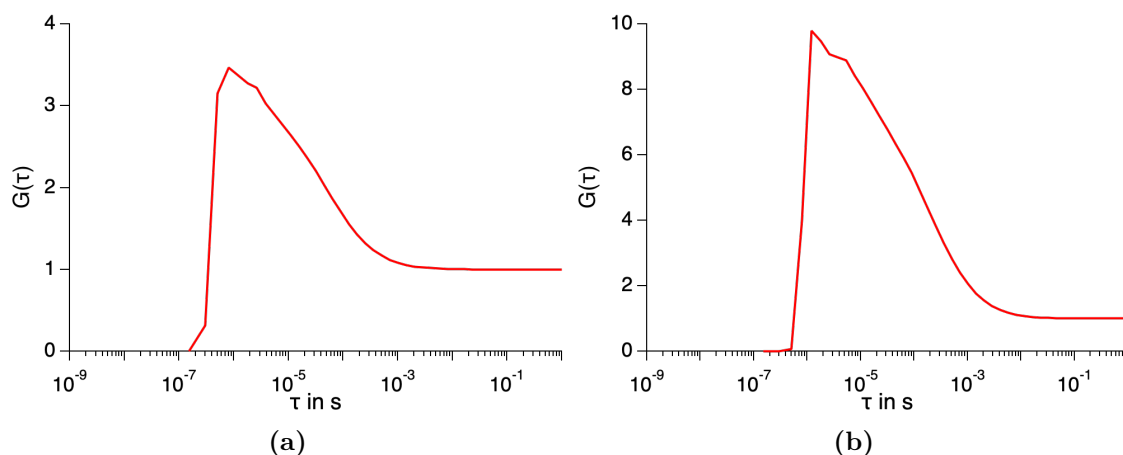


Fig. 3.12: Auto-correlations of the fluorescence signal of Alexa Fluor 488 in solution, exemplifying the effect of the dead time on the correlation functions of both TCSPC modules, (a) Timeharp200 from Picoquant and (b) SPC-134 from Becker & Hickl. Since their respective dead times of 350 ns and 100 ns determine the minimum time difference between two recorded photons, no dynamics can be analyzed at a shorter time scale.

3.3.2 Parallel time tagger

Since the existing single photon counting electronics have characteristic dead times of 350 ns and 100 ns, respectively, they are not suitable for nsFCS or nsFCS-FRET experiments and the investigation of chain dynamics in the nanosecond time regime (see

subsection 2.5.3). To overcome this limitation, alternative counting electronics were implemented. The new counting electronic is the USB2.0-TDC CS - TP 01-04-82 time-to-digital Converter (TDC) from Surface Concept (GPX-TDC). The described properties of the GPX-TDC are taken from the manual of the manufacturer [257] and the most important specifications are described below. The TDC consists of 4 stop input channels with a pulse-pair resolution of 5.5 ns for each channel and 0 ns between two different channels. It runs with a GPX TDC chip (ACAM GmbH) in conjunction with a conventional counter/timer and has a time bin resolution of $r_{\text{bin}} = 82.304$ ps. Due to one common start input channel, one is able to measure the photon arrival times with respect to an external signal. The frequency of the trigger signal f_{trigger} has to be in a range between 100 kHz and 7 MHz and is further divided down by a frequency divider of 2, 4, 8, or 16. This function can be used for pulsed excitation of the sample and a measurement of the photon times with respect to the laser pulse. If no external trigger is connected, the GPX-TDC measures the times with respect to an internal clock. Each event is saved as a 32 bit structure shown in Fig. 3.13. The 3 most significant bits (MSB) are not in use. Bits 28-26 represent the channel number in which the event was detected. Bits 25-18 contain the interval number for the macro time n_{interval} , and the 17 least significant bits (LSB) contain the bin number of the corresponding micro time n_{bin} of an event. Bit 17 is not used as well. The actual arrival time of a photon t_{photon} is then calculated by

$$t_{\text{photon}} = n_{\text{interval}} \cdot t_{\text{interval}} + n_{\text{bin}} \cdot r_{\text{bin}} \quad (3.5)$$

with t_{interval} given either by the length set in the software for the use of the interval trigger or by

$$t_{\text{interval}} = \frac{1}{f_{\text{trigger}}} \quad (3.6)$$

when using an external trigger signal. A calculation of an example arrival time of a detected photon is shown in Fig. 3.14. According to the data structure of the GPX-TDC it follows that the counter of the micro time has an overflow at least after $2^{17} \cdot 82.304$ ps ≈ 10.788 μ s. Since the system does not have an overflow flag it is not practical to have an $t_{\text{interval}} > 10.788$ μ s since one has no information whether an overflow occurred or not. Due to the fact that the counter of the macro time consists of only 8 bits it follows that this counter has an overflow at least every $256 \cdot 10.788$ μ s ≈ 2.76 ms. A crucial advantage of the new implemented counting electronics is that no dead time between two different input channels exists, in contrast to the Timeharp200 and SPC-134. This enables the detection of two

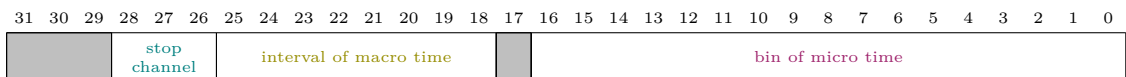
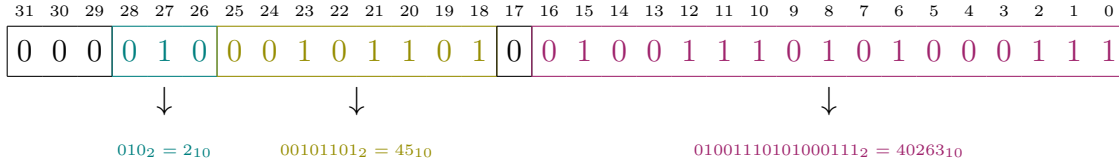


Fig. 3.13: 32 bit data structure of each event recorded by the GPX-TDC. The 3 most significant bits (MSB) and bit 17 are not used (gray).



detector: APD 2

$$t_{\text{photon}} = 45 \cdot 10 \mu\text{s} + 40263 \cdot 82.304 \text{ ps} \approx 453.3 \mu\text{s}$$

Fig. 3.14: Example of a measured event with its binary representation and corresponding decimal values (top). The calculation of the related photon arrival time according to Eq. 3.5 with an example $t_{\text{interval}} = 10 \mu\text{s}$ is shown at the bottom.

photons in two channels and hence the analysis of the correlation function in the sub 100 ns regime as well. Even within one channel the dead time is only 5.5 ns and thus significantly lower than with the existing TCSPC modules. With the detector dead times of $\approx 30 \text{ ns} - 50 \text{ ns}$, however, this advantage cannot be utilized (see below). Correlations resulting from measurements of free diffusing fluorophores using the GPX-TDC are displayed in Fig. 3.15. The auto-correlation function of one detector reveals a new limiting factor with respect to the smallest measurable time difference between two photons (see Fig. 3.15a). The correlation drops at a lag-time $\tau \approx 50 \text{ ns}$ which is due to the dead time of the used APD. A further artifact is detector afterpulsing of the APD leading to a rise in the correlation function towards shorter τ . Both, detector dead time and afterpulsing prevent nsFCS experiments when using only one detector for one signal channel. Since afterpulsing artifacts are uncorrelated between two detectors and the GPX-TDC has no inter channel dead time one can avoid the discussed limitations by using two detectors

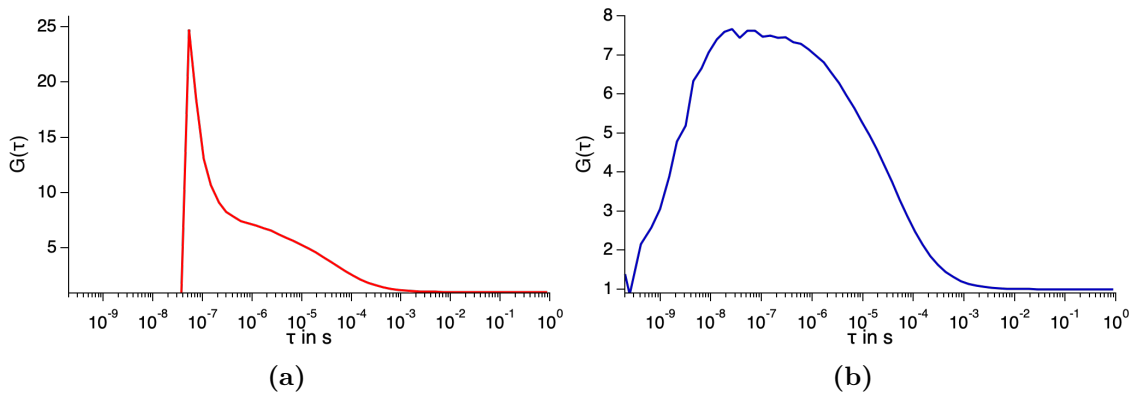


Fig. 3.15: Auto-correlation and pseudo auto-correlation functions of freely diffusing dyes, measured with the GPX-TDC. (a) The auto-correlation function of the photon signal with one detector is limited by the dead time of the detector as well as afterpulsing artifacts. (b) By dividing the photons onto two detectors with a 50/50 beam splitter, one can determine the pseudo auto-correlation function, which does not have these limitations [258, 259].

for the measurement of the same signal and split the emitted photons with a 50/50 beam splitter. The signals are then cross-correlated according to Eq. 2.110. As one records non distinguishable photons in each channel, this cross-correlation is called pseudo auto-correlation (see Fig. 3.15b). As a consequence, nsFRET-FCS experiments (see subsection 2.5.3 and section 2.6) are requiring four detectors, two for the donor and two for the acceptor channel, respectively. For simplicity, in the following all pseudo auto-correlation functions are called auto-correlation functions.

3.4 Pressure capillary sample stage

As described in subsection 3.2.2, the capillary is glued into a pressure plug, which is inserted in a gland and finally connected to the high pressure piston pump. Due to the not completely fixed moveable connections and tubes and additionally the leverage effect caused by the 50 cm long tube towards the optical stage, the capillary is not always at the exact same position and has to be adjusted accordingly before each measurement. The previous implementation had consisted of screwing the coupling adapter between the tube and the capillary gland more or less provisional into a holder (see Fig. 3.16). The holder itself consisted of a pedestal post (Thorlabs) and a slip-on post clamp (Thorlabs) and was mounted to the optical table by a clamping fork (Thorlabs). However, this approach has various disadvantages in terms of how the capillary is positioned above the microscopes objective for a measurement. The

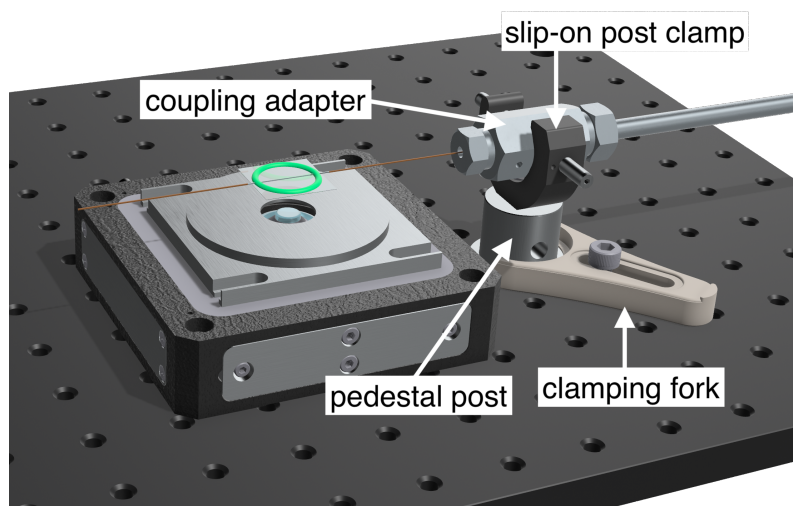


Fig. 3.16: 3D rendering of the previous used holder for the connection of the capillary. In this implementation, the coupling adapter is placed in a slip-on post clamp and tightened with screws. The clamp is mounted on a pedestal post and is fixed with a clamping fork.

height was only roughly adjustable by adding or removing various spacers (Thorlabs) to the pedestal post. A disadvantage of this approach is that it is difficult to adjust the height with sufficient accuracy to ensure that the capillary is resting nearly flat on the optical table. The flat contact of the capillary is necessary for the best possible optical conditions. The coarse adjustment capabilities of the capillary had as consequence that the set height was too low or too high, resulting in strong optical aberrations. When the capillary is fixed to the optical table to force it to lie flat, there is a high risk that the capillary will get damaged due to the strain, in the worst case it can break. But even if the capillary does not break immediately, there is a high chance that tiny ruptures and damages lead to a greatly reduced pressure resistance. In addition, the attachment to the coupling adapter in the oval shaped post clamp is not entirely tight, but slightly unstable. Another significant disadvantage and problem of the previous method is the fact, that the connected capillary can no longer be rotated. As a consequence it is possible that the side wall of the capillary lays slightly rotated above the objective leading to aberrations as well. To correct a rotated capillary, one has to undergo a try and error routine consisting of unscrewing the gland, slightly rotating the capillary and tightening the gland again until the capillary has the intended orientation. To enable the capillary to be moved smoothly and continuously along one lateral axis, an optical table could be installed which can be shifted with a manual micrometer drive, allowing a precise shift along one lateral axis. As the other lateral axis along the direction of the capillary is non critical during adjustment, it is fairly easy to position the capillary in the lateral direction over the objective. Nevertheless, this solution has a disadvantage as well. Not the entire capillary is shifted laterally by the sample stage. The end close to the pressure plug and the connection to the rest of the screw piston pump is not shifted since the pedestal post where the tube is fastened is not attached to the moveable stage and therefore fixed in place. The relative displacement of both capillary ends can again lead to strain and thus a glass breakage or a reduced pressure resistance.

In order to enable an easier and more comfortable way of the whole capillary handling process, a new sample stage was designed to address the described limitations and weaknesses of the previous approach (see Fig. 3.17). To solve the issue of the relative displacement of both capillary ends, both, the lateral piezo scanner with the sample stage as well as the post where the capillary end is attached are mounted on top of one adapter plate made of aluminum (see Fig. 3.17a). Slotted holes in the corners of the plate allow for a lateral movement of the whole assembly along one lateral axis by hand. Once the intended position of the capillary is reached, the adapter plate is fixed to the optical table by four screws. To finely adjust the height above the sample stage, the coupling adapter of the pump is fastened in a custom built clamp which itself is attached to a travel translation stage (MS1S/M, Thorlabs). The stage is connected with the adapter plate via an angle bracket (MS102, Thorlabs) and a small aluminum block (see Fig. 3.17b and Fig. 3.17c). The aluminum block provides two slotted holes along the axis of the capillary to enable small displacements along this axis as well if needed. The last major drawback one has to account for is

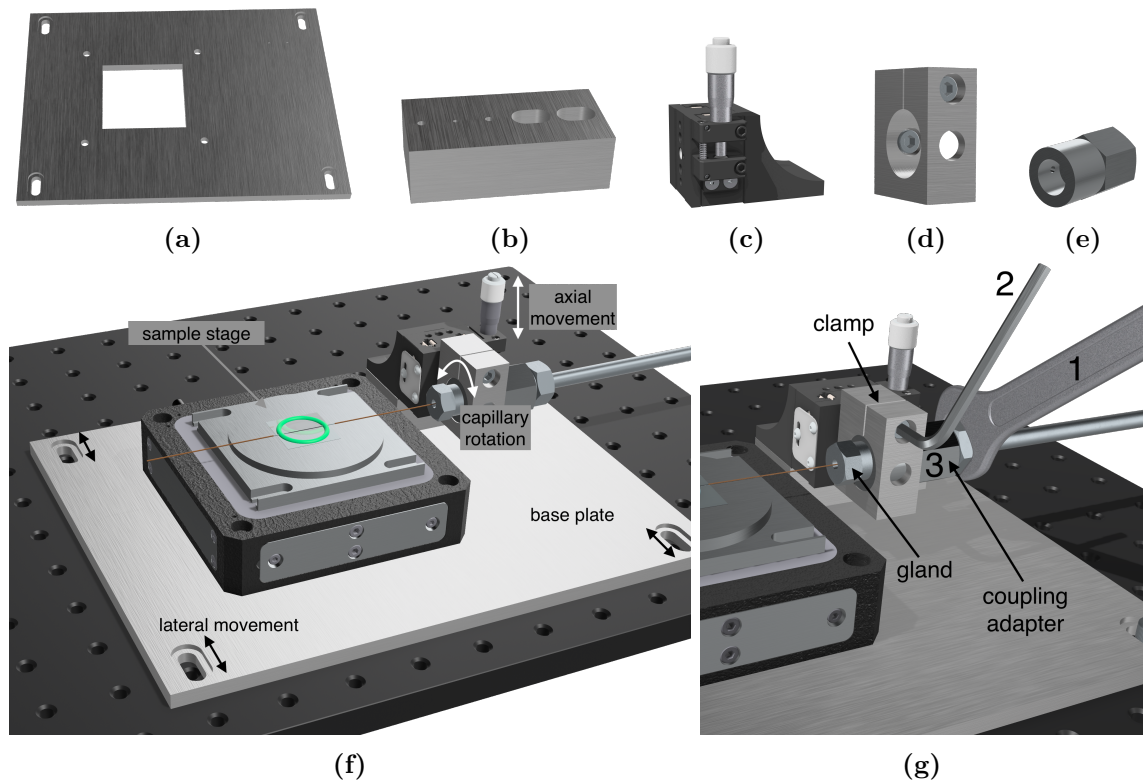


Fig. 3.17: 3D models of the parts of the improved capillary connection point, with (a) the base plate, (b) the small aluminum connection block, (c) the travel translation stage from Thorlabs, (d) the clamp and (e) the adapter for the connection of the capillary with one side being rounded off to enable a rotation of the capillary. (f) shows the assembled construction which is finally mounted to the optical breadboard of the microscope. (g) Workflow of capillary rotation. (1) First, the gland connecting the coupling adapter with the tube of the pump is loosened. (2) Afterwards, the screw of the clamp is loosened as well. Now the coupling adapter with the connected gland and capillary can be slightly rotated in order to adjust the position of the capillary above the objective. After rotation, the clamp screw is tightened again (2) to keep the capillary and its orientation in place. In the last step, the gland at the other end of the coupling adapter is screwed in to connect the pump with the capillary (1).

the impossibility of the capillary to be rotated when connected to the screw piston pump. Since an assembly which allows the whole screw piston pump to be rotated or moved is not practical the idea was to be able to just rotate the coupling adapter where the capillary is connected to the pump. To do so, the edges on one side of the adapter were rounded off (see Fig. 3.17e). This round side is placed in the custom built clamp. In order to be able to rotate the tightened capillary, the gland, which mounts the tube from the pump with the adapter, is loosened (see Fig. 3.17d). If this gland is loose, one can slightly rotate the coupling adapter and consequently the capillary can be rotated until the desired alignment is reached. Then, the screw

of the clamp is tightened, keeping the adapter and capillary in place. Finally, the gland of the tube is tightened to seal the pump. This process of capillary rotation is shown in Fig. 3.17g.

3.5 Samples and buffer

3.5.1 Fluorophores

A total of six different fluorophores were used for spectroscopic measurements. These were either experiments with free diffusing fluorophores in fluorescence correlation spectroscopy measurements or experiments, where the dyes were used as a protein or DNA label for FRET experiments. Two dyes are from ATTO-TEC, TTO 488 (AT488) and ATTO 647N (AT647N). Their spectra are shown in Fig. 3.18. Besides the dyes from ATTO-TEC three dyes belong to the Alexa Fluor dye family from ThermoFisher Scientific, Alexa Fluor 488 (AF488), Alexa Fluor 594 (AF594) and Alexa Fluor 647 (AF647). Their spectra are shown in Fig. 3.19 with an additional fluorophore Cy5 from Cytiva. All dyes are characterized by a comparatively high fluorescence quantum yield and photo stability. Furthermore, they are well soluble in water and show pH-independent fluorescence to a great extent. Key characteristics of the dyes, namely their fluorescence quantum yield, fluorescence lifetime and extinction coefficient as well as excitation and emission maxima are summarized in Tab. 3.1.

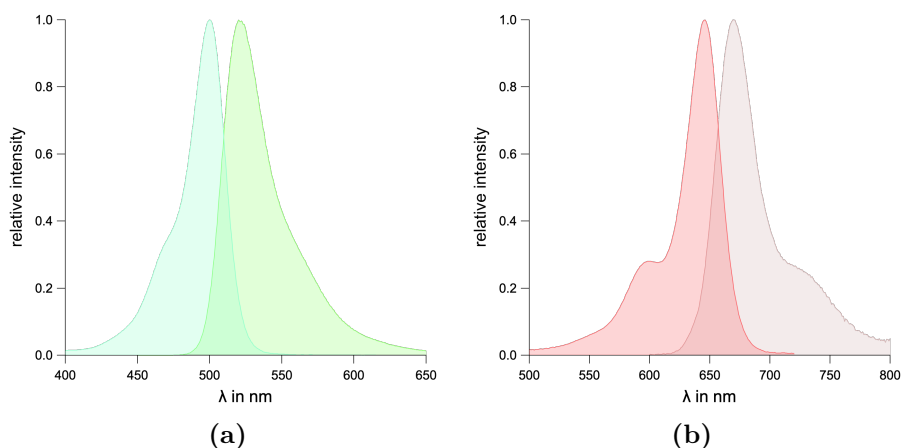


Fig. 3.18: Absorption and emission spectra (left/right) of (a) AT488 and (b) AT647N.

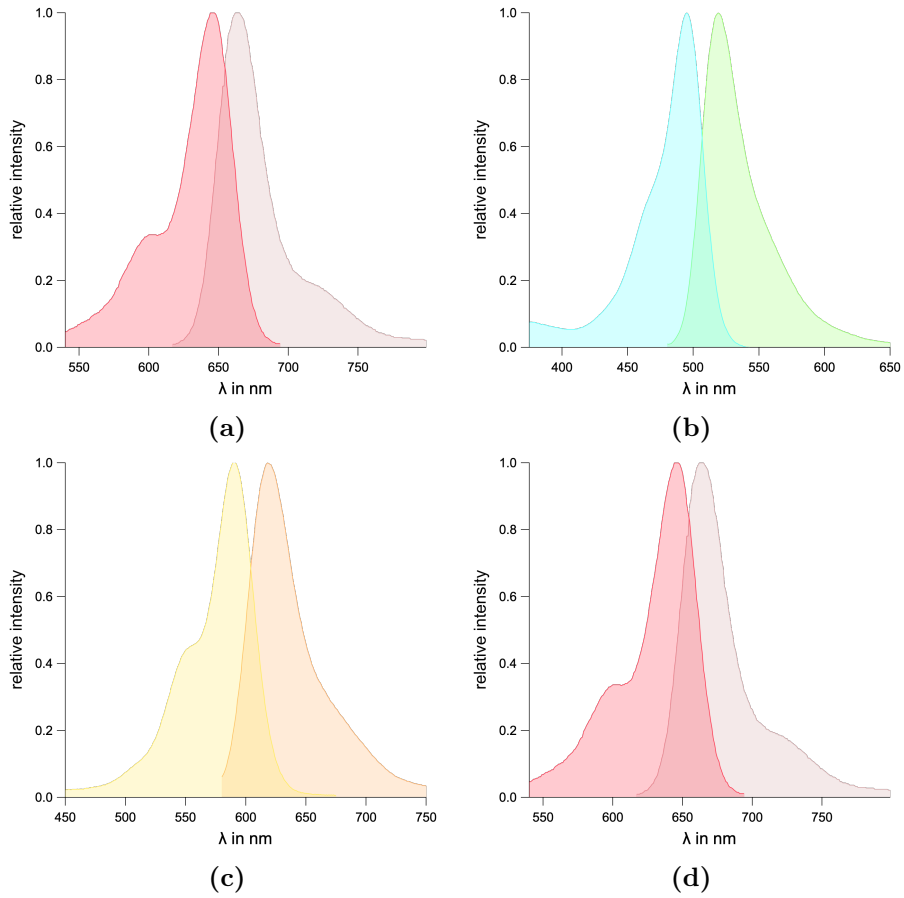


Fig. 3.19: Absorption and emission spectra (left/right) of (a) Cy5 and the Alexa Fluor dyes (b) AF488, (c) AF594 and (d) AF647.

Tab. 3.1: Wavelength of maximum excitation and emission, λ_{exc} and λ_{em} , extinction coefficient ε_{max} as well as the fluorescence quantum yield Φ_f and lifetime τ_f of the used dyes [260–263].

Dye	λ_{exc} in nm	λ_{em} in nm	ε_{max} in $\text{cm}^{-1}\text{M}^{-1}$	Φ_f	τ_f in ns
AF488	495	519	73000	0.92	4.1
AF594	590	617	92000	0.66	3.9
AF647	650	668	270000	0.33	1.0
AT488	500	520	90000	0.80	4.1
AT647N	646	664	150000	0.65	3.5
Cy5	649	667	250000	> 0.28	1.0

3.5.2 Fluorescent microspheres

TetraSpeck™ Microspheres (T7279, Invitrogen™) are latex beads with a diameter of 0.1 μm . They are stained with four different dyes resulting in beads with four well-separated excitation and emission peaks [264]. These excitation/emission peaks are at (365/430) nm, (505/515) nm, (560/580) nm and (660/680) nm, respectively. The corresponding spectra are shown in Fig. 3.20. Since the respective emission and absorption spectra of the dyes overlap and due to the high dye concentration, the dyes are undergoing FRET as well. Therefore, the Microspheres can be used as a FRET reference and setup characterization sample.

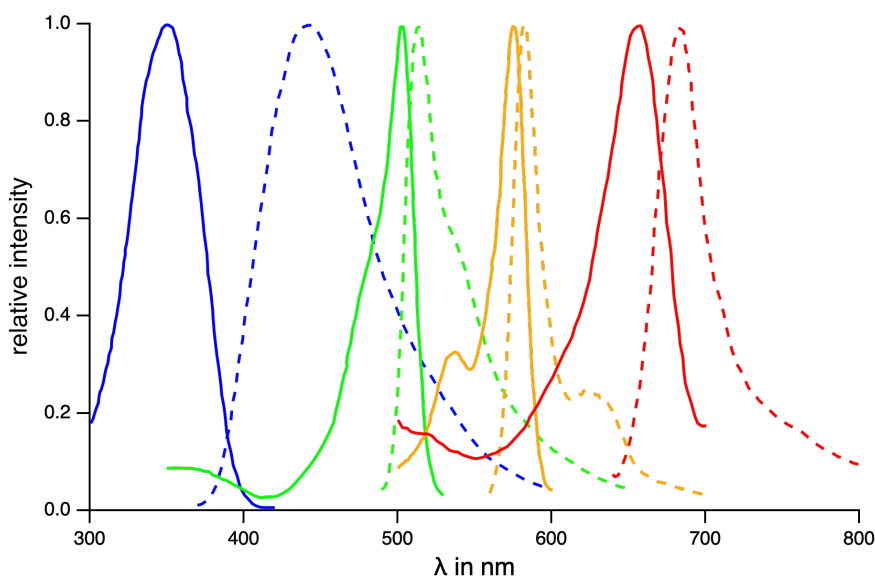


Fig. 3.20: Normalized excitation (solid lines) and emission (dashed lines) spectra of TetraSpeck blue, green, orange and dark red dye embedded in TetraSpeck™ Microspheres T7279 (Invitrogen) [261].

3.5.3 DNA samples

Double stranded DNA

Double-stranded DNA (dsDNA) from metabion was used for the evaluation of the best correction collar setting of the objective when using a fused silica capillary. It consists of 23 base pairs (bp) and is labeled with AT488 and AT647N, as the donor and acceptor fluorophore for FRET experiments (see Fig. 3.21). The donor-acceptor distance is 9 bp.

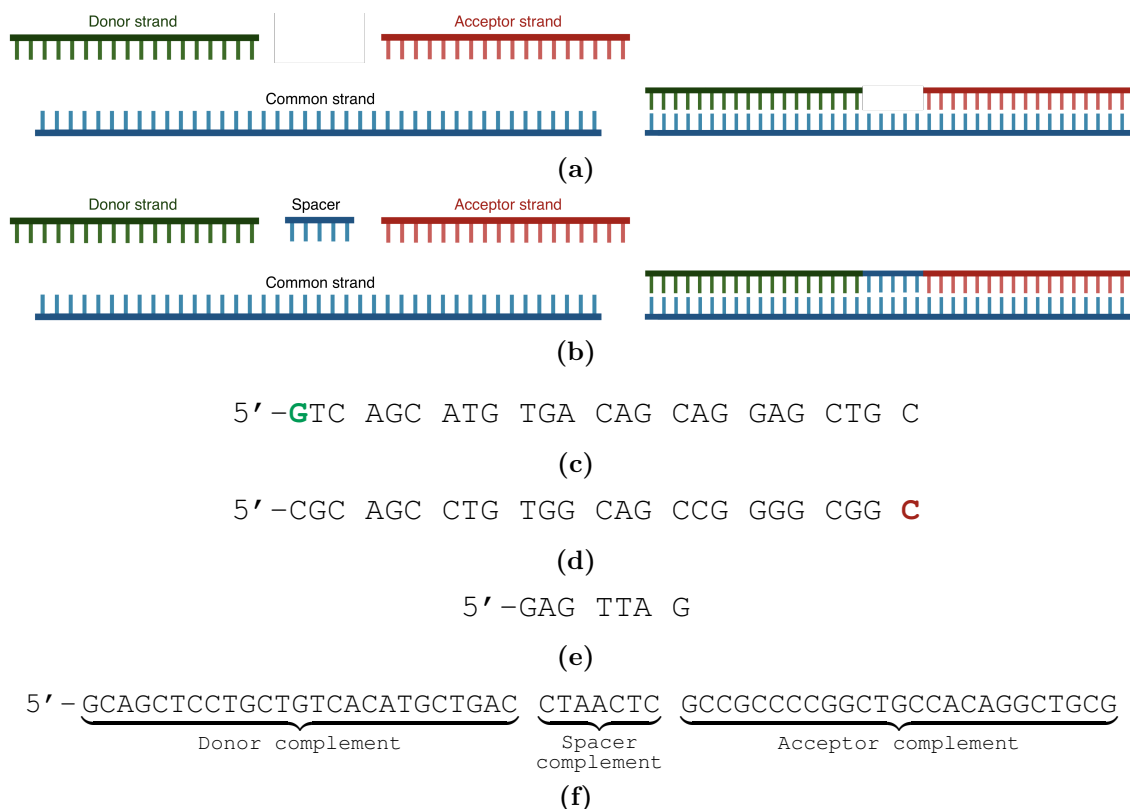


Fig. 3.23: 3/4-stranded DNA hybrids, consisting either of (a) 3 or (b) 4 single DNA strands. Both have (c) a donor (green) and (d) an acceptor (red) strand, which are labeled with the fluorophores AT488 or AT647N, respectively. Position of the dyes is indicated by green or red bases in the sequences. The donor strand is complementary to the 5' end and the acceptor strand to the 3' end of the common strand, shown in (f). The 4-stranded hybrid has an additional spacer (e) matching the gap between the donor and acceptor strand. (a) and (b) show schematic representations of the hybrids, whereas (c)-(f) show the respective sequences [252].

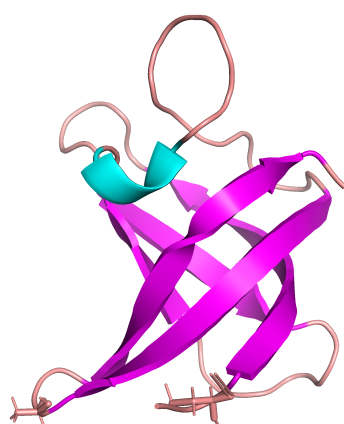
respectively (see Fig. 3.23c and Fig. 3.23d). Both hybrids share a common ssDNA strand (see Fig. 3.23f), whose 5' end is complementary to the donor labeled strand and the 3' end to the acceptor labeled strand. The 4-stranded hybrid contains an additional 7 bp spacer complement (see Fig. 3.23e), matching the gap between the donor and acceptor labeled strands.

3.5.4 Cold shock protein CspA

The cold shock protein CspA from *Escherichia coli* is a two state folding model protein [269]. Its sequence contains 70 amino acids and has secondary structure elements of alpha helices and beta-sheets (see Fig. 3.24) [270]. The protein is FRET labeled with AF488 and AF647 as the donor and acceptor at positions 2 and 59, respectively, where serin and alanin are cystein mutated.

```
1 MCGKM TGIVK WFNAD KGFGF ITPDD GSKDV FVHFS AIQND GYKSL
46 DEGQK VSFTI ESGCK GPAAG NVTSL
```

(a)



(b)



(c)

Fig. 3.24: (a) Sequence of the cold shock protein CspA S2C/A59C of *Escherichia coli* with labeling positions of both dyes, donor (green) and acceptor (red) at position 59 and 2, respectively. (b) shows its secondary structure elements in cyan for alpha helix and magenta for beta-sheet [269, 271]. (c) illustrates the labeling positions of the donor (green) and acceptor (red) dyes.

3.5.5 Prothymosin alpha

The intrinsically disordered protein prothymosin alpha (ProT α) was chosen as a model nsFCS sample since it is known for chain reconfiguration dynamics in the nanosecond time range. It consists of 110 amino acids and has a net charge of $z = -44$ [6, 170, 202, 272]. The sequence of ProT α is shown in Fig. 3.25a with two mutations E56C and D110C [6, 272]. Fig. 3.25b shows the corresponding AlphaFold structure prediction [160, 161, 273]. ProT α is labeled for FRET experiments with AF488 and AF594 as the donor and acceptor fluorophore, respectively [7, 195, 272]. The sample of ProT α was provided by Dr. Andrea Sottini from the research group of Ben Schuler.

```

1 SDAAV DTSSE ITTKD LKEKK EVVVEE AENGR DAPAN GNAEN EENGE
46 QEADN EVDEE CEEGG EEEEE EEEGD GEEED GDEDE EAESA TGKRA
91 AEDDE DDDVD TKKQK TDED C

```

(a)



(b)

Fig. 3.25: (a) Sequence of ProT α E56C/D110C, labeled with AF488 as the donor at position 56 (cyan) and AF594 as the acceptor at position 110 (orange) for FRET experiments [195,272]. (b) AlphaFold structure prediction [160,161] for Prothymosin Alpha with the sequence from (a) without the mutations E56C/D110C [196,273]. The label position of the donor (cyan) and acceptor dye (orange) are shown as well.

3.5.6 Buffers

Tab. 3.2 lists the used buffers for all FCS and FRET experiments, dependent on the sample being investigated (see subsection 3.5.1 - 3.5.5). The hybridization buffer was used for the preparation of the dsDNA as well as 3/4-stranded DNA hybrids.

Tab. 3.2: Components and pH of the buffers including sodium chloride (NaCl), ethylenediaminetetraacetic acid (EDTA), 2-Amino-2-(hydroxymethyl)propane-1,3-diol (TRIS), potassium chloride (KCl), β -mercaptoethanol (BME), Polyoxyethylene (20) sorbitan monolaurate (Tween 20), 3-(N-morpholino)propanesulfonic acid (MOPS) and guanidine hydrochloride (GdmCl).

Buffer	Components	pH
hybridization	500 mM NaCl, 1mMEDTA, 10 mM TRIS	7.75
TRIS	10 mM TRIS, 200 mM KCl, 0.1 % Tween 20, 140 mM BME	7.40
MOPS	20 mM MOPS, 0.1 % Tween 20,	7.20
MOPS _{GdmCl}	20 mM MOPS, 0.1 % Tween 20, 4.5 M GdmCl	7.20

3.6 LabVIEW and data editing

A measurement virtual instrument (VI) was developed in LabVIEW [246,247] in order to enable data acquisitions with the USB2.0-TDC CS - TP 01-04-82 (GPX-TDC) measurement electronics from Surface Concept (see subsection 3.3.2) with the experimental setup. In the following, the basic principle and structure of the program is explained, before going into a little bit more detail regarding some restrictions and workarounds.

One requirement for a measurement VI is that seven different subVIs have to be executed in a specific order to successfully perform a data acquisition (see Fig. 3.26) [257]. These subVIs are provided by Surface Concept and are calling functions of the dynamic linked library (dll) of the GPX-TDC provided by the manufacturer. If the duration of a data acquisition is not varied, the subVIs from *TDC alloc* to *TDC gBlock* can be repeated in a loop without the need of rebooting and reinitializing the GPX-TDC. One drawback is that the raw data from the subVI *TDC gBlock* is not accessible during a running data acquisition. Therefore, in order to avoid data loss and the need of processing giant data blocks at once, the duration of a single measurement is limited. To overcome this problem the LabVIEW measurement VI is designed in such a way, that an experiment is split into multiple shorter submeasurements. By using the same settings for each of those submeasurements, they can be executed directly after one another in a loop without the need for a reboot or reinitialization of the GPX-TDC (see Fig. 3.26). Nevertheless, the time required for a submeasurement is not a fixed parameter. It varies between different submeasurements. As a consequence, the exact time information between photons of different submeasurements is lost. It is evident that the length of a submeasurement has to be longer than the time scale of the processes to be observed. In the case of a freely diffusing sample where the observable timescale is limited by the diffusion time through the focal volume, the duration should be at least two orders of magnitude larger than the diffusion time. Furthermore, the time needed between submeasurements leads to a certain experimental dead time, since all photons detected by an APD during the restart are lost. Therefore, the real duration of an experiment is larger than the

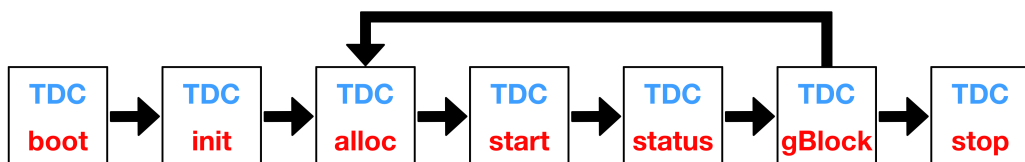


Fig. 3.26: Defined sequence in which the single subVIs (boxes) must be called in LabVIEW to run a data acquisition of the GPX-TDC. If there are no changes in the initialization parameters or more specific in the measurement duration, all subVIs from *TDC alloc* to *TDC gBlock* can be repeated in a loop without the need to reboot and reinitialize the GPX-TDC.

effective measurement time or, more precisely, the data acquisition time. A time of $t_{\text{sm}} = 1$ s was chosen as the length for the submeasurements, since for FCS experiments with freely diffusing molecules, the correlation curves drop to background level well before a lag time of $\tau = 1$ s. This is illustrated in Fig. 3.27 with correlation functions of measurements of free diffusing AF488, the 3-stranded DNA hybrid, the DNA hairpin and ProT α as examples. If a longer submeasurement length is required, its time t_{sm} can be adjusted by the user in the front panel of the VI. In addition, the effective measurement time $t_{\text{m}}^{\text{eff}}$ is also set, resulting in

$$n_{\text{sm}} = \frac{t_{\text{m}}^{\text{eff}}}{t_{\text{sm}}} \quad (3.7)$$

number of submeasurements n_{sm} .

At the start of the experiment, the subVIs *TDC boot* and *TDC init* are loaded. In the second step the subVIs *TDC alloc* to *TDC gBlock* are repeated in a for-loop n_{sm} -times before the data acquisition is ended with the execution of *TDC stop*. The entire raw photon data of one submeasurement is saved in one data array. This data array builds a cluster with a variable containing the number of detected photons. The cluster is put in a queue, where each element is individually removed for further processing. The data editing is realized by another for-loop, which processes all queue elements consecutively. In a first step, the raw data is divided into three different arrays. These contain the macro time, micro time and channel information,

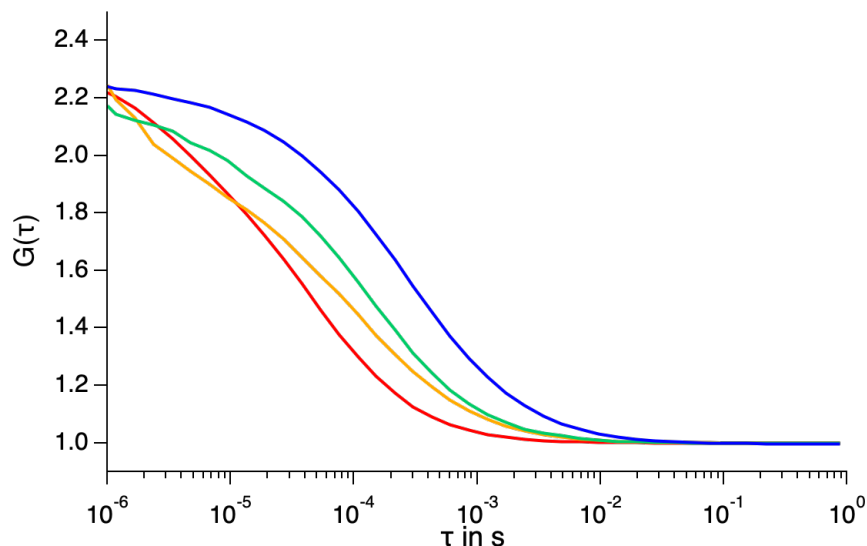


Fig. 3.27: Correlation functions normalized by the average number of molecules in the focal volume. The red curve is an auto-correlation function of AF488, whereas the orange, green and blue curves are donor auto-correlation functions of the 3-stranded DNA hybrid, DNA hairpin and ProT α , respectively.

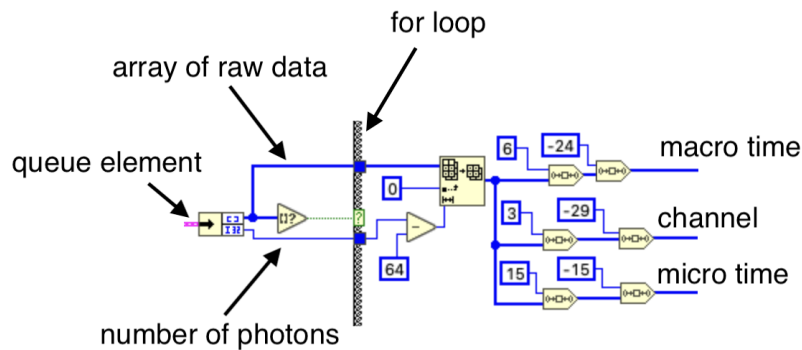


Fig. 3.28: Procession of raw data arrays. Each element of the raw data queue is extracted from the queue. Afterwards all 32-bit photon data elements are divided according the structure (see Fig. 3.13) into the channel as well as macro and micro time information.

respectively (see Fig. 3.28). Since the last 64 entries of each raw data array do not contain real photon data, they are not further considered. In the next step, potential overflows of the macro time counter are analyzed (see subsection 3.6.1). The overflow corrected photon data is then divided into four arrays, each containing the photon data of one detection channel of the experimental setup. Subsequently, the macro time and micro time data arrays are concatenated to create a single entry for each photon, containing its complete time information. Before adding both time values the macro times are shifted 17 bits to the left. This results in a 64 bit structure (see Fig. 3.29). The 17 least significant bits (LSB) contain the micro time information in form of the number of the corresponding time bin. The remaining 47 bits contain the macro time information in form of the interval number in which the photon was detected. These times are finally saved into a HDF5-file.

After loading of the HDF5-file into the analysis software Igor Pro, the photon arrival times are further edited. This is realized with a custom written function in Igor Pro (see Fig. A.2). To account for the structure of each photon timestamp they are converted according to the length of the macro time intervals and the time bin resolution of the micro time. Finally, the times are corrected regarding the time delay between the different APDs, discussed in subsection 4.1.3.



Fig. 3.29: 64 bit data structure of each event processed in LabVIEW, which is saved into a HDF5-file.

the time stamp of the first photon of the following submeasurement and corrected if Eq. 3.8 is not valid. The evident disadvantage of this solution is the loss of one input channel. As a consequence a maximum of 3 APDs can be used for photon detection in this configuration.

3.6.2 Synchronization with the laser pulse

If data acquisition needs to be synchronized with a laser pulse, an external trigger signal has to be applied to the *start in* input of the GPX-TDC. This input signal is divided down by a frequency divider with a value of 2, 4, 8 or 16. The divider is specified in the initialization file loaded, when the GPX-TDC is booted. The frequency arising after the frequency divider has to be in a range between 100 kHz and 7 MHz. A synchronization of the stop signals to a laser pulse can be used for FRET experiments with pulsed overlaid/ interleaved excitation (POE/PIE) of the acceptor fluorophore. In addition to the cw laser for donor excitation, the pulsed laser is used to validate if sample molecules are lacking the acceptor fluorophore. Only these molecules are subsequently included in the data analysis, for example, in the calculation of FRET histograms. Fig. 3.31 shows exemplarily a histogram of recorded micro times of freely diffusing AF647, excited with a laser pulse frequency of 200 kHz.

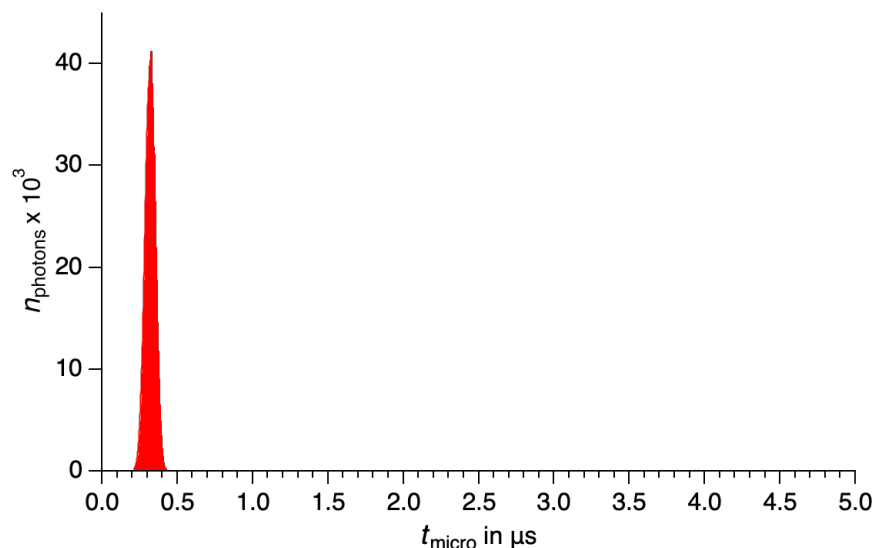


Fig. 3.31: Histogram of micro times of freely diffusing Alexa Fluor 647 excited with a pulsed laser. The frequency of the laser was 200kHz resulting in micro time intervals of 5 μs .

3.7 Data processing

The entire data processing and analysis is carried out with the analysis software Igor Pro (WaveMetrics, version 9.01) [274]. After loading the raw data of the respective channel, the photon arrival times of each APD are corrected for the differences in the optical and electrical path lengths (see subsection 4.1.3). Iterative nonlinear least square curve fitting in Igor Pro is based on the Levenberg-Marquardt algorithm [275, 276].

3.7.1 FCS

To obtain the auto- and cross-correlation functions of the measurements, raw data of all used detection channels are correlated with a custom-written correlator, developed by Jan Pavlita, based on the algorithm in [277]. The correlation procedure offers different binning options: *linear binning*, *logarithmic binning*, and *combined binning* option. The option *linear binning* is similar to the Multiple-Tau Photon Correlation System [278] and was used for the correlation of the experiments. Adjustable parameters of this binning option are the number of steps before a register shift, the starting correlation time and the largest correlation time, which is adapted to the measurement. The starting correlation time was chosen in dependence on the counting electronics as the shortest possible detectable time difference between two subsequent photons. The largest correlation time was set to 1 s for all correlations, independent of the used counting electronics.

The curve fitting to the experimental determined correlation functions is dependent on the investigated sample and experiment. As described in section 2.5, the correlation function is given by [45, 123]

$$G_{\text{Dif}}(\tau) = C + \frac{1}{\langle N \rangle} \left(1 + \frac{\tau}{\tau_{\text{Dif}}}\right)^{-1} \left(1 + S_{\text{ar}}^2 \frac{\tau}{\tau_{\text{Dif}}}\right)^{-\frac{1}{2}}, \quad (3.9)$$

when only diffusion of the fluorescent molecules is the reason for fluorescence intensity fluctuations. To consider transitions to the triplet state of the fluorophores as well, the fit function is expanded by an additional exponential factor: [45, 123, 133]

$$G_{\text{Dif,T}}(\tau) = C + \frac{1}{\langle N \rangle} \left(1 + \frac{\tau}{\tau_{\text{Dif}}}\right)^{-1} \left(1 + S_{\text{ar}}^2 \frac{\tau}{\tau_{\text{Dif}}}\right)^{-\frac{1}{2}} \left[1 + \frac{\bar{T}}{1 - \bar{T}} e^{-\frac{\tau}{\tau_{\text{T}}}}\right]. \quad (3.10)$$

In Eq. 3.9 and Eq. 3.10, $\langle N \rangle$ is the average number of molecules in the focal volume during the measurement, τ_{Dif} the diffusion time, \bar{T} the triplet fraction and τ_{T} the triplet relaxation time. The aspect ratio of the focal volume of the experimental setup S_{ar} is held constant to a value of $S_{\text{ar}} = 0.2$ during the fit. This value was

found in independent FCS experiments to best fit the focal shape of our instrument. It has to be noted that $S_{\text{ar}} = 0.2$ in fact has a very weak impact on the fitting results. The constant C describes the offset or background signal to which the correlation function drops for longer lag times τ . It is expected to have a value of $C = 1$. Values deviating from $C = 1$ are an indicator of a changing background signal during the measurement. To include photon antibunching in nsFCS, a further exponential term is added to the fit function, but with a negative amplitude A_{AB} to account for the decay of the correlation with the characteristic antibunching time constant τ_{AB} [45, 123]:

$$G_{\text{Dif,T,AB}}(\tau) = C + \frac{1}{\langle N \rangle} \left(1 + \frac{\tau}{\tau_{\text{Dif}}}\right)^{-1} \left(1 + S_{\text{ar}}^2 \frac{\tau}{\tau_{\text{Dif}}}\right)^{-\frac{1}{2}} \dots \quad (3.11)$$

$$\dots \left[1 + \frac{\bar{T}}{1 - \bar{T}} e^{-\frac{\tau}{\tau_{\text{T}}}}\right] \left[1 - A_{\text{AB}} e^{-\frac{\tau}{\tau_{\text{AB}}}}\right].$$

For each of n additional processes leading to fluorescence fluctuations at a specific and separated timescale, an exponential term is added to the fit function with the respective fraction \bar{X} and time τ_{X} :

$$G_{\text{Dif,T,AB,X}}(\tau) = C + \frac{1}{\langle N \rangle} \left(1 + \frac{\tau}{\tau_{\text{Dif}}}\right)^{-1} \left(1 + S_{\text{ar}}^2 \frac{\tau}{\tau_{\text{Dif}}}\right)^{-\frac{1}{2}} \dots \quad (3.12)$$

$$\dots \left[1 + \frac{\bar{T}}{1 - \bar{T}} e^{-\frac{\tau}{\tau_{\text{T}}}}\right] \left[1 - A_{\text{AB}} e^{-\frac{\tau}{\tau_{\text{AB}}}}\right] \underbrace{\left[1 + \frac{\bar{X}}{1 - \bar{X}} e^{-\frac{\tau}{\tau_{\text{X}}}}\right]^n}_{n \text{ additional processes}}.$$

nsFRET-FCS

In a nsFRET-FCS experiment and especially in the case of chain dynamics of an unfolded or intrinsically disordered protein for example, an additional term has to be included to Eq. 3.11, which considers the fraction \overline{CD} and relaxation time τ_{CD} of these chain dynamics [195]:

$$G(\tau) = C + \frac{1}{\langle N \rangle} \left(1 + \frac{\tau}{\tau_{\text{Dif}}}\right)^{-1} \left(1 + S_{\text{ar}}^2 \frac{\tau}{\tau_{\text{Dif}}}\right)^{-\frac{1}{2}} \left[1 + \frac{\bar{T}}{1 - \bar{T}} e^{-\frac{\tau}{\tau_{\text{T}}}}\right] \dots \quad (3.13)$$

$$\dots \left[1 + \frac{\overline{CD}}{1 - \overline{CD}} e^{-\frac{\tau}{\tau_{\text{CD}}}}\right] \left[1 - A_{\text{AB}} e^{-\frac{\tau}{\tau_{\text{AB}}}}\right] \left[1 + \frac{\bar{X}}{1 - \bar{X}} e^{-\frac{\tau}{\tau_{\text{X}}}}\right]^n.$$

As in Eq. 3.12, additional terms can be added if necessary for n additional processes that lead to fluctuations of the fluorescence signal. Using the experimental setup described in section 3.1, there are a total of 12 correlations to be analyzed, when auto-correlations of individual channels are neglected. Accordingly, there are 8 cross-correlations between donor and acceptor channels and 4 pseudo auto-correlations, 2 for both acceptor and 2 for both donor channels, respectively. They are given by (see Eq. 2.110)

$$G_{ij}(\tau) = 1 + \frac{\langle \delta I_i(t) \delta I_j(t + \tau) \rangle}{\langle I_i \rangle \langle I_j \rangle}, \quad (3.14)$$

with i, j , representing the acceptor (A_1, A_2) and donor channels (D_1, D_2). In the following, the pseudo auto-correlations of both, donor and acceptor are denominated by G_{A12} and G_{D12} for the forward and G_{A21} , G_{D21} for the backward correlations, respectively. Based on the assumption that all cross-correlation functions, correlated in the same direction, share the same information, they are averaged before curve fitting, resulting in one forward cross-correlation G_{AD} and one backward cross-correlation G_{DA} :

$$G_{AD}(\tau) = \langle G_{A1D1}(\tau) + G_{A1D2}(\tau) + G_{A2D1}(\tau) + G_{A2D2}(\tau) \rangle, \quad (3.15)$$

$$G_{DA}(\tau) = \langle G_{D1A1}(\tau) + G_{D1A2}(\tau) + G_{D2A1}(\tau) + G_{D2A2}(\tau) \rangle. \quad (3.16)$$

Furthermore, as described in section 2.6, chain dynamics have an influence on both, the auto-correlation and cross-correlation functions of the donor and acceptor channels, with the same characteristic relaxation time τ_{CD} . Thus, the resulting six correlation functions are analyzed with a global fitting procedure, where fit parameters like the aspect ratio of the focal volume S_{ar} or the chain relaxation time τ_{CD} are fitted as linked parameters. Additionally, the forward and backward pseudo auto-correlations share information as well. Linked fit parameters between all correlation functions are presented in Tab. 3.3.

For a filtered nsFRET-FCS analysis and the separate correlation analysis of distinct FRET populations or efficiency ranges, a custom written function in Igor Pro was used, which is shown in Fig. A.3. The function needs a wave, which contains the FRET efficiencies per time bin and the start and end efficiency value of the efficiency range to be extracted as input parameters. The created waves then contain just the photon arrival times of photons belonging to FRET efficiencies of the desired range.

Tab. 3.3: Overview of linked fit parameters of auto- and cross-correlation functions during a global fit of nsFRET-FCS correlation curves. Same coloring of cells in a column indicates a linked fit parameter between respective correlations. If additional processes X are present, the fit function is expanded with an additional term describing this process with its fraction \bar{X} and time τ_X . Gray boxes represent entirely independent fit parameters.

Correlation	Fit parameter											
	$\langle N \rangle$	τ_{Dif}	S_{ar}	T	τ_{T}	\overline{CD}	τ_{CD}	A_{AB}	τ_{AB}	C	\bar{X}	τ_X
$G_{\text{A12}}(\tau)$	Red	Orange	Yellow	Green	Olive	Blue	Purple	Pink	Brown	Light Blue	Teal	Red
$G_{\text{A21}}(\tau)$	Red	Orange	Yellow	Green	Olive	Blue	Purple	Pink	Brown	Light Blue	Teal	Red
$G_{\text{D12}}(\tau)$	Dark Red	Dark Orange	Yellow	Dark Green	Olive	Blue	Purple	Pink	Brown	Teal	Teal	Red
$G_{\text{D21}}(\tau)$	Dark Red	Dark Orange	Yellow	Dark Green	Olive	Blue	Purple	Pink	Brown	Teal	Teal	Red
$G_{\text{AD}}(\tau)$	Gray	Gray	Yellow	Gray	Olive	Gray	Purple	Gray	Gray	Cyan	Gray	Red
$G_{\text{DA}}(\tau)$	Gray	Gray	Yellow	Gray	Olive	Gray	Purple	Gray	Gray	Cyan	Gray	Red

3.7.2 Effective triplet transition rate and molecular brightness

Effective transition rate to the triplet state The triplet fraction \bar{T} and triplet time τ_{T} from the fit of the correlation functions can be used to determine the effective transition rate to the triplet state [93]:

$$k_{\text{ISC}}^{\text{eff}} = \frac{\bar{T}}{\tau_{\text{T}}}. \quad (3.17)$$

This is done for every laser power P_{las} of a benchmark experiment in order to determine the laser excitation saturation power $P_{\text{las}}^{\text{sat}}$ with the following fit function [93, 279]:

$$k_{\text{ISC}}^{\text{eff}}(P_{\text{las}}) = \frac{k_{\text{ISC}}}{1 + \frac{P_{\text{las}}^{\text{sat}}}{P_{\text{las}}}}. \quad (3.18)$$

$P_{\text{las}}^{\text{sat}}$ is the laser power, which is needed to saturate the transition to the triplet state. A lower laser power indicates a smaller laser focus, since for a given excitation intensity the excitation of the fluorophores is more efficient with smaller focus dimensions due to a higher photon flux density.

Molecular brightness The molecular brightness ε_{mb} of the molecules was determined by using the mean intensity of the signal $\langle I \rangle$ as well as average number of particles in the focal volume $\langle N \rangle$ according to [132, 280]

$$\varepsilon_{\text{mb}} = \frac{\langle I \rangle}{\langle N \rangle}. \quad (3.19)$$

The mean intensity, in units of average number of photons per 1 ms, was directly determined from the time traces of both APDs. The average number of particles was obtained from the fit of the correlation curves. The laser power dependent molecular brightness was fitted with a three-level system model according to [103]

$$\varepsilon_{\text{mb}}(\phi_e) = \eta_d \sigma \Phi_f \frac{\phi_e}{1 + \frac{\phi_e}{\phi_{S1}} + \frac{\phi_e^2}{\phi_{S2}}}, \quad (3.20)$$

with

$$\sigma = \frac{\ln 10}{N_A} \varepsilon_{\text{det}} \quad (3.21)$$

and

$$\phi_e = \frac{2P_{\text{las}}}{h\nu\pi w_{\text{wy}}^2}. \quad (3.22)$$

In Eq. 3.20 to Eq. 3.22, ϕ_e is the excitation photon flux density, σ the absorption cross section of the fluorophore, η_d the collection efficiency of the microscope, ν the frequency of the photons and w_{wy} the lateral radius of the observation volume. ϕ_{S1} and ϕ_{S2} are the photon fluxes required to saturate the singlet states S_1 or S_2 , respectively.

3.7.3 FRET

In order to analyze FRET measurements, the raw data or rather the number of detected fluorescence photons were binned into time intervals with a width of 1 ms. This was done for each detection channel individually. Afterwards, the transfer efficiency was calculated for each time bin with (see Eq. 2.80)

$$E_T = \frac{F_A}{F_A + F_D}, \quad (3.23)$$

where F_A and F_D are the number of photons in the respective time bins for the acceptor or donor channel, respectively. The possible transfer efficiency values $\{E_T | 0 \leq E_T \leq 1\}$ were split into a FRET efficiency histogram containing 50 bins. Only those time intervals are considered for the creation of the histogram, in which the sum of detected donor and acceptor photons exceeds a previously defined threshold value $T_{\text{sum}}^{\text{DA}}$ (see subsection 2.4.3), depending on the measurement and was chosen in a range between 30 cts/ms and 50 cts/ms. Histograms were not corrected for spectral properties of the dyes and characteristics of the experimental setup since absolute distances are not in the focus of this work. Since the resulting

FRET efficiency histograms are always broadened due to shot noise, they were fitted with a Gaussian fit function

$$n_{\text{FRET}}(E_{\text{T}}) = N_0 + Ae^{-\left(\frac{E_{\text{T}} - \langle E_{\text{T}} \rangle}{w_{\text{G}}}\right)^2} \quad (3.24)$$

to determine the mean FRET efficiency $\langle E_{\text{T}} \rangle$ (see Fig. 3.32). n_{FRET} is the number of FRET events for a certain transfer efficiency. A is the amplitude, N_0 the vertical offset and w_{G} the width of the Gaussian peak, related with the standard deviation of the peak σ_{G} as

$$w_{\text{G}} = \sqrt{2} \sigma_{\text{G}}. \quad (3.25)$$

If two overlapping FRET populations are present a fit function containing two Gaussian peaks was used:

$$n_{\text{FRET}}(E_{\text{T}}) = N_0 + A_1 e^{-\left(\frac{E_{\text{T}} - \langle E_{\text{ET1}} \rangle}{w_{\text{G1}}}\right)^2} + A_2 e^{-\left(\frac{E_{\text{T}} - \langle E_{\text{ET2}} \rangle}{w_{\text{G2}}}\right)^2}. \quad (3.26)$$

As in Eq. 3.24, N_0 is the vertical offset. $\langle E_{\text{ET1}} \rangle$ and $\langle E_{\text{ET2}} \rangle$ are the mean FRET efficiencies, w_{G1} and w_{G2} the widths and A_1 and A_2 the amplitudes of both peaks. For even more FRET populations, the fit function was further expanded with additional Gaussian peaks. For further comparison of FRET-FCS experiments, a quality indicator

$$Q_{\text{FRET}} = \frac{F_{\text{peak}}}{\langle F_{\text{D}} \rangle \cdot w_{\text{G}}}, \quad (3.27)$$

was used, which was introduced by Schneider [5]. $\langle F_{\text{D}} \rangle$ is the mean number of donor fluorophores in the focal volume and F_{peak} are the counts at the peak position.

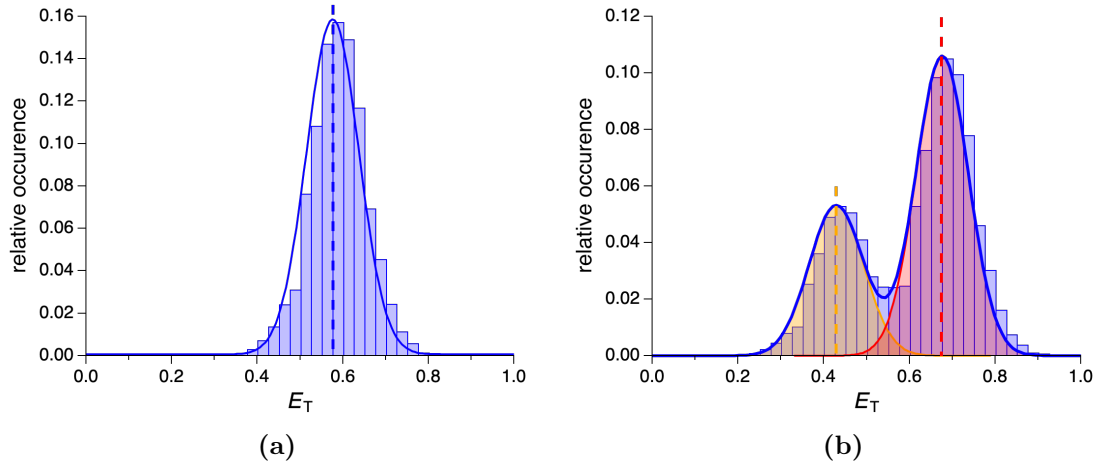


Fig. 3.32: Example of FRET transfer efficiency histograms with (a) one and (b) two FRET populations (orange, red). Histograms are fitted with a Gaussian fit function (solid lines) to determine the mean efficiencies of the respective peaks. Dashed lines indicate the determined mean transfer efficiencies of the populations.

Chapter 4

GPX-TDC implementation and experimental setup improvements

This chapter focusses on the evaluation of the implementation of the parallel time tagger GPX-TDC and its comparison with the present implemented counting electronics, Timeharp200 and SPC-134 TCSPC. The performance of different correction collar settings of the microscopes objective and different optical assemblies using a capillary as the sample container are tested as well, including a potential replacement of the fused silica coverslip with a PMMA film. Furthermore, improvements of the microscopes sample stage and changes of the capillary handling and preparation protocol are discussed.

4.1 Implementation of GPX-TDC

To evaluate the implementation of the GPX-TDC, measurements were made and compared with measurements of the existing Timeharp200. Furthermore, it is evaluated, if there is a difference in the outcome, depending on the fit function being used (Eq. 3.10 and 3.11), regarding the inclusion or exclusion of fluorescence antibunching. Free diffusing AF488 diluted to 1 nM in water was used as the sample. Photons were split with a 50/50 beam splitter onto two APDs. The duration of each measurement was 20 minutes. Auto-correlation functions, fits and derived fit parameters are shown Fig. 4.1. Despite identical experimental conditions, the amplitudes of the correlation functions and hence, the average number of detected photons differ between both electronics. They are slightly lower for the Timeharp200.

This results in a lower molecular brightness. Fitting the whole correlation curve with an additional term for fluorescence antibunching has no significant effect on the outcome of the experiments. Only the fitting error is increasing, which is due to more fit parameters in the fit function. To further analyze the different outcomes when using the GPX-TDC or Timeharp200, FCS benchmark experiments were carried out with both electronics (see subsection 4.1.1).

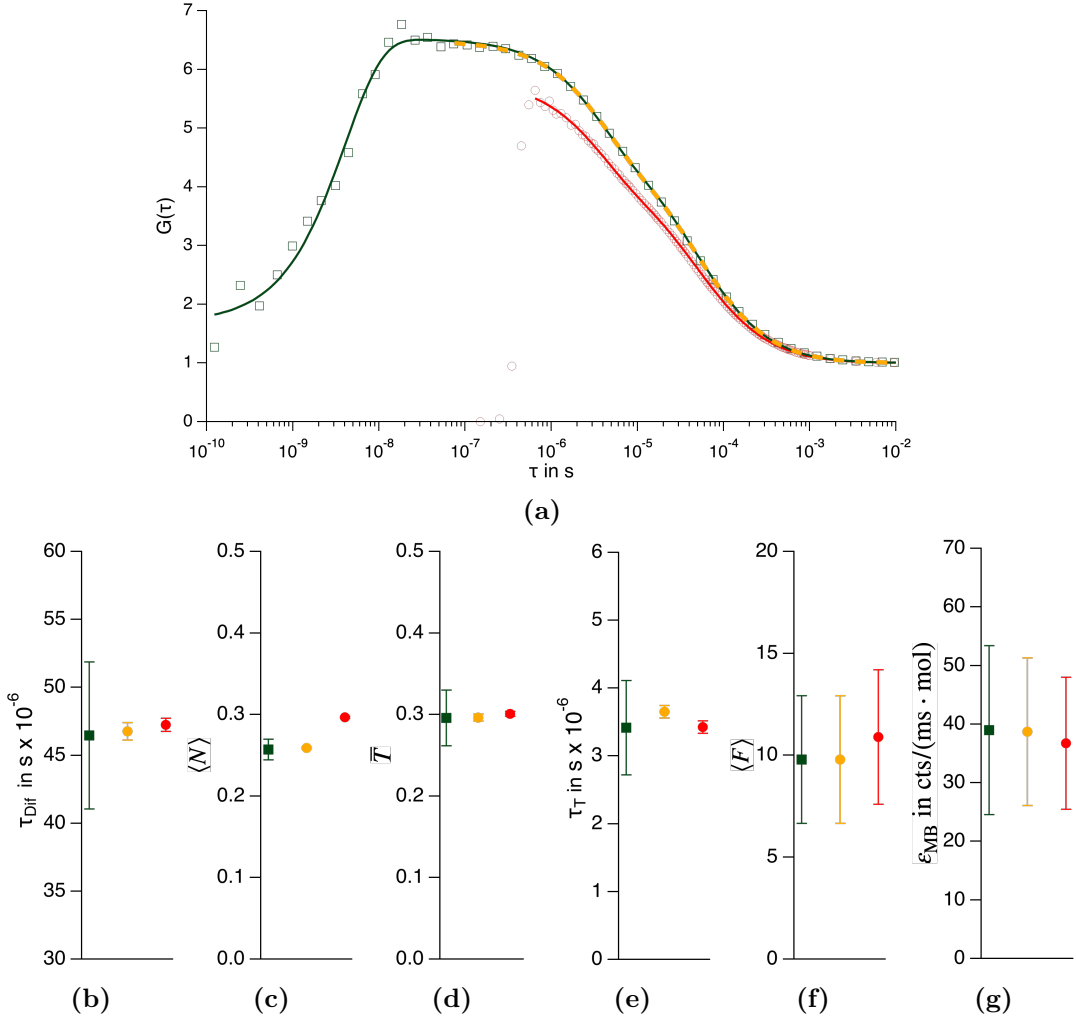


Fig. 4.1: (a) Auto-correlation functions of AF488 diluted in water, processed with the Timeharp200 (red circles) and GPX-TDC (green rectangles). Solid lines represent fits including diffusion and transitions to the triplet state (red/orange) and with an additional term for fluorescence antibunching (green), according to Eq. 3.10 and Eq. 3.11, respectively. Fit parameters with coloring like in (a): (b) diffusion time τ_{Dif} , (c) average number of molecules $\langle N \rangle$, (d) triplet fraction \bar{T} , (e) triplet relaxation time τ_{T} , (f) average number of detected photons $\langle F \rangle$, (g) molecular brightness ϵ_{MB} . (b-e,g) Error bars represent \pm one standard deviation of the fits and (f) $\pm\sqrt{\langle F \rangle}$, respectively.

4.1.1 FCS benchmarks

In order to further compare the different measurement electronics and evaluate the newly implemented GPX-TDC, FCS benchmark experiments were made with the existing Timeharp200 electronics as well as GPX-TDC. These benchmark experiments consisted of multiple FCS measurements with increasing laser excitation powers. AF488 diluted in water at a concentration of 1 nM was used as the sam-

ple. The various laser excitation powers and measurement durations of the series of FCS measurements for both electronics are listed in Tab. A.1. In order to evaluate and compare characteristics of both electronics, auto-correlations were fitted with Eq. 3.10 for the Timeharp200 and Eq. 3.11 for the GPX-TDC measurements. In addition to the parameters, which are directly obtained from the fits, the excitation and detection properties in terms of the transition rate to the triplet state and the molecular brightness were analyzed as described in subsection 3.7.2. The amplitude and the time constant of fluorescence antibunching obtained with the GPX-TDC will not be discussed since it is not comparable between both electronics. Both can be found in the appendix in Fig. A.1.

Excitation Fig. 4.2 shows the diffusion time, triplet fraction and triplet relaxation time obtained at each excitation power. As expected, the obtained diffusion times are increasing with increasing laser power. This is due to optical saturation effects in FCS. This results in a flattened MDF profile of the microscope, which then leads to a seemingly larger observation volume and therefore diffusion time [281–286]. The triplet fraction is increasing as well, whereas the triplet relaxation time is decreasing with increasing excitation power [282]. The effective transition rate to the triplet state, calculated from the triplet fraction and time, is shown as well (see Fig. 4.2d). They were fitted according to Eq. 2.19, giving $P_{\text{las}}^{\text{sat}} = (391 \pm 30) \mu\text{W}$, $k_{\text{ISC}} = (5.85 \pm 0.18) \cdot 10^5 \text{ s}^{-1}$ for the GPX-TDC and $P_{\text{las}}^{\text{sat}} = (143 \pm 5) \mu\text{W}$, $k_{\text{ISC}} = (2.62 \pm 0.03) \cdot 10^5 \text{ s}^{-1}$ for the Timeharp200, respectively. The lower saturation power of the Timeharp200 is a result of the reduced apparent triplet fraction and increased triplet relaxation time compared to the GPX-TDC. The diffusion time is larger when using the Timeharp200 than by the use of the GPX-TDC. These findings can be explained with the saturation behavior of the Timeharp200. To analyze if the different results of both electronics are solely due to their different dead time characteristics, the FCS measurements using the GPX-TDC were analyzed in an alternative way. An artificial dead time was simulated in such a way, that all consecutive photons with a time difference smaller than 350 ns were excluded from the analysis. The further analysis procedure was the same as for the Timeharp200 measurements. The results of this benchmark (GPX-TDC_{350 ns}) are shown in Fig. 4.2 as well (blue triangles). All results show a good agreement between the Timeharp200 experiments and the GPX-TDC_{350 ns}. The calculated saturation power and transition rate to the triplet state have values of $P_{\text{las}}^{\text{sat}} = (152 \pm 9) \mu\text{W}$ and $k_{\text{ISC}} = (2.55 \pm 0.04) \cdot 10^5 \text{ s}^{-1}$, respectively. Based on this outcome, the differences of the results when using the Timeharp200 or GPX-TDC can be entirely explained by the dead time of the Timeharp200. When a fluorophore is diffusing through the observation volume, bursts of fluorescence photons are detected by the APDs. Due to the dead time of 350 ns, the Timeharp200 is not capable of detecting all photons, which leads to a saturation at high count rates. Since statistically more photons originating from the center of the observation volume are lost, the peak intensity decreases and consequently causes a broadening of the MDF, similar to the satura-

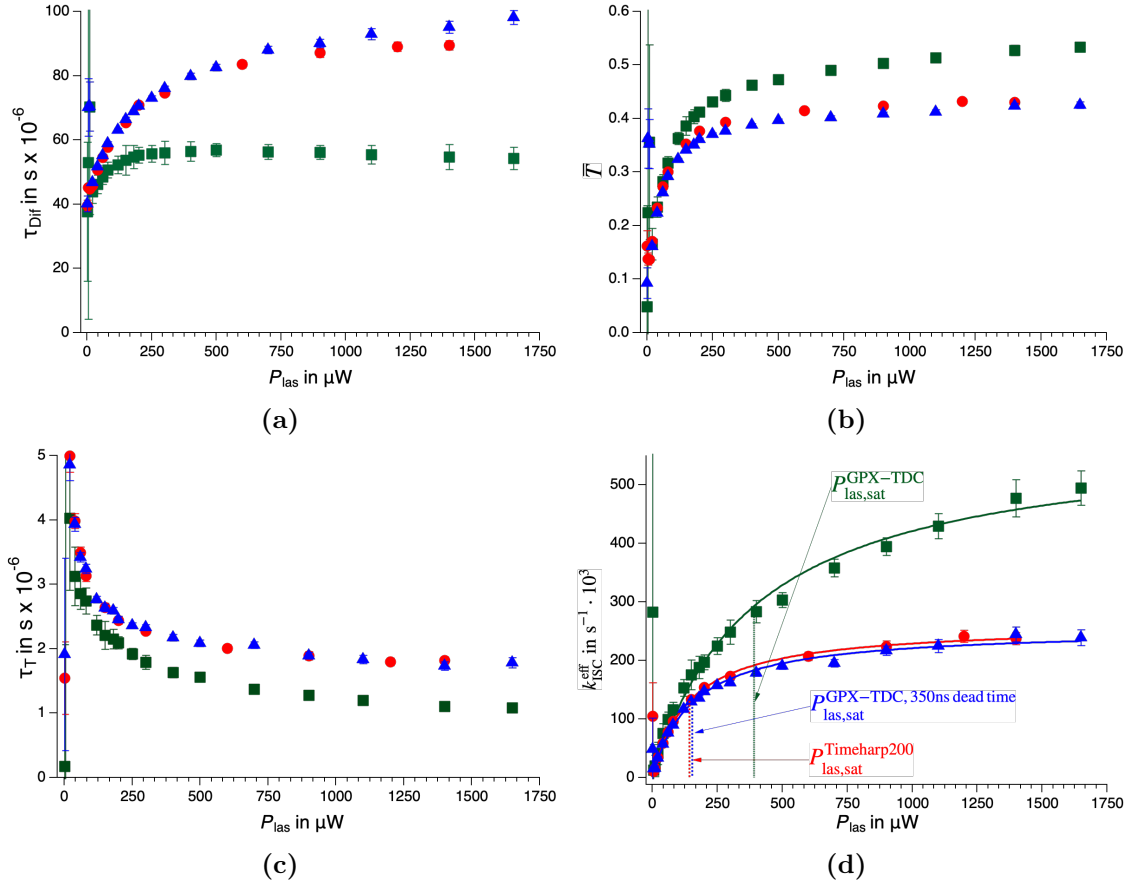


Fig. 4.2: Excitation benchmark results using the GPX-TDC (green rectangles) and Timeharp200 (red circles). Blue triangles represent the GPX-TDC experiments as well, but with an added artificial dead time of 350 ns, matching the dead time of the Timeharp200. Solid lines in (d) represent fits of the effective transition rate to the triplet state $k_{\text{ISC}}^{\text{eff}}$ to determine the respective saturation power $P_{\text{las,sat}}^{\text{electronic}}$ (dashed lines) and transition rate to the triplet state k_{ISC} . Error bars represent \pm one standard deviation of the fit.

tion effects when using high laser excitation powers [282,284]. The flattened MDF results in an increased weighting of the periphery of the observation volume, which then leads to reduced triplet fractions and increased triplet relaxation times when using the Timeharp200.

Detection Furthermore, the mean fluorescence intensity, the average number of molecules in the focus and the molecular brightness were analyzed (see Fig. 4.3) with an additional analysis of the GPX-TDC experiments with an artificial dead time of 350 ns (GPX-TDC_{350ns}). Like expected, both, the mean intensity and the average number of molecules are increasing with increasing laser intensity. Even though the fluorophore concentration is not varying between the measurements, the seemingly

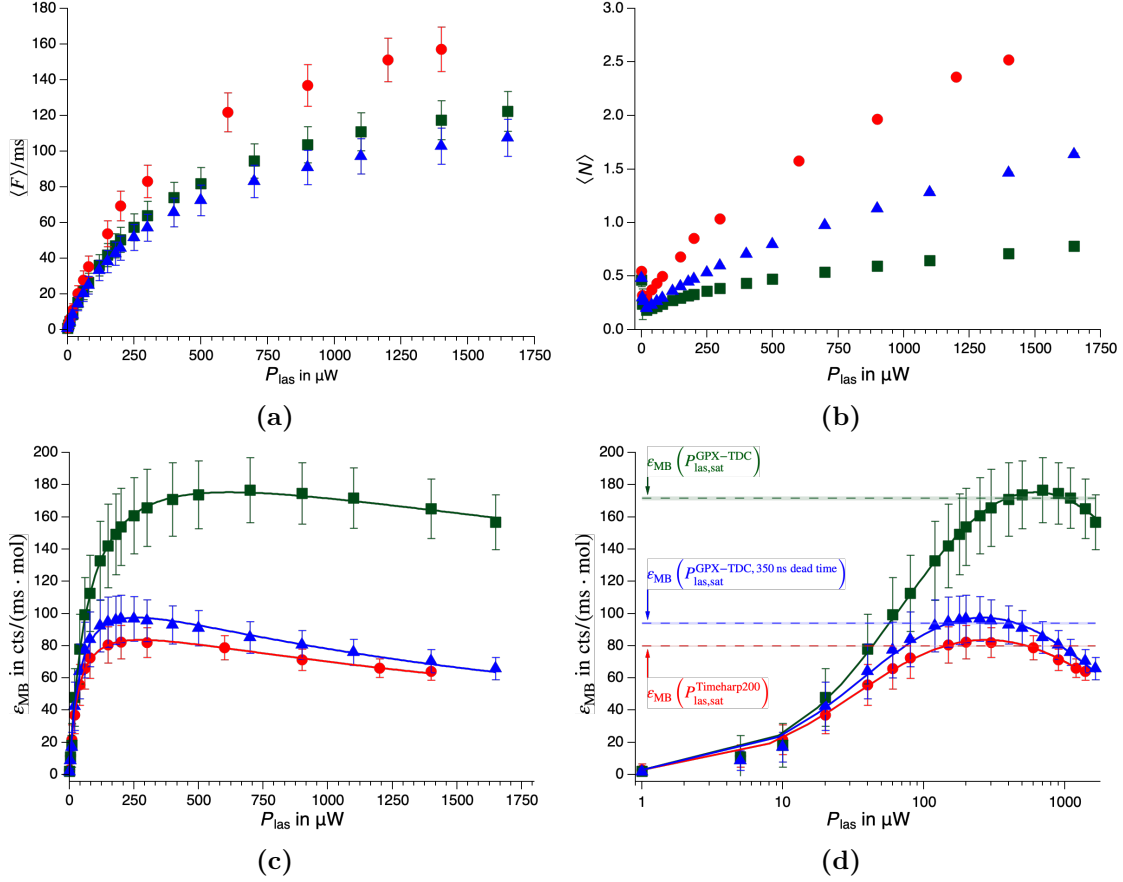


Fig. 4.3: Detection characteristics of AF488 analyzed for the Timeharp200 (red circles), the GPX-TDC (green squares) as well as GPX-TDC data with an added artificial dead time of 350 ns (blue triangles), matching the dead time of the Timeharp200. The molecular brightness ϵ_{MB} is shown in (c) in linear and (d) logarithmic form with solid lines representing the fits according to Eq. 3.20 and dashed lines indicate ϵ_{MB} at the respective laser saturation power $P_{\text{las, sat}}^{\text{electronic}}$. Error bars are representing \pm one standard deviation of the fits.

increasing number of molecules can be explained with a flattening of the MDF due to a higher excitation power resulting in an apparently larger focal volume as for the diffusion time discussed in the paragraph before. The difference between the Timeharp200 and GPX-TDC could be due to the fact that the benchmark experiments were made on different days with new prepared samples resulting in a deviating dye concentration for example. Therefore, due to the good agreement of the results shown in Fig. 4.2, it is worth to compare the GPX-TDC with the GPX-TDC_{350 ns}. The results show less detected photons, but an increased number of molecules in the focal volume for the GPX-TDC_{350 ns}. Due to the artificial dead time the number of detected fluorescence photons is saturated at high count rates. Nevertheless, the number of molecules appears higher for the same reason as the saturation leads to a reduction of the MDF peak. The molecular brightness ϵ_{MB} shows a saturation

behavior as well as it initially increases but decreases again at even higher laser excitation powers. This can be explained with an absorption of another laser photon while the fluorophore is still in an excited state [93,281]. Fits were applied according to Eq. 3.20 and the results are summarized in Tab. 4.1. The fluorescence quantum yield $\Phi_f = 0.92$ and absorption cross section $\sigma = 2.46 \cdot 10^{-20} \text{ m}^2$ [261] were treated as fixed parameters during the fit. Furthermore, the molecular brightness at the respective saturation power and at a laser power of $40 \mu\text{W}$, which is typically used for cw excitation of fluorophores with this experimental setup, are listed. The molecular brightness is consistently higher with the GPX-TDC than with the Timeharp200. At saturation level of excitation ε_{MB} is more than twice as high with the GPX-TDC and almost 40 % higher at an excitation power of $40 \mu\text{W}$.

In summary, the results show, that the use of different measurement electronics can have a significant impact on the results, depending on the type of experiment. This can be inferred from various parameters obtained from the correlation functions. For example, the determined saturation powers for the saturation of the transition to the triplet state as well as the molecular brightness differ strongly from each other depending on the electronics used. The evaluation of the GPX-TDC experiments with an added artificial dead time of 350 ns show that the observed deviations can be entirely attributed to the dead time of the Timeharp200. This dead time creates an additional saturation factor, which flattens the MDF of the confocal microscope leading to a reduced rate of detected photons and a seemingly enlarged focal volume. To ensure that the effects can be explained solely by the different dead times of the measurement electronics and to exclude artifacts on the result due to the detector, the saturation behavior was directly addressed with ensemble fluorescence measurements (see Fig. 4.4a). AF488 diluted in water at a concentration of $10 \mu\text{M}$ was excited at multiple excitation powers. The signal shows a strong saturation behavior when using the Timeharp200, whereas using the GPX-TDC no saturation

Tab. 4.1: Fit results of the molecular brightness ε_{MB} of AF488 benchmark experiments using different measurement electronics. Fits were made according to Eq. 3.20 with fixed values for the following properties of AF488: fluorescence quantum yield $\Phi_f = 0.92$ and absorption cross section $\sigma = 2.46 \cdot 10^{-20} \text{ m}^2$. In addition, ε_{MB} at the respective saturation power $P_{\text{las}}^{\text{sat}}$ and at a typical cw laser excitation power of the experimental setup of $40 \mu\text{W}$ are listed as well. η_d is the detection efficiency of the experimental setup and ϕ_{S1} and ϕ_{S2} mark the excitation photon fluxes needed to saturate the singlet states S_1 or S_2 , respectively.

Electronics	GPX-TDC	Timeharp200	GPX-TDC _{350 ns}
η_d	$(3.31 \pm 0.10) \cdot 10^{-6}$	$(3.33 \pm 0.10) \cdot 10^{-6}$	$(3.50 \pm 0.21) \cdot 10^{-6}$
ϕ_{S1} in $\frac{\text{cts}}{\text{m}^2\text{s}}$	$(2.90 \pm 0.12) \cdot 10^{27}$	$(1.39 \pm 0.06) \cdot 10^{27}$	$(1.62 \pm 0.14) \cdot 10^{27}$
ϕ_{S2} in $\frac{\text{cts}}{\text{m}^2\text{s}}$	$(5.90 \pm 0.37) \cdot 10^{56}$	$(1.18 \pm 0.04) \cdot 10^{56}$	$(1.06 \pm 0.07) \cdot 10^{56}$
$\varepsilon_{\text{MB}} (40\mu\text{W})$ in $\frac{\text{cts}}{\text{ms}\cdot\text{mol}}$	75.8	54.9	62.1
$\varepsilon_{\text{MB}} (P_{\text{las}}^{\text{sat}})$ in $\frac{\text{cts}}{\text{ms}\cdot\text{mol}}$	171.7	79.9	94.0

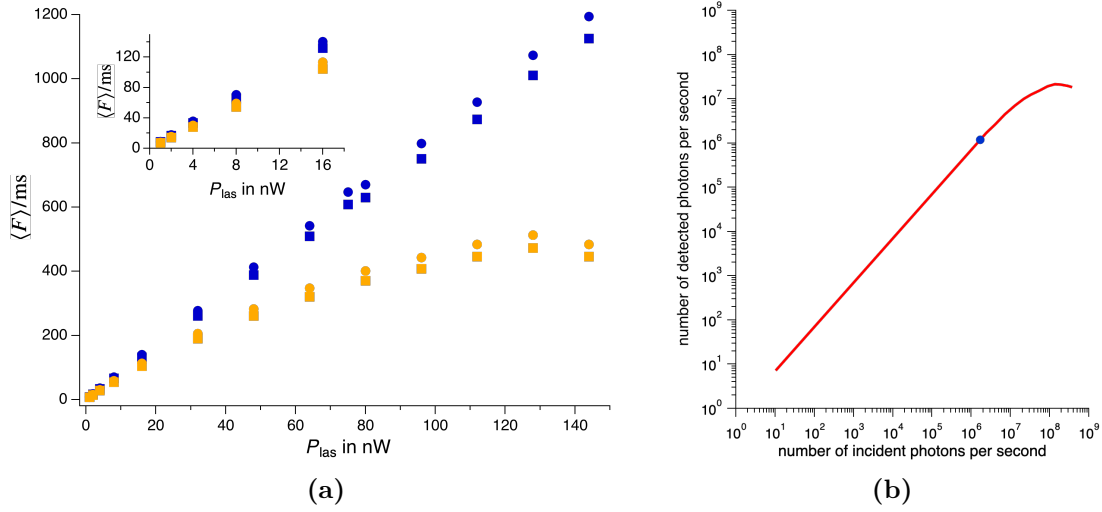


Fig. 4.4: (a) Detection behavior of both counting electronics, Timeharp200 (yellow) and the GPX-TDC (blue), illustrated with the number of detected photons per ms $\langle F \rangle$ for different laser powers P_{las} of 10 μM AF488, diluted in water. As detectors, two PerkinElmer APDs (SPCM-AQRH-14) were used (circles, squares). (b) shows the saturation curve of both Hamamatsu detectors (C11202-100) from the manufacturer with the highest average count rate observed in the experiment marked with a blue circle [249].

effect is visible. Accordingly, the detectors can be discarded as the cause for the observed differences between both measurement electronics. Even though the saturation behavior of the Hamamatsu APDs (C11202-100) were not evaluated, they should have no influence either, since the count rates used in the experiments are lower than the count rates where the detectors start to saturate according to the data sheet of the manufacturer (see Fig. 4.4b).

4.1.2 Antibunching of free diffusing AF488

The characteristic time of the fluorescence antibunching process is directly dependent on the excitation power or rather excitation photon flux density ϕ_{ex} or excitation rate k_{ex} [287, 288]. In the case of an infinitely small excitation power the time constant of fluorescence antibunching τ_{AB} equals the characteristic fluorescence lifetime of the dye τ_{f} (see Eq. 2.23):

$$\tau_{\text{AB}} \stackrel{k_{\text{ex}}, \phi_{\text{ex}} \rightarrow 0}{=} \tau_{\text{f}}. \quad (4.1)$$

Therefore, in order to evaluate the sensitivity and accuracy of the newly implemented parallel time tagger GPX-TDC in this time range, several measurements of free diffusing AF488 were made with a duration of 10 minutes each. The dye was diluted in water at a concentration of 1 nM. In total, seven experiments were performed

with laser excitation powers of 10 μW , 40 μW , 100 μW , 300 μW , 600 μW , 800 μW and 1200 μW , corresponding to photon flux densities between $\phi_{\text{ex}} \approx 2.5 \cdot 10^{26} \text{ m}^{-2}\text{s}^{-1}$ and $\phi_{\text{ex}} \approx 3 \cdot 10^{28} \text{ m}^{-2}\text{s}^{-1}$. The determined time constants of the respective antibunching terms are presented in Fig. 4.5. As expected, the results show a decrease of the antibunching time constant with increasing laser power [287, 288]. With the condition

$$k_{\text{ex}}, k_{\text{rad}}, k_{\text{IC}} \gg k_{\text{ISC}}, k_{\text{rISC}} \quad (4.2)$$

the fluorescence antibunching decay can be fitted with the following fit function

$$\tau_{\text{AB}}(\phi_e) = \frac{1}{k_{\text{ex}} + k_{\text{f}}} = \frac{1}{\phi_e \sigma + \tau_{\text{f}}^{-1}} \quad (4.3)$$

in order to determine the fluorescence lifetime τ_{f} and absorption cross section σ of the fluorophore [281]. The fit results give a fluorescence lifetime of $\tau_{\text{f}} = (3.85 \pm 0.23) \text{ ns}$ and an absorption cross section of $\sigma = (2.25 \pm 0.42) \cdot 10^{-20} \text{ m}^2$. These results are in good agreement with the values provided by the manufacturer (see Tab. 3.1), confirming a high sensitivity and accuracy of the GPX-TDC in the nanosecond time range. The fluorescence lifetime is specified with $\tau_{\text{f}} = 4.1 \text{ ns}$. The absorption cross section of the dye corrected for the excitation wavelength of 488 nm is $\sigma_{488\text{nm}} \approx 2.46 \cdot 10^{-20} \text{ m}^2$. Since the fluorescence lifetime is dependent on the ambient pressure,

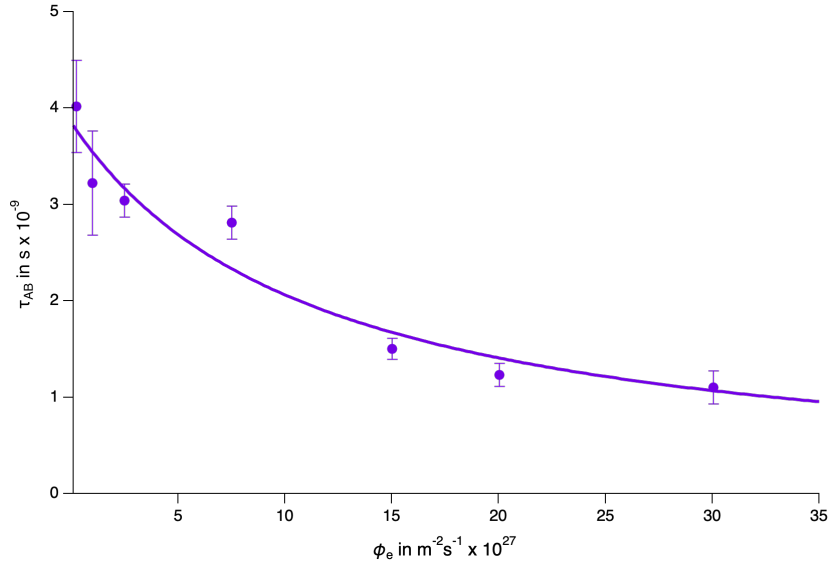


Fig. 4.5: Fluorescence antibunching time constants τ_{AB} of free diffusing AF488 using multiple excitation photon flux densities ϕ_e . Values were fitted with Eq. 4.3 in order to determine the fluorescence lifetime and absorption cross section of the fluorophore. Error bars represent \pm one standard deviation of the fit.

these kind of measurements at varying excitation powers could potentially be used to determine the pressure in the capillary and compare it with the value from the manometer of the screw piston pump. However, this approach has to be further tested since measurements with the fused silica capillary suffer from a reduced signal-to-noise ratio.

4.1.3 Time differences between detection channels

The GPX-TDC allows for the simultaneous determination of photon arrival times in different detection channels without any dead time issues. As a consequence, even small differences in the optical path length or slightly deviating electronic paths have an influence on the correlation curves. In the case that two fluorescence photons are emitted at the exact same time within the sample solution, the arrival time determined by two distinct APDs and counting electronics is different due to varying optical and electronic path lengths. The effect and influence on a correlation function is shown in Fig. 4.6 with free diffusing AF488 and a 50/50 beam splitter between two APDs being used. Even though forward and backward auto-correlations are expected to have the same shape, they reveal a shift in the time range of fluorescence antibunching.

To correct for this effect, an experiment was performed with the protein prothymosin alpha, using all 4 APDs simultaneously in order to analyze the photon arrival times with respect to their time differences to each other. Therefore, all time differences Δt were analyzed when subsequent arrived photons were detected by two different detectors. For a correction of the arrival times it is sufficient to analyze the time differences between APD1 & APD2 (Δt_{12}), ADP2 & APD3 (Δt_{23}) and APD3

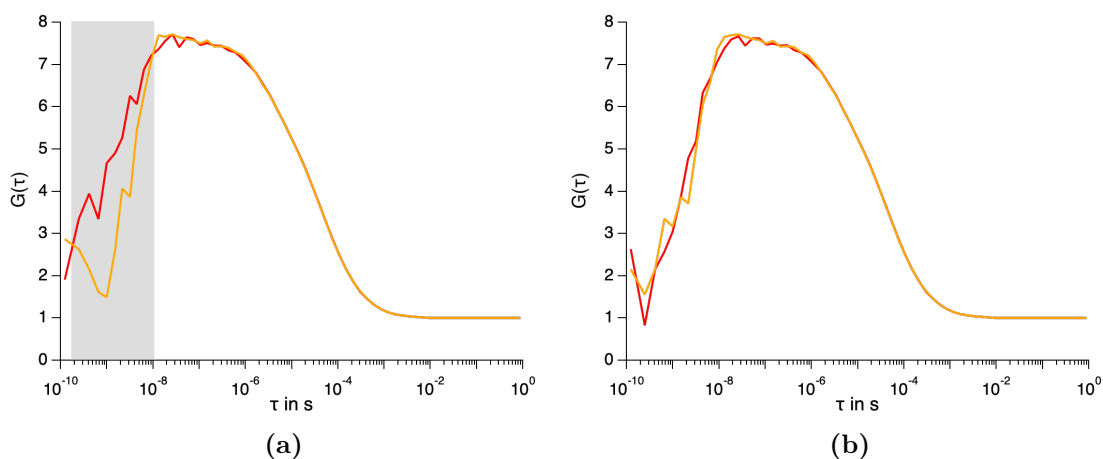


Fig. 4.6: Forward (orange) and backward (red) auto-correlation functions of free diffusing AF488, (a) without and (b) with a correction of the photon arrival times of APD2 with respect to APD1.

& APD4 (Δt_{34}). As a control, the time difference between APD1 & APD4 (Δt_{14}) was evaluated as well. Subsequently, histograms were created from the determined time differences, shown in Fig. 4.7. Given that the arrival times of two consecutive photons in different channels are examined, time differences are displayed as both, negative and positive values, depending on the channel in which a photon was detected first. In the graph, negative time differences indicate that a photon was first detected in the APD with the longer optical path length. In the range of up to a few nanoseconds the time difference histograms are proportional to the actual correlation function [74, 79]. To determine the time lag between two detection channels, all histograms were fitted with the following fit function:

$$f(t) = A + B \left(1 - e^{-\left| \frac{t-t_0}{\tau_0} \right|} \right). \quad (4.4)$$

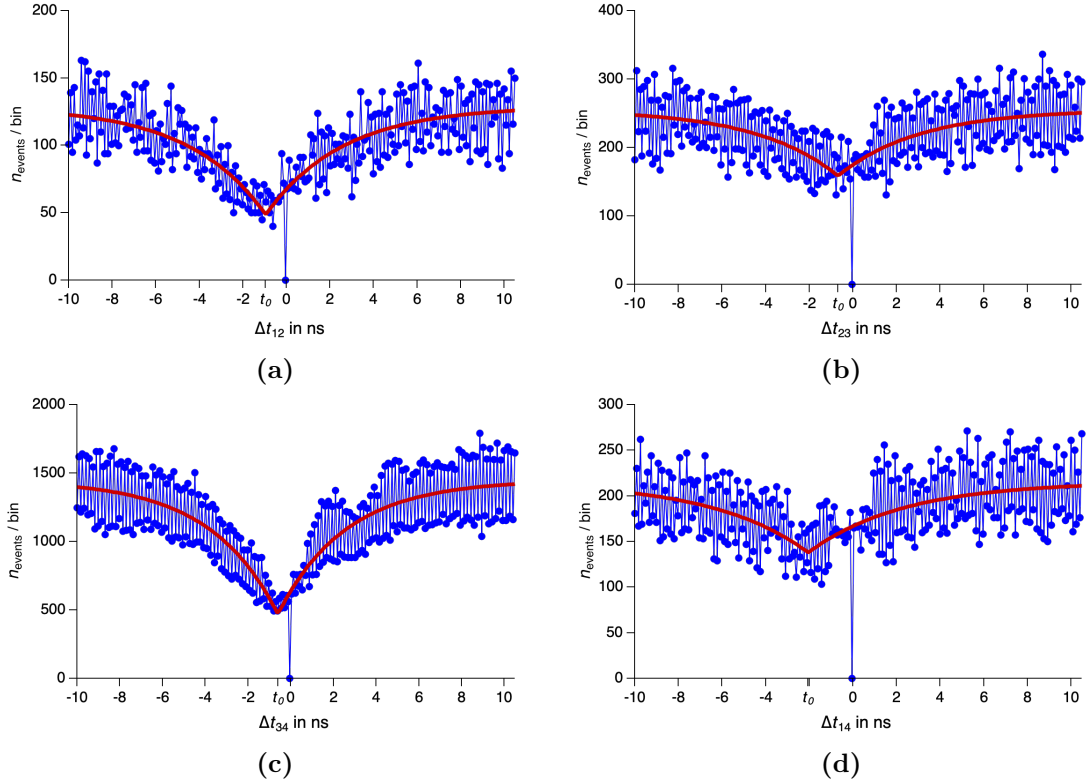


Fig. 4.7: Histograms of time differences Δt of two consecutive photons (blue circles), which were detected with different APDs indicated by the indices of Δt : (a) APD1 & APD2, (b) APD2 & APD3, (c) APD3 & APD4 and (d) APD1 & APD4. Negative time differences have the meaning, that the first photon was detected in the detection channel with the lower index, whereas positive values imply the opposite. Solid red lines represent fits according to Eq. 4.4. Solid blue lines have no physical origin and are for illustration purposes only.

Tab. 4.2: Determined time differences Δt between two subsequent photons, detected by two distinct APDs, characterized by identifiers 1-4.

APDs	$\Delta t \pm \sigma_{\text{fit}}$ in ns
1 & 2	-0.96 ± 0.13
2 & 3	-0.69 ± 0.24
3 & 4	-0.60 ± 0.11
1 & 4	-2.05 ± 0.28

A describes the offset at the lowest point of the histogram. B is the amplitude and τ_0 the time constant of fluorescence antibunching. t_0 is the time difference between the channels, where the histogram has the least number of events. The maximum antibunching of the photon signals, i.e. the lowest point of the histograms, is expected to occur at a time difference of $\Delta t = 0$ s. It follows that the arrival times of the photons have to be corrected by the time differences determined by the fit parameter t_0 . All obtained time differences are summarized in Tab. 4.2.

To correct the arrival times of the photons, the times of APD1 are used as the reference value. Consequently, for the time correction of APD2, the determined value of $t_0 = 0.96$ ns is added to the time stamps of photons recorded by APD2. Accordingly, times of $t = (0.96 + 0.69)$ ns and $t = (0.96 + 0.69 + 0.60)$ ns are added to the times of APD3 and APD4, respectively. Furthermore, the control time difference of $t_0 \approx (2.05 \pm 0.28)$ ns between APD1 and APD4 is in good agreement with the sum of the other three time differences as it is in the range of the fit errors. To illustrate the effect of the correction, Fig. 4.6b shows the correlation functions of the same measurement, which is shown in Fig. 4.6a, but with the correction of the arrival

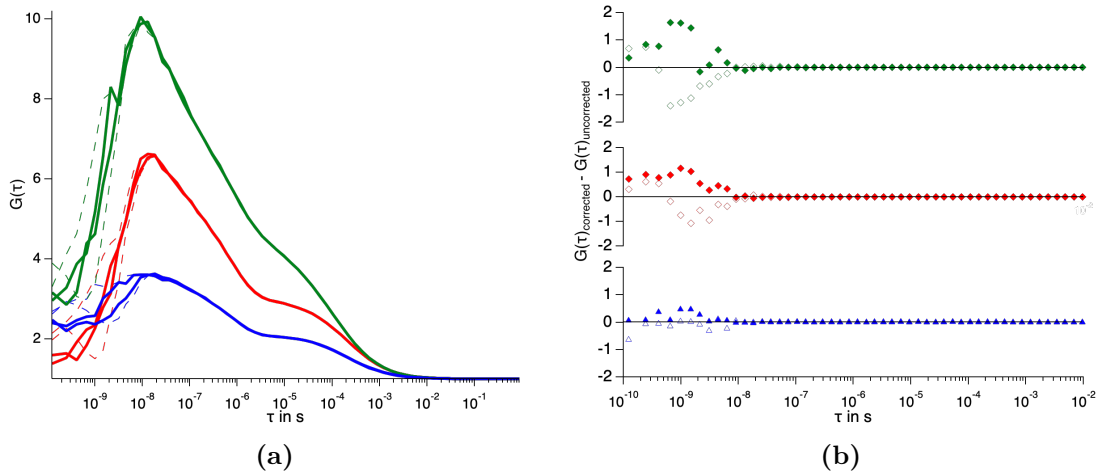


Fig. 4.8: (a) Forward and backward auto- and cross-correlation functions of a measurement of the 3-stranded DNA hybrid. (a) shows the correlations without (dashed lines) and with time correction (solid lines). (b) shows the difference between the uncorrected and corrected correlations, respectively.

times of APD2. Fig. 4.8 shows the correlations of a measurement of the 3-stranded DNA hybrid with corrected time stamps. The differences between the correlation functions calculated with uncorrected and corrected arrival times of the photons are displayed as well, underlining the effect of the time correction in the nanosecond time regime.

4.2 Avalanche photodiodes

The performance of the C11202-100 avalanche photo diodes (APDs) from Hamamatsu were evaluated and compared with the SPCM-AQR-14 from PerkinElmer, which are the most widely used detectors for confocal single molecule fluorescence detection. Again, diffusing, 1 nM solutions of AF488 were used, excited with a laser power of 40 μ W at a wavelength of 488 nm. Photons were distributed onto either both SPCM-AQR-14 or both C11202-100 APDs via a 50/50 beam splitter. Finally, the photons were processed with the GPX-TDC or BeckerHickl measurement electronics. The fit results of the correlation functions are shown in Fig. 4.9 with a comparable outcome regarding the APDs for both measurement electronics. The difference between the GPX-TDC and BeckerHickl is expected to be caused by

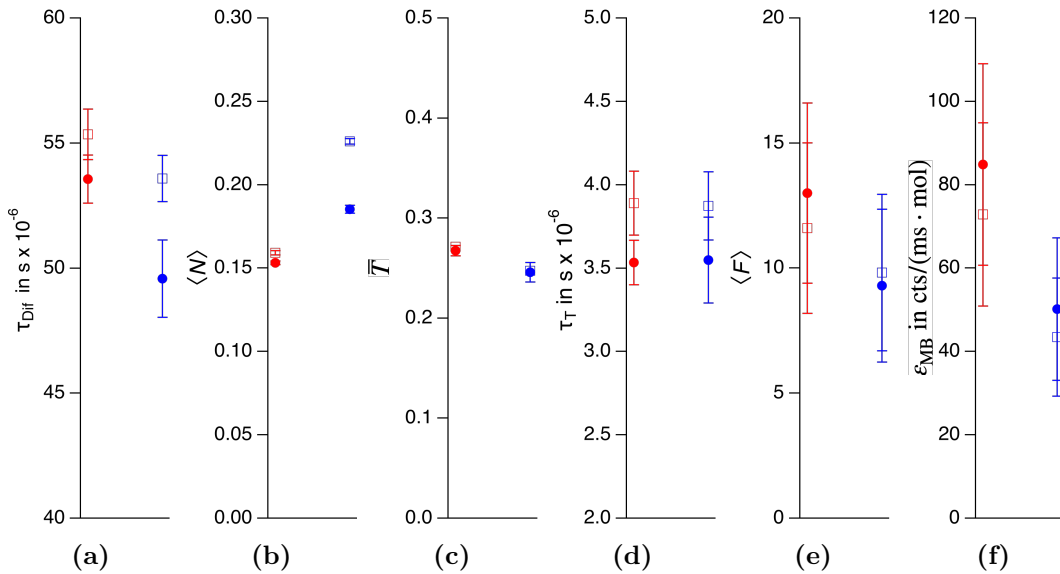


Fig. 4.9: FCS fit results of AF488 diluted in water. Photons were detected with either two C11202-100 (blue) or two SPCM-AQR-14 (red) and were processed with the GPX-TDC (circles) and BeckerHickl (squares). (a) shows the diffusion time τ_{Dif} , (b) the average number of molecules $\langle N \rangle$, (c) the triplet fraction \bar{T} , (d) the triplet relaxation time τ_T , (e) the mean number of detected photons $\langle F \rangle$ and (f) the molecular brightness ϵ_{MB} . (a-d,g) Error bars represent \pm one standard deviation of the fit and (e) $\pm \sqrt{\langle F \rangle}$, respectively.

similar saturation effects like for the Timeharp200, discussed in section 4.1. However, there is a significant difference depending on the detector model. The average number of molecules in the focal volume is higher for the Hamamatsu detectors, whereas the number of detected photons is higher for the PerkinElmer APDs. Consequently, the largest difference can be observed for the molecular brightness due to its dependence on both parameters. Initially, these results seem to contradict the supposed properties of the detectors. Since the effective detection efficiency is even slightly higher for the Hamamatsu than for the PerkinElmer APDs (see Fig. 4.10a), the number of detected photons should be higher for the Hamamatsu detector. Furthermore, the APDs from Hamamatsu have a much more prominent afterpulsing peak and an approximately 3.5 times larger number of detected afterpulsing signals (see Fig. 4.10b). Additionally the dead time of the detector is smaller as well and should actually lead to a higher and not lower number of detected photons. The difference in the average number of molecules is most likely due to effects of the more pronounced afterpulsing of the Hamamatsu detector leading to an artificially higher value. In contrast the triplet relaxation time shows no dependency on the detector model. This is an indication that the differences observed for the other parameters are due to different detection characteristics. However, the difference in the triplet portion does not fit this explanation, but one has to keep in mind that the results are from separate experiments, so there may be small differences. In addition, the deviation within the fit errors is very small. The diffusion time is lower for the Hamamatsu detectors as well. A possible explanation for the lower

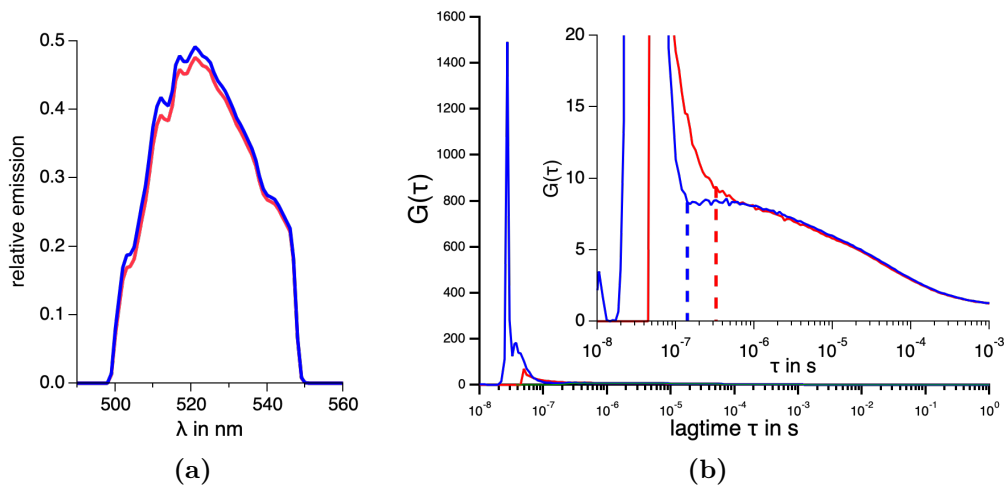


Fig. 4.10: (a) Effective detection efficiency of AF488, calculated with the spectra of the detection efficiency of the APDs, the used bandpass filter and emission characteristics of the dye. (b) Auto-correlation functions demonstrate the afterpulsing effect of both detector types. Blue lines represent the C11202-100 APD from Hamamatsu and red lines the SPCM-AQR-14 from PerkinElmer. Dashed lines represent the cut off lag time used to determine the number of photons within the afterpulse peak, ≈ 207000 and 60000 for the C11202-100 and SPCM-AQR-14, respectively.

diffusion time along with a higher count rate of the C11202-100 from Hamamatsu, despite the theoretically slightly higher detection efficiency, could be a non constant detection efficiency over the whole detector area. Whereas for the SPCM-AQR-14 a tophat profile is specified, there is no information available from Hamamatsu regarding the detection profile. With a decreasing efficiency towards the edge of the active detection area the detection profile is more deviating from a tophat shape.

4.3 Experimental setup and capillary handling improvements

4.3.1 Immersion water protection

Due to the low probability of two subsequent photons having a time difference in the nanosecond time range, a large disadvantage of nsFCS and nsFCS-FRET experiments is the requirement of long measurement times to enable sufficient statistics. In this context one limiting factor is the immersion water being used, which, without further effort evaporates before the measurement is complete. As illustrated in Fig. 4.11, the count rate of fluorescence photons first begins to decrease before dropping to dark counts due to a complete evaporation of the immersion water. The exact length of time it takes for the immersion water to vanish depends on various factors and cannot be specified precisely. In the time trace shown, it takes about 180 minutes. Nevertheless, for a sufficient number of consecutive photons with nano- and sub-nanosecond time differences, measurement durations of up to 16 hours or longer are typical for nsFRET-FCS experiments [8]. With the use of

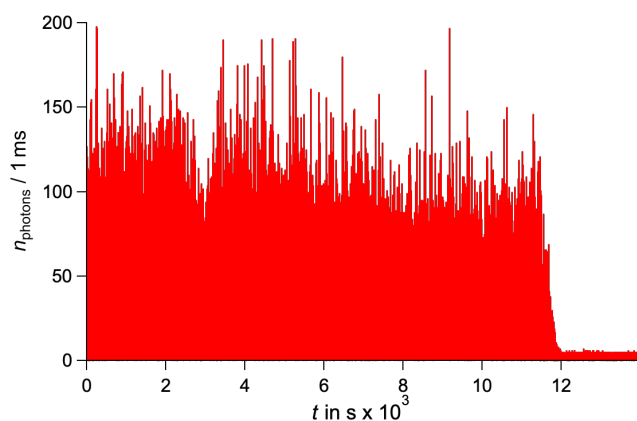


Fig. 4.11: Example time trace of binned photon data of a measurement without the usage of a immersion water protection device. Due to evaporation of the immersion water, the number of detected photons decreases to background signals after a time of approximately 12000 s.

zero-mode waveguides the required data acquisition time could be successfully reduced by an order of magnitude [77], but this approach is not suitable for high pressure nsFRET-FCS experiments and the use of a fused silica capillary.

Theoretically, one could repeat the experiment a couple of times and combine the outcome of all experiments, but this approach has a few disadvantages and is not practical. First of all one has to ensure, that all parameters of the experiment remain unchanged after the restart of the measurement. Another problem is present when dealing with pressure experiments and the usage of the optical multi layer (see subsection 3.2.3) since it is not trivial and not always possible to lift the whole assembly with the fused silica coverslip, the capillary and the index matching gel in such a way that nothing is altered or moved. Therefore, a solution enabling longer durations of single measurements is preferable. To achieve this, a small device consisting of two 3D-printed cylinders was designed (see Fig. 4.12). One of the



Fig. 4.12: 3D drawing of the immersion water protection device. (a) Two overlaying cylinders prevent an air flow, which would accelerate the evaporation of the immersion water. (b) The bottom cylinder is placed onto the objective. In addition to the immersion water, a little groove of the objective is filled with water to serve as a water reservoir. (c) To create a little chamber, the upper ring is positioned above and (d) is attached to the optical table by magnetic beads. (e) shows all components at once.

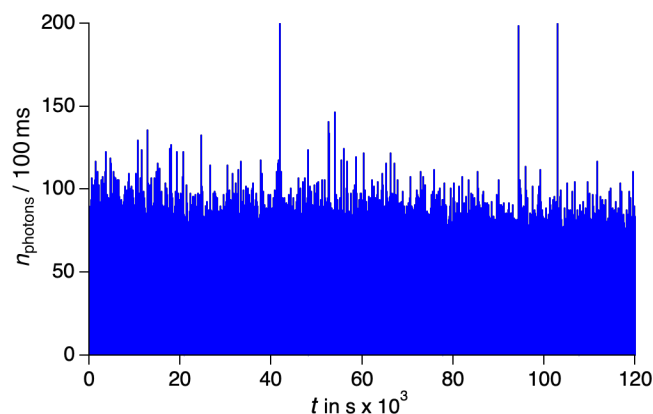


Fig. 4.13: Example time trace of binned photon data of a measurement with the usage of both protection cylinders for the immersion water, leading to a successful data collection of over 120000 s.

cylinders is slightly expanded at the top, enabling an attachment with magnetic beads to the bottom of the sample stage (see Fig. 4.12d). Since both cylinders have a slightly different diameter, the position of the objective along the optical axis can be adjusted without the risk of damage due to its rigidity. Towards the sample, the resulting little chamber containing the immersion water is sealed with the coverslip placed on top of the sample stage. Even though both rings have a small gap between each other in the lateral direction, they severely reduce air exchange or air flow. To perform a long measurement, in addition to a large drop of immersion water a little groove of the objective, which is inside both cylinders is filled with immersion water as well to create a water reservoir inside the little chamber. A precise evaluation or definitive statement of how long it takes for the immersion water to completely evaporate is not possible, even with this solution. Various parameters, such as an unevenly placed coverslip or a bad positioned ring may cause a faster evaporation of the immersion water. Nevertheless, the presented assembly achieved a significant improvement. Measurement times of at least 30 hours were obtained with great reproducibility. Fig. 4.13 shows an example of a time trace of such a long measurement. In this case the last time of a recorded photon is about 120000 s. This example shows, that the solution enables constant, sufficient measurement conditions of at least 30 hours, sufficient for a nsFRET-FCS experiment.

Bare capillary

When using a bare capillary instead of an assembly with a (fused silica) coverslip like the optical multi layer (see subsection 3.2.3), the solution outlined in subsection 4.3.1 is not sufficient. This is due to the fact that the created little chamber containing the immersion water is not sealed at the top with a coverslip, making long measurement durations impossible. In contrast, the missing protection due to the coverslip leads to an even further accelerated evaporation of the immersion water and consequently even shorter measurement time. To enable long measurement durations when using a bare capillary, an additional device has been constructed and 3D printed (see Fig. 4.14). It consists of two parts as well. The bottom part can be placed on the sample stage above the capillary. It has two openings at the lower end to allow the capillary to pass through. At the top is a grid, which serves as a tray for wet tissues. These tissues are saturated with immersion water in order to create a more humid environment. The top part is a cover placed onto the bottom part to seal the tissues and immersion water from the surrounding. To achieve a sealing even at the bottom of the construction, where the capillary passes through, rubber cement (Fixogum) can be used to close the openings. In this way, in combination with the device beneath the optical table (see Fig. 4.12), the immersion water can be protected to the best possible extent. This allows for long measurement durations, even when using a bare capillary, of at least 16 hours with great reproducibility and reliability.

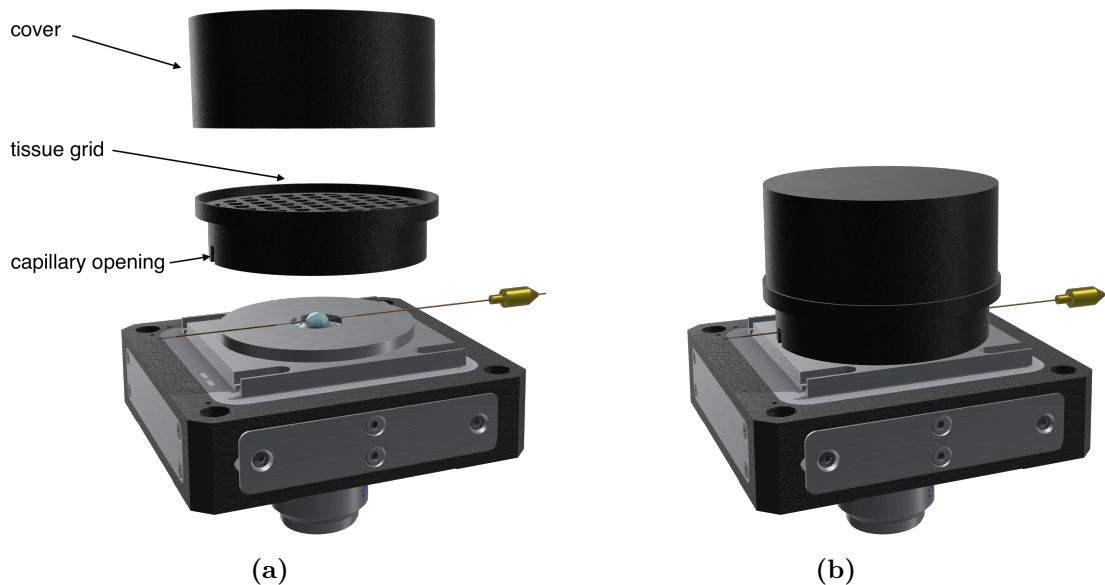


Fig. 4.14: Rendering of the immersion water protection assembly when using a bare capillary for (pressure) experiments. (a) shows the parts of the device and (b) its installation onto the optical table.

4.3.2 Sample stage

As described in section section 3.4, the entire sample stage and the capillary connection to the screw piston pump were redesigned. This was necessary to enable a robust handling and connection of the capillary to the pressure pump and reduce potential damages to the capillary due to large movements or stress, which could lead to glass breakages and a reduced pressure resistance. One potential problem when using square capillaries is their orientation above the microscopes objective, since the initial position of the capillary is random. To ensure best optical imaging properties it is necessary to position the capillary centered above the microscope objective. As pointed out earlier, the sample stage was designed to enable an easy rotation of the capillary above the objective, while reducing other movements of the capillary, especially lateral movements, to the greatest extend. Due to lateral movements, the capillary could exit the scanning area, which would require a more complex readjustment. The new sample stage shall enable a rotation of the capil-

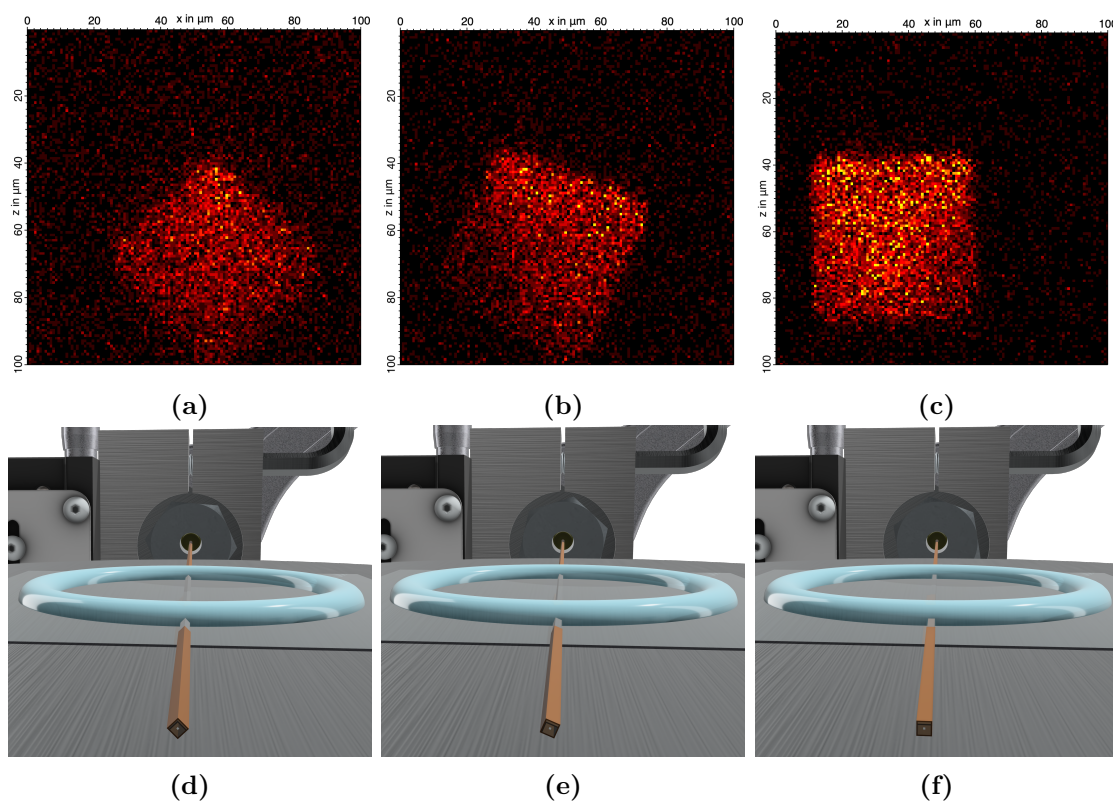


Fig. 4.15: Cross section images of a square capillary (a) after its initial installation. (b) shows the capillary after a first slight rotation and attempt to improve the orientation and (c) the desired orientation of the capillary centered above the objective after a second improvement step. Illumination is from top to bottom. (d-f) show renderings, which illustrate the positions of the capillary within the optical multi layer (OML) on the sample stage above the objective for each orientation from (a-c).

lary while maintaining a fixed lateral position. Fig. 4.15 shows axial cross section images of a square capillary connected to the experimental setup with different orientations alongside corresponding renderings of each orientation within the optical multi layer OML. Fig. 4.15a shows the capillary with a rotation of the side walls to the objective of $\approx 45^\circ$. As described in section 3.4, to change the orientation of the capillary, the gland of the connection tube and screw of the clamp is loosened in a first step. Afterwards, the capillary is rotated, and the screw and gland are tightened again, before checking the orientation with a new cross section image. This workflow and improved design of the sample stage enables a simple and time efficient way to change the orientation of the capillary. Fig. 4.15b shows an improved position of the capillary after a first correction attempt and Fig. 4.15c the desired final position after a second rotation step. As can be seen, the lateral position of the capillary remains almost unchanged, but stays within the sampling range of the scanner. Moreover, even when the whole rotation process leads to a larger lateral movement of the capillary, it can be easily and precisely adjusted and corrected due to the slotted holes in the base plate, which enables a steady movement of the whole assembly at once.

4.3.3 Capillary preparation

As mentioned in subsection 3.2.2, after inserting the sample solution in the capillary, it has to be verified if the capillary is filled with a sufficient amount of sample solution in order to be able to successfully perform a single molecule high pressure fluorescence measurement. Up to present, the capillary had to be held in hand or the capillary was put under the microscope and was lying on the pressure plug. This approach has several disadvantages. When holding the pressure plug with the glued in capillary in hand, it is not trivial to keep the capillary steady enough to reach an appropriate position above the objective of the microscope. The capillary easily vibrates and makes it hard to bring it into focus under the microscope. Furthermore, this approach increases the risk, that the capillary will hit against the microscope or other objects and become dirty or, in the worst case, gets damaged and breaks. To simplify the whole procedure and enable a more comfortable and secure way of inspecting the sample filling, a capillary holder was designed and 3D printed. The holder is shown in Fig. 4.16. It holds the capillary, which is glued into the pressure plug in a horizontal position and enables an easy movement of the capillary under the microscope without many vibrations. This greatly simplifies the process of finding the sample solution inside the capillary and checking the filling level, because the capillary stays permanently in the focus of the microscope. Furthermore, it reduces the risk of the capillary getting damaged or dirty. This has the advantage that there is no need for an additional intermediate step of cleaning the capillary again and

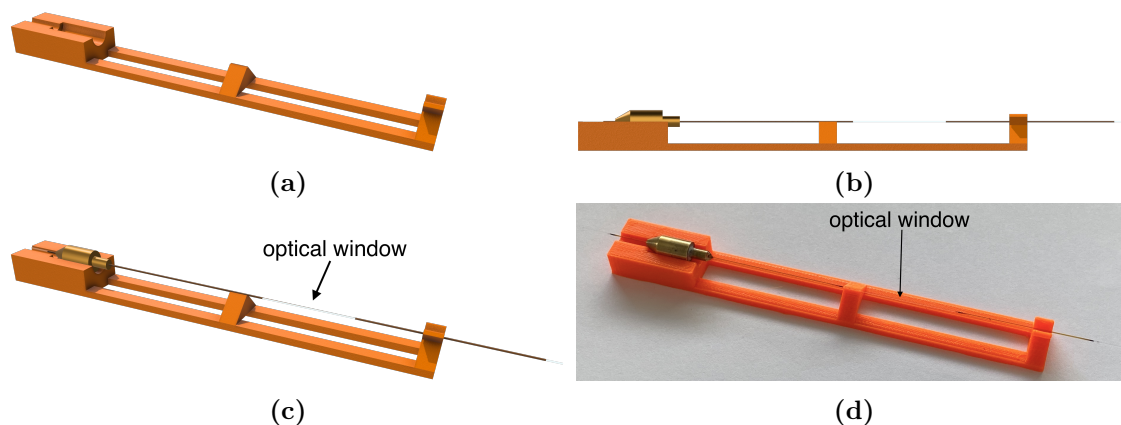


Fig. 4.16: (a) Rendering of the 3D-printed capillary holder. (b,c) show the capillary holder alongside the capillary glued into the pressure plug. The holder keeps the capillary in a horizontal position and allows it to be moved with few vibrations to check the filling level of the capillary prior to an experiment. (d) shows a picture of the holder with the capillary inside the pressure plug.

one can proceed with the next step of the work flow immediately without further delay.

4.4 Capillary PMMA multi layer

For the evaluation of the capillary PMMA multi layer (cap/PMMA) described in subsection 3.2.4, FRET and FCS experiments were performed with both, free diffusing fluorescent microspheres (subsection 4.4.1) and the free diffusing fluorophore AF488 (subsection 4.4.2), respectively. The measurements were made with different optical setups using a standard borosilicate coverslip (cs/BG) as a reference, the cap/PMMA and a bare square capillary (cap). Furthermore, a combination of three stacked layers of the PMMA film were evaluated, mimicking a 150 μm thick PMMA coverslip (cs/PMMA). Additionally, cross section images of the cap/PMMA were taken to check for any shifts or displacements of the optical assembly (see subsection 4.4.3).

4.4.1 Fluorescent microspheres as a test system

FRET and FCS measurements of the fluorescent microspheres were performed with a bead concentration of approximately 30 pM. Every FRET transfer efficiency histogram was calculated with a sum threshold for the donor and acceptor bins of

$T_{\text{sum}}^{\text{DA}} = 50 \text{ cts/ms}$ and not corrected otherwise. FRET histograms and the corresponding number of recorded FRET events are shown in Fig. 4.17 for all four optical assemblies described in section 4.4. As expected, most FRET events are observed when using a borosilicate coverslip (cs/BG) for which the microscopes objective is designed. Second most FRET events are obtained by using the cap/PMMA followed by the use of the bare capillary. The worst result is achieved with the cs/PMMA. It should be noted, that the donor and the acceptor signal of the cs/PMMA experiment drops to background signals after a time of about 550 s (see Fig. 4.17c). This could indicate significantly worsened optics and one possible reason for the reduced number of FRET events using the cs/PMMA. But even if the events are roughly scaled to the experiment time of 1800 s (dashed histogram and open square in Fig. 4.17a and Fig. 4.17b), they are still the lowest of all evaluated configurations. The FRET efficiency of the cs/PMMA is the lowest with a value of $E_T = 0.502 \pm 0.002$, whereas the efficiencies of the borosilicate coverslip ($E_T = 0.576 \pm 0.001$) and the cap/PMMA ($E_T = 0.580 \pm 0.001$) are in a similar range. The transfer efficiency of the bare capillary has a value of $E_T = 0.552 \pm 0.001$. Differences in the efficiency can be explained with optical aberrations and different imaging properties of the used assembly when using a capillary or PMMA.

The correlation functions of the experiments were analyzed with a fitting model, which only considers diffusion as the cause for intensity fluctuations of the fluorescence signal (see Eq. 3.9). Transitions to the triplet state were not taken into account

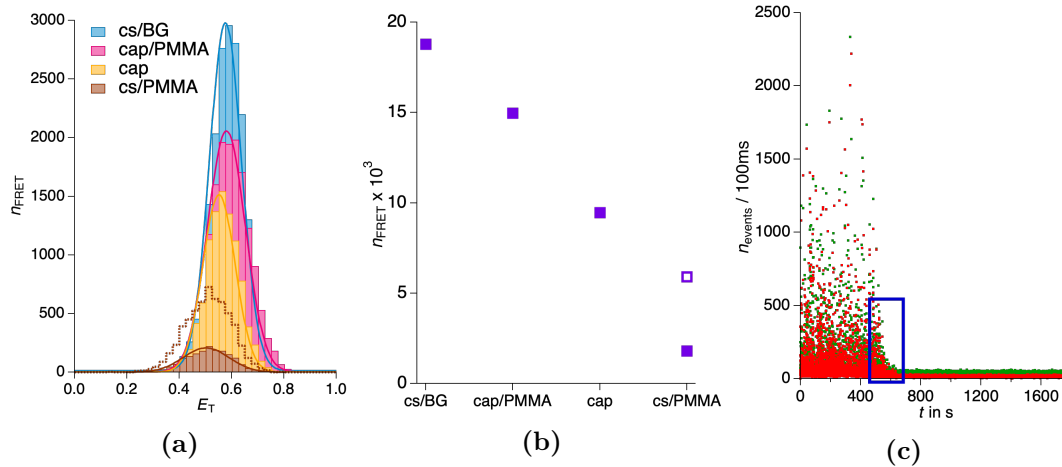


Fig. 4.17: (a) FRET histograms of fluorescent microsphere measurements made with a borosilicate coverslip (cs/BG), the PMMA multi layer (cap/PMMA), a bare capillary (cap) and the PMMA coverslip (cs/PMMA). (b) Integrals of all histograms and optical assemblies. The open rectangle belongs to the dashed histogram. (c) Visualization of the signal drop after about 550 s (blue rectangle) during the cs/PMMA measurement. The dashed histogram in (a) and open square in (b) are an estimate value for a cs/PMMA experiment without a signal loss during the measurement.

since the beads are stained with a high number of dyes essentially averaging out triplet fluctuations. The average number of molecules in the focal volume $\langle N \rangle$ shows the lowest number of molecules for the experiment with the borosilicate coverslip, and increasing numbers for the cap/PMMA and the bare capillary (see Fig. 4.18). The cs/PMMA on the other hand shows a similar number of particles for the cross-correlation curves resulting from an even larger $\langle N \rangle$ for the donor and a decreased value in the acceptor channel in comparison to the bare capillary. These results indicate an enlarged focal volume containing more beads for all arrangements in comparison to the reference with the coverslip. The different result between the donor and acceptor channel in the cs/PMMA experiment could be due to a different dispersion and as a result a decreasing overlap between the donor and acceptor focus, leading to the observed shift in the FRET histogram as well. Furthermore, these results illustrate that the bare analysis of the FRET histograms and events are not a fully appropriate indicator of optical properties since relatively small differences in the number of events between the cap/PMMA and the coverslip is due to a larger number of beads measured with a larger focal volume. Therefore, the quality indicator Q_{FRET} and molecular brightness ϵ_{MB} (see Fig. 4.18 b and Fig. 4.18 c) are more suitable as they take the average number of molecules into account. They display the same order as the number of FRET events but reveal a larger gap between the optical assemblies, especially in comparison to the measurement with a borosilicate coverslip. Another observation can be made when looking at the molecular brightness. In all assemblies, except for the cs/PMMA, ϵ_{MB} of the cross-correlations is highest, followed by the ones of the acceptor and the donor. However, when using the cs/PMMA, donor and acceptor are exchanged with each other, which again suggests the

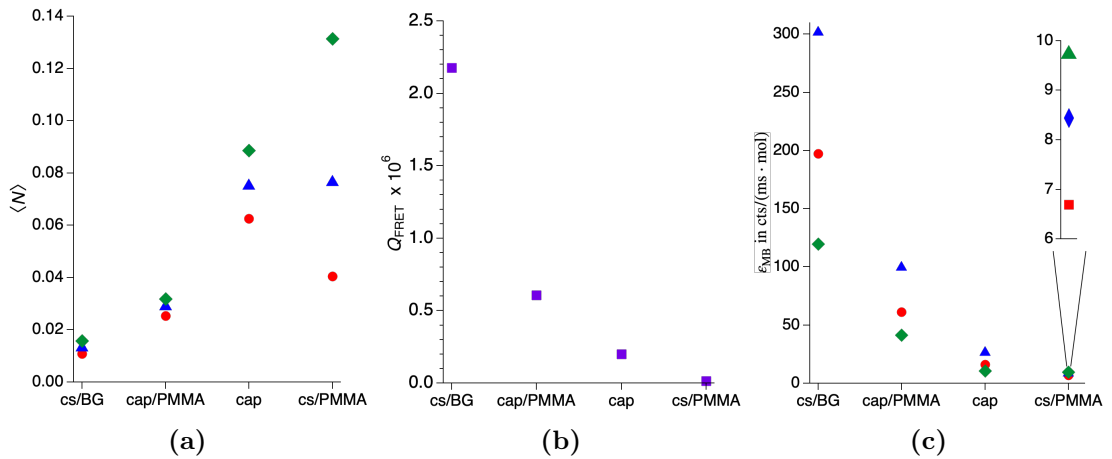


Fig. 4.18: (a) Average number of molecules $\langle N \rangle$, (b) FRET quality indicator Q_{FRET} and (c) molecular brightness ϵ_{MB} of fluorescent microsphere measurements with four configurations: borosilicate coverslip (cs/BG), PMMA multi layer (cap/PMMA), bare capillary (cap), PMMA coverslip (cs/PMMA). Parameters of donor-donor, acceptor-acceptor and acceptor-donor correlation functions in (a) and (c) are shown in green, red and blue, respectively.

presence of dispersion effects. The diffusion time with each assembly (see Fig. 4.19) shows a slightly different behavior since the diffusion time determined with the cap/PMMA is in the same range as with the borosilicate coverslip, even though the average number of molecules in the focal volume is higher for the cap/PMMA and the molecular brightness and quality factor are worse as well. This suggests mainly an increase of the axial dimensions of the focal volume, whereas the lateral focus dimensions demonstrating the diffusion time seem to remain almost unchanged.

To validate the outcome, the experiments with beads were repeated with all optical configurations except the cs/PMMA. The results are displayed in Fig. 4.20. In contrast to the previous bead experiments described above, all analyzed quantities indicate less aberrations for the bare square capillary than for the cap/PMMA. The number of detected FRET events (see Fig. 4.20b) is highest for the borosilicate coverslip, followed by the cap and the cap/PMMA. The average number of molecules as well as the diffusion times show best results for the coverslip, indicating the smallest focal volume and thus the shortest diffusion time (Fig. 4.20d) and average number of molecules within (Fig. 4.20c). The FRET quality indicator (Fig. 4.20e) and molecular brightness (Fig. 4.20f) show the same tendency as well, indicating worst optical conditions for the cap/PMMA. In addition, FRET efficiency histograms (Fig. 4.20a) show a shift of the transfer efficiency with respect to the efficiency of the cs/BG measurement with $E_T = 0.573 \pm 0.001$. This is for both, the cap and cap/PMMA, in which the shift of the efficiency of the cap is in the same range as before with a transfer efficiency of $E_T = 0.553 \pm 0.002$. In contrast to the results showed in Fig. 4.17a, the efficiency determined by using the cap/PMMA has a much greater shift towards lower efficiencies with $E_T = 0.480 \pm 0.002$, comparable to the one observed when

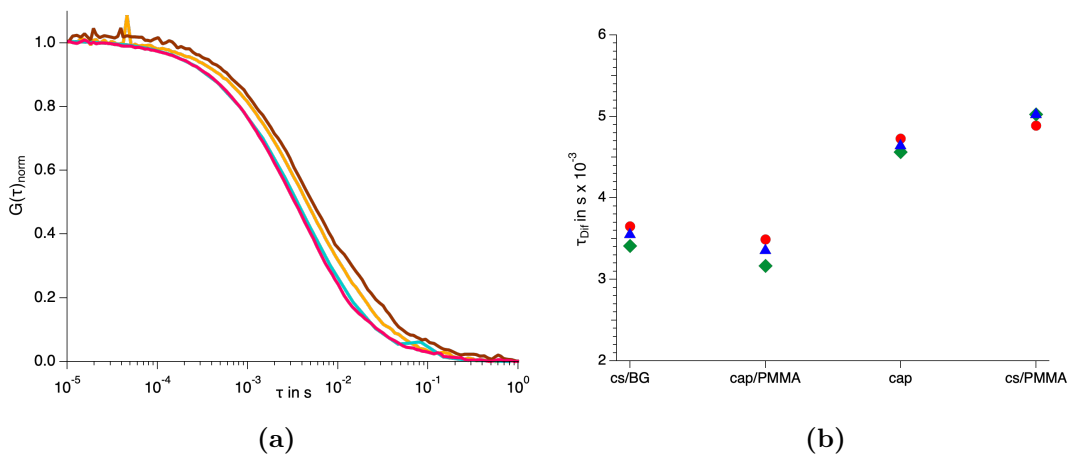


Fig. 4.19: (a) Donor and acceptor channel cross-correlation functions of fluorescent microspheres measurements with a borosilicate coverslip (cs/BG), a bare capillary (cap), the PMMA multi layer (cap/PMMA) and the PMMA coverslip (cs/PMMA), normalized by the average number of molecules. (b) shows the corresponding diffusion times τ_{Diff} of the donor-donor (green), acceptor-acceptor (red) and acceptor-donor (blue) correlation functions.

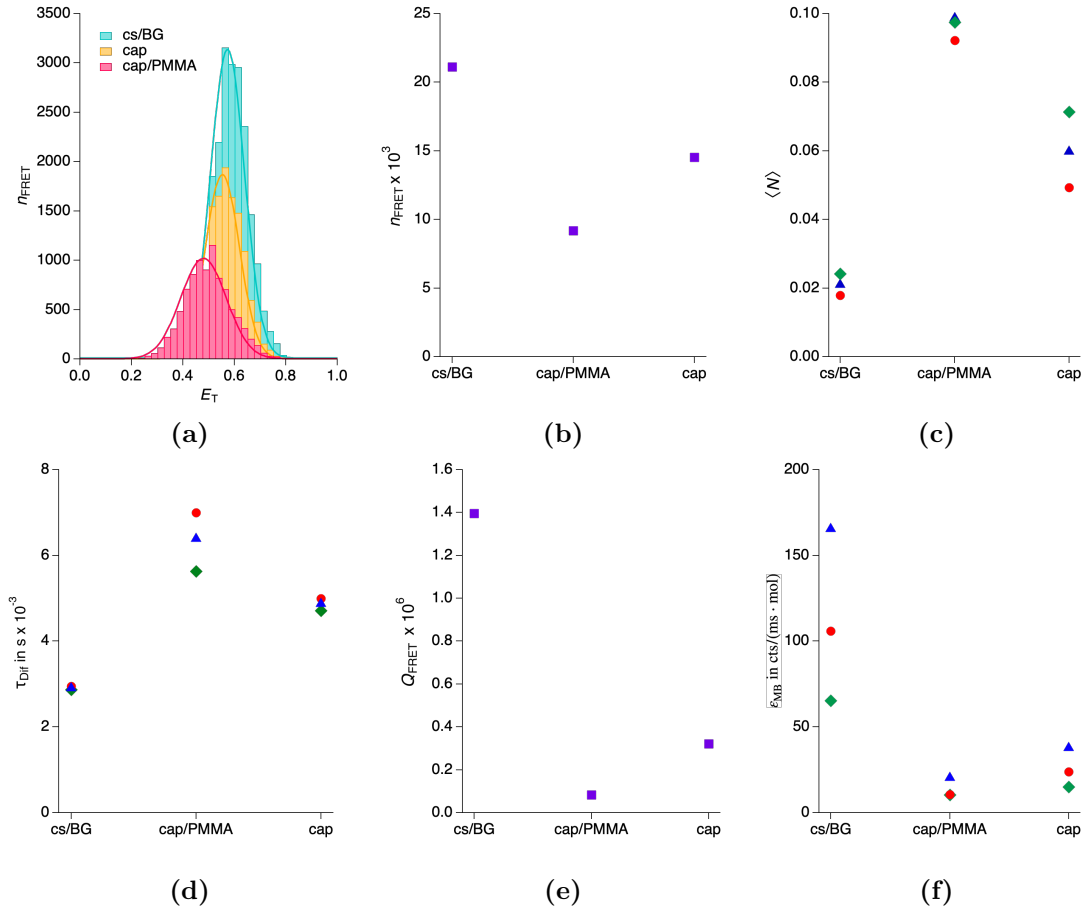


Fig. 4.20: FCS and FRET results of experiments of fluorescent microspheres. Three different optical assemblies were used: a borosilicate coverslip (cs/BG), a bare capillary (cap) and the PMMA multi layer (cap/PMMA). (a) shows the FRET efficiency distributions, (b) the corresponding number of FRET events n_{FRET} , (c) the average number of molecules $\langle N \rangle$, (d) the diffusion time τ_{Dif} , (e) the FRET quality indicator Q_{FRET} and (f) the molecular brightness ϵ_{MB} for the donor-donor (green), acceptor-acceptor (red) and acceptor-donor (blue) correlation functions.

using the cs/PMMA. Errors of the transfer efficiencies are \pm one standard deviation of the fit.

4.4.2 Alexa Fluor 488

Besides experiments with fluorescent beads, measurements with freely diffusing Alexa Fluor 488 (AF488) were made as well, using the same configurations as with the bead measurements, a borosilicate coverslip (cs/BG), a square capillary (cap), the capillary PMMA multi layer (cap/PMMA) and the PMMA coverslip consisting of three PMMA films laid on top of each other (cs/PMMA). In contrast to the bead measurements the correlation functions were fitted with a model taking into account both, diffusion and triplet blinking (see Eq. 3.10). Fig. 4.21 shows the fit parameters of all optical assemblies, the diffusion time, average number of molecules, number of events, molecular brightness as well as the triplet fraction and time. Like with the fluorescent beads, best results were achieved with the cs/BG followed by the cs/PMMA, cap and the cap/PMMA. This is similar to the second series of bead

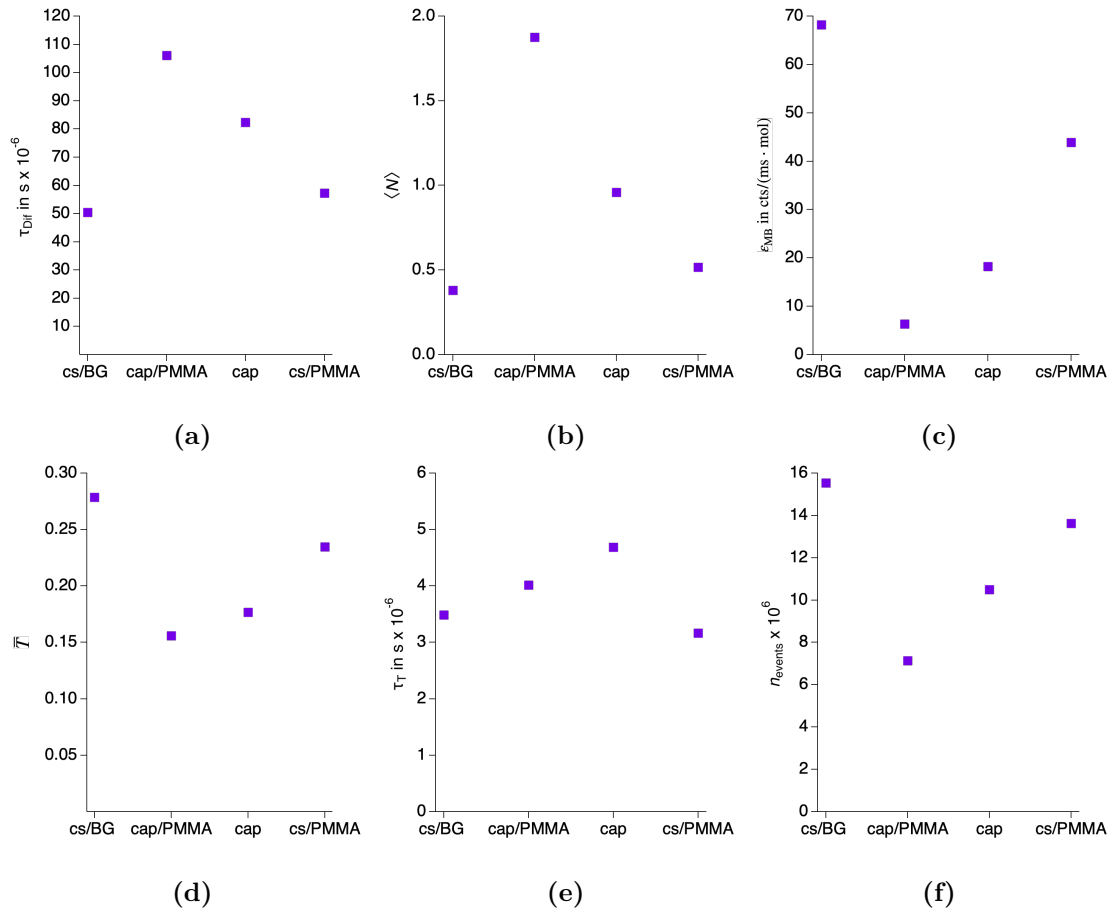


Fig. 4.21: FCS results of free diffusing AF488 using four different assemblies: borosilicate coverslip (cs/BG), PMMA multi layer (cap/PMMA), bare capillary (cap) and PMMA coverslip (cs/PMMA). (a) shows the diffusion time τ_{Dif} , (b) the average number of molecules $\langle N \rangle$, (c) molecular brightness ϵ_{MB} , (d) the triplet fraction \bar{T} , (e) triplet time constant τ_T and (f) number of detected photons n_{events} .

experiments for the same reasons. An enlarged focal volume leads to a higher average number of molecules within and subsequently a larger diffusion time. This is in good agreement with the triplet fraction. Since the excitation power is distributed over a larger area, the photon flux density is reduced, leading to a less efficient excitation and thus lower triplet fraction and longer relaxation time. The decrease of the molecular brightness and detected number of photons is an indicator for deteriorated optical conditions as well. However, the results for the cs/PMMA differ with respect to the bead measurements. This could be due to smaller dispersion effects when measuring a single dye instead of a FRET pair with a relatively large spectral gap between excitation and detection. In contrast the results of the cap/PMMA are worse than for both, the cs/PMMA and the cap.

4.4.3 Cross section images

In order to evaluate possible deformations of the PMMA film, axial x - z -scans were taken. x denotes one lateral direction and z the direction along the optical axis. The PMMA film was positioned above the objective with water as the immersion fluid. The film was fixed to the optical table with magnets like in the spectroscopic experiments as well. Afterwards, two x - z -scans were made with a 5 minute interval between them. The result is shown in Fig. 4.22a and Fig. 4.22d. At first, the whole film with a thickness of $50\ \mu\text{m}$ can be identified and it lies almost flat atop the objective. The second image, taken 5 minutes later, reveals a displacement of the film of $\approx 30\ \mu\text{m}$ along the optical axis and additionally a slight tilt. This finding might explain the inconsistent results of different diffusion experiments with the cap/PMMA system. A shift in the range of $30\ \mu\text{m}$ along the optical axis in combination with a tilt can lead to severe aberrations or even cause the excitation focus of the laser not being in the sample volume of the capillary, rendering experiments impossible with single molecule sensitivity. In order to better understand this effect, several cross section images were made using the cap/PMMA (see Fig. 4.22). They show the possibility to achieve a sufficient result when using the cap/PMMA with a clearly visible square or round cross section of the sample volume of the respective capillary with an inner diameter of $\approx 50\ \mu\text{m}$ (see Fig. 4.22b and Fig. 4.22c). On the other hand, cross section images shown in Fig. 4.22e and 4.22f show significantly worsened results, with severe elongations along the optical axis. This could be either due to bad optical conditions or due to a movement of the PMMA film and therefore the whole assembly of the cap/PMMA during the scan. This result indicates a strong sensitivity of the assembly to weak vibrations. In addition, it makes the use for high-pressure experiments questionable since a usage of the pressure pump to generate hydrostatic pressure makes these vibrations inevitable. Moreover, scans in advance of an experiment are necessary to adjust the whole assembly properly above the objective and adjust the focus properly into the sample volume of the capillary.

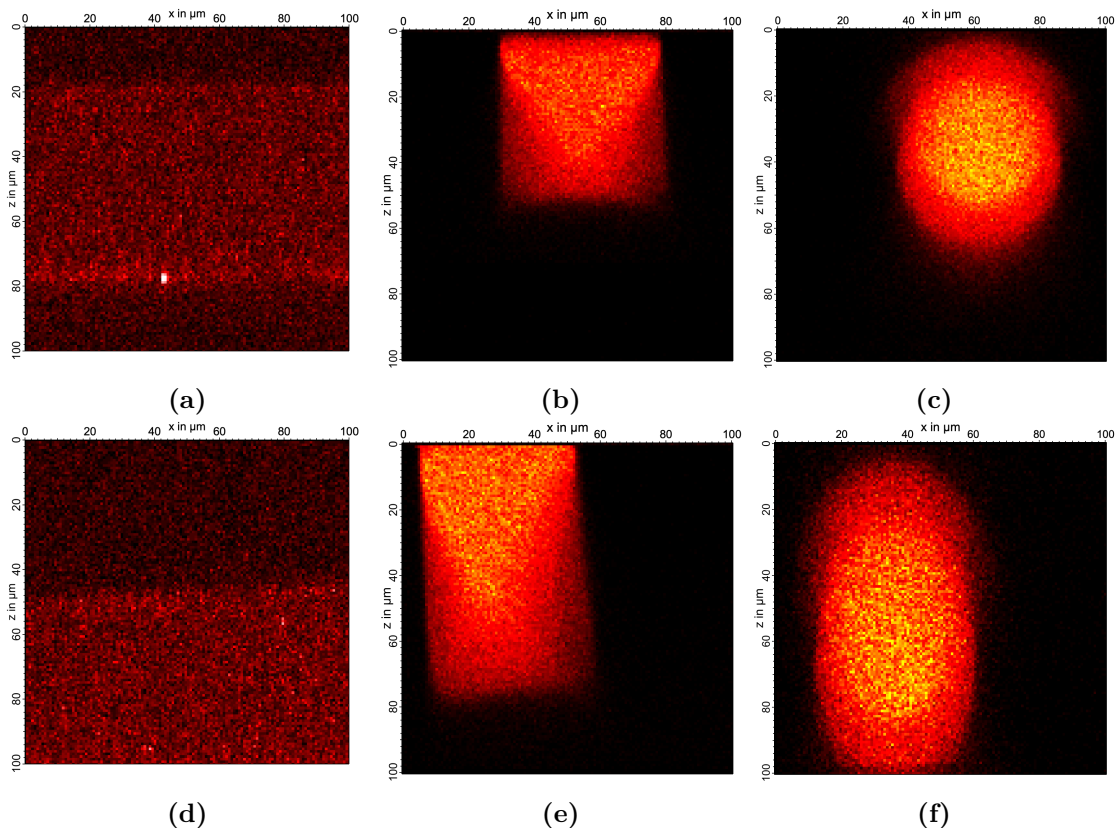


Fig. 4.22: Axial cross section images of the PMMA film (a) right after positioning and (d) after a time period of 5 minutes. (b) and (e) show images of the sample volume of a square capillary using the PMMA multi layer. (c) and (f) show the same kind of images, but of a round capillary. Whereas the experimental prerequisites were equal, (b) and (c) show a clear visible square or round cross section with a diameter of $d \approx 50 \mu\text{m}$, while (e) and (f) show a significant elongation along the optical axis. Excitation/ detection from the top. Shadowing at the edges is due to light passing through the side walls of the capillary.

4.4.4 Discussion

The results of measurements using a PMMA film are somewhat inconsistent. The results of the bead measurements (see Fig. 4.17 and Fig. 4.18) indicate improved results by using the cap/PMMA compared to measurements with the bare square capillary. Although the measurements with AF488 (see subsection 4.4.2) show worsened results with the cap/PMMA, results of the PMMA coverslip are comparable to those of the borosilicate coverslip measurements. However, it should be noted that any dispersion effects are potentially not as significant for measurements with

just one dye as they are for FRET experiments with a larger spectral gap between the donor and acceptor fluorophores. Nevertheless, the FCS experiments and the cross section images suggest that the cs/PMMA with the PMMA film instead of the fragile fused silica coverslip can be principally considered to improve the imaging properties in comparison to bare capillaries. But to really serve as a reliable replacement of fused silica coverslips some issues have to be solved. Besides comparable or improved results in some of the discussed FCS experiments, the results showed problems using the PMMA film as well. One of the biggest problems is the reliability of the measurements when using a PMMA film. Even with the same sample and experimental prerequisites the results are varying between experiments. This seems to be caused by the fact that the PMMA film is not entirely fixed in place and can move during measurements or scans (see subsection 4.4.3). This can lead to a strong shift of the focus. The movement of the PMMA film can also lead to a bending of the film, which could lead to lens effects and thus optical aberrations and a subsequent deterioration of the optics. Additional dispersion effects can also reduce the performance, especially with FRET experiments and a large shift between the excitation and detection focus of different fluorophores.

4.5 Influence of the microscope objective correction collar

4.5.1 Bare square capillary

The microscope objective is equipped with an adjustable correction collar and designed for the usage of coverslips made of borosilicate glass with a refractive index of 1.53 and a thickness between 130 μm and 190 μm . Therefore, when using fused silica capillaries or materials with other refractive indices, the setting of the correction collar needs adjustment. To evaluate the best setting of the correction collar (cc) for the use of a bare square capillary, measurements with double stranded DNA (dsDNA) were performed for cc settings of 13, 15, 16, 17, 18 and 19. Each of the measurements had a duration of 10 minutes. FRET efficiency histograms were calculated with a sum threshold for the donor and acceptor bins of $T_{\text{sum}}^{\text{DA}} = 30$ cts/ms (see Fig. 4.23). As can be inferred from Eq. 3.2 to Eq. 3.4, the optimal correction collar setting for the correction of the marginal rays for a 125 μm fused silica wall thickness would be like for a 100 μm thick borosilicate coverslip, which is not possible with the microscope objective being used. However, when evaluating the histograms they reveal the highest number of recorded FRET events and the highest FRET peak for a correction collar setting of 13. The FRET quality indicator shows the same behavior as well. The remaining results indicate worsening optical conditions with increasing correction collar setting. Despite these results, the average number of molecules

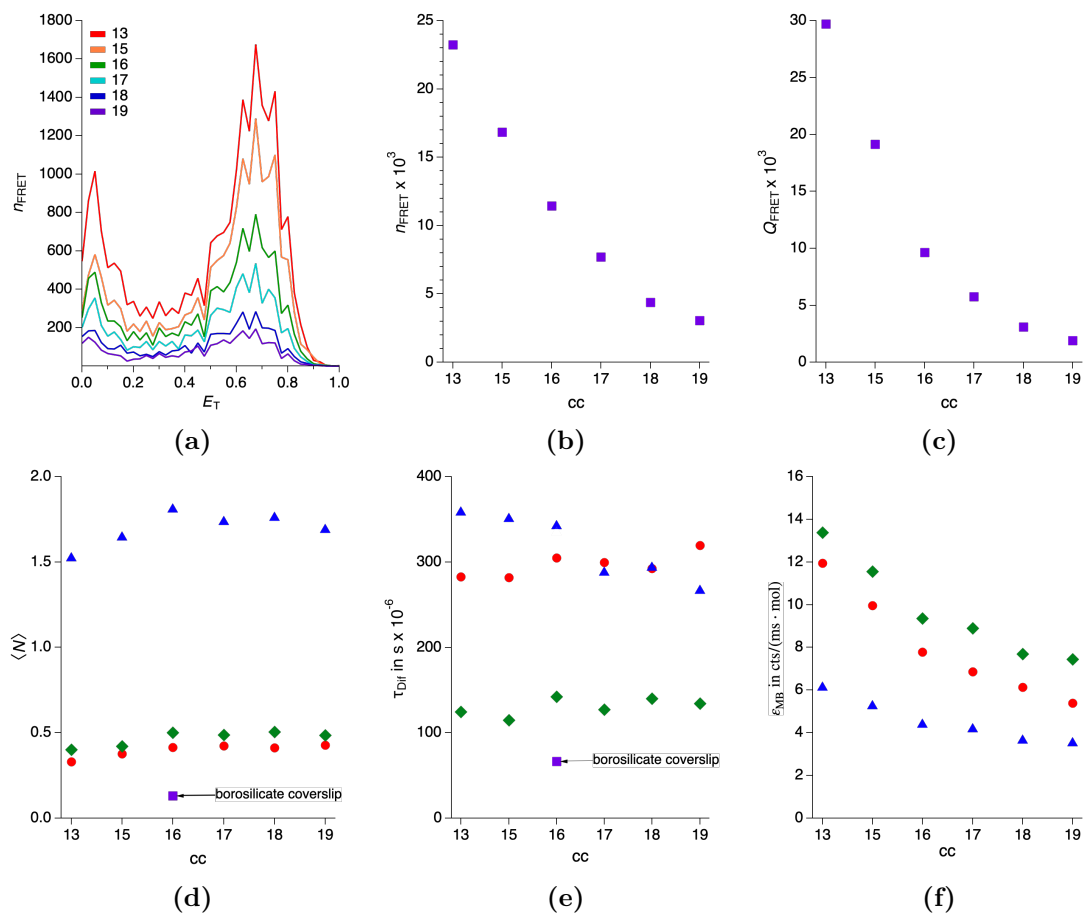


Fig. 4.23: Influence of the microscope objectives correction collar (cc) setting using a bare capillary. The sample was dsDNA, with AT488 and A647N for FRET experiments. (a) shows FRET efficiency histograms with cc between 13 and 19. (b) shows the corresponding number of FRET events, (c) the FRET quality indicator Q_{FRET} , (d) the average number of molecules $\langle N \rangle$, (e) the diffusion time τ_{Dif} and (f) the molecular brightness ϵ_{MB} . In (d-f) results of the donor-donor, acceptor-acceptor and acceptor-donor correlation functions are shown in green, red and blue, respectively.

as well as the diffusion times show no clear tendency and remain almost constant with only slight deviations between the different settings. The molecular brightness on the other hand is showing a similar behavior like the FRET results. The reason that the average number of molecules and the diffusion time show almost no changes between different settings is probably due to already much worse optical conditions with a cc setting of 13, when compared to a borosilicate coverslip (see Fig. 4.23d and Fig. 4.23e). Furthermore, it could indicate, that the worsening of the optical conditions with increasing setting of the correction collar is due to an expansion of the focal volume along the optical axis rather than in the lateral direction.

4.5.2 Optical multi layer

The optimal correction collar setting for the use of the optical multi layer (OML) with a square capillary was investigated. Like within the bare square capillary, a dsDNA sample was diluted in water and measured for 10 minutes. FRET efficiency histograms were calculated with a sum threshold of donor and acceptor bins of $T_{\text{sum}}^{\text{DA}} = 30$ cts/ms and are shown in Fig. 4.24a with the corresponding number of events in Fig. 4.24b. The histograms indicate best results for a correction collar setting of 17, where the FRET peak in the histogram and the quality indicator is the highest of all evaluated correction collar settings. Whereas a setting of 18 reveals comparable results, settings of ≤ 16 show significantly poorer results. The

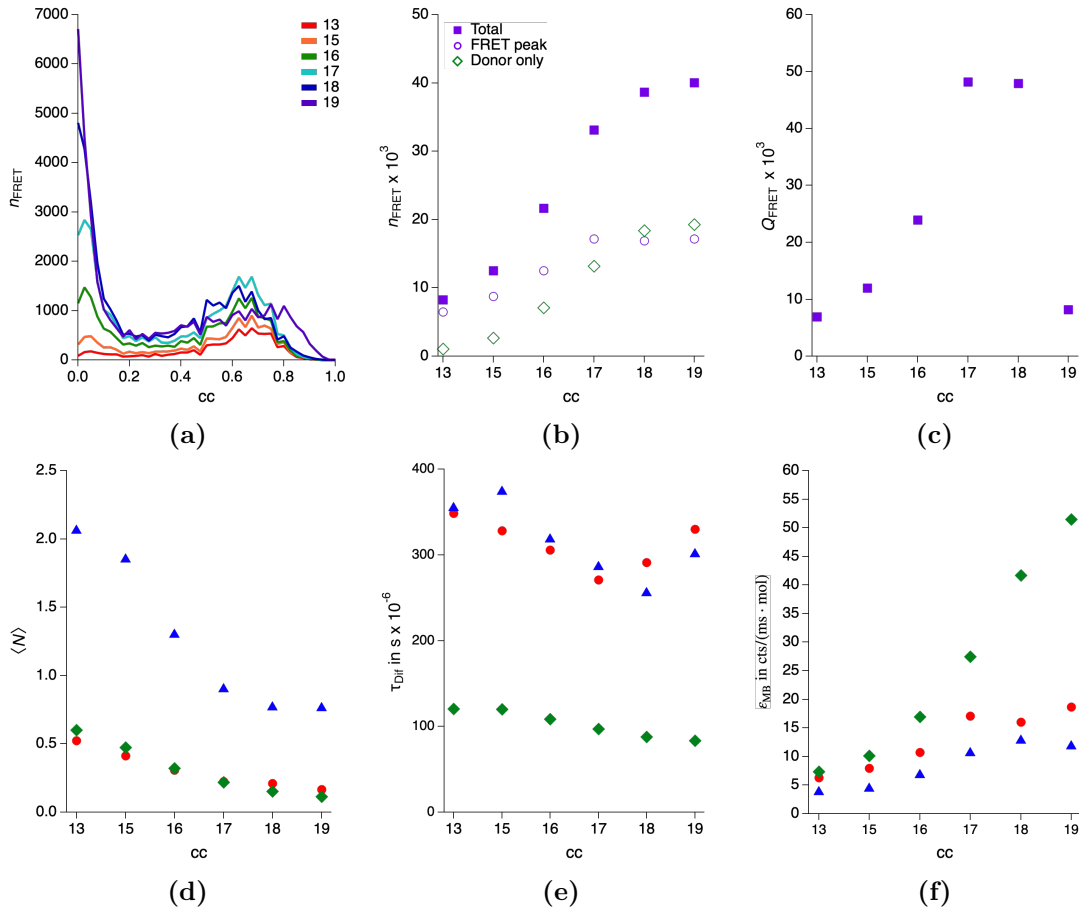


Fig. 4.24: Influence of the objective correction collar setting (cc) using the optical multi layer (OML). (a) shows the FRET efficiency histograms for cc between 13 and 19, (b) the corresponding number of FRET events n_{FRET} , (c) the FRET quality indicator Q_{FRET} , (d) the average number of molecules $\langle N \rangle$, (e) the diffusion times τ_{Dif} and (f) the molecular brightness ϵ_{MB} . In (d-f), results obtained from donor-donor, acceptor-acceptor and acceptor-donor correlation functions are shown in green, red and blue, respectively.

measurement with a cc setting of 19 shows a number of FRET events, which is in the same range as with setting 17 and 18 (see Fig. 4.24b), but the FRET histogram shows a shift towards higher transfer efficiencies with respect to the measurements with other correction collar settings. More importantly, the FRET quality indicator (see Fig. 4.24c) is much worse in comparison to settings of 17 and 18 and is in the same range as setting 13. The average number of molecules (see Fig. 4.23d) as well as diffusion times (see Fig. 4.23e) confirm the results with decreasing values with increasing correction collar setting. The increased diffusion time visible in the acceptor correlations and cross-correlations show a deterioration of the optics with a cc setting of 19, whereas the diffusion time of the donor slightly further decreases. This is an indication of dispersion effects and larger effect in the acceptor channel, when choosing a cc setting of 19. The molecular brightness (see Fig. 4.24f) behaves similarly to the average number of molecules with an increasing brightness for the acceptor auto-correlations and cross-correlation. For the donor, ε_{MB} increases even more significantly with a setting of 19, but this is probably due to the strong increase of the donor only peak and again indicates more pronounced dispersion effects when measuring with this setting. In summary, best results were achieved with correction collar settings of 17 and 18. Despite having comparable results regarding the total number of recorded events or with the molecular brightness for example, no real improvements regarding FRET experiments could be achieved with the correction collar setting of 19. It yielded a much lower value of the FRET quality indicator, which takes the average number of molecules and the width of the histograms into account. Therefore, a setting of 19 is not recommended when using the OML for FRET experiments, but rather a setting of 17 or 18. For FCS experiments with a single dye and not a FRET pair it could be different, since no compromise between the foci of both spectral channels has to be made.

4.6 Focus position within the sample volume of the capillary

In addition to the evaluation of the ideal correction collar setting, the focus position within the sample volume of the fused silica capillary was evaluated as well. Three different axial positions of the focus were tested (see Fig. 4.25). One position is close to the surface between the sample volume and the fused silica glass, one in the center of the capillary with an axial distance to the surface of $d_{\text{axial, surface}} \approx 25 \mu\text{m}$ and the last approximately in the middle between the other two positions, with $d_{\text{axial, surface}} \approx 12.5 \mu\text{m}$. Measurements were made with the 3-stranded DNA hybrid. Durations of the measurements were 20 minutes. Auto-correlation functions of the donor and acceptor dye as well as average number of molecules and diffusion times

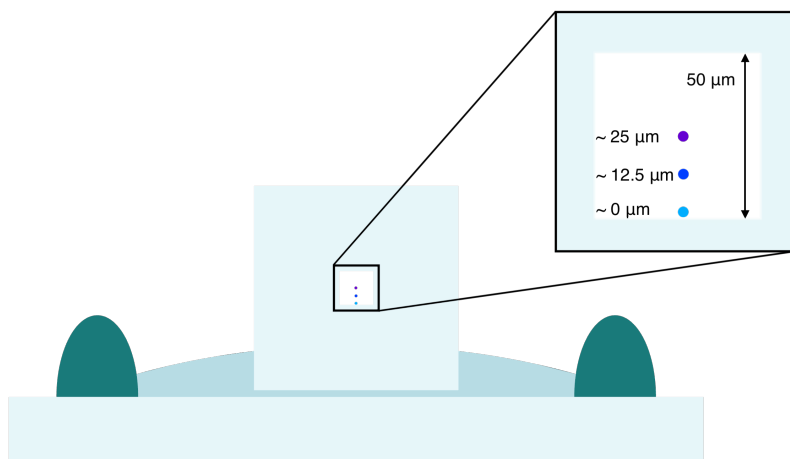


Fig. 4.25: Illustration of three focus positions inside the sample volume of the fused silica capillary to evaluate, which is best for smFRET experiments under high pressure. Positions were close to the surface (cyan), in the middle of the sample volume (purple) and centered in between those two positions (blue).

are shown in Fig. 4.26. The average number of molecules indicate a smaller focal volume with decreasing distance to the glass surface. Since the concentration is the same in all experiments, the smaller number of molecules is most likely due to a smaller focus. The same holds for the diffusion times (see Fig. A.4d), which are increasing with increasing axial distance to the fused silica surface, indicating slightly larger focus dimensions in the center of the sample volume of the capillary than near the surface. The number of fluorescence photons per 100 ms time bin is not significantly changing between all focus positions. It follows a higher molecular brightness for the focus position near the capillary wall due to a lower number of average molecules within the observation volume. This is because of a higher photon flux density and thus more efficient excitation of the dye. These results are in good agreement with the other findings and indicate a larger focal volume in the center than closer to the fused silica glass surface. The reason for a larger focus volume in the center of the capillary are probably more pronounced aberrations. Focussing into the center could lead to more rays entering the sample volume through its side walls instead of the bottom. This would effect the marginal rays and therefore reduce the effective NA of the objective, leading to an enlarged focal volume. In the context of another scientific project, measurements were made using the protein EsxF. In the course of this, the same measurements were performed to examine and evaluate the different focus positions within the sample volume of the capillary. The results of these measurements can be found in the appendix in section A.3. They are in good agreement with those of the DNA measurements.

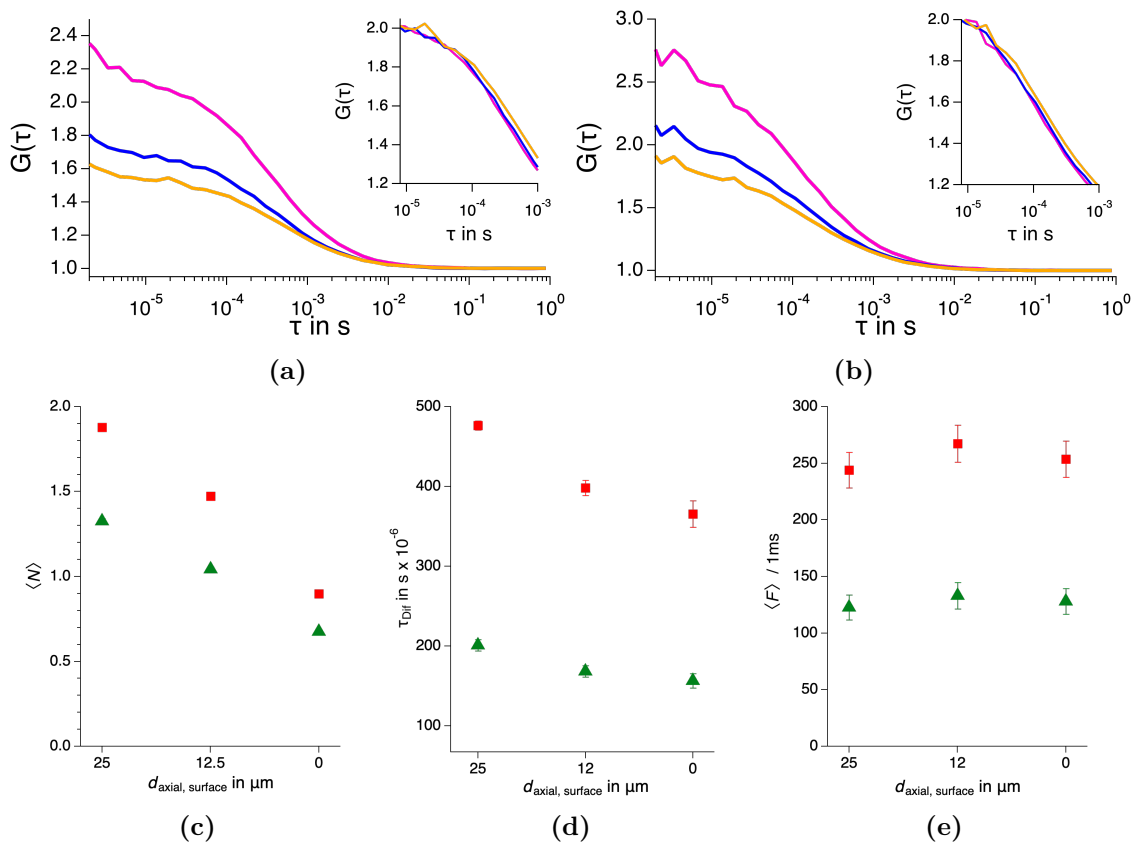


Fig. 4.26: FCS results of 20 minute experiments of the 3-stranded DNA hybrid. Experiments were made with three different focus positions within the sample volume, with distances to the surface of $d_{\text{axial, surface}} \approx 25 \mu\text{m}$ (orange), $12.5 \mu\text{m}$ (blue) and $0 \mu\text{m}$ (pink), respectively. (a) and (b) show the auto-correlation functions of both, acceptor and donor. Insets show the correlation functions, normalized to the average number of molecules. (c-e) show the average number of molecules $\langle N \rangle$, diffusion time τ_{Dif} and average number of photons $\langle n_{\text{photons}} \rangle$ per 1 ms time bin for the donor (green) and acceptor (red) channel, determined by fits of the correlation functions according to Eq. 3.10.

Chapter 5

nsFRET-FCS

5.1 Ambient pressure

5.1.1 3/4-stranded DNA hybrids

Due to the high pressure resistance of DNA, the 3- and 4-stranded DNA hybrids (3-strand, 4-strand) were used as negative control samples i.e., showing no dynamics, for high pressure fluorescence experiments [265–268]. Furthermore, they serve as a control of the detection of fast dynamics as well since it is not expected that they show any dynamics leading to fluctuations in the FRET signal in the sub-100 ns time range. The duration of each measurement was 16 hours with an excitation power of $40 \mu\text{W}$ at a wavelength of 488 nm. The FRET efficiency histograms were calculated with a sum threshold for donor and acceptor photons of $T_{\text{sum}}^{\text{DA}} = 40 \text{ cts/ms}$. They are shown in Fig. 5.1 with two populations for the 3-strand and three populations for the 4-strand, respectively. Consequently, the histograms were fitted with fit functions containing two and three Gaussians. The populations with the lowest

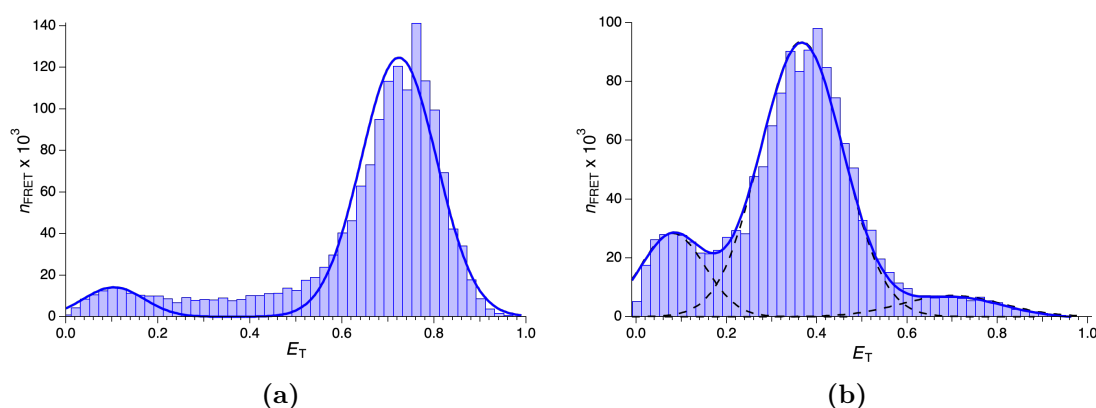


Fig. 5.1: FRET efficiency histograms of the (a) 3- and (b) 4-stranded DNA hybrid including Gaussian fits (solid lines) for determining the mean transfer efficiencies of the donor only and FRET populations.

efficiencies are assigned to DNA hybrids only labeled with a donor fluorophore (donor only). The FRET peak of the 3-strand is centered at an efficiency of $E_T = 0.725 \pm 0.003$. The population with the highest efficiency of the 4-strand has an efficiency of $E_T = 0.700 \pm 0.029$, which is comparable with the FRET efficiency of the 3-strand. Therefore, this population is most likely due to 4-stranded DNA hybrids lacking the spacer complement and being actually 3-strand samples. The most dominant FRET population of the 4-strand has a lower efficiency compared to the 3-strand with $E_T = 0.366 \pm 0.003$. These efficiencies suggest the 3-stranded DNA hybrid being more flexible. This increased flexibility leads to a shorter mean distance of the FRET pair in contrast to the 4-stranded hybrid, which is rigid since it is lacking single stranded regions.

For further analysis, all photon arrival times belonging to time bins with FRET efficiencies above 0.4 were correlated for the 3-strand and FRET events with $0.2 < E_T < 0.6$ were considered for the 4-strand. These filtered correlations are shown in Fig. 5.2 and derived parameters obtained from global fits, according to Eq. 3.13, are

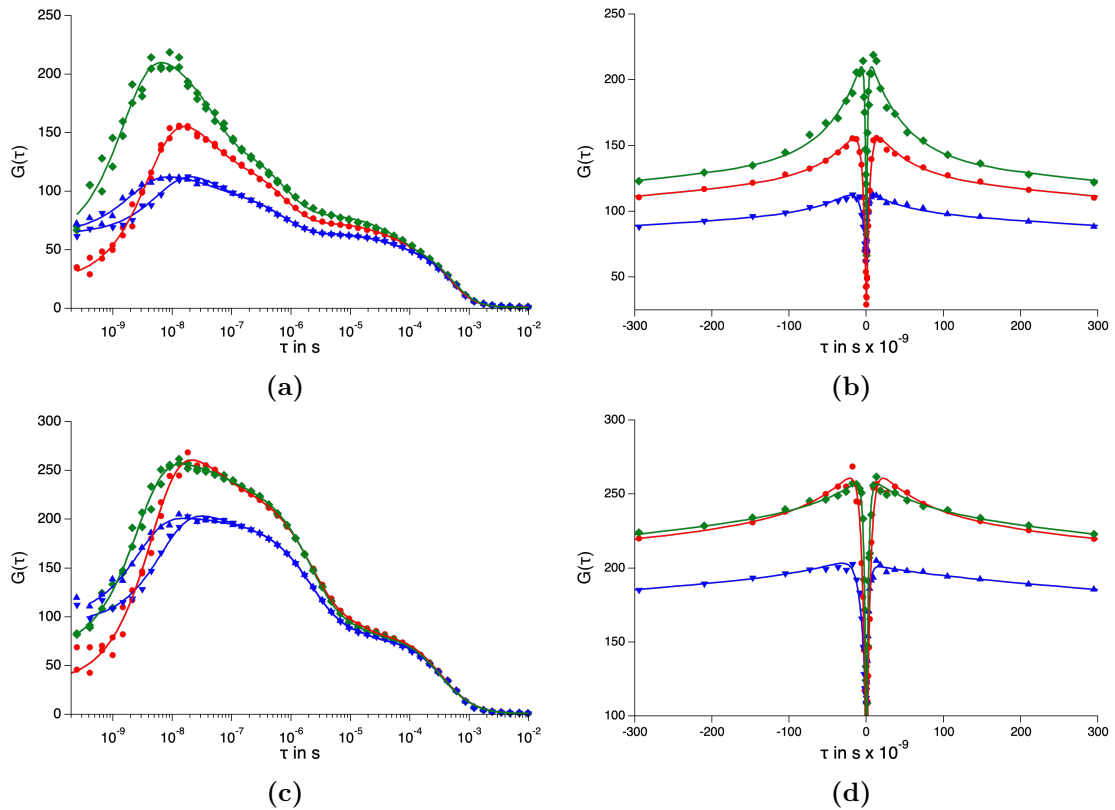


Fig. 5.2: Acceptor-acceptor (red), donor-donor (green), acceptor-donor (blue upward triangles) and donor-acceptor (blue downward triangles) correlation functions of the (a, b) 3- and (c, d) 4-stranded DNA hybrid. Positive and negative lag times in (b, d) correspond to forward and backward correlations, respectively. Solid lines are global fits according to Eq. 3.13.

shown in Fig. 5.3. Both samples show the characteristic drop of the correlations towards longer lag times due to diffusion of the sample through the focal volume. The diffusion times are in the same range for all different correlations, but are slightly faster for the 4-strand than for the 3-strand. Additional processes are present as well, evident by an additional increase towards lag times in a range of approximately $1 \cdot 10^{-8} \text{ s} < \tau < 1 \cdot 10^{-5} \text{ s}$. The drop of the correlation functions in a time range of a few nanoseconds is due to fluorescence antibunching. The amplitude of fluorescence antibunching A_{AB} is strongly dependent on the SNR and background signal [289]. The SNR is typically larger for the acceptor than the donor channel and therefore, the acceptors amplitude of fluorescence antibunching is usually larger in most experiments as well. In principle the correlation function should drop to zero at $\tau = 0$ since one dye cannot emit two photons at the same time [96, 289, 290]. However, this assumption only holds for single emitters. A too high sample con-

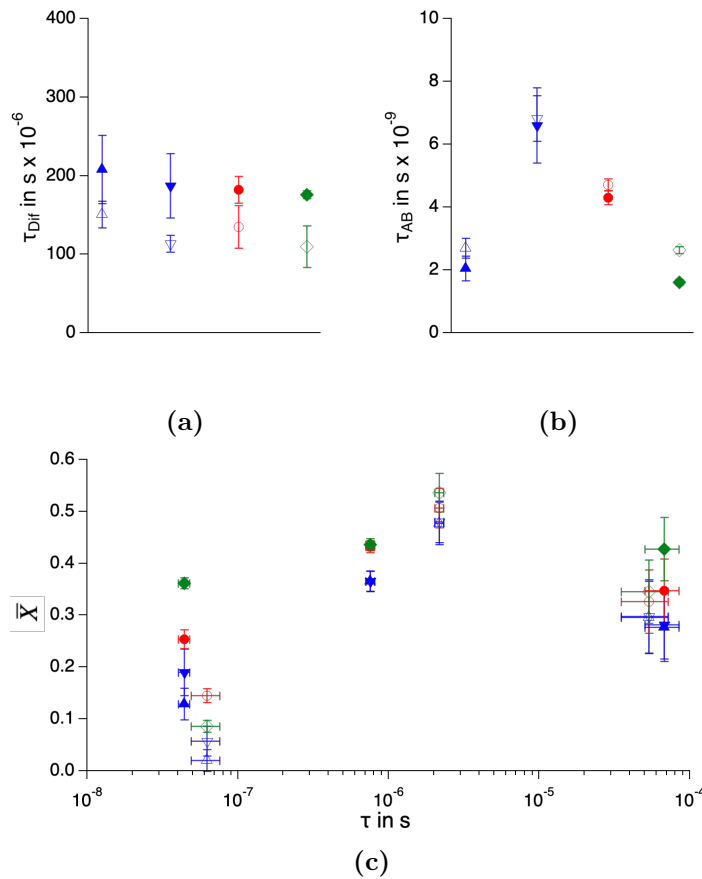


Fig. 5.3: (a) Diffusion times τ_{Dif} , (b) antibunching time constants τ_{AB} and (c) relaxation times of involved processes τ with their respective fractions \bar{X} of the 3-stranded (closed symbols) and 4-stranded (open symbols) DNA hybrid. Fit parameters of the donor-donor, acceptor-acceptor auto-correlation functions are shown in green and red, parameters from the acceptor-donor and donor-acceptor cross-correlation functions are shown as blue upward and downward triangles, respectively.

centration for example increases the probability of more than one DNA molecule within the focus at the same time. Consequently, for more than one dye the amplitude of fluorescence antibunching is reduced. The same holds for a low SNR and high background signal since the probability of accidental pair correlations increases [289]. For FRET experiments the fluorescence antibunching characteristics of the acceptor-donor correlation functions are dependent on the background signals of both channels. Regarding the donor-acceptor cross-correlation functions, there is in principle the chance that the donor and the acceptor dyes emit fluorescence photons at the same time. However, double excitations are typically depleted by singlet-singlet annihilation (SSA) [291].

For the 4-stranded DNA hybrids, A_{AB} of the donor-acceptor cross-correlation functions is smaller for the 3-stranded hybrid due to the larger FRET efficiency and thus lower signal of the donor dye. Since there is no conformational dynamics expected in the antibunching time regime, the correlation functions in this time window will not be discussed. The same holds for the mean number of molecules in the focal volume. The time constants of fluorescence antibunching τ_{AB} are dependent on the excitation power of the laser and are thus only in the limit of extremely low excitation rates corresponding to the actual fluorescence lifetime (see subsection 2.1.2). Nevertheless, it can be seen that the antibunching time constant and therefore also the fluorescence lifetime of the donor of the 3-stranded sample is shorter compared to the 4-stranded sample. This can be rationalized by an increased FRET efficiency and thus more efficient quenching of the donor in the 3-stranded DNA hybrid.

For curve fitting, a model had to be used, which includes three additional processes besides translational diffusion and fluorescence antibunching. The corresponding relaxation times with their amplitudes are illustrated in Fig. 5.3c. It has to be noted, that the global fitting routine is very sensitive in determining the diffusion times depending on the fitting model and the inclusion of exponential terms for one or two additional processes leading to fluorescence intensity fluctuations. This can be explained with the use of an inappropriate model of diffusion for this part of the correlation function. If the observation volume deviates from the three-dimensional Gaussian model, it can lead to signals from the diffusion process appearing at shorter time scales, causing them to overlap with correlations of other processes. This, in turn, can lead to fitting problems and could be an indication of problems with the experimental setup. Because of this, the exponential with the longest relaxation time of $\approx 500 \mu\text{s}$ is rather related to diffusion, as the determined times align within the error for both samples and all correlations. Additionally, the determined time is atypical for triplet dynamics. However, it should be noted that a potentially inappropriate model for the diffusion process should have no significant effect in the determination and analysis of fluctuations due to processes like transitions to the triplet state or chain dynamics, since these intensity fluctuations occur on a different, significantly shorter time scale. The component in the lower microsecond range can be assigned to transitions to the triplet states, where the times for the 3-stranded sample are slightly lower than for the 4-stranded sample. In addition

to triplet dynamics, both samples reveal an additional component with relaxation times below 100 ns, which is a typical time range for protein dynamics. However, the cross-correlation function shows no anti-correlated signal but is correlated like the auto-correlation function of the donor and acceptor. Therefore, the underlying process cannot be attributed to FRET distance dynamics. A possible explanation could be movements of the dyes due to their flexible linker [292]. Even though these movements do not significantly alter the mean donor-acceptor distance, the flexibility of the dyes at the end of the linker enables interactions with the bases of the DNA. These interactions can lead to blinking of the dyes at this short time scale due to processes like photo-induced electron transfer [293,294]. In order to further investigate these processes, multiple measurements with increasing excitation power could be realized in order to validate if they are power dependent, which would rather indicate photo physical processes as the origin of these fluctuations. Since these properties are not in the focus of this work these processes are not further investigated in detail. However, the detection of fluorescence fluctuations on this time scale proves the sensitivity of the experimental setup.

5.1.2 DNA hairpin

As another reference sample, a donor-acceptor labeled DNA hairpin (hpDNA) was investigated. It was measured for a duration of 16 hours with continuous laser excitation of 40 μW at a wavelength of 488 nm. Two populations can be identified in the FRET efficiency histogram (see Fig. 5.4). One population with an apparent efficiency of $E_T = 0.110 \pm 0.002$ is originating from hairpins without an acceptor dye (donor only). The FRET population has an efficiency of $E_T = 0.418 \pm 0.002$. Like for the DNA hybrids, the correlation functions of the high FRET population are fitted with a function containing fluorescence antibunching, diffusion as well as three exponentials (Eq. 3.13). The results are shown in Fig. 5.5. The slowest of these processes has a relaxation time of $\tau = (10.3 \pm 3.1) \mu\text{s}$. Like for the DNA hybrids this slowest exponential is assigned to diffusion in conjunction with a potential non Gaussian-shaped observation volume, which leads to an inappropriate modeling of the diffusion process in the diffusion fit function.

A second exponential has a relaxation time of $\tau = (1.1 \pm 0.5) \mu\text{s}$. This is probably caused by transitions to the triplet state. Since the acceptor Cy5 is a carboxyl cyanine fluorophore, it can switch between a *cis* and a *trans* isomeric form, where the *trans* isomer can emit fluorescence photons and the *cis* isomer is not able to fluoresce [295,296]. Switching between both isomer forms can lead to fluorescence fluctuations as well. The time range of these fluctuations are similar to these of transitions to the triplet state and may overlap [296]. For this reason, this exponential could also

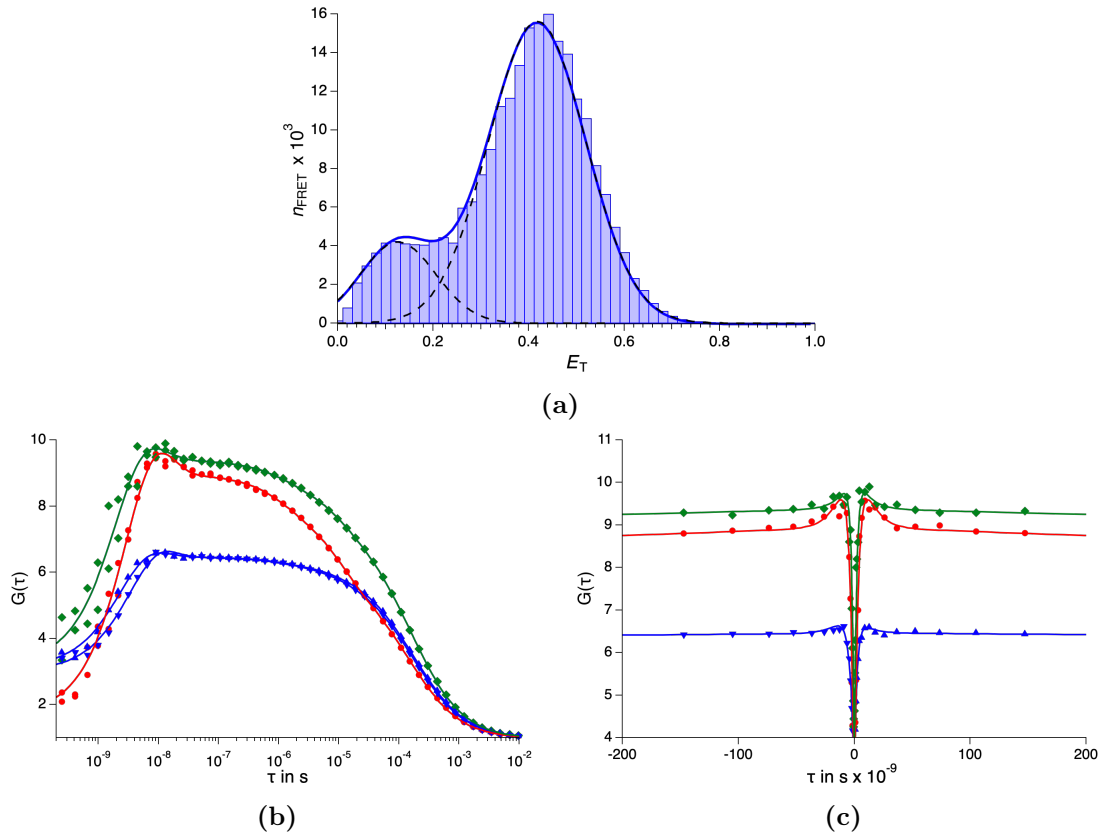


Fig. 5.4: Results of a nsFRET-FCS experiment of the DNA hairpin. (a) FRET efficiency histogram including a Gaussian fit (solid line). (b,c) Donor-donor (green), acceptor-acceptor (red), acceptor-donor (blue upward triangles) and donor-acceptor (blue downward triangles) correlation functions with global fits (solid lines) according to Eq. 3.13. Positive and negative lag times indicate forward and backward correlation functions, respectively.

be due to switching of the acceptor dye between the *cis* and *trans* isomeric form or a combination of both processes.

The third exponential has a relaxation time of $\tau = (10 \pm 5)$ ns and leads to a correlated signal in both, the auto- and cross-correlation functions. Conformational dynamics leading to changes in the donor-acceptor distance and thus in the FRET efficiency can therefore be excluded as its origin. As with the DNA hybrids, movements of the fluorophores attached to a linker remain as an explanation. The movements may cause the dye to come into contact with the DNA where processes like photo induced electron transfer lead to interactions and blinking at this short time scale due to base induced quenching of the fluorophore.

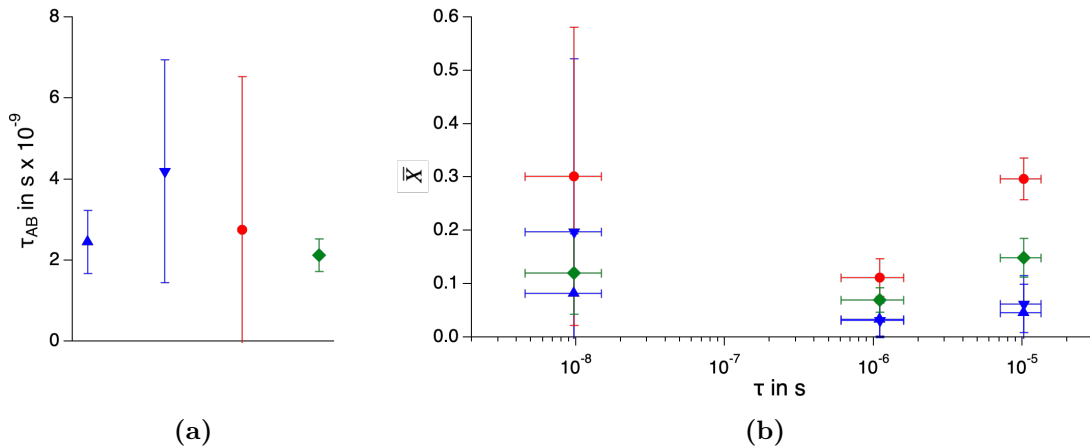


Fig. 5.5: Results of a nsFRET-FCS experiment of the DNA hairpin (hpDNA). (a) shows the antibunching time constants τ_{AB} and (b) the amplitudes \bar{X} of involved processes leading to fluctuations at times τ . Fit parameters of the donor-donor, acceptor-acceptor auto-correlation functions are shown in green and red, parameters of the acceptor-donor and donor-acceptor cross-correlation functions are shown as blue upward and downward triangles, respectively.

5.1.3 Cold shock protein CspA

The cold shock protein CspA is a simple two state folder and suitable as a model protein for protein unfolding FRET experiments. CspA has already been investigated by single molecule FRET experiments using pressure as well as chemical denaturant unfolding [4, 5]. However, these experiments were focussed on the comparison between different folding mechanisms and transitions between the folded and unfolded state and not on dynamics. Therefore, nsFRET-FCS experiments of CspA were performed to check for dynamics of the unfolded protein chain and further investigate and evaluate the experimental setup. A first measurement of 10 minutes was done without denaturant to evaluate the condition of the sample. The excitation was set to a power of $40 \mu\text{W}$ at a wavelength of 488 nm. The FRET efficiency histogram as well as correlation functions are shown in Fig. 5.6. The histogram reveals two peaks. The high efficiency peak with an efficiency of $E_T = 0.905 \pm 0.003$ can be assigned to the folded population of the protein, whereas the low efficiency peak with $E_T = 0.039 \pm 0.005$ is due to donor only molecules. The rather large donor only population is also reflected in the correlation functions. The donor auto-correlation

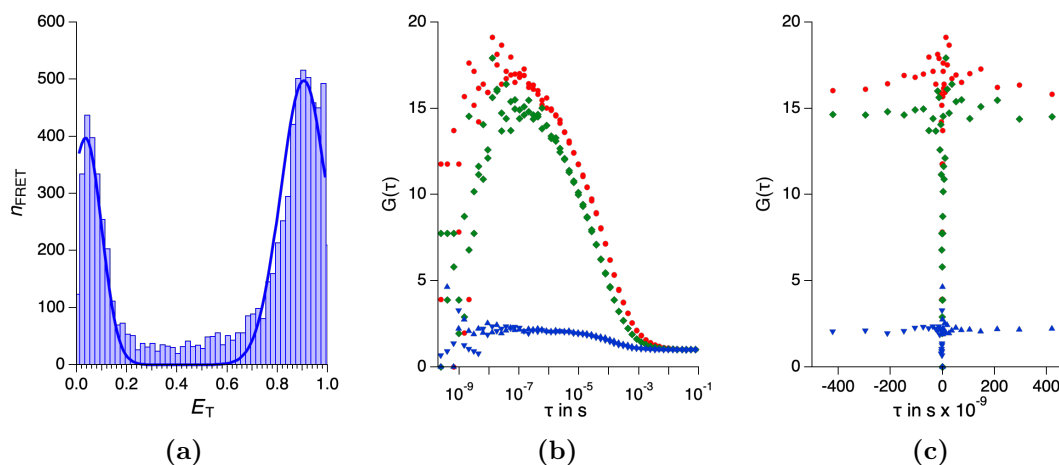


Fig. 5.6: Results of a nsFRET-FCS experiment of the cold shock protein CspA. (a) shows the FRET efficiency histogram including a Gaussian fit (solid line). (b,c) show the donor-donor (green), acceptor-acceptor (red), acceptor-donor (blue upward triangles) and donor-acceptor (blue downward triangles) correlation functions.

presumably originates purely from the donor only fraction, and the donor-acceptor cross-correlation functions from spectral cross talk into the acceptor channel. The cold shock protein CspA is a β -barrel protein with high stability. Due to the β -barrel structure and the labeling positions of the dyes (see Fig. 3.24) no changes of the donor-acceptor distance and thus no dynamics are expected for the native state of the protein. However, even if dynamics would be present it would barely be visible in the correlation functions. Due to the short distance between the donor and the acceptor in the folded state, reflected in a FRET efficiency close to unity, subtle distance changes, if present, would not lead to a significant change in the transfer rate (see Fig. 2.18) and thus not to fluctuations in the emission rates of both dyes that were strong enough to become visible in the correlation functions. A different dye pair with a Förster radius similar to the mean donor-acceptor distance would allow for detecting distance changes in the folded protein.

However, in order to investigate if there are any indications of protein dynamics in the unfolded state of CspA, a second measurement was performed with an addition of ≈ 4.5 M guanidinium chloride (GdmCl) to the buffer. Due to the high donor only population, the measurement duration was chosen with 30 hours in order to have enough events with time differences in the low time regime for the analysis. The laser excitation power and wavelength were $40 \mu\text{W}$ and 488 nm , respectively. The FRET efficiency histogram is shown in Fig. 5.7 and reveals an increased number of FRET events in the efficiency range between the donor only and folded CspA population in comparison to the experiment without the denaturant. This is due to an unfolded population of CspA caused by GdmCl.

Despite the 4.5 M denaturant concentration in the buffer, the protein is not completely unfolded and still contains a large fraction of folded CspA. Therefore, the ar-

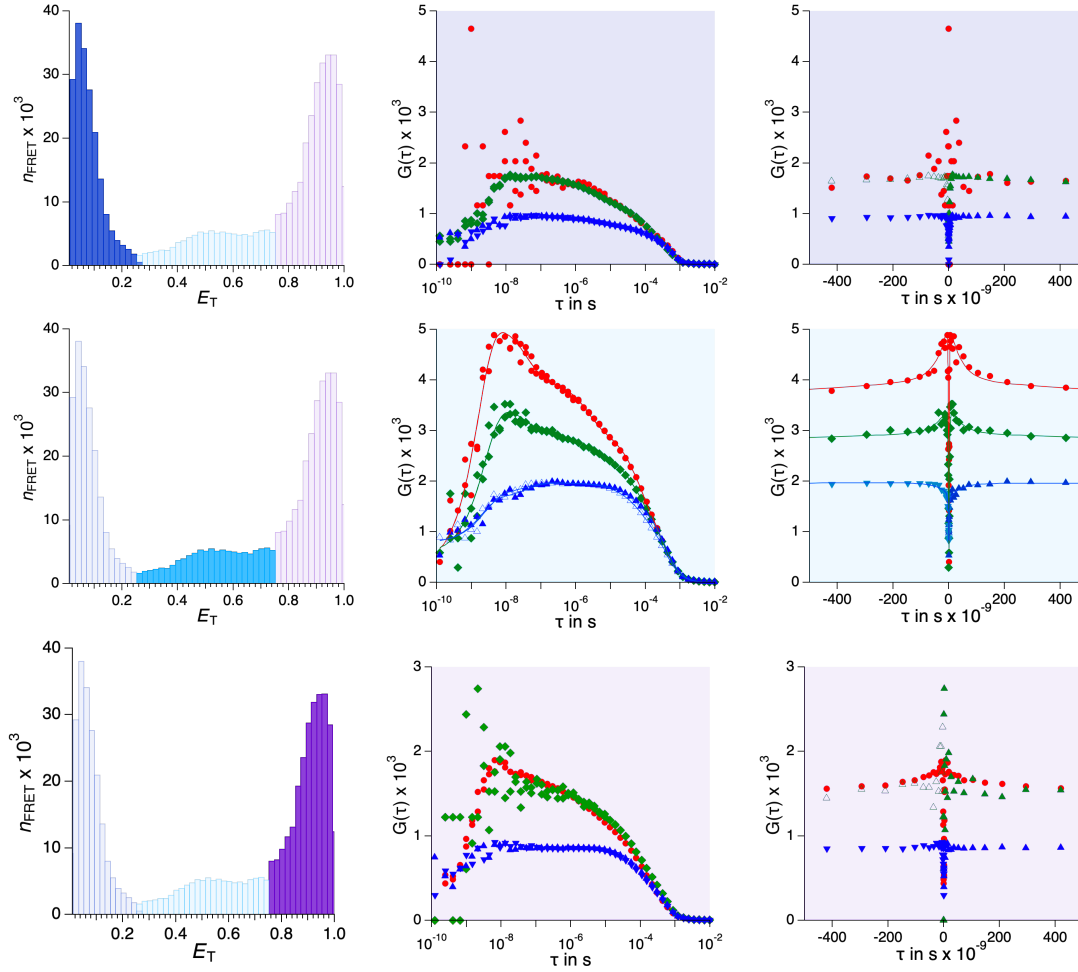


Fig. 5.7: (left column) FRET efficiency histograms and (middle, right columns) correlation functions of a measurement of CspA in MOPS buffer containing 4.5 M GdmCl. Different rows correspond to a filtered correlation analysis of the low (blue), middle (cyan) and high (purple) FRET population, respectively. Coloring of the correlations functions: donor-donor (green), acceptor-acceptor (red), acceptor-donor (blue upward triangle), donor-acceptor (blue downward triangle). Solid lines in the middle row represent global fits according to Eq. 3.13.

rival times of photons with respect to the corresponding populations were correlated and analyzed individually, similar to the work of Nettels et al. with the cold shock protein CspTM [79]. The donor only population contains photon times of all events with $E_T < 0.25$, the folded population events with $E_T > 0.75$ and the unfolded population in the range in between, with $0.25 \leq E_T \leq 0.75$, indicated by different colors in the histograms. For donor only molecules, the acceptor's auto-correlation function is highly noisy as expected. The lower noise in the cross-correlation functions is a result of the spectral crosstalk of the donor into the acceptor channel. The same holds for the donor channel and the folded population since the donor is heavily quenched due to the high efficiency of FRET. The correlation functions

of the unfolded population, however, show the usual characteristics of protein dynamics. The donor-acceptor cross-correlation functions are anti-correlated and the auto-correlation functions of the acceptor and donor channel are correlated at an identical time scale in a range below 100 ns. The global fit gives a time constant of $\tau_{\text{CD}} = (42 \pm 9)$ ns for the reconfiguration time of the chain of the unfolded cold shock protein CspA.

Soranno et al. studied CspTM with nsFRET-FCS [8]. CspTM was labeled with the same dye pair, but with a larger distance of the dyes along the chain. Its sequence contains 68 amino acids instead of 70 for the cold shock protein CspA. However, the general structure of both proteins is very similar and comparable. Soranno et al. made different experiments that included the investigation of the dependence of the reconfiguration time on the segment length being probed. Generally, the reconfiguration time is increasing with increasing segment length. For dye distances of 57 and 66 amino acids corresponding to CspA and CspTM, respectively, the increase in τ_{CD} is not expected to be significant. Soranno et al. found reconfiguration times of $\tau_{\text{CD}} \approx 45$ ns - 50 ns with CspTM at 4 M and 5 M GdmCl. Even though slightly different proteins were examined with deviating dye distances, the outcome of the experiments is in good agreement with each other. Considering the similar structure of CspTM and CspA and the little impact of the different segment lengths probed, the reconfiguration times $\tau_{\text{CD}} \approx (45 - 50)$ ns of CspTM agree well with $\tau_{\text{CD}} = (42 \pm 9)$ ns obtained here for CspA at a GdmCl concentration of 4.5 M.

On the one hand these results show the capability and accuracy of the experimental setup in the detection of chain dynamics in the nanosecond time regime of unfolded proteins. Furthermore, the results show the great potential and strength of filtered nsFRET-FCS analysis since it enables different populations or protein conformations and their characteristics to be analyzed individually. If FRET populations are well separated from donor only molecules, no sophisticated excitation schemes like pulsed overlaid excitation (POE) or alternate laser excitation (ALEX) are needed.

5.1.4 Prothymosin alpha

The intrinsically disordered protein (IDP) prothymosin alpha (ProT α) was chosen as a sample in order to further evaluate the functionality of the experimental setup and the implemented GPX-TDC. Multiple experiments were made to validate the capability of the experimental setup in measuring and detecting chain dynamics within the nanosecond time range. ProT α is suited for this task since it has been previously investigated and revealed relaxation times in the sub-100 ns time domain. First, a measurement of ProT α was made with a borosilicate coverslip at ambient pressure. The measurement had a duration of 33 hours with an excitation power of 40 μ W at a wavelength of 488 nm. The correlation functions are shown in Fig. 5.8. The auto- and cross-correlation functions of the donor and acceptor channel exhibit the expected and characteristic correlated and anti-correlated behavior in the sub-100 ns time range expected for chain dynamics associated with frequent changes of the donor-acceptor distance. The FRET efficiency histogram is shown as well. It was calculated with a sum threshold for the number of photons in the donor and acceptor bins of $T_{\text{sum}}^{\text{DA}} = 40$ cts/bin. However, the FRET efficiency histogram reveals two populations with efficiencies of $E_T = 0.248 \pm 0.007$ for the low and $E_T = 0.501 \pm 0.002$ for the high FRET population, respectively. Since in [6, 272, 297], no second population has been reported besides a population of proteins lacking an acceptor dye (donor only), the origin of this peak was further evaluated. First a filtered correlation analysis were performed, where the arrival times for a smaller or larger cut off efficiency of 0.3 were correlated separately (see Fig. 5.9). Correlations of the high FRET population show the characteristic correlated and anticorrelated behavior for the auto- and cross-correlation functions, respectively. In contrast, the low FRET

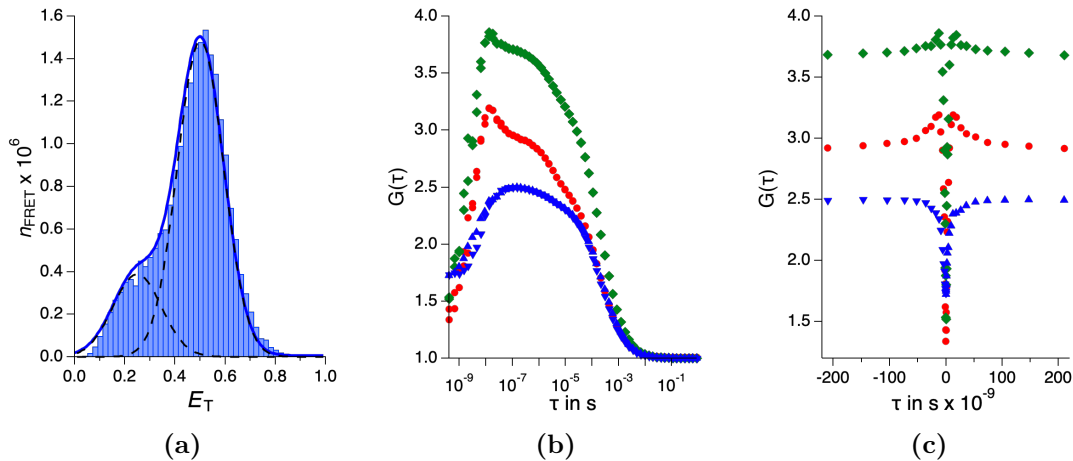


Fig. 5.8: nsFRET-FCS results of a 33 hour experiment of ProT α . (a) shows the FRET efficiency distribution revealing two populations. (b,c) show the results of the donor-donor (green), acceptor-acceptor (red), acceptor-donor (blue upward triangles) and donor-acceptor (blue downward triangles) correlation functions. (c) Positive and negative lag times correspond to forward and backward correlations, respectively.

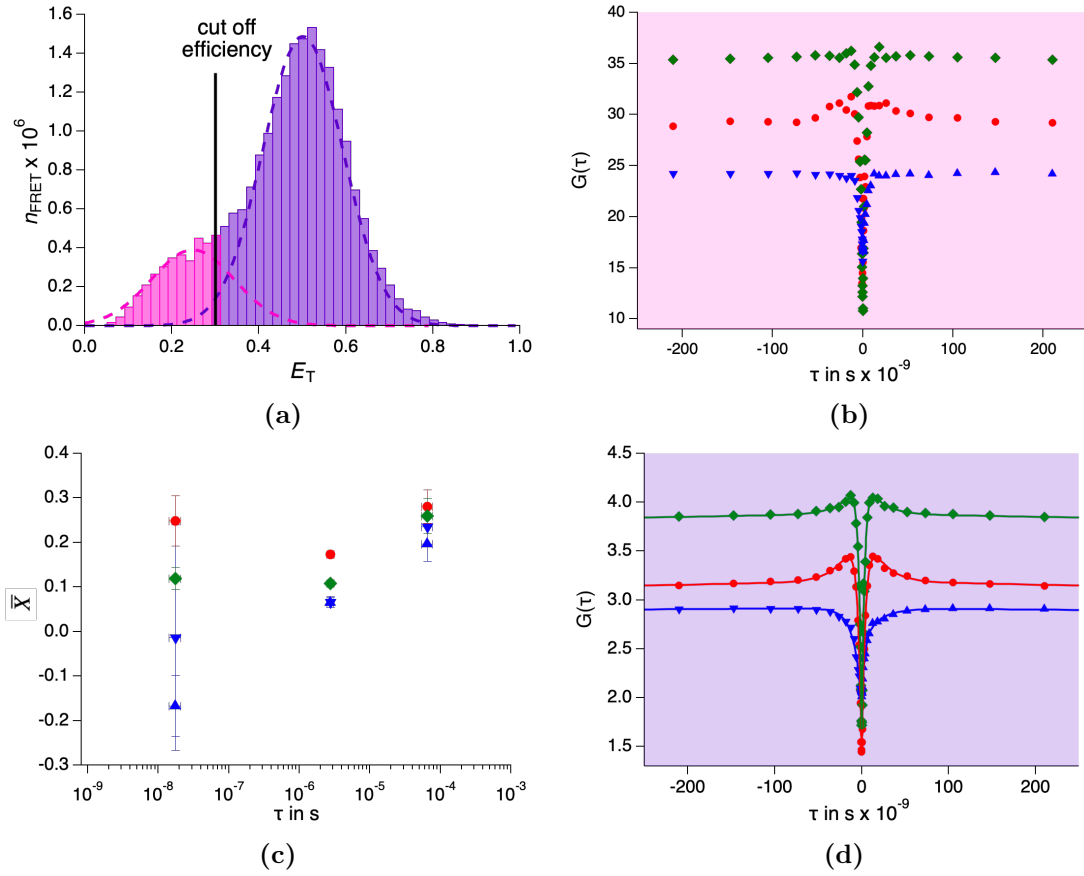


Fig. 5.9: (a) shows the FRET efficiency histogram of ProT α with a cut off efficiency of $E_T = 0.3$ for separated correlation analysis of populations. (b,d) show the filtered nsFRET-FCS correlation functions of the low and high FRET population. Donor-donor, acceptor-acceptor and acceptor-donor correlation functions are shown in green, red and blue, where positive and negative lag times correspond to forward and backward correlations, respectively. (d) Solid lines are global fits according to Eq. 3.13 including three exponentials, shown in (c) with their respective fractions \bar{X} and relaxation times τ .

population shows almost no characteristics for dynamics on a nanosecond time scale. Only the auto-correlation of the acceptor on the other hand shows a similar shape of the correlation function like for the high FRET population. This is most likely due to components of the high FRET population analyzed within the low FRET regime due to overlapping peaks. Additionally, the experiment was divided into 3 hour intervals, which were analyzed individually. The FRET efficiency decreases with increasing measurement duration for both peaks (see Fig. 5.10). Furthermore, the relative fraction of the lower FRET population increases continuously with advancing measurement duration. The diffusion times of the acceptor and donor-acceptor correlation functions are decreasing as well, whereas the donor and acceptor-donor correlation functions show no significant change over time.

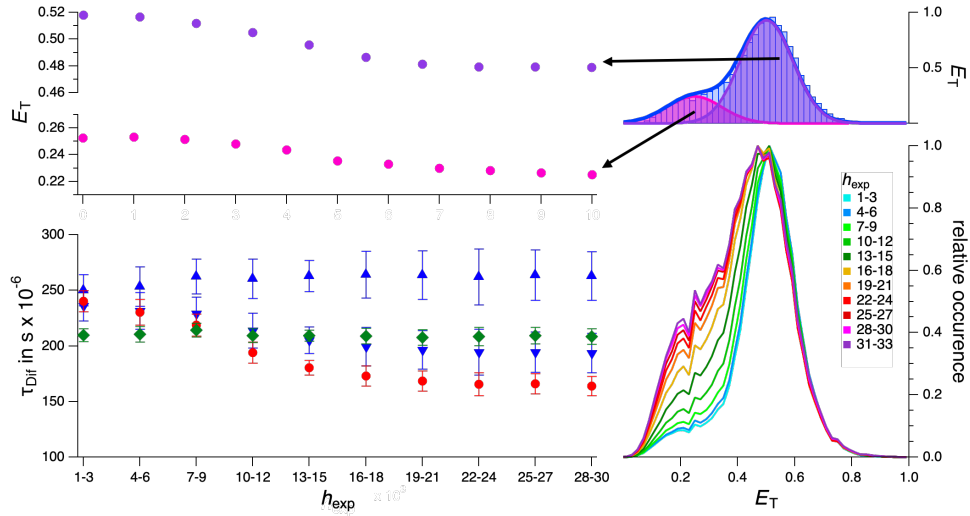


Fig. 5.10: Interval analysis of a 33 hour ProT α experiment realized by splitting the measurement in consecutive intervals with a length of 3 hours each. (Top) FRET efficiencies of both, the low and high FRET population. (Bottom right) Histograms normalized by the average number of molecules for different hours of the experiment h_{exp} . (Bottom left) Progression of the diffusion times τ_{Dif} with increasing measurement duration.

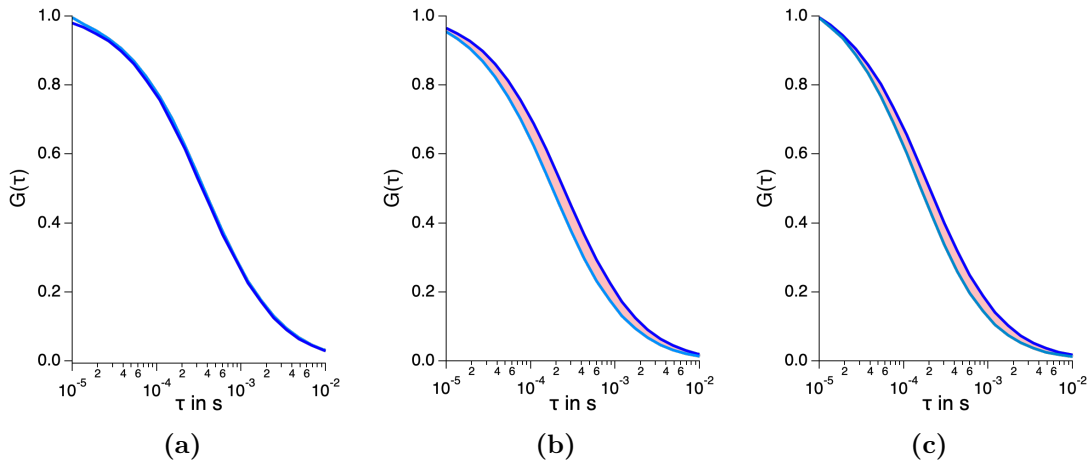


Fig. 5.11: Comparison of acceptor-donor cross-correlation functions (a) of the first three and (b) last three hours of a 33 hour measurement of ProT α . Forward- and backward correlation functions are shown in cyan and blue, respectively. In the last three hours, a shift between both correlation curves is visible indicating acceptor bleaching during the transit through the focal volume. (c) shows the correlation functions of the first hour of a 33 hour experiment without BME in the buffer, where the shift is visible from the start of the measurement. All correlation functions are normalized by the respective average number of molecules.

A reduced acceptor diffusion time indicates a bleaching of the acceptor fluorophore during the transit through the focal volume. Another indicator of acceptor photobleaching is the different diffusion time of the forward and backward correlations of the acceptor and donor channel [298, 299], that is directly visible as a shift between both correlation functions in the time range of diffusion (see Fig. 5.11). The remaining fit parameters of the 3 hour interval analysis, which are not discussed here, can be found in the appendix in subsection A.4.1.

Binned photon counts of both, the acceptor and donor channel indicate the same effect. The acceptor signal starts to decrease after a time of approximately 6-7 hours (see Fig. 5.12a). Nevertheless, the effect of photobleaching due to a high laser excitation power alone does not explain why there is no change in the diffusion time of the acceptor, acceptor-donor cross-correlation functions, FRET efficiency or number of detected acceptor photons in the first hours of the experiment. Furthermore, it does not explain the growing relative fraction of the low FRET population over time.

In order to investigate the effect of BME in the buffer, a measurement without its addition was made as well. All remaining experimental parameters were equal. The FRET efficiency histogram is shown in Fig. 5.12b. This measurement shows a large donor only population with $E_T < 0.1$, alongside a smaller FRET population with a higher efficiency. Both populations are not clearly separated, which again can be explained with acceptor bleaching during the diffusion through the focal volume, resulting in intermediate FRET efficiency values. Forward and backward cross-correlation functions of the acceptor and donor channel show a shift in the time range of diffusion. In contrast to the experiment performed with BME, the shift is visible even from the beginning of the experiment. This is shown in Fig. 5.11c with the correlation functions of the first hour already showing the difference in the diffusion times. These results illustrate the effectiveness of the BME serving as

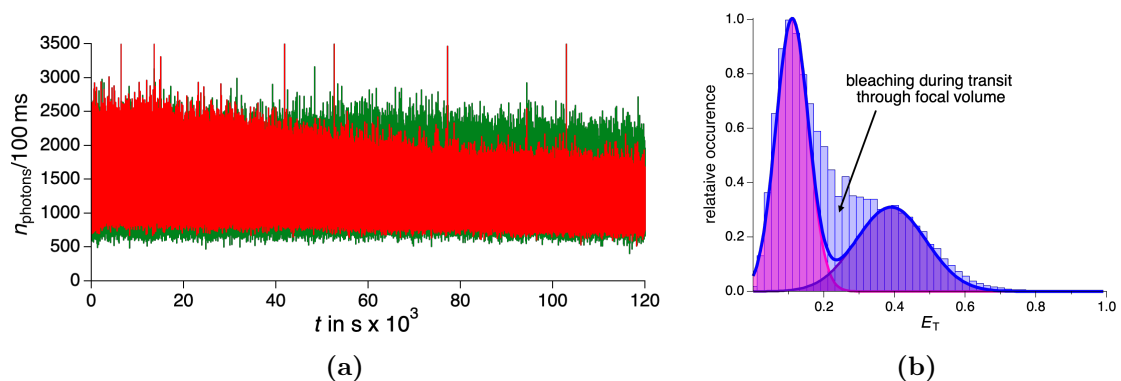


Fig. 5.12: (a) Time traces of the donor and acceptor channels of a 33 hour measurement of ProT α with a BME containing buffer. (b) FRET efficiency histogram of a 33 hour experiment, but without BME in the buffer showing a large donor only (pink) and smaller FRET population (purple). Events between both peaks indicate photobleaching of the acceptor dye while it is in the focus.

a protector for photobleaching [187, 300, 301]. However, BME hydrolyzes in water resulting in the formation of hydrogen sulfide (SH) and a decreasing concentration over time, with the protection effect decreasing as well.

Taking all results into account, the low FRET population of ProT α (Fig. 5.8) is explained with a donor only population. The relative fraction of this population grows over time since the BME, which serves as a bleaching protection agent [300], vanishes due to hydrolysis and the formation of SH. As a consequence of the acceptor bleaching, FRET efficiencies shift slightly towards lower values and the apparent diffusion time of the acceptor decreases. The assumption of a donor only population is supported by the fact that the absence of a donor only component would be uncommon for such labeled protein samples. Furthermore, it can be identified in the experiment without BME as well and is also reported in other publications [6, 195, 297]. The reason for the donor only population having a comparatively high efficiency is attributed to a missing histogram correction and its calculation solely due to a sum threshold of the time bins of the acceptor and donor dye.

For further evaluation of the measurement the correlation functions were analyzed as well. In order to achieve a satisfying fit result a global fit was used according to Eq. 3.13 including three exponentials. The fit results are shown in Fig. 5.9c. The slowest process has a relaxation time of $\tau = (65 \pm 11) \mu\text{s}$. Like for the DNA hairpin and DNA hybrids it is assigned to the diffusion process and a non ideal model for the diffusion correlation function. The second exponential with a relaxation time of $\tau = (2.7 \pm 0.3) \mu\text{s}$ is due to transitions to the triplet state and is at the expected time scale for the fluorophores [133]. The last exponential has a relaxation time of $\tau = (19 \pm 3) \text{ns}$ and is in the time range of $\approx 10 \text{ns} - 200 \text{ns}$ that is characteristic for chain movements of IDPs and segment lengths of approximately 30-200 amino acids [8, 74, 79, 152]. Furthermore, the correlation functions show the expected correlated signal in the auto-correlation functions and anti-correlated signal in the cross-correlation functions of the donor and acceptor channel at this lag time τ (see Fig. 5.9d). Therefore, this exponential is attributed to movements of the chain of ProT α .

However, the wild type protein is highly negatively charged with a net charge of $z = -44$ and the segment length probed of $z_{56-110} = -27$. As a consequence the expansion of the chain as well as its reconfiguration times are highly dependent on the conditions of the buffer like the pH or ionic strength [170, 198, 201, 302–304]. This is reflected in a spectrum of determined reconfiguration times. In two studies with varying buffers, but for the same segment probed and the same donor-acceptor dye pair, reconfiguration times of $\tau_{\text{CD}} = (45 \pm 9) \text{ns}$ and $\tau_{\text{CD}} = (29 \pm 2) \text{ns}$ were observed [6, 8].

Galvanetto et al. found a shorter reconfiguration time of $\tau_{\text{CD}} = (14 \pm 2) \text{ns}$ for the same segment but different dyes and buffer [195]. However, in principle the use of different dyes are not expected to cause any deviations in the chain reconfiguration times in FCS analysis as long as their fluorescence emission is not affected by the buffer and salt concentration. For the same conditions but a different segment (N-

terminal segment) with a net charge of $z = -15$ the determined relaxation time was $\tau_{\text{CD}} = (21 \pm 2)$ ns. The probed segment has a comparable length and ProT α is known to be entirely unstructured [170, 201], which excludes potential structure differences between both segments. Again, this demonstrates the strong influence and effect of charge interactions on the behavior of the chain of an IDP. König et al. found a comparable relaxation time of $\tau_{\text{CD}} = (24 \pm 4)$ ns for the N-terminal segment. Considering the proven dependency of the chain reconfiguration times of IDPs on buffer conditions and salt concentration the observed reconfiguration time of $\tau_{\text{CD}} = (19 \pm 2)$ ns agrees well with these previous findings.

In addition to the analysis of 3 hour intervals, different durations of the experiment were mimicked by not analyzing the whole photon data, but the first 3 hours, 6 hours, 9 hours and so on. The outcome indicates that durations of up to 33 hours are not necessarily required to investigate chain dynamics in the nanosecond time regime. A shorter duration can already be sufficient for a nsFCS analysis. This is shown in the appendix in subsection A.4.2, with the determined reconfiguration time of the chain not significantly altering with further increasing measurement time. This is even the case after the first interval of three hours, proving the high performance of the experimental setup with respect to the detection of fluorescence fluctuations in this time regime.

Increased solvent viscosity

ProT α was also examined with an increased solvent viscosity η_{buf} , which is expected to cause a larger chain reconfiguration time due to an associated increase in solvent friction [8, 78, 305, 306]. The increase in viscosity was achieved by the addition of glycerol to the buffer. The viscosity was calculated according to [307, 308] and was $\eta_{\text{buf}} \approx 2.4$ mPa·s. The measurement duration was 16 hours, about half the time of the experiment without glycerol and a viscosity of $\eta_{\text{buf}} \approx 1$ mPa·s since these measurements indicate that this duration should be sufficient to detect and evaluate chain reconfiguration times of ProT α . The efficiency histogram reveals two populations assigned to FRET with $E_{\text{T}} = 0.739 \pm 0.002$ and to a donor only population of the protein with $E_{\text{T}} = 0.171 \pm 0.018$ (see Fig. 5.13a). Like in the experiment without glycerol in the buffer, FRET events in between both peaks indicate bleaching of the acceptor dye during the diffusion through the focus. This again is supported by a difference of the forward and backward correlations of the donor and acceptor channel, which is more prominent than without glycerol and reaches into shorter lag times (see Fig. 5.13b and Fig. 5.13c). This suggests a slower diffusion of the proteins and thus more efficient bleaching of the attached fluorophore. The correlation functions of the measurement are shown in Fig. 5.14 with fitted model functions according to the experiment without glycerol. The time constant of fluorescence antibunching and the fractions and relaxation times of other processes involved are

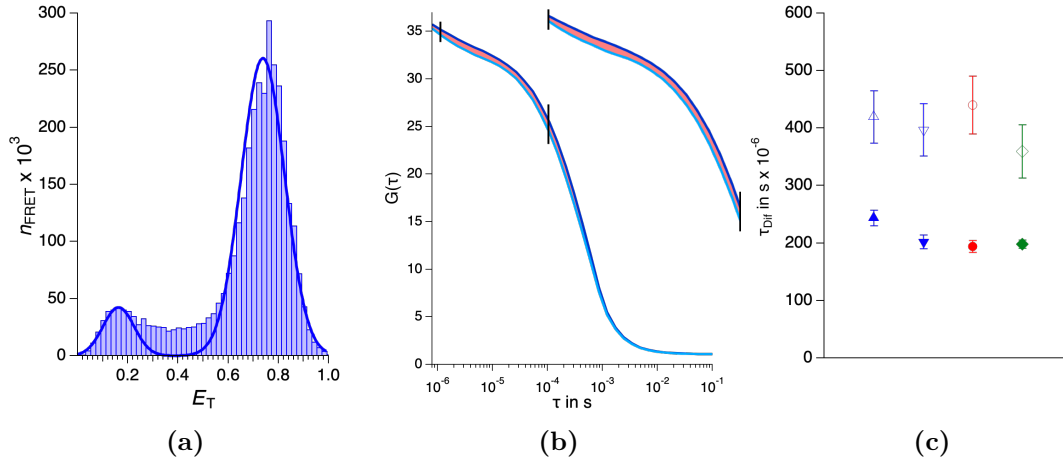


Fig. 5.13: (a) FRET efficiency histogram of a ProT α measurement with an increased buffer viscosity of $\eta_{\text{buf}} \approx 2.4$ mPa.s. (b) illustrates the shift between the donor-acceptor forward (cyan) and backward (blue) correlation functions due to acceptor bleaching during the transit through the focal volume. (c) shows the diffusion times from the auto-correlation functions of the donor (green) and acceptor (red) as well as the forward and backward cross-correlation functions of both channels without (closed symbols) and with glycerol (open symbols) in the buffer.

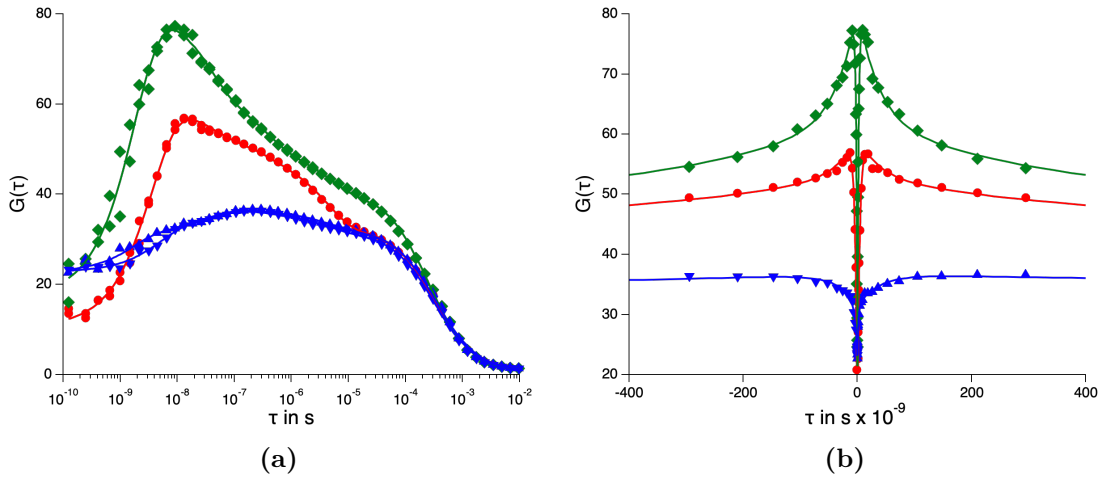


Fig. 5.14: (a, b) Donor-donor (green), acceptor-acceptor (red), acceptor-donor (blue upward triangles) and donor-acceptor (blue downward triangles) correlation functions of a 16 hour ProT α measurement with an increased viscosity of the buffer of $\eta_{\text{buf}} \approx 2.4$ mPa.s. (b) Positive and negative lag times correspond to forward and backward correlations, respectively. Solid lines represent global fits according to Eq. 3.13.

displayed in Fig. 5.15. The time constant of fluorescence antibunching shows a general decrease with a higher viscosity. The diffusion times confirm a slower diffusion due to the increased viscosity of the buffer (see Fig. 5.13c). The approximately doubled viscosity leads to a corresponding linear increase in the apparent diffusion time

by a factor of approximately two. The slowest process described by the three exponentials in the fit function has a relaxation time of $\tau = (151 \pm 36) \mu\text{s}$. Like for the experiment without glycerol, it is assigned to the diffusion process, already discussed in subsection 5.1.1. The hypothesis that this component is due to the diffusion process is supported by the fact that the relaxation time is, like the apparent diffusion time, increased compared to a viscosity of $\eta_{\text{buf}} \approx 1 \text{ mPa}\cdot\text{s}$. The second exponential has a relaxation time of $\tau = (2.7 \pm 0.3) \mu\text{s}$. It shows no change due to the addition of glycerol and is due to transitions to the triplet state. This is in contrast to the work of Pavlita [281], where an increase of the triplet fraction and relaxation time could be observed, but for free diffusing dyes and not a FRET pair attached to a protein.

The third exponential is due to the movement of the polypeptide chain and has a relaxation time of $\tau_{\text{CD}} = (72 \pm 5) \text{ ns}$. It is nearly four times larger than without glycerol in the buffer $\tau_{\text{CD}} = (19 \pm 3) \text{ ns}$. This principle increase of the chain reconfiguration time with increasing viscosity of the solvent is in good agreement with previous findings [7, 8, 195]. However, the reconfiguration time of the chain is nearly four times larger than without glycerol and is therefore unlikely solely due to an effect of the higher viscosity. A possible reason could be a reduction of repulsive interactions due to the high glycerol concentration, which eventually lead to a compaction of the chain and more (internal) friction as well. The compaction could explain the increased FRET efficiency as well.

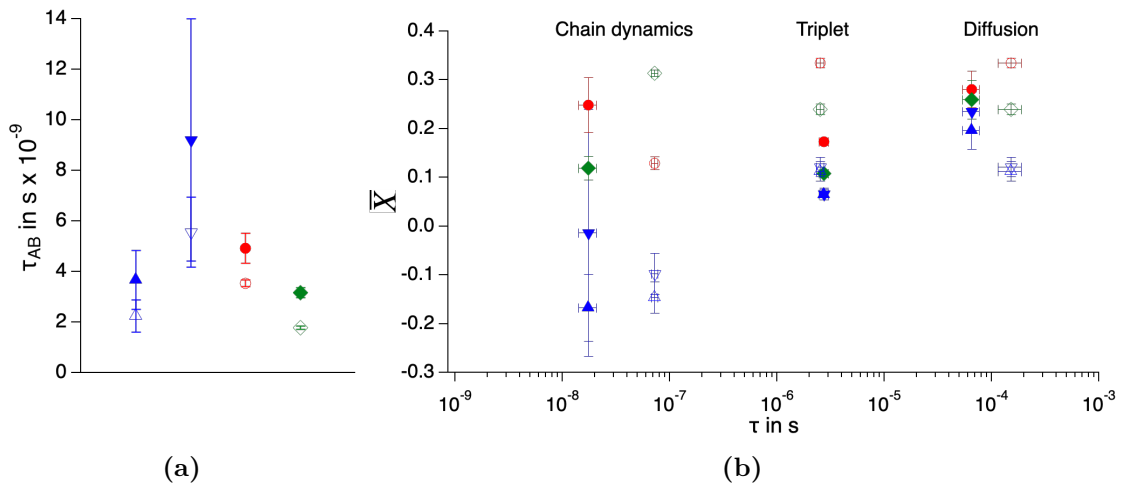


Fig. 5.15: Fit results of nsFRET-FCS measurements of ProT α in TRIS buffer without (closed symbols) and with glycerol (open symbols). (a) shows the fluorescence antibunching time constants τ_{AB} and (b) the fractions \overline{X} and time constants τ of other processes involved. Results of the auto-correlation functions of the donor and acceptor are shown in green and red, respectively. Results of the forward (upward triangles) and backward (downward triangles) acceptor-donor correlation functions are shown in blue.

5.2 High-pressure experiments

5.2.1 3-stranded DNA hybrid

The 3-stranded DNA hybrid was used as a negative control in high pressure experiments. Due to their high stability, the DNA sample should be comparatively insensitive to high hydrostatic pressures. Therefore, it is suitable to verify, that the applied high pressures have no significant influence on the measurements results, e.g. refractive index changes or bending of the capillary, which both could result in FRET efficiency changes that could be misinterpreted. Experiments were made with the optical multi layer (OML) at ambient pressure as well as with pressures of 500 bar, 1000 bar and 1500 bar, respectively. The sample concentration was 1 nM. Each experiment had a duration of 900 s. The same capillary was used for all experiments to ensure the same experimental conditions for each measurement and a better comparability. After each measurement, the pressure was increased and the position of the capillary and focus were checked by a cross-section image of the sample volume. FRET efficiency histograms were calculated with a sum threshold of $T_{\text{sum}}^{\text{DA}} = 40$ cts/ms and normalized to their respective maximum value. They

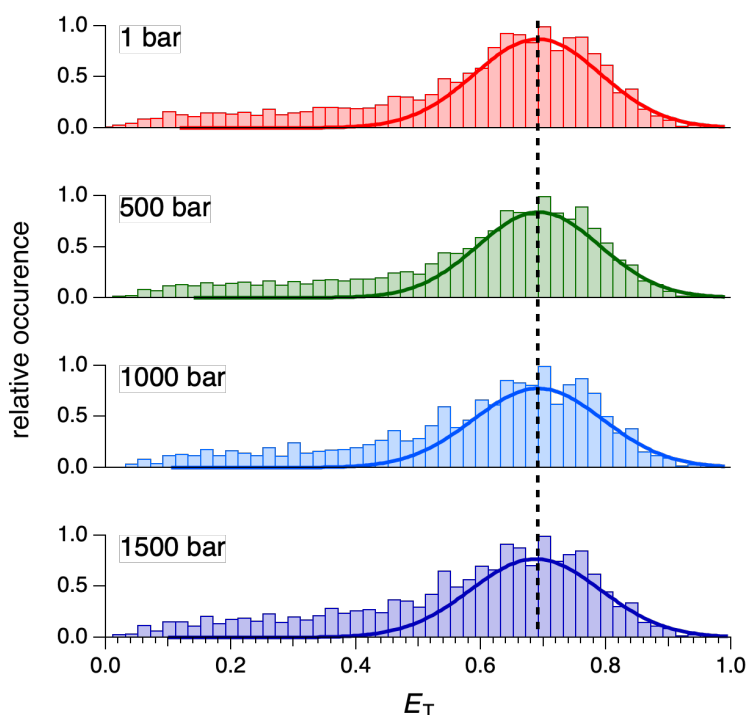


Fig. 5.16: FRET efficiency histograms of the 3-stranded DNA hybrid. Experiments were made with the optical multi layer (OML) at ambient pressure (red) and hydrostatic pressures of 500 bar (green), 1000 bar (blue) and 1500 bar (purple). Solid lines are Gaussian fits for the determination of the mean transfer efficiency.

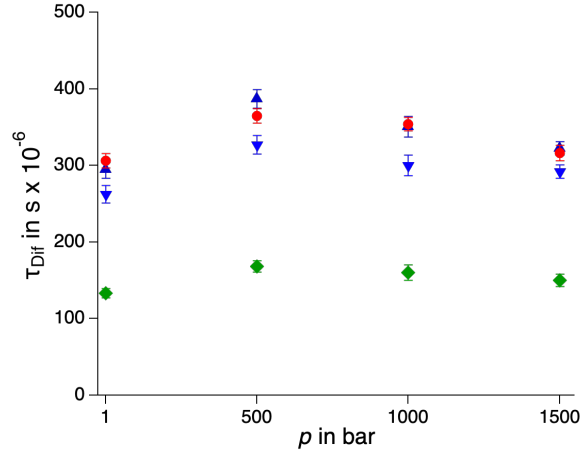


Fig. 5.17: Diffusion times τ_{Dif} of the 3-stranded DNA hybrid at different pressures p . Diffusion times of the auto-correlation functions of the donor and acceptor are shown in green and red, respectively. Forward (upward triangles) and backward (downward triangles) acceptor-donor correlation functions are shown in blue. Error bars represent \pm one standard deviation of the fit.

are shown in Fig. 5.16 with efficiencies ranging between $E_T = 0.667 \pm 0.007$ for 1500 bar and $E_T = 0.678 \pm 0.004$ for 500 bar. In addition, Fig. 5.17 shows the apparent diffusion times. Both, the FRET efficiencies as well as diffusion times indicate no significant pressure dependency. In accordance with this, it does not suggest that increasing pressure has a significant influence on the focal volume or molecule detection function of the experimental setup.

10 hour measurement In order to gain improved statistics even in the shorter time regimes and to make a first nsFRET-FCS experiment under high pressure, a 10 hour long measurement of the 3-stranded DNA hybrid was made at a pressure of 1000 bar. The FRET efficiency histogram as well as correlations for photon times belonging to efficiencies of 0.4 and larger are shown in Fig. 5.18. Like for the short measurements, the histogram reveal a donor only and a FRET population with an efficiency of $E_T = 0.676 \pm 0.004$, which is in good agreement with the other experiments. In contrast to measurements with a coverslip, the relative fraction of the donor only population as well as events in between both efficiency peaks are increased due to more background signal and a lower signal-to-noise ratio. Despite that, the correlations show a comparable shape including a visible antibunching component in each correlation including the typical difference in the antibunching time constant between the acceptor-donor forward and backward correlation (compare Fig. 5.2). The diffusion time is slightly increased compared to the measurement with the coverslip with a value of approximately $250 \mu\text{s}$, which is due to the discussed optical aberrations when using the capillary. The triplet state lifetime of $\tau_T = (1.14 \pm 0.08) \mu\text{s}$ is slightly larger than for the measurement with the

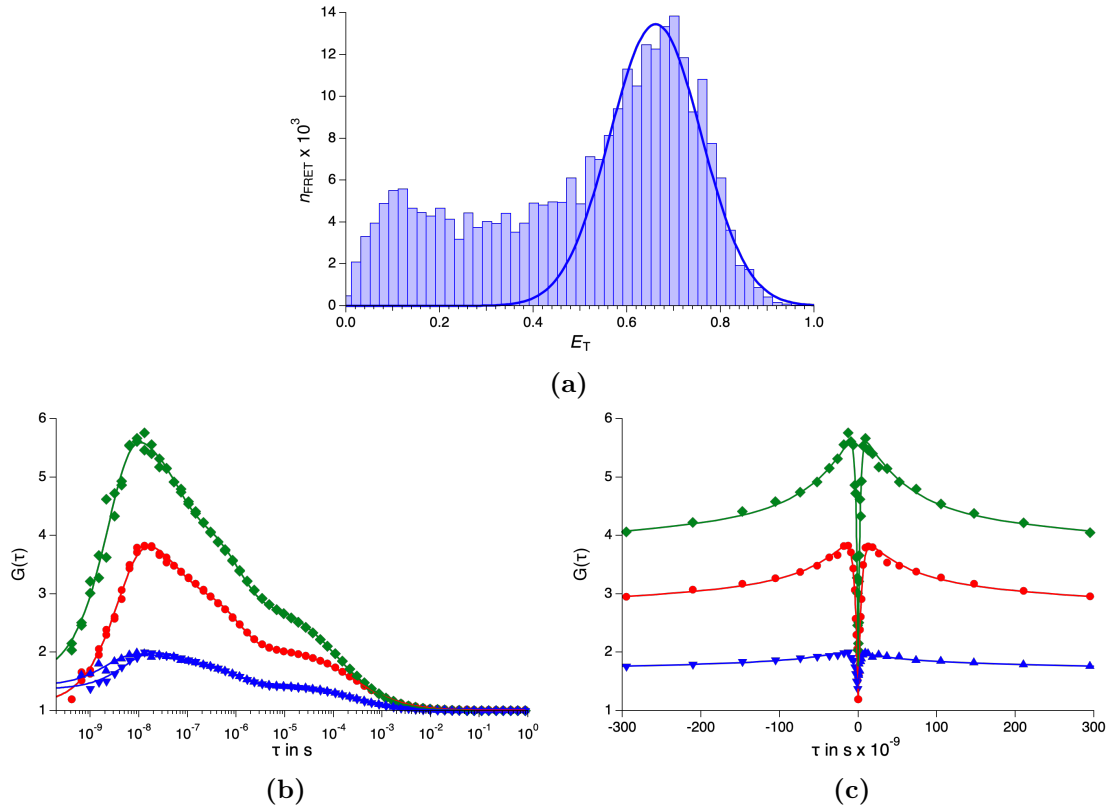


Fig. 5.18: Results of a 10 hour 1000 bar experiment of the 3-stranded DNA hairpin. (a) shows the FRET efficiency distribution with a Gaussian fit (solid line) for determining the mean fret efficiency. (b) and (c) show the donor-donor (green), acceptor-acceptor (red), acceptor-donor (blue upward triangles) and donor-acceptor (blue downward triangles) correlation functions. (c) Positive and negative lag times correspond to forward and backward correlation functions, respectively. Solid lines represent global fits according to Eq. 3.13.

coverslip, which is most likely a result of the same effect as well, a less efficient excitation due to the refractive index mismatch of fused silica and thus enlarged focal volume (see Fig. 5.19). The fastest component, assigned to movements of the dyes at the end of the linker, are in a comparable range and have no significant difference within the range of the fit error. Furthermore, the small difference could also be due to the lower SNR and statistics within the capillary.

Like expected, the DNA hybrid shows no significant changes when a pressure of 1000 bar is applied, making it a suitable reference sample for high pressure spectroscopic experiments. Furthermore, a first nsFRET-FCS measurement at high hydrostatic pressure could be achieved, showing the capability of the experimental setup for this kind of experiments. Even though the SNR is worse than with a coverslip, fluorescence antibunching can clearly be identified in all auto-correlations and cross-correlations. However, for the correlation functions of the experiment within

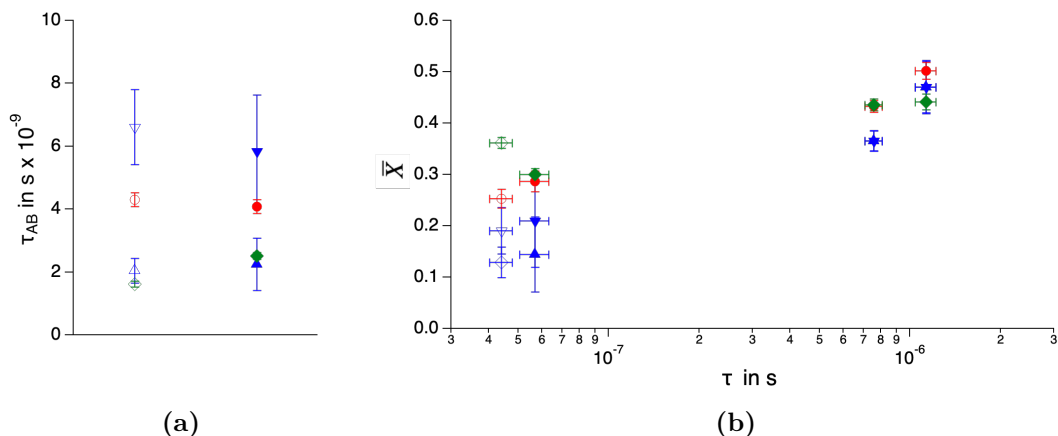


Fig. 5.19: Fit results of nsFRET-FCS measurements of the 3-stranded DNA hybrid. Experiments were made with a coverslip at ambient pressure (open symbols) and with a capillary at a pressure of 1000 bar (closed symbols). (a) shows the fluorescence antibunching time constants τ_{AB} and (b) the fractions \bar{X} and time constants τ of other processes involved. Auto-correlation functions of the donor and acceptor are shown in green and red, respectively. Forward (upward triangles) and backward (downward triangles) acceptor-donor correlation functions are shown in blue. Error bars represent \pm one standard deviation of the fit.

the capillary a good agreement between the model function and the experimental data was achieved with one component less than for the coverslip measurement. This could be a cause of the lower SNR and the inability to resolve more exponential components or due to a more Gaussian shaped MDF, which better corresponds to the theory for the derivation of the diffusional correlation function.

5.2.2 Prothymosin alpha

Multiple high pressure nsFRET-FCS experiments were performed with the intrinsically disordered protein (IDP) prothymosin alpha (ProT α) in order to evaluate and analyze potential pressure dependencies of its properties, e.g. FRET efficiency and, of particular interest, chain reconfiguration times and dynamics.

30 minute measurements First, multiple short measurements with a duration of half an hour were made in the capillary with pressures of 1 bar, 500 bar, 1000 bar, 1500 bar and 2000 bar. A short reference measurement with a borosilicate coverslip (cs/BG) was made as well. All experiments were made with an excitation power of 40 μ W at a wavelength of 488 nm. FRET histograms were calculated with a sum threshold for donor and acceptor bins of $T_{\text{sum}}^{\text{DA}} = 40$ cts/ms. These short experiments

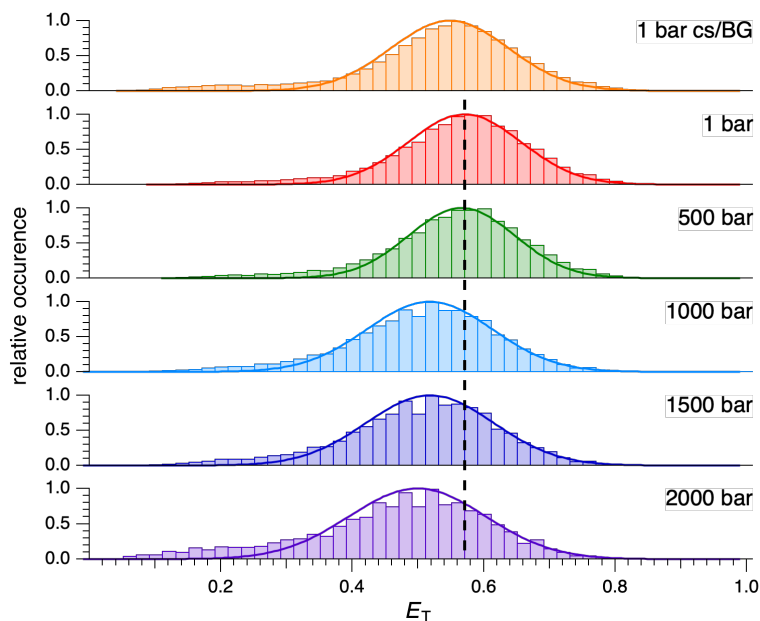


Fig. 5.20: FRET efficiency histograms of 30 minute measurements of ProT α at multiple pressures p made with the optical multi layer (OML) and at ambient pressure with a borosilicate coverslip (cs/BG). Solid lines are Gaussian fits for determining the the mean FRET efficiency E_T . The dashed line marks E_T with the OML at 1 bar.

serve as a control for the results of longer nsFRET-FCS measurements, like the ones made with the 3-stranded DNA hybrid. Longer measurements were performed on different days with a new optical multi layer (OML) and are thus more prone to potential changes in the experimental setup and parameters. Therefore, short measurements were made with the identical OML by simply increasing the pressure after one experiment without the need for a new capillary or other changes of the experimental setup. Only the focus position was checked with a cross section image of the sample volume and was adjusted if necessary. The FRET efficiency histograms including Gaussian fits of both, the measurement with a coverslip and with the OML at different pressures are shown in Fig. 5.20. At ambient pressure the efficiency with the capillary is slightly shifted to $E_T = 0.566 \pm 0.002$ in comparison to the measurement with a borosilicate coverslip and an efficiency of $E_T = 0.546 \pm 0.002$. This is most likely due to varying focus characteristics and spectral properties of both assemblies. The same holds for a pressure of 500 bar with an efficiency of 0.560. Further increasing pressures lead to a drop in the efficiency to $E_T = 0.509 \pm 0.002$ for 1000 bar and 1500 bar and $E_T = 0.488 \pm 0.003$ for 2000 bar, respectively. A possible explanation could be a measurement artifact due to a bulging of the capillaries with increasing pressure. This would increase optical aberrations and lead to changed imaging properties of the microscope and eventually a change between the focus of the donor and acceptor channel. Another explanation could be a further expansion of the protein with increasing pressure, which would lead to a larger donor-acceptor distance.

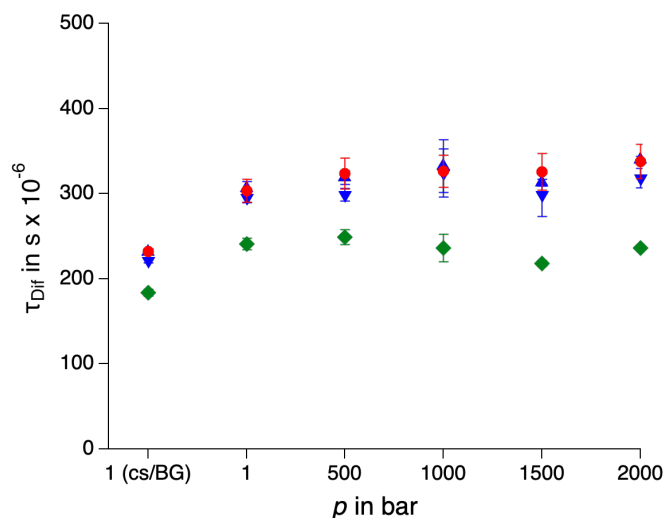


Fig. 5.21: Apparent diffusion times τ_{Dif} of 30 minute measurements of ProT α at multiple pressures p made with the optical multi layer (OML) and at ambient pressure with a borosilicate coverslip. Diffusion times of the auto-correlation functions of the donor and acceptor are shown in green and red, respectively. Forward (upward triangles) and backward (downward triangles) acceptor-donor correlation functions are shown in blue. Error bars represent \pm one standard deviation of the fit.

The apparent diffusion times at each pressure are shown in Fig. 5.21. They show a light increase using the optical multi layer (OML) compared to a borosilicate coverslip. This is due to the refractive index mismatch and enlarged focal volume when using fused silica and the OML. A pressure dependence of the diffusion time, on the other hand, is not identifiable. The diffusion times slightly fluctuate but with no evident tendency. Consequently, the results do not show a significant change of the properties of the experimental setup with increasing pressure. The reference experiments with the 3-stranded DNA hybrid do not indicate changes of the optical properties within the capillaries either. Therefore, the shift of the transfer efficiency suggests a real distance change within the protein rather than an experimental measurement artifact.

16 hour measurements To analyze and evaluate the observed shift in the transfer efficiencies further, longer experiments of ProT α with durations of 16 hour were made. The excitation power was, like for the shorter measurements, 40 μ W at a wavelength of 488 nm. The longer measurement duration additionally enable the investigation of the chain dynamics of the protein even under high hydrostatic pressures, a type of experiment, which was never realized until present. The pressures of the measurements were 1000 bar, 1500 bar and 2000 bar, respectively. The outcome is compared to the measurement at ambient pressure using a borosilicate coverslip (see subsection 5.1.4).

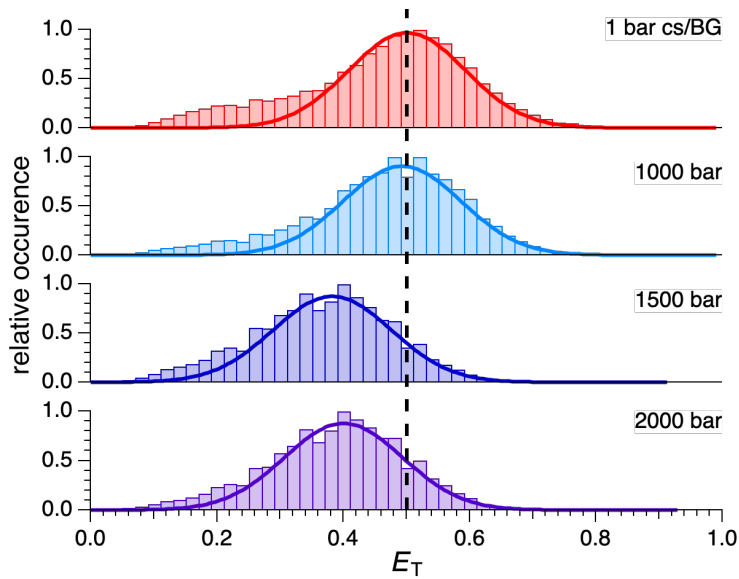


Fig. 5.22: FRET efficiency distributions of ProT α experiments at multiple hydrostatic pressures. The measurement at a pressure of 1 bar was performed with a borosilicate coverslip (cs/BG), high pressure experiments with the optical multi layer (OML), respectively. Solid lines are Gaussian fits for determining the respective mean transfer efficiency. The dashed lines indicate the mean transfer efficiency of the measurement at ambient pressure.

The transfer efficiency histograms are shown in Fig. 5.22 with the corresponding Gaussian fits. The histograms were calculated with a sum threshold for the donor and acceptor time bins of $T_{\text{sum}}^{\text{DA}} = 40$ cts/ms. Like for the shorter measurements, the FRET efficiency seem to drop with increasing pressure. At ambient pressure the efficiency is $E_T = 0.502 \pm 0.019$. But in contrast to the shorter experiments a pressure of 1000 bar has no significant effect on the transfer efficiency, since it is only marginally shifted to $E_T = 0.493 \pm 0.021$, but still well within the experimental uncertainty. With further increasing pressures of 1500 bar and 2000 bar, however, the transfer efficiency shows a significant drop as well to $E_T = 0.382 \pm 0.021$ and $E_T = 0.400 \pm 0.020$, respectively.

The nsFRET-FCS correlation functions of all measurements are shown in Fig. 5.23 with the corresponding global fits. The correlation functions are much more noisy compared to those with the borosilicate coverslip. This is due to the already discussed aberrations and the refractive index mismatch of fused silica and borosilicate glass when using the optical multi layer (OML). The lower SNR within the capillary particularly affects the low time range of a few nanoseconds and thus leads to a lower amplitude of fluorescence antibunching. When using the coverslip, the fit function contained three additional exponentials for processes causing fluorescence fluctuations besides translational diffusion and fluorescence antibunching. With the capillaries one process less is needed for a sufficient fitting of the experimental data.

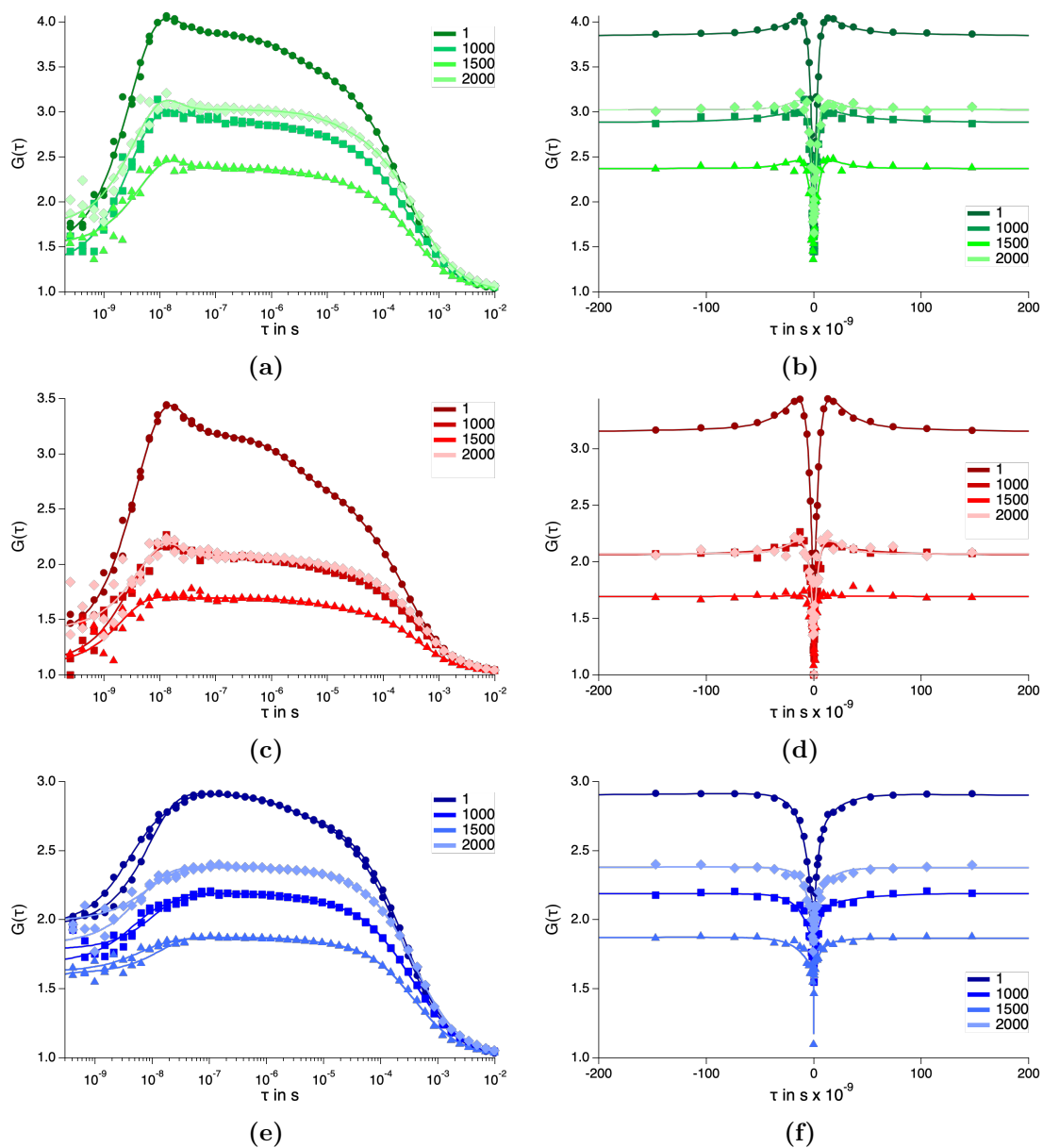


Fig. 5.23: Correlation functions of 16 hour high pressure nsFRET-FCS measurements of ProT α at pressures of 1 bar (circles), 1000 bar (squares), 1500 bar (triangles) and 2000 bar (diamonds). (a,b) show the donor-donor, (c,d) the acceptor-acceptor and (e,f) the acceptor-donor correlation functions, with (b,d,f) positive and negative lag times τ belong to forward and backward correlations, respectively. Solid lines are corresponding global fits according to Eq. 3.13. The experiment at 1 bar was performed with a borosilicate coverslip and the high pressure experiments with the optical multi layer (OML).

The inclusion of a third exponential leads to no further improvement of the fit result. A possible explanation is a more Gaussian profile of the observation volume, when using the capillaries since the slowest process when using a coverslip was potentially assigned to diffusion. Another reason could be the worse SNR within the capillaries and the inability to resolve and distinguish both processes. This would agree with the observed fitting errors, which are much larger in the high pressure nsFRET-FCS experiments as compared to the experiments using a borosilicate coverslip.

However, despite the worse SNR the correlation functions of all high pressure measurements show the expected correlated behavior in the auto-correlation functions of the donor and acceptor channel and an anti-correlation in the acceptor-donor cross-correlation functions at the same time scale below 100 ns. This is characteristic for chain dynamics and frequent changes of the donor-acceptor distance. It follows that these results prove the capability of the experimental setup to detect chain dynamics of proteins in the range of a few nanoseconds even under high hydrostatic pressures with this first successful realization of high pressure nsFRET-FCS experiments.

Fig. 5.24 shows the determined diffusion times. It is slightly increased within the capillary in contrast to the coverslip. As for the shorter measurements this can be explained with a larger focus and aberrations due to a difference of the refractive index of the fused silica capillary and the borosilicate coverslip. With increasing pressure no clear dependence of the diffusion time can be determined. Even though one can see a slight potential increase, the diffusion times are within the errors of the fit, which are much larger than for the coverslip. Since all experiments were

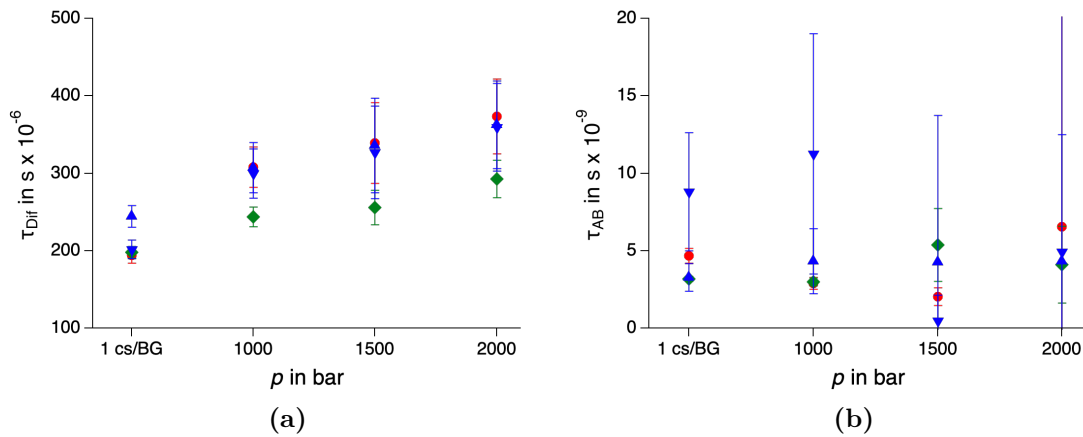


Fig. 5.24: (a) Diffusion times τ_{Dif} and (b) fluorescence antibunching time constants τ_{AB} of ProT α at multiple pressures p using the optical multi layer (OML) and a borosilicate coverslip (1 bar). Results of the donor-donor, acceptor-acceptor and acceptor-donor correlation functions are shown in green, red and blue, respectively. Upward triangles represent acceptor-donor forward and downward triangles acceptor-donor backward correlation functions. Error bars represent \pm one standard deviation of the fit.

made at different days, small fluctuations of the diffusion time are most likely due to characteristics of the experimental setup, e.g. a slightly varying focal volume and no pressure effect. Furthermore, the shorter experiments of the DNA hybrid as well as ProT α , which were made directly one after each other show no effect as well. The time constants of fluorescence antibunching are also shown in Fig. 5.24. The fit errors of this parameter are very large due to the the low SNR and noisy data in this time range. However, the antibunching time constant of the donor is increasing from approximately 3 ns at 1 bar and 1000 bar to over 4 ns at pressures of 1500 bar and 2000 bar, respectively. Even though, the time constant of fluorescence antibunching is dependent on the excitation power and does not reflect the actual fluorescence lifetime, the relative increase indicates a reduced donor quenching by the acceptor dye. A less efficient quenching indicates a larger donor-acceptor distance and is in good agreement with the observed decrease of the transfer efficiency with increasing pressure.

The remaining fit parameters are shown in Fig. 5.25. As explained above, the correlation functions in the capillary were only fitted with two additional exponentials. These two are assigned to transitions to the triplet state and to chain dynamics of ProT α . The triplet fraction is highest for the coverslip and lower with the optical multi layer (OML), but with no visible pressure effect. A higher triplet fraction with the coverslip is expected since it indicates a more efficient excitation and thus smaller focal volume due to fewer optical aberrations. The same holds for the triplet relaxation time, which is lowest with the coverslip and higher with the OML. In contrast to the triplet fraction the triplet relaxation time shows a potential increase with higher pressures. However, the fitting error of the parameter is comparatively large and the effect might be not that significant.

The fraction of the chain reconfiguration shows no dependency on pressure or the optical assembly, which is also not expected for the movement of the chain and the corresponding fluorescence fluctuations. The chain reconfiguration time on the other hand shows, with the exception of the 1000 bar measurement, a decrease with increasing pressure. This finding is in qualitative agreement with the observed further expansion of the polypeptide chain. An expansion could potentially further reduce the effect of internal friction processes and enable a faster chain movement. A similar behavior has already been identified for several proteins with further expansion of the unfolded proteins due to increasing denaturant concentration [24]. For example it has been observed for the chymotrypsin inhibitor 2 [51, 309], the B domain of protein A [310], protein L [7, 183, 311, 312] and RNase H [313, 314]. A further expansion of the polypeptide chain with a correlated decreasing chain reconfiguration time has been observed by Nettels et al. in CspTM [8, 79]. Borgia et al. made the same observations for the two domains R16 and R17 of spectrin [78]. However, experiments of Soranno et al. with ProT α showed almost no dependency on the reconfiguration time of denaturant concentration. However, in the framework of simple polymer models the chain reconfiguration time τ_{CD} can be divided into two components, the reconfiguration time in the absence of internal friction, which is

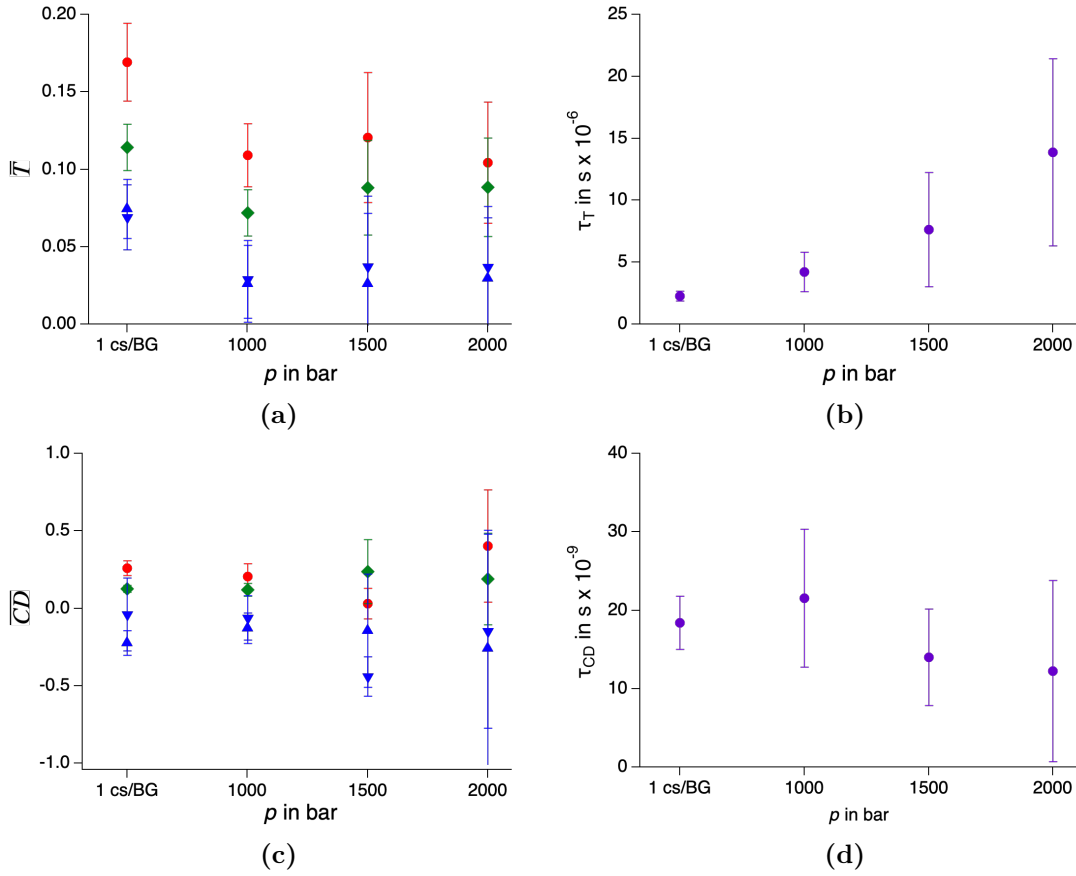


Fig. 5.25: Determined fit parameters of 16 hour ProT α nsFRET-FCS experiments at different pressures p using a borosilicate coverslip (1 bar) and the optical multi layer (OML) (1000 bar, 1500 bar 2000 bar). (a) Triplet fraction \bar{T} and (c) fraction of chain dynamics \overline{CD} with the corresponding (b) triplet relaxation times τ_T and (d) chain reconfiguration times τ_{CD} . In (a,c), results of the donor-donor, acceptor-acceptor and acceptor-donor correlation functions are shown in green, red and blue, respectively. Upward triangles represent results of the acceptor-donor forward and downward triangles acceptor-donor backward correlation functions. (a-d) Error bars represent \pm one standard deviation of the fit.

proportional to solvent viscosity τ_s and a time scale due to internal friction τ_i [7,8]:

$$\tau_{CD} = \tau_s + \tau_i. \quad (5.1)$$

Even though Soranno et al. observed no significant change of τ_{CD} with increasing denaturant concentration τ_s and τ_i showed a different behavior. Due to the increasing solvent viscosity with higher denaturant concentration the solvent dependent τ_s is increasing as well [8,78]. In contrast, the solvent independent relaxation time τ_i , attributed to internal friction, is decreasing with increasing GdmCl concentration. This is in good agreement with the observed decrease of τ_{CD} with increasing pres-

sure. With increasing pressure, no significant influence is expected on the solvent viscosity and thus for τ_s . Therefore, the decrease of the reconfiguration time of the polypeptide chain of ProT α can be explained by a reduction of internal friction with increasing pressure, like for an increasing denaturant concentration.

High pressure single molecule FRET experiments with Frataxin showed a similar result and a slightly decreasing FRET efficiency with increasing pressure [5]. In contrast, high pressure measurements with the cold shock protein CspA showed no further expansion of its unfolded state with further increasing pressure and thus a different behavior than the denaturant unfolded protein [4]. This could indicate that the unfolded states due to pressure or denaturant unfolding are deviating even though pressure has a similar effect on the IDPs. The fact that Frataxin shows a different behavior might be due to its rather unstable configuration at room temperature. To investigate possible differences regarding the characteristics of the unfolded states of the cold shock protein CspA due to pressure or denaturant unfolding, ns-FRET experiment of CspA have to be made at multiple pressures and denaturant concentrations to analyze if there is a measurable differences in the FRET efficiency as well as reconfiguration time of the chain.

Summarizing the results from the nsFRET-FCS experiments of ProT α under high hydrostatic pressures, there are two possible lines of their interpretation. On the one hand, a possible explanation could be a bending of the capillary with increasing pressure. A bending would cause more pronounced optical aberrations and consequently a larger focal volume as well. As a consequence, the smaller photon flux density would lead to a smaller triplet fraction and increase of the observed triplet relaxation time. Additionally, stronger aberrations could lead to changes in the foci of the donor and acceptor channel and be responsible for a shift of the FRET efficiency. With this explanation, no changes of the reconfiguration time would be expected as well, since the dimensions of the focal volume are not expected to have a strong influence. In this case, the observed changes would be a measurement artifact and may be caused by the large uncertainties of the global fits and the low SNR within the capillary.

On the other hand, there are several indicators that the results are due to a pressure effect that could cause a kind of phase transition on the protein. One reason is the outcome of the control measurements with the 3-stranded DNA hybrid. These experiments show no apparent pressure dependency of both, the transfer efficiency and diffusion time. A larger diffusion time would be expected for an increased focal volume due to additional aberrations. However, if the aberrations cause an elongation primarily along the optical axis, the apparent diffusion time would be less affected. Nevertheless, Schneider [5] and Schneider et al. [4] made reference measurements using the optical multi layer as well, with double stranded DNA oligonucleotides as sample, labeled with the same donor-acceptor pair and observed no pressure dependency of the experimental setup. This supports the hypothesis of a real pressure effect on the protein. Furthermore, the 30 minute experiments of ProT α show no change in the diffusion time with increasing pressure despite a decrease in the trans-

fer efficiency. The decrease in the efficiency is also in principle agreement with the longer measurements of ProT α . The pressure could lead to a further expansion of the IDP resulting in a larger mean donor-acceptor distance. This shows a similar effect like for GdmCl and denaturant unfolded proteins, which further expand with increasing denaturant concentration [7,24,51,183,311–314]. This agrees qualitatively with an increase of the time constant of fluorescence antibunching of the donor fluorophore indicating a real distance change rather than an artifact. Consistent with this interpretation is the decrease of the time constant of chain dynamics associated with a more flexible polypeptide chain due to reduced internal friction. This is in qualitative agreement with experiments of ProT α and a reduction of the time constant of internal friction due to GdmCl [7]. However, in order to make more reliable interpretations and to discuss the results with larger confidence, longer and more nsFRET-FCS experiments have to be made under high hydrostatic pressure. Despite the success of realizing, to our knowledge, the first nsFRET-FCS experiments under high pressure and the analysis of chain reconfiguration times, measurements within the capillary and the optical multi layer still suffer from a worse SNR compared to a coverslip. The lower SNR leads to large uncertainties of the fit parameters, which could be improved with longer and more measurements as well. To compare possible differences of the unfolded states of proteins due to temperature, denaturant or pressure unfolding, nsFRET-FCS measurements have to be made with the same protein under those conditions.

Chapter 6

Conclusion, summary and outlook

Unfolded and intrinsically disordered proteins are of significant interest since they serve as a starting point for the entire protein folding process [30–32]. Additionally, intrachain diffusion and the rate of contact formation between distinct regions along the polypeptide chain are the limiting parameters for the folding speed limit [23,24]. Due to the different unfolding mechanism of pressure in contrast to temperature or chemical denaturants, nsFRET-FCS experiments under high pressure can give additional insights into the folding process and dynamics of unfolded proteins and IDPs [89]. The aim of this work was the first realization of single molecule high pressure nsFRET-FCS experiments using a fused silica capillary as the pressure cell. Basis was the extension of the experimental setup with adequate measurement electronics and the evaluation of its implementation. Furthermore, the capillary handling procedure was improved and multiple measurement parameters regarding the best imaging properties when using the optical multi layer (OML) were tested. Section 6.1 summarizes the experiments and results regarding the measurement electronic implementation as well as characteristics of the experimental setup and the measurement parameters. In section 6.2 the performed nsFRET-FCS experiments at ambient and under high pressures are discussed. Section 6.3 gives a short conclusion and outlook for future work.

6.1 GPX-TDC implementation and experimental setup improvements

GPX-TDC and four detectors Requirement for nsFRET-FCS experiments was the extension of the existing confocal microscope. Until present the measurement electronics Timeharp200 from Picoquant and SPC-134 TCSPC from BeckerHickl were used, which are classical TCSPC electronics. However, these systems suffer from a characteristic dead time after a detected event. Thus, both measurement electronics are not suitable for the investigation of fast protein dynamics in the nanosecond range. In order to perform nanosecond fluorescence correlation spectroscopy (ns-FCS) measurements and, in combination with fluorescence resonance energy transfer

(FRET), nsFRET-FCS measurements, the experimental setup was equipped with a time-to-digital converter USB2.0-TDC CS-TP 01-04-82 (GPX-TDC) from Surface Concept. The GPX-TDC operates with a conventional counter/timer principle and has no limiting dead time between two different input channels. That allows for the detection of time intervals in the range of a few nanoseconds or even the detection of two photons simultaneously. Due to technical limitations of the GPX-TDC, the measurement VI in LabVIEW was designed in such a manner that a measurement is divided into several shorter submeasurements that are executed consecutively. Additionally, to overcome afterpulsing and dead time limitations of the detectors and to be able to obtain all required correlation functions of nsFRET-FCS measurements from one measurement at once, two additional detectors were implemented.

The correct functionality of the upgraded experimental setup with the GPX-TDC and detectors was initially investigated by measurements with the freely diffusing fluorophore Alexa Fluor 488 (AF488) (section 4.1). The results were compared with these of the previously used Timeharp200. Additionally, with the free fluorophore and the GPX-TDC, measurements were first performed, where the entire time range of fluctuations could be captured, from fluorescence antibunching in the range of a few nanoseconds to the decay of the correlation function at longer lag times due to the diffusion process. This was not possible with the previous measurement technique. While there was a generally good agreement between both measurement setups, a difference was observed in the number of detected photons as well as the average number of molecules in focus. The difference between both electronics was further investigated with fluorescence benchmark experiments (subsection 4.1.1). Even though the overall shape and progression of the analyzed benchmark parameters are comparable, the absolute scale differs significantly between the GPX-TDC and Timeharp200. An analysis of the GPX-TDC data with an artificially inserted dead time of 350 ns shows that the saturation effects can be attributed to the dead time of the Timeharp200. The dead time leads to an additional saturation factor, which flattens the MDF of the experimental setup and thus causes the deviating results between the Timeharp200 and GPX-TDC. The GPX-TDC on the other hand does not indicate any additional saturation factor. Performance-dependent measurements of fluorescence antibunching also demonstrate the high accuracy of the new measurement electronics in the range of a few nanoseconds. The determined fluorescence lifetime as well as the absorption cross section of AF488 are in good agreement with the manufacturer's specifications of the fluorophore.

Long measurement durations In addition to the technical capabilities necessary for nsFCS, which were successfully established by the implementation of the GPX-TDC and two additional APDs, long data acquisition times are mandatory to ensure sufficient statistics. Measurement times of at least 16 hours or longer are used for this purpose. Although the required measurement time can in principle already be reduced by an order of magnitude with the use of zero-mode waveguides [77], this

approach is unsuitable for the intended experiments under high pressure with the combination of a fused silica coverslip, the refractive index matching gel, and the fused silica capillary. For very long measurements lasting several hours to days, evaporation of the immersion water poses the limiting factor. Nevertheless, to enable long measurements, a small device was designed and 3D-printed, which is mounted between the objective and the sample stage and primarily reduces the airflow, thereby significantly increasing the service life of the immersion water (subsection 4.3.1). With high reliability and reproducibility, measurement durations of 16-33 hours were achieved in approximately 90% - 95% of all measurements. For the use of a bare capillary without a fused silica coverslip, a protection device was developed and tested as well, which allows measurement times of 16 hours and more (subsection 4.3.1).

Simplification of capillary connection, handling and measurements Another goal of the work was the simplification of experiments under high pressure and to overcome the error prone sample preparation. For this reason, a complete redesign of the sample stage was done, which includes the junction point to the pressure pump (section 3.4 and subsection 4.3.2). The new sample stage enables, on the one hand, a secure lateral translation of the entire sample stage above the objective without the risk of the end of the pressure pump being shifted against the end of the capillary. This could potentially lead to a breakage or significantly lower pressure resistance of the capillary. Furthermore, the height of the capillary above the objective can be continuously adjusted with the help of a travel translation stage. This allows the capillary to be precisely aligned, which also increases the durability of the capillary. Another fundamental improvement is the simple rotation of the capillary. This is important for square capillaries, as the initial orientation during adjustment is not well defined. By being able to rotate the capillary without significantly affecting the lateral or axial position, the capillary can be positioned easily as needed, and the focus for the measurement can be (re)adjusted without the requirement of a complete realignment as before. The key features of the novel sample stage described above, and the associated simplification of capillary installation for high-pressure experiments, represent a fundamental improvement over the previous implementation. It enables an easier execution of measurements with greater reliability and reproducibility, which is fundamental for nsFCS experiments at high pressure.

To further simplify measurements with the fused silica capillary, PMMA was tested as a possible substitute for the fused silica coverslip (section 4.4). It is significantly more cost-effective and durable than the very brittle 100 μm thick fused silica coverslip. In some measurements, comparable results were achieved with the PMMA film. However, these results could not be reproduced with great reliability, primarily due to the high flexibility of the PMMA film and the use of two 50 μm thick PMMA films with water in between. A shift in FRET efficiency also indicates possible dispersion effects, which could be due to a decreasing overlap of the donor and

acceptor detection volumes. Therefore, these effects do not occur or only occur very weakly in experiments with one fluorophore. Potentially, the reproducibility of the measurements could be improved and tested in future measurements with a 100 μm thick PMMA film [315], which was not at hand during the experiments. This would eliminate the need for water between the two PMMA layers and would make the film more rigid. However, in the tested configuration, the solution with the PMMA film is not suitable as a substitute for the fused silica coverslips.

Focus position and objective's correction collar FRET experiments with different focus positions inside the sample volume of the capillary showed a potential benefit with a focus position near the glass surface of the capillary (see section 4.6). Furthermore, measurements with different correction ring settings of the objective showed the best results with settings between 17 and 18. The deviations are due to the setup of the optical assemblies. Depending on the exact positioning of the capillary above the fused silica coverslip and the amount of refractive index gel between the capillary and coverslip, deviations in the ideal setting of the correction ring can occur. In addition, microscope images show that the structure of the capillary wall is not perfectly flat and accordingly can lead to deviations between different measurements as well [5]. To achieve the best possible measurement conditions, one possible solution is to perform multiple short FRET/FCS measurements at varying focus positions within the capillary and correction ring settings prior to a nsFRET-FCS measurement of several hours.

6.2 nsFRET-FCS

DNA as a negative control Initial nsFRET-FCS experiments were carried out with DNA samples, a 3- and 4-stranded DNA hybrid (subsection 5.1.1) as well as a DNA hairpin (hpDNA) (subsection 5.1.2). The experiments were made with a borosilicate coverslip at ambient pressure. Due to their high stability and rigidity, no changes in the donor-acceptor distance due to DNA dynamics are expected. Therefore, the DNA samples serve as a negative control for dynamics in the sub-100 ns range. All auto- and cross-correlation functions reveal pronounced fluorescence antibunching with similar shape. Additionally, all correlation functions exhibit an exponential decay below 100 ns with relaxation times of $\tau_{\text{CD}} = (44 \pm 4)$ ns and $\tau_{\text{CD}} = (62 \pm 13)$ ns for the 3- and 4-stranded hybrid, and $\tau_{\text{CD}} = (10 \pm 5)$ ns for the hpDNA, respectively.

However, this exponential decay shows a positive amplitude in all correlation functions. Therefore, the fluctuations cannot be caused by changes in the donor-acceptor distance due to dynamics of the DNA strands. A possible cause could be the flexibility of the fluorophores attached at the end of a linker and potential interactions

of the dyes with the DNA bases and processes such as photo-induced electron transfer (PET). In future experiments, the power dependence of this process should be investigated, to inspect if the fluctuations have photophysical origin. Irrespective of the origin of these fast relaxation times, the detection of fluorescence fluctuations in this time range highlights the sensitivity of the experimental setup here.

Filtered nsFRET-FCS analysis and chain dynamics The cold shock protein CspA was also examined (subsection 5.1.3), as it has already been successfully unfolded and studied with pressure and chemical denaturants [4, 5]. Additionally, the cold shock protein from *Thermotoga maritima* (CspTM), which is similar to CspA, showed dynamics of the unfolded polypeptide chain during unfolding with denaturing agents [8, 79]. Unfortunately, the sample showed a significant fraction of CspA without a functioning acceptor fluorophore (donor only), but also a small fraction of the unfolded protein in a measurement with 4.5 M GdmCl in the buffer. Despite the high concentration of GdmCl, the fraction of the folded protein was still significantly higher, unlike in previous measurements [5]. Due to the high fractions of donor only and folded protein, a filtered analysis of the different populations was made, similar to previous studies of CspTM [79]. In contrast to the negative control, the correlation functions of the unfolded protein (low FRET) exhibited typical characteristics of protein dynamics. The donor-acceptor cross-correlation functions showed an anti-correlation whereas the auto-correlations of both fluorophores exhibited a correlation with a relaxation time of $\tau_{CD} = (42 \pm 9)$ ns. This is within the typical time range below 100 ns for dynamics of proteins with these segment lengths and are in good agreement with previous studies by Soranno et al. [8]. These results demonstrate the capability and accuracy of the experimental setup and the strength of the filtered correlation analysis.

ProT α The last sample for nsFRET-FCS measurements was the intrinsically disordered protein (IDP) prothymosin alpha (ProT α). The protein is strongly negatively charged (net charge $z = -44$) and lacks secondary structure elements [201]. It has already been studied with nsFCS and showed dynamics with chain reconfiguration times below 100 ns. Although the performed measurements exhibited typical characteristics of correlation and anti-correlation in the auto- and cross-correlation functions, two FRET populations were observed in the histogram. The origin of the low FRET population was initially investigated, as no second population had been reported in previous studies, except for a donor-only population [6, 272, 297]. However, the transfer efficiency of this population component was $E_T = 0.248 \pm 0.007$. Through interval analysis, filtered correlation analysis, and the comparison to a nsFRET-FCS measurement of ProT α without the addition of β -mercaptoethanol (BME) to the buffer, the low FRET population is most likely due to donor only molecules. The comparatively high transfer efficiency of the donor only population can be explained by the lack of histogram correction.

Due to the strongly negative charge of ProT α , the expansion of the chain as well as its chain reconfiguration times are highly dependent on buffer conditions such as pH or ionic strength [170, 198, 201, 303, 304, 316]. Considering this dependency, the observed reconfiguration time of $\tau_{\text{CD}} = (19 \pm 2)$ ns agrees well with previous findings [6, 8, 195]. To further assess the sensitivity of the setup, ProT α was also examined with increased solvent viscosity, as increased solvent viscosity is expected to slow down chain dynamics due to increased solvent friction, as shown in numerous studies [7, 8, 30, 78]. This observation was qualitatively confirmed with an increase in relaxation time of $\tau_{\text{CD}} = (72 \pm 5)$ ns, although the increase was more pronounced than in previous measurements by Soranno et al. [8]. However, in contrast to previous observations, the FRET Efficiency of ProT α with glycerol in the buffer experienced a significant increase from $E_{\text{T}} = 0.501 \pm 0.002$ to $E_{\text{T}} = 0.739 \pm 0.002$, which could indicate a compaction of the polypeptide chain. This compaction would lead to a higher increase in the reconfiguration time, than expected for a higher viscosity of the buffer alone, due to an associated increase of internal friction.

High pressure experiments After the initial successful execution of nsFRET-FCS measurements and the proven capability to detect chain reconfiguration times, high-pressure nsFRET-FCS experiments were carried out (subsection 5.2.1). To exclude potential pressure artifacts on the fluorescence measurements, the 3-stranded DNA hybrid was investigated as negative control like at ambient pressure. Due to the high stability of the DNA hybrid, no changes in the FRET efficiency are expected with a pressure increase, and shifts in efficiency would be attributed to artifacts caused by high pressure rather than actual changes in the donor-acceptor distance. Initially, short high-pressure measurements were made. The advantage of short measurements is the ability to use the identical capillary for each measurement at different pressures, thus minimizing influences of the experimental setup on the results. As expected, both, the transfer histograms and diffusion times show no pressure dependency, consistent with previous studies and double stranded DNA oligonucleotide experiments at multiple pressures [4, 5]. As a negative control for potential dynamics under high pressure, a measurement with a duration of 10 hours and a pressure of $p = 1000$ bar was made with the 3-stranded DNA hybrid. No significant changes compared to the measurement of the sample at ambient pressure were observed. Additionally, the correlation functions showed no signs of chain dynamics. In addition to demonstrating that DNA is suitable as a reference sample for nsFRET-FCS under high pressure, this measurement also represents the first-ever nsFRET-FCS measurement under high hydrostatic pressure. With this proof that high-pressure nsFRET-FCS experiments are possible and provide adequate signal-to-noise ratios (SNRs), measurements of the IDP ProT α under high pressure were finally made as well (subsection 5.2.2).

Similar to the 3-stranded DNA hybrid, short measurements were made first. In contrast to the reference measurement with the DNA hybrid, a shift to lower efficiencies with increasing pressure was observed. While the transfer efficiency at 1 bar was

$E_T = 0.566 \pm 0.002$, it decreased to $E_T = 0.488 \pm 0.003$ at a pressure of 2000 bar. Since the diffusion time shows no dependency on a pressure increase, and the control measurements with DNA show no pressure dependence either, the reduction in efficiency is likely due to an actual chain expansion with increasing pressure. Another possible explanation is that, despite the control measurements, it could be a measurement artifact with bending of the capillary due to pressure leading to these effects.

Since nsFRET-FCS analysis is not possible with the shorter measurements due to a too low SNR, long measurements were made at multiple high pressures. The transfer efficiencies are in principle agreement with the shorter measurements, indicating a further expanding chain of the protein due to the applied pressure. This leads to a larger donor-acceptor distance and subsequently lower FRET efficiency. This observation shows a similar effect as observed for unfolded proteins, with chain expansion occurring with increasing denaturant concentration [7, 8, 24, 51, 79, 183, 309–314]. Furthermore, it qualitatively agrees with the determined fluorescence antibunching time constants of the donor, which increase with pressure. The apparent decrease in chain reconfiguration time with increasing pressure is consistent with this argumentation. The faster reconfiguration time is caused by a more flexible chain due to a reduction of internal friction. This is in qualitative agreement with measurements of ProT α from Soranno et al. and a reduction of the time constant of internal friction with increasing denaturant concentration [8, 78]. These first measurements are the first high-pressure nsFRET-FCS experiments, paving the way to an application of this methodology for a broad range of folding model proteins. The results are promising and indicate the great potential of this investigative method. Fluorescence fluctuations can also be detected in the capillary and the optical multi layer (OML) over the entire time range accessible with free diffusing molecules in solution, from fluorescence antibunching to translational diffusion through the focus. The results with ProT α also suggest a pressure sensitivity of the IDP with pressure-dependent chain dynamics due to a reduction of internal friction and an expansion of the chain.

6.3 Conclusion and outlook

With the goal of realizing nsFCS and nsFRET-FCS measurements under high pressure, new measurement electronics (GPX-TDC) and detectors were successfully implemented into the existing experimental setup. The correct functioning and high sensitivity of the new measurement electronics were evaluated and confirmed through various spectroscopic measurements. Furthermore, the sample stage of the experimental setup was significantly improved to simplify the execution of experiments under high pressure while simultaneously increasing their reproducibility. However, the attempt to replace the fragile and expensive fused silica coverslip of the optical multi layer (OML) with a PMMA film was not successful in the tested

version. To decrease the flexibility of the optical assembly and potentially reduce aberrations, the approach could be repeated in the future with a PMMA film that already has the desired thickness of 100 μm . Additionally, the influence of the correction collar of the objective and the focus position within the sample volume of the capillary were observed. To avoid the need to verify the best settings for each measurement (as the exact thickness of the OML can vary), future work could focus on achieving a more constant effective coverslip thickness.

Furthermore, this work presents the first-ever nsFRET-FCS measurements conducted under high hydrostatic pressure. Despite compromises regarding the imaging quality due to the use of the fused silica capillary and the OML, fluorescence antibunching is evident in the pressure experiments, as well as the characteristic correlation and anti-correlation in the auto- and cross-correlation functions in the presence of chain dynamics, which could be investigated for the first time in a pressure-dependent manner. Nevertheless, the SNR in the capillary measurements is significantly lower than under standard conditions with a borosilicate coverslip. Therefore, an ongoing potential avenue for future improvements is an increase of the SNR in the capillary. As described by [5], the use of a custom-made square capillary could be considered. However, this option is very expensive (\$10,000), but it would most likely improve the optical conditions and correspondingly the SNR. Another possibility is to further increase the measurement duration. With more and longer measurements, the statistics in the sub-nanosecond time range can be further improved, thus significantly enhancing the interpretability of the derived results. This approach is the simplest and could be realized immediately since the experimental setup is capable of measurements of 30 hours or longer and the experiments showed that the pressure in the capillary can be maintained many hours as well.

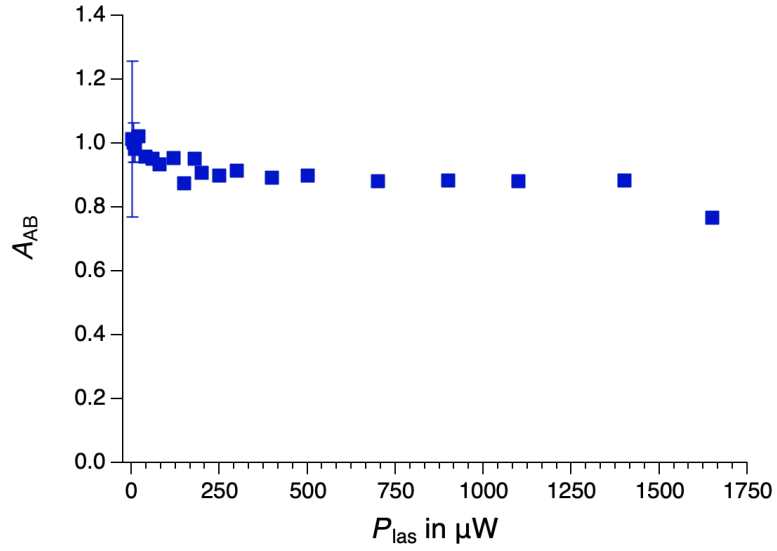
Furthermore, in future experiments, the same protein, such as the cold shock protein CspA, should be unfolded with both, denaturants and pressure. Potential differences in the chain reconfiguration time could provide new insights into the characteristics of the unfolded states and the underlying unfolding mechanism. Since some intrinsically disordered proteins (IDPs) fold upon binding, it would also be of great interest to investigate the folding behavior of such systems under high pressure.

Appendix

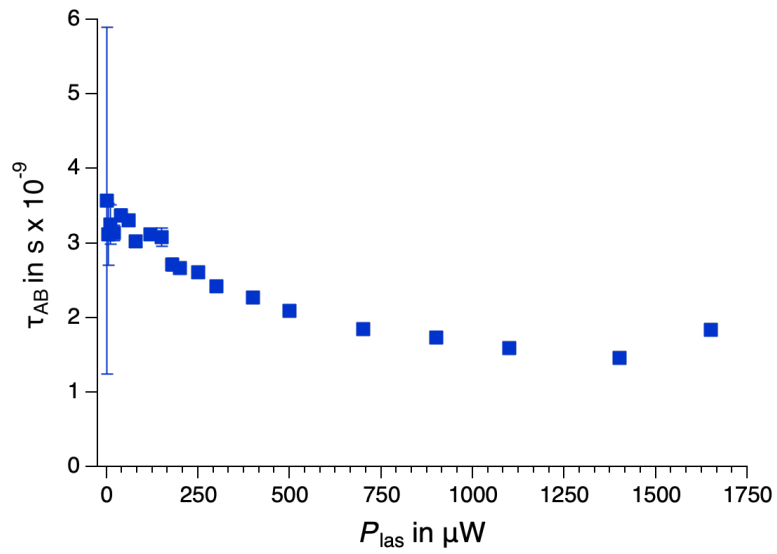
A.1 FCS benchmarks

Tab. A.1: Laser excitation powers P_{las} at a wavelength of 488 nm and corresponding measurement times t_{exp} of benchmark experiments made with AF488 and both measurement electronics, GPX-TDC and Timeharp200.

P_{las} in μW	t_{exp} in s	
	GPX-TDC	Timeharp200
1	4500	3600
5	3600	2700
10	1800	1500
20	1200	900
40	900	900
60	600	600
80	600	600
120	300	
150	300	300
180	300	
200	300	300
250	300	
300	300	300
400	300	
500	300	
600		180
700	180	
900	180	180
1100	120	
1200		120
1400	120	120
1650	60	



(a)



(b)

Fig. A.1: (a) Amplitude of fluorescence antibunching A_{AB} and (b) time constant of fluorescence antibunching τ_{AB} of AF488 from FCS benchmark measurements using the GPX-TDC at different laser excitation powers P_{las} (see Tab. A.1).

A.2 Igor Pro procedures

A.2.1 Editing of raw data and time correction

```
function edit_waves(interval_length, resolution)
variable interval_length, res
//length of macro time interval and time bin resolution in seconds
wave APD1, APD2, APD3, APD4

Redimension/L/U APD1, APD2, APD3, APD4

duplicate APD1, APD1_mic, APD1_mac; duplicate APD2, APD2_mic, APD2_mac
duplicate APD3, APD3_mic, APD3_mac; duplicate APD4, APD4_mic, APD4_mac
//deleting bits containing the micro time 'mic'
APD1_mac = APD1>>17; APD2_mac = APD2>>17
APD3_mac = APD3>>17; APD4_mac = APD4>>17
//deleting bits containing the macro time 'mac'
APD1_mic = APD1_mic << 47; APD1_mic = APD1_mic >> 47
APD2_mic = APD2_mic << 47; APD2_mic = APD2_mic >> 47
APD3_mic = APD3_mic << 47; APD3_mic = APD3_mic >> 47
APD4_mic = APD4_mic << 47; APD4_mic = APD4_mic >> 47

Redimension/D APD1_mac, APD2_mac, APD3_mac, APD4_mac
//computation of macro time in seconds
APD1_mac *= interval_length; APD2_mac *= interval_length
APD3_mac *= interval_length; APD4_mac *= interval_length

Redimension/D APD1_mic, APD2_mic, APD3_mic, APD4_mic
//computation of micro time in seconds
APD1_mic *= res; APD2_mic *= res; APD3_mic *= res; APD4_mic *= res

Redimension/D APD1, APD2, APD3, APD4
//combining macro and micro time, correct the time delay and save the time information
//as a multiple of the time bin resolution (res) as required by the correlator
APD1 = APD1_mic + APD1_mac; APD1 /= res
APD2 = APD2_mic + APD2_mac + 0.9e-9; APD2 /= res
APD3 = APD3_mic + APD3_mac + 1.6e-9; APD3 /= res
APD4 = APD4_mic + APD4_mac + 2.1e-9; APD4 /= res
//tt: true time
rename APD1 tt_APD1; rename APD2 tt_APD2; rename APD3 tt_APD3; rename APD4 tt_APD4
//kill redundant waves
KillWaves APD1_mic, APD2_mic, APD3_mic, APD4_mic, APD1_mac, APD2_mac, APD3_mac, APD4_mac
end function
```

Fig. A.2: Custom function in Igor Pro, which processes the raw data and calculates the photon arrival times according to Eq. 3.5 of each APD and corrects their time delays due to optical or electronically path length differences.

A.2.2 Filtered nsFRET-FCS analysis

```
function filtered_nsFRET_FCS(efficiency_range_start, efficiency_range_end)
variable efficiency_range_start, efficiency_range_end
//FRET contains FRET efficiencies per time bin
wave smartroute, FRET

//create wave with information which time bin meets condition
smartroute = FRET >= efficiency_range_start & FRET <= efficiency_range_end ? 1:NaN

variable i, j, counter
variable ch_counter = 0
variable sr_size = 0
variable min_time = 0
string wave_name

//get size of smartroute wave
wavestats/Q smartroute
sr_size = V_npnts + V_numNans + V_numINfs

//calculate for each APD
for(i=1; i < 5; i++)
  counter = 0
  wave_name = "tt_apd"+num2str(i)
  wave tmp_wave = $wave_name
  //conversion of times to seconds with time bin resolution
  tmp_wave *=82.304e-12

  string wave_name_bin = "tt_apd"+num2str(i)+"_bin"
  wave tmp_bin = $wave_name_bin
  string filtered_name = wave_name+"_filtered"
  //get minimum time for time binning of lms
  min_time = floor(tmp_wave[0]*1000)

  MatrixOP/O copy_tmp = tmp_wave/tmp_wave - 1

  for(j = min_time; j < sr_size; j++)
    if(numtype(smartroute[j]) == 2)
      counter += tmp_bin[j]
    else
      if(tmp_bin[j] == 0)
        else
          copy_tmp[counter, counter + tmp_bin[j]-1] = 1
          counter += tmp_bin[j]
        endif
      endif
    endif
  endfor

  MatrixOP/O tmp_filtered = tmp_wave*copy_tmp
  tmp_filtered = tmp_filtered[p]==0? Nan : tmp_filtered
  Wavetransform ZapNans tmp_filtered
  //conversion of original and filtered waves to multiples
  //of time bin resolution for correlation
  tmp_wave /= 82.304e-12
  tmp_filtered /=82.304e-12
  Matrixop $filtered_name = tmp_filtered
endfor
//Kill redundant waves
KillWaves copy_tmp, tmp_filtered
end
```

Fig. A.3: Custom function in Igor Pro, which extracts the time stamps of photons belonging to certain FRET efficiencies.

A.3 Focus position within the capillary

Fig. A.4 shows the correlation functions and fit results of FCS measurements of the protein EsxF, which was investigated in the scope of another scientific project. For this work it was used as an additional sample for evaluating different focus positions within the sample volume of the fused silica capillary in the optical multi layer (OML). The protein is labeled with AF488 and AF647 as the donor and acceptor dye, respectively. As in section 4.6, three different focus positions were investigated, varying in the distance ($d_{\text{axial, surface}}$) to the capillary wall. One approximately close to the surface, with $d_{\text{axial, surface}} \approx 0 \mu\text{m}$ and two positions with distances of $d_{\text{axial, surface}} \approx 12.5 \mu\text{m}$ and $d_{\text{axial, surface}} \approx 25 \mu\text{m}$. The donor dye was excited with a laser power of $40 \mu\text{W}$ at a wavelength of 488 nm .

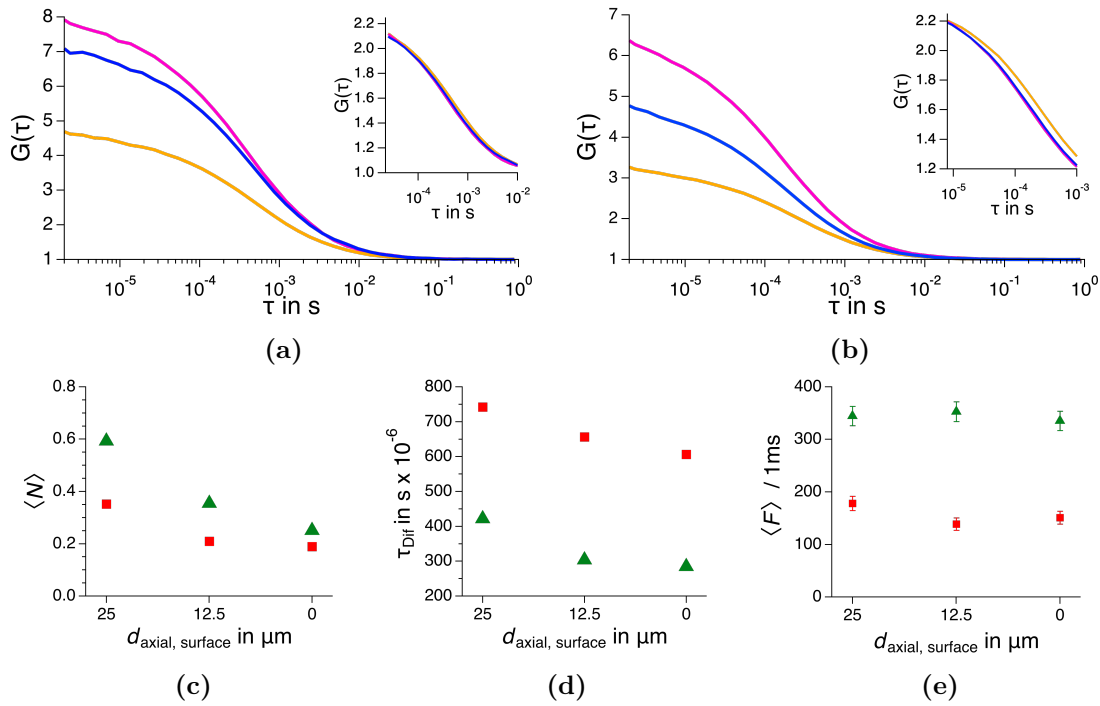


Fig. A.4: FCS results of EsxF measurements at three different focus positions within the sample volume of the capillary. The positions differ in their axial distances to the surface of the capillary wall $d_{\text{axial, surface}}$ with distances of $d_{\text{axial, surface}} \approx 25 \mu\text{m}$ (purple), $d_{\text{axial, surface}} \approx 12.5 \mu\text{m}$ and $d_{\text{axial, surface}} \approx 0 \mu\text{m}$ (cyan). (a,b) show the auto-correlation functions of the acceptor and donor, respectively. Insets show the correlation curves, normalized to the average number of molecules. (c-e) show the average number of molecules $\langle N \rangle$, diffusion times τ_{Dif} and average number of photons $\langle F \rangle$ per 1 ms time bin of the donor (green) and acceptor (red) channel obtained from fits according to Eq. 3.10.

A.4 Prothymosin alpha

A.4.1 Interval analysis of prothymosin alpha

In order to evaluate if certain parameters are changing during the 33 hour long measurement of ProT α (see subsection 5.1.4), consecutive intervals of the experiment with a length of 3 hours are analyzed individually. The results are shown in Fig. A.5 and Fig. A.6. Correlation functions were globally fitted with Eq. 3.13 including three exponentials. Despite the diffusion time τ_{Dif} and average number of molecules in the focal volume $\langle N \rangle$, which were obtained from the whole photon data, the other parameters were derived from filtered correlation functions. These were calculated with all photons belonging to the high FRET peak with a cut off FRET efficiency of $E_T = 0.3$.

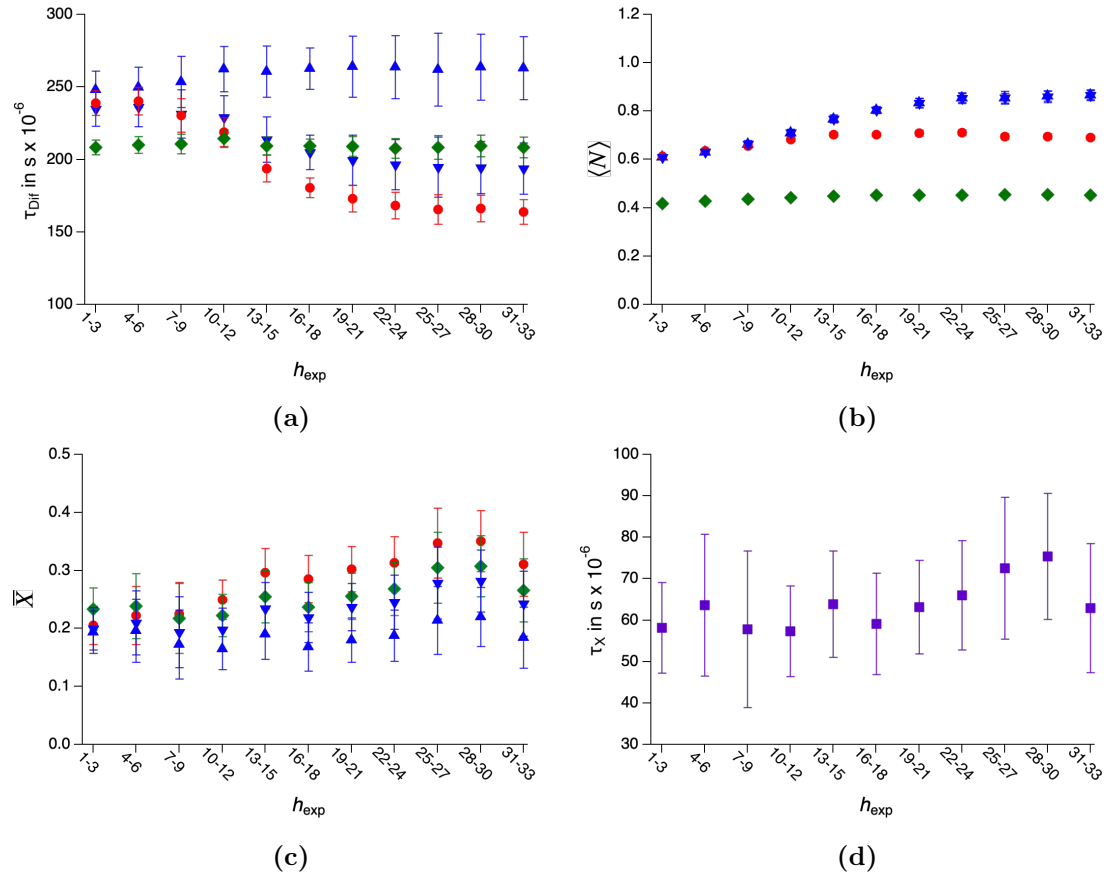


Fig. A.5: Results of interval analysis of different hours of the experiment h_{exp} of a 33 hour long measurement of ProT α : (a) diffusion time τ_{Dif} , (b) average number of molecules $\langle N \rangle$, (c) fraction of the process additionally assigned to diffusion \bar{X} and (d) relaxation time of process X τ_X .

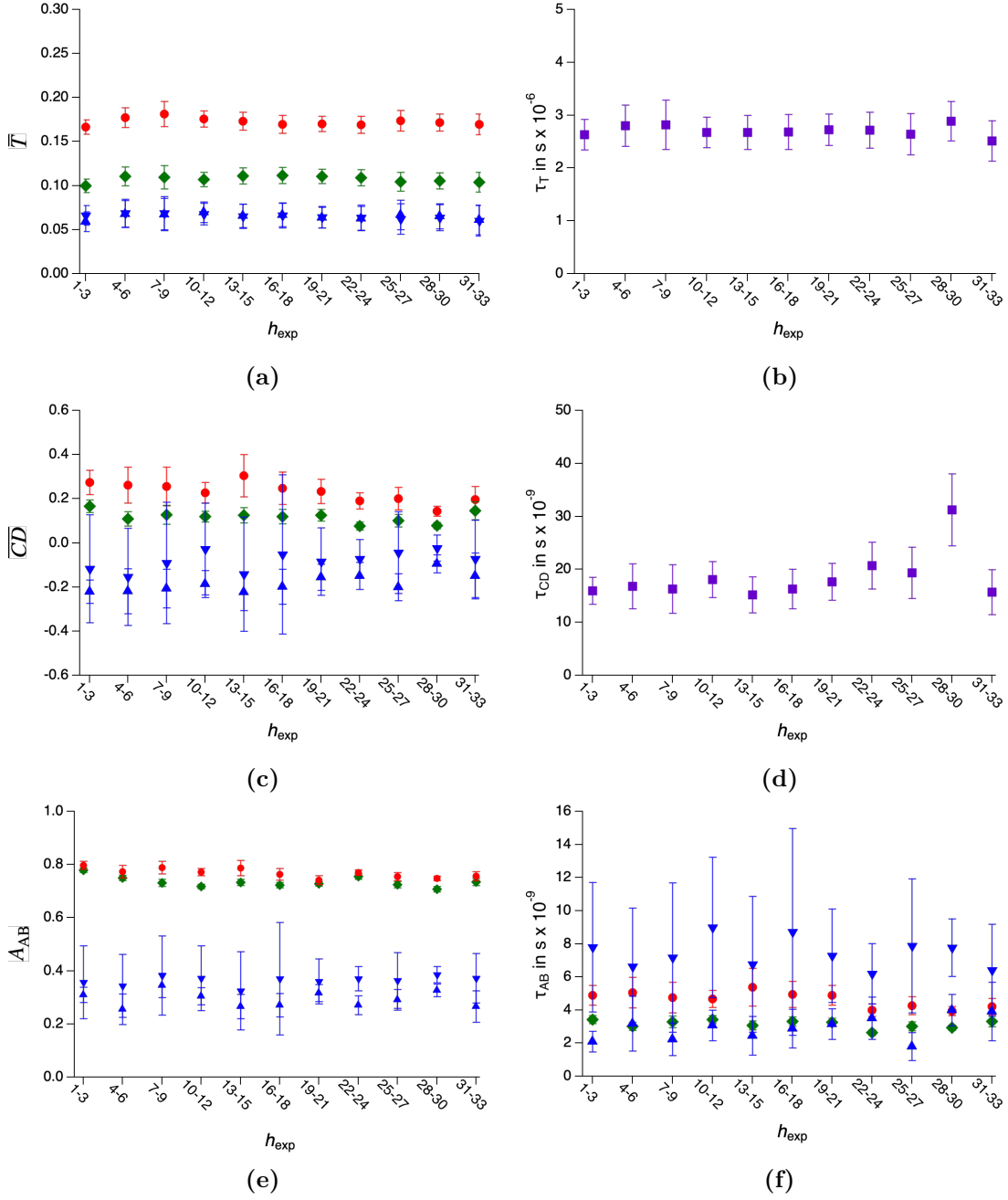


Fig. A.6: Results of interval analysis of different hours of the experiment h_{exp} of a 33 hour long measurement of ProT α : (a) triplet fraction \bar{T} , (b) triplet relaxation time τ_T , (c) fraction of chain dynamics \bar{CD} , (d) chain reconfiguration time τ_{CD} , (e) amplitude of fluorescence antibunching A_{AB} and (f) the time constant of fluorescence antibunching τ_{AB} .

A.4.2 Influence of the measurement duration for prothymosin alpha

In addition to the analysis of 3 hour intervals, different durations of the experiment were mimicked by not analyzing the whole photon data, but the first 3 hours, 6 hours or 9 hours and so on. The results are shown in Fig. A.7 and Fig. A.8. Correlation functions were globally fitted with Eq. 3.13 including three exponentials. Despite the diffusion time τ_{Dif} and average number of molecules in the focal volume $\langle N \rangle$, which were obtained from the whole photon data, the other parameters were derived from filtered correlation functions. These were calculated with all photons belonging to the high FRET peak with a cut off FRET efficiency of $E_T = 0.3$.

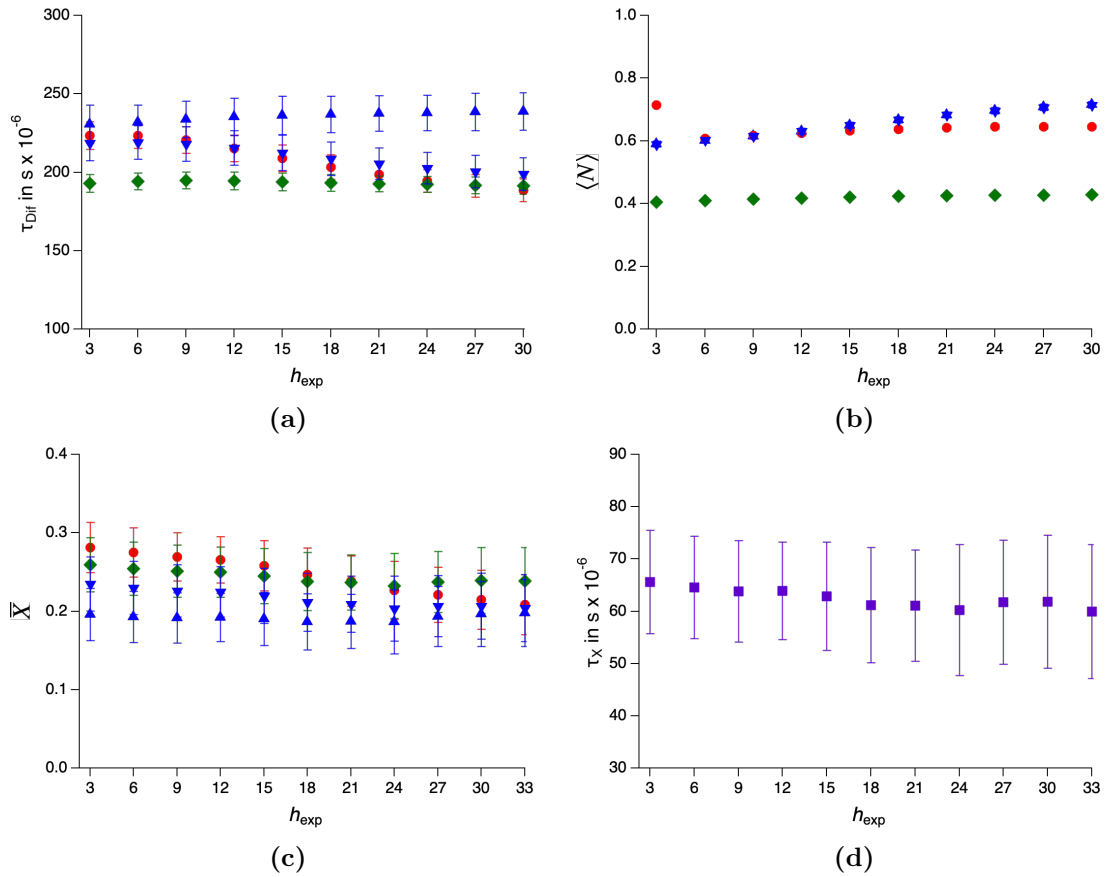


Fig. A.7: Results of the analysis of intervals of a 33 hour nsFRET-FCS measurement of ProT α with different lengths h_{exp} :(a) diffusion time τ_{Dif} , (b) average number of molecules $\langle N \rangle$, (c) fraction of the process additionally assigned to diffusion \bar{X} and (d) relaxation time of process X τ_X .

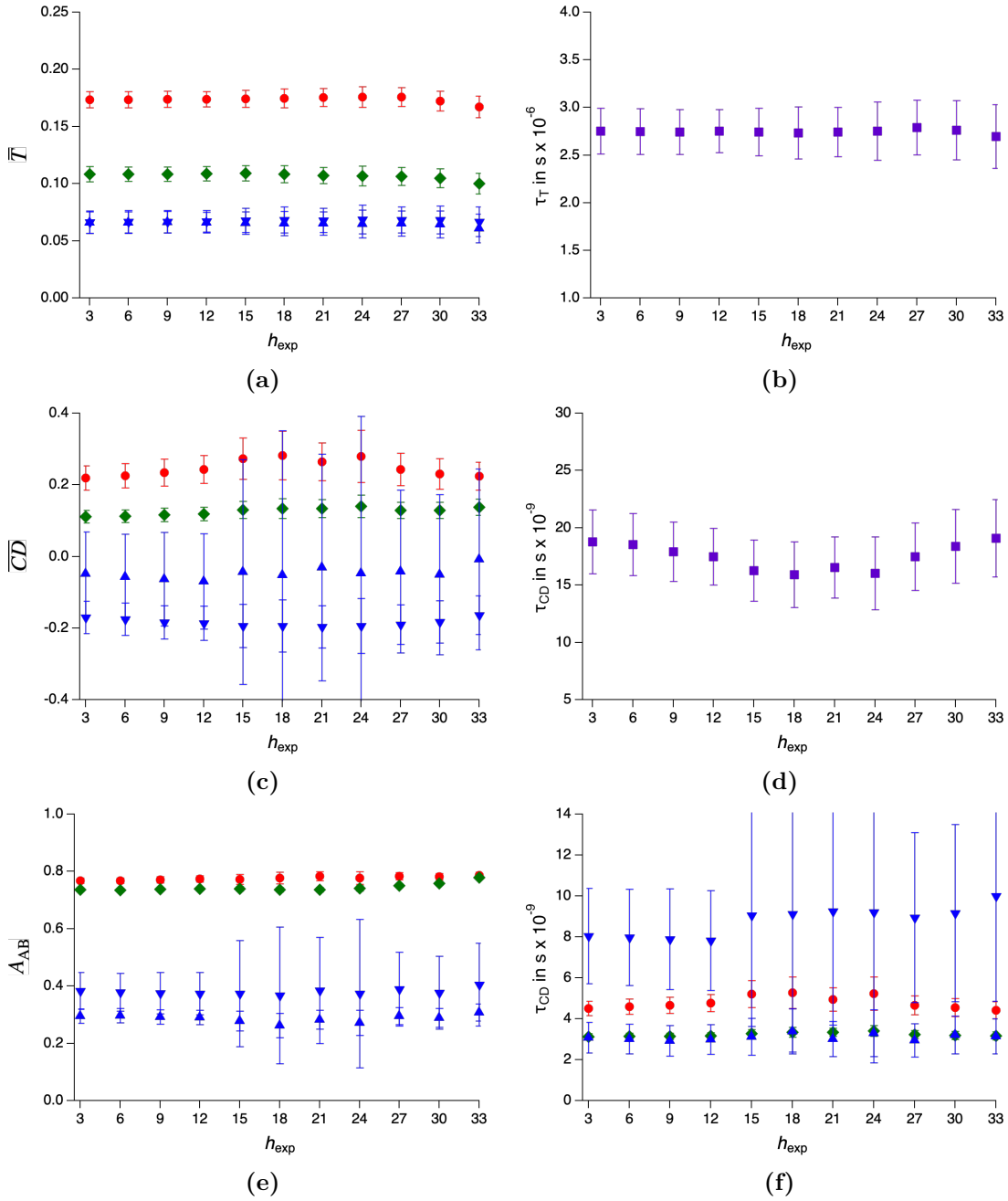


Fig. A.8: Results of the analysis of intervals of a 33 hour nsFRET-FCS measurement of ProT α with different lengths h_{exp} : (a) fraction of chain dynamics \overline{CD} , (b) relaxation time of chain dynamics τ_{CD} , (c) amplitude of fluorescence antibunching A_{AB} and (d) antibunching lifetime τ_{AB} .

List of Figures

2.1	Jablonski diagram	8
2.2	Effective ISC rate in dependence on the laser power	10
2.3	Franck-Condon principle	11
2.4	Stokes shift	12
2.5	Exponential decay of fluorescence intensity	14
2.6	Stern-Volmer relation	16
2.7	Effects of static and dynamic quenching on fluorescence intensity . . .	17
2.8	Pressure dependence of the refractive index of water	19
2.9	Sketch of a confocal microscope by Marvin Minsky	20
2.10	Confocal microscope with epi-illumination	20
2.11	Illustration of a Gaussian beam	22
2.12	Observation volume in confocal microscopy	24
2.13	Airy disk and its radial intensity distribution	25
2.14	Two light sources at the Rayleigh criterion and their intensity distribution	26
2.15	PSFs of a conventional and confocal microscope	27
2.16	Signal-to-noise ratio	30
2.17	Basic Jablonski diagram for FRET	32
2.18	FRET efficiency as a function of the donor-acceptor distance	34
2.19	Overlap integral between donor and acceptor	36
2.20	Orientation factor in FRET	37
2.21	Comparison of en- and smFRET	38
2.22	Fluorescence fluctuations for different dye concentrations	40
2.23	Correlation curve for diffusion	42
2.24	Simplified Jablonski diagram for the rates involved to describe the transition to the triplet state.	44
2.25	Correlation functions for diffusion and triplet dynamics	45
2.26	Correlation curve for nsFCS	46
2.27	Basic structure of amino acid	48
2.28	Amino acid sequence of the cold shock protein from the hyperthermophilic bacterium <i>Thermotoga Maritima</i>	49
2.29	Alpha-helix and beta sheet structures of proteins	49
2.30	Structure of the cold shock protein <i>Thermotoga Maritima</i>	50
2.31	Cro-protein as an example of a homodimer	51
2.32	Sequence and AlphaFold structure prediction of the sperm histone protein	52

2.33	Number of new publications related to intrinsically disordered proteins	52
2.34	Sequence and AlphaFold structure prediction of ProT α	53
2.35	Visualization of different energy landscape concepts	55
2.36	Free energy surface of a protein	59
3.1	Scheme of the experimental setup	62
3.2	Detection efficiencies of SPCM-AQR-14 and C11202-100 APDs	64
3.3	Schematic drawing and 3D rendering of the high-pressure setup	65
3.4	Schematic cross section of the fused silica capillary	66
3.5	Refractive index of fused silica, a fused silica matching liquid and borosilicate glass	66
3.6	Pictures of a fused silica capillary with sample solution	67
3.7	Capillary preparation and handling protocol	68
3.8	Illustration of aberrations when using a bare square capillary	69
3.9	Dependence of the optimal fused silica coverslip thickness on the angle of incidence of an objective corrected for borosilicate coverslips	70
3.10	Schematic illustration of the optical multi layer (OML)	71
3.11	Reuse protocol of pressure plugs	72
3.12	Comparison of FCS auto-correlations using Timeharp200 from Picoquant and SPC-134 from BeckerHickl	73
3.13	Data structure of events recorded by the GPX-TDC	74
3.14	Example of the binary representation of a recorded event of the GPX-TDC	75
3.15	Comparison of FCS auto- and pseudo auto-correlation functions using the GPX-TDC	75
3.16	3D rendering of the previous capillary connection solution	76
3.17	3D rendering of the new designed sample stage	78
3.18	Absorption and emission spectra of AT488 and A647N	79
3.19	Absorption and emission spectra of Cy5, AF488, AF594 and AF647	80
3.20	Excitation of emission spectra of TetraSpeck TM Microspheres T7279	81
3.21	Sequence of the dsDNA from metabion	82
3.22	Sequence and structure of the DNA hairpin	82
3.23	3/4-stranded DNA hybrids	83
3.24	Sequence and structure of the cold shock protein CspA	84
3.25	Sequence and AlphaFold structure prediction of ProT α	85
3.26	Calling sequence of GPX-TDC subVIs in LabVIEW	86
3.27	Normalized correlation functions of AF488, 3-stranded DNA hybrid, DNA hairpin and ProT α	87
3.28	Processing of raw data arrays in LabVIEW	88
3.29	Data structure of photon events processed in LabVIEW	88
3.30	Overflow detection in LabVIEW	89
3.31	Histogram of photon arrival times with respect to a laser pulse	90
3.32	Example of FRET efficiency histograms including Gaussian fits	96

4.1	Auto-correlation functions and fit results of AF488 processed with the Timeharp200 and GPX-TDC	98
4.2	Excitation benchmark comparison of the Timeharp200 and the GPX-TDC	100
4.3	Detection benchmark comparison of the Timeharp200 and the GPX-TDC	101
4.4	Detection characteristics of counting electronics	103
4.5	Fluorescence antibunching time constants of free diffusing AF488 at multiple excitation photon flux densities	104
4.6	Uncorrected and corrected auto-correlations of AF488	105
4.7	Histograms of time differences of two consecutive photons detected with two different APDs	106
4.8	Correlation functions of the 3-stranded DNA hybrid with differences between corrected and uncorrected photon arrival times	107
4.9	FCS fit results using different detector types	108
4.10	Effective detection efficiency of AF488 and afterpulsing of both APD types	109
4.11	Example time trace without a immersion water protection device	110
4.12	3D drawing of the immersion water protection device	111
4.13	Example time trace with immersion water protection device	112
4.14	Rendering of the immersion water protection assembly for bare capillary experiments	113
4.15	Cross section images and renderings of different orientations of a square capillary	114
4.16	Rendering of the 3D-printed capillary holder	116
4.17	FRET histograms of fluorescent microsphere measurements made with a borosilicate coverslip, the PMMA multi layer, a bare capillary and a PMMA coverslip	117
4.18	Comparison of $\langle N \rangle$, Q_{FRET} and ϵ_{MB} of different assemblies evaluating the application of PMMA film	118
4.19	Diffusion times of fluorescent microspheres using multiple optical assemblies	119
4.20	FCS and FRET results of experiments of fluorescent microspheres using three different optical assemblies	120
4.21	FCS results of free diffusing AF488 using four different optical assemblies	121
4.22	Cross section images of a PMMA film and PMMA multi layer	123
4.23	Correction collar influence when using a bare square capillary	125
4.24	Correction collar influence when using the optical multi layer	126
4.25	Illustration of different evaluated focus positions within the sample volume of a capillary	128
4.26	FCS results of 20 minute experiments of the 3-stranded DNA hybrid at different focus positions inside the sample volume of the capillary.	129

5.1	FRET efficiency histograms of the 3- and 4-stranded DNA hybrid . . .	131
5.2	Correlation functions of the 3- and 4-stranded DNA hybrid	132
5.3	Diffusion times, antibunching time constants and relaxation times of involved processes with their respective fractions of the 3-stranded and 4-stranded DNA hybrid	133
5.4	FRET efficiency histogram and correlation functions of a nsFRET- FCS experiment of the DNA hairpin	136
5.5	Results of a nsFRET-FCS experiment of the DNA hairpin	137
5.6	Results of a nsFRET-FCS experiment of CspA	138
5.7	Filtered nsFRET-FCS analysis of CspA	139
5.8	FRET-nsFCS results of a 33 hour measurement of ProT α with a borosilicate coverslip	141
5.9	Filtered nsFRET-FCS analysis of ProT α	142
5.10	Interval analysis of a 33 hour ProT α experiment	143
5.11	Comparison of acceptor-donor cross-correlation functions of the first three and last three hours of a 33 hour measurement of ProT α	143
5.12	Photon count rates of ProT α with BME and FRET efficiency his- togram without BME in the buffer	144
5.13	FRET efficiency histogram, cross-correlation functions and diffusion times of ProT α	147
5.14	Correlation functions of a 16 hour nsFRET-FCS measurement of ProT α with increased buffer viscosity	147
5.15	Fit results of nsFRET-FCS measurements of ProT α in TRIS buffer without and with glycerol	148
5.16	FRET efficiency histograms of the 3-stranded DNA hybrid at multiple hydrostatic pressures	149
5.17	Diffusion times of the 3-stranded DNA hybrid at different pressures .	150
5.18	Results of a 10 hour 1000 bar experiment of the 3-stranded DNA hairpin	151
5.19	Fit results of nsFRET-FCS measurements of the 3-stranded DNA hybrid	152
5.20	FRET histograms of ProT α at multiple hydrostatic pressure from 30 minute measurements	153
5.21	Apparent diffusion times of 30 minute measurements of ProT α at multiple pressures	154
5.22	FRET efficiency distributions of ProT α experiments at multiple hy- drostatic pressures	155
5.23	Correlation functions of 16 hour high pressure nsFRET-FCS mea- surements of ProT α at pressures of 1 bar, 1000 bar, 1500 bar and 2000 bar	156
5.24	Diffusion times and fluorescence antibunching time constants of ProT α at multiple pressures p using the optical multi layer (OML) and a borosilicate coverslip	157

5.25	Determined fit parameters of 16 hour ProT α nsFRET-FCS experiments at different pressures using a borosilicate coverslip and the OML	159
A.1	Fit results of fluorescence antibunching of FCS benchmark measurements of AF488	172
A.2	Custom function in Igor Pro processing photon raw data	173
A.3	Custom function in Igor Pro extracting time stamps of photons belonging to certain FRET efficiencies	174
A.4	FCS results of EsxF measurements at different focus positions within the capillary	175
A.5	Results of interval analysis of a 33 hour experiment of ProT α	176
A.6	Results of interval analysis of a 33 hour experiment of ProT α	177
A.7	Correlation analysis of intervals of different length of a 33 hour measurement of ProT α	178
A.8	Correlation analysis of intervals of different length of a 33 hour measurement of ProT α	179

List of Tables

2.1	Overview of depopulation pathways of excited fluorophores	7
3.1	Characteristics of used dyes	80
3.2	Components and pH of used buffers	85
3.3	Overview of linked fit parameters of auto- and cross-correlation functions during a nsFRET-FCS global fit	94
4.1	Fit results of the molecular brightness from benchmark experiments with AF488	102
4.2	Determined time differences between two subsequent photons, detected by different APDs	107
A.1	Laser excitation powers and measurement durations of FCS benchmarks	171

References

- [1] Jan Kubelka, James Hofrichter, and William A Eaton. The protein folding 'speed limit'. *Curr Opin Struct Biol*, 14(1):76–88, Feb 2004.
- [2] H.A. Kramers. Brownian motion in a field of force and the diffusion model of chemical reactions. *Physica*, 7(4):284–304, 1940.
- [3] Eli Pollak and Peter Talkner. Reaction rate theory: what it was, where is it today, and where is it going? *Chaos*, 15(2):26116, Jun 2005.
- [4] Sven Schneider, Hauke Paulsen, Kim Colin Reiter, Erik Hinze, Cordelia Schiene-Fischer, and Christian G. Hübner. Single molecule fret investigation of pressure-driven unfolding of cold shock protein a. *The Journal of Chemical Physics*, 148(12):123336, 2018.
- [5] Sven Schneider. *High pressure Single Molecule FRET*. PhD thesis, Universität zu Lübeck, 2017.
- [6] Alessandro Borgia, Madeleine B. Borgia, Katrine Bugge, Vera M. Kissling, Pétur O. Heidarsson, Catarina B. Fernandes, Andrea Sottini, Andrea Soranno, Karin J. Buholzer, Daniel Nettels, Birthe B. Kragelund, Robert B. Best, and Benjamin Schuler. Extreme disorder in an ultrahigh-affinity protein complex. *Nature*, 555(7694):61–66, 2018.
- [7] Andrea Soranno, Andrea Holla, Fabian Dingfelder, Daniel Nettels, Dmitrii E. Makarov, and Benjamin Schuler. Integrated view of internal friction in unfolded proteins from single-molecule fret, contact quenching, theory, and simulations. *Proceedings of the National Academy of Sciences*, 114(10):E1833–E1839, 2017.
- [8] Andrea Soranno, Brigitte Buchli, Daniel Nettels, Ryan R. Cheng, Sonja Müller-Späth, Shawn H. Pfeil, Armin Hoffmann, Everett A. Lipman, Dmitrii E. Makarov, and Benjamin Schuler. Quantifying internal friction in unfolded and intrinsically disordered proteins with single-molecule spectroscopy. *Proceedings of the National Academy of Sciences*, 109(44):17800–17806, 2012.
- [9] J. Buchner and T. Kiefhaber, editors. *Protein Folding Handbook*. Wiley-VCH Verlag GmbH, 2008.

- [10] L PAULING, R B COREY, and H R BRANSON. The structure of proteins; two hydrogen-bonded helical configurations of the polypeptide chain. *Proc Natl Acad Sci U S A*, 37(4):205–211, Apr 1951.
- [11] Emil Fischer. Einfluss der configuration auf die wirkung der enzyme. *Berichte der deutschen chemischen Gesellschaft*, 27(3):2985–2993, 1894.
- [12] C B Anfinsen. Principles that govern the folding of protein chains. *Science*, 181(4096):223–230, Jul 1973.
- [13] C B ANFINSEN, E HABER, M SELA, and F H Jr WHITE. The kinetics of formation of native ribonuclease during oxidation of the reduced polypeptide chain. *Proc Natl Acad Sci U S A*, 47(9):1309–1314, Sep 1961.
- [14] C B Anfinsen. The formation and stabilization of protein structure. *Biochemical Journal*, 128(4):737–749, 07 1972.
- [15] Levinthal, Cyrus. Are there pathways for protein folding? *J. Chim. Phys.*, 65:44–45, 1968.
- [16] Shu-Qun Liu, Xing-Lai Ji, Yan Tao, De-Yong Tan, Ke-Qin Zhang, and Yun-Xin Fu. *Protein Folding, Binding and Energy Landscape: A Synthesis*. 02 2012.
- [17] Martin Karplus. The levinthal paradox: yesterday and today. *Folding and Design*, 2:S69–S75, 1997.
- [18] R Zwanzig, A Szabo, and B Bagchi. Levinthal's paradox. *Proc Natl Acad Sci U S A*, 89(1):20–22, Jan 1992.
- [19] J D Bryngelson, J N Onuchic, N D Socci, and P G Wolynes. Funnels, pathways, and the energy landscape of protein folding: a synthesis. *Proteins*, 21(3):167–195, Mar 1995.
- [20] W A Eaton. Searching for "downhill scenarios" in protein folding. *Proc Natl Acad Sci U S A*, 96(11):5897–5899, May 1999.
- [21] Victor Muñoz and Michele Cerminara. When fast is better: protein folding fundamentals and mechanisms from ultrafast approaches. *Biochemical Journal*, 473(17):2545–2559, 08 2016.
- [22] Maria M Garcia-Mira, Mourad Sadqi, Niels Fischer, Jose M Sanchez-Ruiz, and Victor Muñoz. Experimental identification of downhill protein folding. *Science*, 298(5601):2191–2195, Dec 2002.
- [23] S J Hagen, J Hofrichter, A Szabo, and W A Eaton. Diffusion-limited contact formation in unfolded cytochrome c: estimating the maximum rate of protein folding. *Proc Natl Acad Sci U S A*, 93(21):11615–11617, Oct 1996.
- [24] Benjamin Schuler and William A Eaton. Protein folding studied by single-molecule fret. *Curr Opin Struct Biol*, 18(1):16–26, Feb 2008.

- [25] Bojan Zagrovic, Christopher D. Snow, Michael R. Shirts, and Vijay S. Pande. Simulation of folding of a small alpha-helical protein in atomistic detail using worldwide-distributed computing. *Journal of Molecular Biology*, 323(5):927–937, 2002.
- [26] Christopher D Snow, Bojan Zagrovic, and Vijay S Pande. The trp cage: folding kinetics and unfolded state topology via molecular dynamics simulations. *J Am Chem Soc*, 124(49):14548–14549, Dec 2002.
- [27] Christopher D Snow, Houbi Nguyen, Vijay S Pande, and Martin Gruebele. Absolute comparison of simulated and experimental protein-folding dynamics. *Nature*, 420(6911):102–106, Nov 2002.
- [28] Jan Kubelka, William A Eaton, and James Hofrichter. Experimental tests of villin subdomain folding simulations. *J Mol Biol*, 329(4):625–630, Jun 2003.
- [29] Linlin Qiu, Suzette A Pabit, Adrian E Roitberg, and Stephen J Hagen. Smaller and faster: the 20-residue trp-cage protein folds in 4 micros. *J Am Chem Soc*, 124(44):12952–12953, Nov 2002.
- [30] Benjamin Schuler. Perspective: Chain dynamics of unfolded and intrinsically disordered proteins from nanosecond fluorescence correlation spectroscopy combined with single-molecule fret. *The Journal of Chemical Physics*, 149(1):010901, 2018.
- [31] Benjamin Schuler and Hagen Hofmann. Single-molecule spectroscopy of protein folding dynamics—expanding scope and timescales. *Curr Opin Struct Biol*, 23(1):36–47, Feb 2013.
- [32] K A Dill and D Shortle. Denatured states of proteins. *Annu Rev Biochem*, 60:795–825, 1991.
- [33] A Keith Dunker, M Madan Babu, Elisar Barbar, Martin Blackledge, Sarah E Bondos, Zsuzsanna Dosztányi, H Jane Dyson, Julie Forman-Kay, Monika Fuxreiter, Jörg Gsponer, Kyou-Hoon Han, David T Jones, Sonia Longhi, Steven J Metallo, Ken Nishikawa, Ruth Nussinov, Zoran Obradovic, Rohit V Pappu, Burkhard Rost, Philipp Selenko, Vinod Subramaniam, Joel L Sussman, Peter Tompa, and Vladimir N Uversky. What’s in a name? why these proteins are intrinsically disordered: Why these proteins are intrinsically disordered. *Intrinsically Disord Proteins*, 1(1):e24157, Jan-Dec 2013.
- [34] Sarah C Bickers, Jonathan S Sayewich, and Voula Kanelis. Intrinsically disordered regions regulate the activities of atp binding cassette transporters. *Biochim Biophys Acta Biomembr*, 1862(6):183202, Jun 2020.
- [35] Sagie Brodsky, Tamar Jana, Karin Mittelman, Michal Chapal, Divya Krishna Kumar, Miri Carmi, and Naama Barkai. Intrinsically disordered regions direct transcription factor in vivo binding specificity. *Mol Cell*, 79(3):459–471, Aug 2020.

- [36] H. Jane Dyson and Peter E. Wright. Intrinsically unstructured proteins and their functions. *Nature Reviews Molecular Cell Biology*, 6(3):197–208, 2005.
- [37] Vincent J Hilser and E Brad Thompson. Intrinsic disorder as a mechanism to optimize allosteric coupling in proteins. *Proc Natl Acad Sci U S A*, 104(20):8311–8315, May 2007.
- [38] V.N. Uversky. *Intrinsically Disordered Proteins*. SpringerBriefs in Molecular Science. Springer International Publishing, 2014.
- [39] Francois-Xavier Theillet, Andres Binolfi, Tamara Frembgen-Kesner, Karan Hingorani, Mohona Sarkar, Ciara Kyne, Conggang Li, Peter B Crowley, Lila Gierasch, Gary J Pielak, Adrian H Elcock, Anne Gershenson, and Philipp Selenko. Physicochemical properties of cells and their effects on intrinsically disordered proteins (idps). *Chem Rev*, 114(13):6661–6714, Jul 2014.
- [40] C.M. Gomes and P.F.N. Faisca. *Protein Folding: An Introduction*. Springer-Briefs in Molecular Science. Springer International Publishing, 2019.
- [41] E. Brooks Shera, Newton K. Seitzinger, Lloyd M. Davis, Richard A. Keller, and Steven A. Soper. Detection of single fluorescent molecules. *Chemical Physics Letters*, 174(6):553–557, 1990.
- [42] W. E. Moerner, Yoav Shechtman, and Quan Wang. Single-molecule spectroscopy and imaging over the decades. *Faraday Discuss.*, 184:9–36, 2015.
- [43] Benjamin Schuler, Sonja Müller-Späth, Andrea Soranno, and Daniel Nettels. *Application of Confocal Single-Molecule FRET to Intrinsically Disordered Proteins*, pages 21–45. Springer New York, New York, NY, 2012.
- [44] Allan Chris M Ferreon, Yann Gambin, Edward A Lemke, and Ashok A Deniz. Interplay of alpha-synuclein binding and conformational switching probed by single-molecule fluorescence. *Proc Natl Acad Sci U S A*, 106(14):5645–5650, Apr 2009.
- [45] Joseph R. Lakowicz. *Principles of Fluorescence Spectroscopy*. Springer, 3 edition, 2006.
- [46] Markus Sauer, Johan Hofkens, and Jörg Enderlein. *Handbook of Fluorescence Spectroscopy and Imaging: From Single Molecules to Ensembles*. 02 2011.
- [47] Bernard Valeur. *Molecular Fluorescence: Principles and Applications*. Wiley-VCH Verlag GmbH, 2001.
- [48] Theodor Förster. Zwischenmolekulare energiewanderung und fluoreszenz. *Annalen der Physik*, 437(1-2):55–75, 1948.
- [49] L Stryer and R P Haugland. Energy transfer: a spectroscopic ruler. *Proc Natl Acad Sci U S A*, 58(2):719–726, Aug 1967.

- [50] T Ha, T Enderle, D F Ogletree, D S Chemla, P R Selvin, and S Weiss. Probing the interaction between two single molecules: fluorescence resonance energy transfer between a single donor and a single acceptor. *Proc Natl Acad Sci U S A*, 93(13):6264–6268, Jun 1996.
- [51] A A Deniz, T A Laurence, G S Beligere, M Dahan, A B Martin, D S Chemla, P E Dawson, P G Schultz, and S Weiss. Single-molecule protein folding: diffusion fluorescence resonance energy transfer studies of the denaturation of chymotrypsin inhibitor 2. *Proc Natl Acad Sci U S A*, 97(10):5179–5184, May 2000.
- [52] Benjamin Schuler, Everett A Lipman, and William A Eaton. Probing the free-energy surface for protein folding with single-molecule fluorescence spectroscopy. *Nature*, 419(6908):743–747, Oct 2002.
- [53] Benjamin Schuler, Andrea Soranno, Hagen Hofmann, and Daniel Nettels. Single-molecule fret spectroscopy and the polymer physics of unfolded and intrinsically disordered proteins. *Annual Review of Biophysics*, 45(1):207–231, 2016. PMID: 27145874.
- [54] Liming Ying, Jeremy J. Green, Haitao Li, David Klenerman, and Shankar Balasubramanian. Studies on the structure and dynamics of the human telomeric g quadruplex by single-molecule fluorescence resonance energy transfer. *Proceedings of the National Academy of Sciences*, 100(25):14629–14634, 2003.
- [55] Sean A. McKinney, Anne-Cécile Déclais, David M. J. Lilley, and Taekjip Ha. Structural dynamics of individual holliday junctions. *Nature Structural Biology*, 10(2):93–97, 2003.
- [56] X Zhuang, L E Bartley, H P Babcock, R Russell, T Ha, D Herschlag, and S Chu. A single-molecule study of rna catalysis and folding. *Science*, 288(5473):2048–2051, Jun 2000.
- [57] Xiaowei Zhuang, Harold Kim, Miguel J B Pereira, Hazen P Babcock, Nils G Walter, and Steven Chu. Correlating structural dynamics and function in single ribozyme molecules. *Science*, 296(5572):1473–1476, May 2002.
- [58] Gregory Bokinsky, David Rueda, Vinod K Misra, Maria M Rhodes, Andrew Gordus, Hazen P Babcock, Nils G Walter, and Xiaowei Zhuang. Single-molecule transition-state analysis of rna folding. *Proc Natl Acad Sci U S A*, 100(16):9302–9307, Aug 2003.
- [59] Elliot Tan, Timothy J Wilson, Michelle K Nahas, Robert M Clegg, David M J Lilley, and Taekjip Ha. A four-way junction accelerates hairpin ribozyme folding via a discrete intermediate. *Proc Natl Acad Sci U S A*, 100(16):9308–9313, Aug 2003.

- [60] Taekjip Ha, Ivan Rasnik, Wei Cheng, Hazen P Babcock, George H Gauss, Timothy M Lohman, and Steven Chu. Initiation and re-initiation of dna unwinding by the escherichia coli rep helicase. *Nature*, 419(6907):638–641, Oct 2002.
- [61] M. Margittai, J. Widengren, E. Schweinberger, G. F. Schröder, S. Felekyan, E. Haustein, M. König, D. Fasshauer, H. Grubmüller, R. Jahn, and C. A. M. Seidel. Single-molecule fluorescence resonance energy transfer reveals a dynamic equilibrium between closed and open conformations of syntaxin 1. *Proceedings of the National Academy of Sciences*, 100(26):15516–15521, 2003.
- [62] Michael Börsch, Manuel Diez, Boris Zimmermann, Rolf Reuter, and Peter Gräber. Stepwise rotation of the gamma-subunit of ef(0)f(1)-atp synthase observed by intramolecular single-molecule fluorescence resonance energy transfer. *FEBS Lett*, 527(1-3):147–152, Sep 2002.
- [63] Keith Weninger, Mark E. Bowen, Steven Chu, and Axel T. Brunger. Single-molecule studies of snare complex assembly reveal parallel and antiparallel configurations. *Proceedings of the National Academy of Sciences*, 100(25):14800–14805, 2003.
- [64] Mikayel Aznauryan, Daniel Nettels, Andrea Holla, Hagen Hofmann, and Benjamin Schuler. Single-molecule spectroscopy of cold denaturation and the temperature-induced collapse of unfolded proteins. *J Am Chem Soc*, 135(38):14040–14043, Sep 2013.
- [65] D S Talaga, W L Lau, H Roder, J Tang, Y Jia, W F DeGrado, and R M Hochstrasser. Dynamics and folding of single two-stranded coiled-coil peptides studied by fluorescent energy transfer confocal microscopy. *Proc Natl Acad Sci U S A*, 97(24):13021–13026, Nov 2000.
- [66] E. Shane Price, Matthew S. DeVore, and Carey K. Johnson. Detecting intramolecular dynamics and multiple förster resonance energy transfer states by fluorescence correlation spectroscopy. *The Journal of Physical Chemistry B*, 114(17):5895–5902, 05 2010.
- [67] E. Shane Price, Marek Aleksiejew, and Carey K. Johnson. FRET-FCS detection of intralobe dynamics in calmodulin. *The Journal of Physical Chemistry B*, 115(29):9320–9326, 07 2011.
- [68] Harekrushna Sahoo and Petra Schwille. Fret and fcs—friends or foes? *ChemPhysChem*, 12(3):532–541, 2011.
- [69] Brian D. Slaughter, Michael W. Allen, Jay R. Unruh, Ramona J. Bieber Urbauer, and Carey K. Johnson. Single-molecule resonance energy transfer and fluorescence correlation spectroscopy of calmodulin in solution. *The Journal of Physical Chemistry B*, 108(29):10388–10397, 07 2004.

- [70] Tedman Torres and Marcia Levitus. Measuring conformational dynamics: A new fcs-fret approach. *The Journal of Physical Chemistry B*, 111(25):7392–7400, 06 2007.
- [71] Elke Haustein and Petra Schwille. Single-molecule spectroscopic methods. *Curr Opin Struct Biol*, 14(5):531–540, Oct 2004.
- [72] Oleg Krichevsky and Grégoire Bonnet. Fluorescence correlation spectroscopy: the technique and its applications. *Reports on Progress in Physics*, 65(2):251–297, jan 2002.
- [73] R. Rigler, Ü. Mets, J. Widengren, and P. Kask. Fluorescence correlation spectroscopy with high count rate and low background: analysis of translational diffusion. *European Biophysics Journal*, 22(3):169–175, 1993.
- [74] Daniel Nettels, Armin Hoffmann, and Benjamin Schuler. Unfolded protein and peptide dynamics investigated with single-molecule fret and correlation spectroscopy from picoseconds to seconds. *The Journal of Physical Chemistry B*, 112(19):6137–6146, 05 2008.
- [75] Irina V. Gopich, Daniel Nettels, Benjamin Schuler, and Attila Szabo. Protein dynamics from single-molecule fluorescence intensity correlation functions. *The Journal of Chemical Physics*, 131(9):095102, 09 2009.
- [76] Armin Hoffmann, Avinash Kane, Daniel Nettels, David E Hertzog, Peter Baumgärtel, Jan Lengefeld, Gerd Reichardt, David A Horsley, Robert Seckler, Olgica Bakajin, and Benjamin Schuler. Mapping protein collapse with single-molecule fluorescence and kinetic synchrotron radiation circular dichroism spectroscopy. *Proc Natl Acad Sci U S A*, 104(1):105–110, Jan 2007.
- [77] Nüesch, Mark F. and Ivanović, MilošT. and Claude, Jean-Benoît and Nettels, Daniel and Best, Robert B. and Wenger, Jérôme and Schuler, Benjamin. Single-molecule detection of ultrafast biomolecular dynamics with nanophotonics. *Journal of the American Chemical Society*, 144(1):52–56, 01 2022.
- [78] Alessandro Borgia, Beth G. Wensley, Andrea Soranno, Daniel Nettels, Madeleine B. Borgia, Armin Hoffmann, Shawn H. Pfeil, Everett A. Lipman, Jane Clarke, and Benjamin Schuler. Localizing internal friction along the reaction coordinate of protein folding by combining ensemble and single-molecule fluorescence spectroscopy. *Nature Communications*, 3(1):1195, 2012.
- [79] Daniel Nettels, Irina V. Gopich, Armin Hoffmann, and Benjamin Schuler. Ultrafast dynamics of protein collapse from single-molecule photon statistics. *Proceedings of the National Academy of Sciences*, 104(8):2655–2660, 2007.
- [80] M. Doi and H. See. *Introduction to Polymer Physics*. Introduction to Polymer Physics. Clarendon Press, 1996.

- [81] P. W. Bridgman. The coagulation of albumen by pressure. *Journal of Biological Chemistry*, 19(4):511–512, 2024/02/23 1914.
- [82] Alejandro A. Jr. Paladini and Gregorio Weber. Pressure-induced reversible dissociation of enolase. *Biochemistry*, 20(9):2587–2593, 04 1981.
- [83] Joachim D. Müller and Enrico Gratton. High-pressure fluorescence correlation spectroscopy. *Biophysical Journal*, 85(4):2711–2719, 2003.
- [84] Mohac Tekmen and Joachim D. Müller. High-pressure cell for fluorescence fluctuation spectroscopy. *Review of Scientific Instruments*, 75(12):5143–5148, 2004.
- [85] Hsuan-Lei Sung and David J Nesbitt. Dna hairpin hybridization under extreme pressures: A single-molecule fret study. *J Phys Chem B*, 124(1):110–120, Jan 2020.
- [86] Hsuan-Lei Sung and David J. Nesbitt. Ligand-dependent volumetric characterization of manganese riboswitch folding: A high-pressure single-molecule kinetic study. *The Journal of Physical Chemistry B*, 126(47):9781–9789, 12 2022.
- [87] Hsuan-Lei Sung and David J. Nesbitt. High pressure single-molecule fret studies of the lysine riboswitch: cationic and osmolytic effects on pressure induced denaturation. *Phys. Chem. Chem. Phys.*, 22:15853–15866, 2020.
- [88] Hsuan-Lei Sung and David J. Nesbitt. Single-molecule kinetic studies of dna hybridization under extreme pressures. *Phys. Chem. Chem. Phys.*, 22:23491–23501, 2020.
- [89] Julien Roche and Catherine A Royer. Lessons from pressure denaturation of proteins. *J R Soc Interface*, 15(147), Oct 2018.
- [90] Nathan Hillson, José Nelson Onuchic, and Angel E. García. Pressure-induced protein-folding/unfolding kinetics. *Proceedings of the National Academy of Sciences*, 96(26):14848–14853, 1999.
- [91] Jerson L Silva, Debora Foguel, and Catherine A Royer. Pressure provides new insights into protein folding, dynamics and structure. *Trends in Biochemical Sciences*, 26(10):612–618, 2001.
- [92] Wolfgang Bechmann and Ilko Bald. *Einstieg in die Physikalische Chemie für Naturwissenschaftler*. Springer Spektrum, 6 edition, 2018.
- [93] Pascale Winckler and Rodolphe Jaffiol. Multiphoton cascade absorption in single molecule fluorescence saturation spectroscopy. *Analytical Chemistry*, 85(9):4735–4744, 05 2013.
- [94] David M. Jamescon. *Introduction to Fluorescence*. CRC Press, 2014.

- [95] A. Jabłoński. Über den mechanismus der photolumineszenz von farbstoffphosphoren. *Zeitschrift für Physik*, 94(1):38–46, 1935.
- [96] Michael Prummer and Christian G. Hübner. *Single Molecule Biophysics with Fluorescence*. John Wiley & Sons, Ltd, 2009.
- [97] Michel Schott. *Optical Properties of Single Conjugated Polymer Chains (Polydiacetylenes)*, chapter 3, pages 49–151. John Wiley & Sons, Ltd, 2005.
- [98] Peter Atkins and Ronald Friedman. *Molecular Quantum Mechanics*. Oxford University Press, 4 edition, 2005.
- [99] Peter Atkins, Julio de Paula, and James Keeler. *Atkins' Physical Chemistry*. Oxford University Press, 11 edition, 2006.
- [100] Michael Kasha. Characterization of electronic transitions in complex molecules. *Discuss. Faraday Soc.*, 9:14–19, 1950.
- [101] J. W. Verhoeven. Glossary of terms used in photochemistry. *Pure and Applied Chemistry*, 68(12):2223–2286, 1996.
- [102] William W. Parson. *Modern Optical Spectroscopy*. Springer, 2009.
- [103] S. J. Strickler and Robert A. Berg. Relationship between absorption intensity and fluorescence lifetime of molecules. *The Journal of Chemical Physics*, 37(4):814–822, 1962.
- [104] A. Dewaele, J. H. Eggert, P. Loubeyre, and R. Le Toullec. Measurement of refractive index and equation of state in dense he, h₂, h₂O, and ne under high pressure in a diamond anvil cell. *Phys. Rev. B*, 67:094112, Mar 2003.
- [105] K. Vedam and Pichet Limsuwan. Piezo- and elasto-optic properties of liquids under high pressure. ii. refractive index vs density. *The Journal of Chemical Physics*, 69(11):4772–4778, 1978.
- [106] Marvin Minsky. Microscopy apparatus. *US-Pat. US3013467A*, 1961.
- [107] M. Minsky. Memoir on inventing the confocal scanning microscope. *Scanning*, 10(4):128–138, 1988.
- [108] Claxton, Nathan S and Fellers, Thomas J and Davidson, Michael W. Laser scanning confocal microscopy. *Encyclopedia of Medical Devices and Instrumentation*, 21(1):1–37, 2006.
- [109] S.W. Paddock. *Confocal Microscopy: Methods and Protocols*. Methods in Molecular Biology. Springer New York, 2013.
- [110] U. Kubitscheck. *Fluorescence Microscopy: From Principles to Biological Applications*. Wiley, 2017.
- [111] James B. Pawley, editor. *Handbook of Biological Confocal Microscopy*. Springer, 3 edition, 2006.

- [112] Akira Ichihara, Takeo Musano Tanaami, Katsumi Isozaki, Yumiko Musashino Sugiyama, Yasuhito Kosugi, Kenta Mikuriya, Michio Abe, and Isao Uemura. High-speed confocal fluorescence microscopy using a nipkow scanner with microlenses for 3-d imaging of single fluorescent molecule in real time. 1996.
- [113] A. Egner, V. Andresen, and S. W. Hell. Comparison of the axial resolution of practical nipkow-disk confocal fluorescence microscopy with that of multifocal multiphoton microscopy: theory and experiment. *Journal of Microscopy*, 206(1):24–32, 2002.
- [114] Eugene Hecht. *Optics, Global Edition*. Pearson Education, 2016.
- [115] J. Eichler and H.J. Eichler. *Laser: Bauformen, Strahlführung, Anwendungen*. Springer Berlin Heidelberg, 2007.
- [116] Robert H Webb. Confocal optical microscopy. *Reports on Progress in Physics*, 59(3):427–471, mar 1996.
- [117] F. Pedrotti, L. Pedrotti, W. Bausch, and H. Schmidt. *Optik für Ingenieure: Grundlagen*. Springer Berlin Heidelberg, 2007.
- [118] Hong Qian and Elliot L. Elson. Analysis of confocal laser-microscope optics for 3-d fluorescence correlation spectroscopy. *Appl. Opt.*, 30(10):1185–1195, Apr 1991.
- [119] Bo Zhang, Josiane Zerubia, and Jean-Christophe Olivo-Marin. Gaussian approximations of fluorescence microscope point-spread function models. *Appl. Opt.*, 46(10):1819–1829, Apr 2007.
- [120] M. Bass, C. DeCusatis, J.M. Enoch, V. Lakshminarayanan, G. Li, C. MacDonald, V.N. Mahajan, and E. Van Stryland. *Handbook of Optics, Third Edition Volume I: Geometrical and Physical Optics, Polarized Light, Components and Instruments(set)*. Handbook of Optics. McGraw Hill LLC, 2009.
- [121] R.T. Borlinghaus. *Konfokale Mikroskopie in Weiß: Optische Schnitte in allen Farben*. Springer Berlin Heidelberg, 2016.
- [122] T. Hirschfeld. Optical microscopic observation of single small molecules. *Appl. Opt.*, 15(12):2965–2966, Dec 1976.
- [123] C. Gell, D. Brockwell, and A. Smith. *Handbook of Single Molecule Fluorescence Spectroscopy*. Oxford University Press, 2006.
- [124] W. E. Moerner and L. Kador. Optical detection and spectroscopy of single molecules in a solid. *Phys. Rev. Lett.*, 62:2535–2538, May 1989.
- [125] P.R. Selvin and T. Ha. *Single-molecule Techniques: A Laboratory Manual*. Cold Spring Harbor Laboratory Series. Cold Spring Harbor Laboratory Press, 2008.

- [126] M. Orrit and J. Bernard. Single pentacene molecules detected by fluorescence excitation in a p-terphenyl crystal. *Phys. Rev. Lett.*, 65:2716–2719, Nov 1990.
- [127] Shuming Nie, Daniel T. Chiu, and Richard N. Zare. Probing individual molecules with confocal fluorescence microscopy. *Science*, 266(5187):1018–1021, 1994.
- [128] Rudolf Rigler and Ulo Mets. Diffusion of single molecules through a Gaussian laser beam. In Jouko E. Korppi-Tommola, editor, *Laser Spectroscopy of Biomolecules*, volume 1921, pages 239 – 248. International Society for Optics and Photonics, SPIE, 1993.
- [129] W. E. Moerner and David P. Fromm. Methods of single-molecule fluorescence spectroscopy and microscopy. *Review of Scientific Instruments*, 74(8):3597–3619, 2003.
- [130] Samuel S. M. Wong. *Introductory Nuclear Physics*. Wiley-VCH Verlag GmbH & Co. KGaA, 2 edition, 2004.
- [131] Ammasi Periasamy and Richard N. Day, editors. *Molecular Imaging*. American Physiological Society, 2005.
- [132] Dennis E. Koppel. Statistical accuracy in fluorescence correlation spectroscopy. *Phys. Rev. A*, 10:1938–1945, Dec 1974.
- [133] Jerker Widengren, Uelo Mets, and Rudolf Rigler. Fluorescence correlation spectroscopy of triplet states in solution: a theoretical and experimental study. *The Journal of Physical Chemistry*, 99(36):13368–13379, 09 1995.
- [134] Lloyd M Davis and Guoqing Shen. Accounting for triplet and saturation effects in fcs measurements. *Curr Pharm Biotechnol*, 7(4):287–301, Aug 2006.
- [135] Jerker Widengren, Rudolf Rigler, and Ülo Mets. Triplet-state monitoring by fluorescence correlation spectroscopy. *Journal of Fluorescence*, 4(3):255–258, 1994.
- [136] Hagen Hofmann, Frank Hillger, Cyrille Delley, Armin Hoffmann, Shawn H Pfeil, Daniel Nettels, Everett A Lipman, and Benjamin Schuler. Role of denatured-state properties in chaperonin action probed by single-molecule spectroscopy. *Biophys J*, 107(12):2891–2902, Dec 2014.
- [137] Reeta Vyas and Surendra Singh. Antibunching and photoemission waiting times. *J. Opt. Soc. Am. B*, 17(4):634–637, Apr 2000.
- [138] Malvin C. Teich and Bahaa E.A. Saleh. Photon Bunching and Antibunching. volume 26 of *Progress in Optics*, pages 1–104. Elsevier, 1988.
- [139] R. Short and L. Mandel. Observation of sub-poissonian photon statistics. *Phys. Rev. Lett.*, 51:384–387, Aug 1983.

- [140] H. J. Kimble, M. Dagenais, and L. Mandel. Photon antibunching in resonance fluorescence. *Phys. Rev. Lett.*, 39:691–695, Sep 1977.
- [141] Hoi Sung Chung and William A Eaton. Protein folding transition path times from single molecule fret. *Current Opinion in Structural Biology*, 48:30–39, 2018. Folding and binding in silico, in vitro and in cellula * Proteins: An Evolutionary Perspective.
- [142] R.H. Austin, H. Frauenfelder, S.S. Chan, C.E. Schulz, W.S. Chan, G.U. Nienhaus, and R.D. Young. *The Physics of Proteins: An Introduction to Biological Physics and Molecular Biophysics*. Biological and Medical Physics, Biomedical Engineering. Springer New York, 2010.
- [143] A. Kessel and N. Ben-Tal. *Introduction to Proteins: Structure, Function, and Motion, Second Edition*. Chapman & Hall/CRC Computational Biology Series. CRC Press, 2018.
- [144] J.M. Berg, J.L. Tymoczko, G.J. Gatto, L. Stryer, A. Held, G. Maxam, L. Seidler, B. Häcker, and B. Jarosch. *Stryer Biochemie*. Springer Berlin Heidelberg, 8 edition, 2017.
- [145] D. Whitford. *Proteins: Structure and Function*. Wiley, 2013.
- [146] Welker, C and Böhm, G and Schurig, H and Jaenicke, R. Cloning, overexpression, purification, and physicochemical characterization of a cold shock protein homolog from the hyperthermophilic bacterium *thermotoga maritima*. *Protein Sci*, 8(2):394–403, Feb 1999.
- [147] Werner Kremer, Benjamin Schuler, Stefan Harrieder, Matthias Geyer, Wolfram Gronwald, Christine Welker, Rainer Jaenicke, and Hans R. Kalbitzer. Solution nmr structure of the cold-shock protein from the hyperthermophilic bacterium *thermotoga maritima*. *European Journal of Biochemistry*, 268(9):2527–2539, 2001.
- [148] Kremer, W., Schuler, B., Harrieder, S., Geyer, M., Gronwald, W., Welker, C., Jaenicke, R., and Kalbitzer, H.R. Solution NMR Structure of the cold shock protein from the hyperthermophilic bacterium *thermotoga maritima* - PDB entry 1G6P, Last access: 2024-01-08 2010.
- [149] H. Bannwarth, B.P. Kremer, and A. Schulz. *Basiswissen Physik, Chemie und Biochemie: Vom Atom bis zur Atmung - für Biologen, Mediziner und Pharmazeuten*. Bachelor. Springer Berlin Heidelberg, 2013.
- [150] C Chothia and J Janin. Principles of protein-protein recognition. *Nature*, 256(5520):705–708, Aug 1975.
- [151] Douglas H Ohlendorf, Dale E Tronrud, and Brian W Matthews. Refined structure of Cro repressor protein from bacteriophage λ suggests both flexibility and plasticity. *Journal of Molecular Biology*, 280(1):129–136, 1998.

- [152] Aritra Chowdhury, Daniel Nettels, and Benjamin Schuler. Interaction dynamics of intrinsically disordered proteins from single-molecule spectroscopy. *Annu Rev Biophys*, 52:433–462, May 2023.
- [153] A.Keith Dunker, J.David Lawson, Celeste J Brown, Ryan M Williams, Pedro Romero, Jeong S Oh, Christopher J Oldfield, Andrew M Campen, Catherine M Ratliff, Kerry W Hipps, Juan Ausio, Mark S Nissen, Raymond Reeves, ChulHee Kang, Charles R Kissinger, Robert W Bailey, Michael D Griswold, Wah Chiu, Ethan C Garner, and Zoran Obradovic. Intrinsically disordered protein. *Journal of Molecular Graphics and Modelling*, 19(1):26–59, 2001.
- [154] Christopher J. Oldfield and A. Keith Dunker. Intrinsically disordered proteins and intrinsically disordered protein regions. *Annual Review of Biochemistry*, 83(1):553–584, 2014. PMID: 24606139.
- [155] Peter Tompa, Eva Schad, Agnes Tantos, and Lajos Kalmar. Intrinsically disordered proteins: emerging interaction specialists. *Curr Opin Struct Biol*, 35:49–59, Dec 2015.
- [156] M Nakano, T Tobita, and T Ando. Studies on a protamine (galline) from fowl sperm. 3. the total amino acid sequence of intact galline molecule. *Int J Pept Protein Res*, 8(6):565–578, 1976.
- [157] R Oliva and G H Dixon. Chicken protamine genes are intronless. the complete genomic sequence and organization of the two loci. *J Biol Chem*, 264(21):12472–12481, Jul 1989.
- [158] The UniProt Consortium. UniProt: the Universal Protein Knowledgebase in 2023. *Nucleic Acids Research*, 51(D1):D523–D531, 11 2022.
- [159] AlphaFold Data Copyright (2022) DeepMind Technologies Limited. Sperm histone. <https://alphafold.ebi.ac.uk/entry/P15340>, Last access: 2024-01-08.
- [160] Mihaly Varadi, Stephen Anyango, Mandar Deshpande, Sreenath Nair, Cindy Natassia, Galabina Yordanova, David Yuan, Oana Stroe, Gemma Wood, Agata Laydon, Augustin Židek, Tim Green, Kathryn Tunyasuvunakool, Stig Petersen, John Jumper, Ellen Clancy, Richard Green, Ankur Vora, Mira Lutfi, Michael Figurnov, Andrew Cowie, Nicole Hobbs, Pushmeet Kohli, Gerard Kleywegt, Ewan Birney, Demis Hassabis, and Sameer Velankar. AlphaFold Protein Structure Database: massively expanding the structural coverage of protein-sequence space with high-accuracy models. *Nucleic Acids Research*, 50(D1):D439–D444, 11 2021.
- [161] Jumper, John and Evans, Richard and Pritzel, Alexander and Green, Tim and Figurnov, Michael and Ronneberger, Olaf and Tunyasuvunakool, Kathryn and Bates, Russ and Židek, Augustin and Potapenko, Anna and Bridgland, Alex and Meyer, Clemens and Kohl, Simon A. A. and Ballard, Andrew J.

- and Cowie, Andrew and Romera-Paredes, Bernardino and Nikolov, Stanislav and Jain, Rishub and Adler, Jonas and Back, Trevor and Petersen, Stig and Reiman, David and Clancy, Ellen and Zielinski, Michal and Steinegger, Martin and Pacholska, Michalina and Berghammer, Tamas and Bodenstein, Sebastian and Silver, David and Vinyals, Oriol and Senior, Andrew W. and Kavukcuoglu, Koray and Kohli, Pushmeet and Hassabis, Demis. Highly accurate protein structure prediction with AlphaFold. *Nature*, 596(7873):583–589, 2021.
- [162] Tomonao Inobe, Susan Fishbain, Sumit Prakash, and Andreas Matouschek. Defining the geometry of the two-component proteasome degron. *Nat Chem Biol*, 7(3):161–167, Mar 2011.
- [163] Pedro R Romero, Saima Zaidi, Ya Yin Fang, Vladimir N Uversky, Predrag Radivojac, Christopher J Oldfield, Marc S Cortese, Megan Sickmeier, Tanguy LeGall, Zoran Obradovic, and A Keith Dunker. Alternative splicing in concert with protein intrinsic disorder enables increased functional diversity in multicellular organisms. *Proc Natl Acad Sci U S A*, 103(22):8390–8395, May 2006.
- [164] Vladimir N Uversky, Christopher J Oldfield, and A Keith Dunker. Intrinsically disordered proteins in human diseases: introducing the d2 concept. *Annu Rev Biophys*, 37:215–246, 2008.
- [165] Peter Tompa and Monika Fuxreiter. Fuzzy complexes: polymorphism and structural disorder in protein-protein interactions. *Trends Biochem Sci*, 33(1):2–8, Jan 2008.
- [166] Peter E Wright and H Jane Dyson. Linking folding and binding. *Curr Opin Struct Biol*, 19(1):31–38, Feb 2009.
- [167] Johnny Habchi, Peter Tompa, Sonia Longhi, and Vladimir N Uversky. Introducing protein intrinsic disorder. *Chem Rev*, 114(13):6561–6588, Jul 2014.
- [168] Dana Reichmann and Ursula Jakob. The roles of conditional disorder in redox proteins. *Curr Opin Struct Biol*, 23(3):436–442, Jun 2013.
- [169] Albert H Mao, Scott L Crick, Andreas Vitalis, Caitlin L Chicoine, and Rohit V Pappu. Net charge per residue modulates conformational ensembles of intrinsically disordered proteins. *Proc Natl Acad Sci U S A*, 107(18):8183–8188, May 2010.
- [170] Sonja Müller-Späth, Andrea Soranno, Verena Hirschfeld, Hagen Hofmann, Stefan Rügger, Luc Reymond, Daniel Nettels, and Benjamin Schuler. Charge interactions can dominate the dimensions of intrinsically disordered proteins. *Proceedings of the National Academy of Sciences*, 107(33):14609–14614, 2010.
- [171] National Library of Medicine. Pubmed. <https://pubmed.ncbi.nlm.nih.gov>, Last access: 2024-01-08.

- [172] Google LLC. Google scholar. <https://scholar.google.com>, Last access: 2024-01-08.
- [173] A.K. Dunker, Z Obradovic, Pedro Romero, Ethan Garner, and Celeste Brown. Intrinsic protein disorder in complete genomes. *Genome informatics. Workshop on Genome Informatics*, 11:161–71, 01 2000.
- [174] Robin van der Lee, Marija Buljan, Benjamin Lang, Robert J Weatheritt, Gary W Daughdrill, A Keith Dunker, Monika Fuxreiter, Julian Gough, Joerg Gsponer, David T Jones, Philip M Kim, Richard W Kriwacki, Christopher J Oldfield, Rohit V Pappu, Peter Tompa, Vladimir N Uversky, Peter E Wright, and M Madan Babu. Classification of intrinsically disordered regions and proteins. *Chem Rev*, 114(13):6589–6631, Jul 2014.
- [175] A Keith Dunker, Israel Silman, Vladimir N Uversky, and Joel L Sussman. Function and structure of inherently disordered proteins. *Curr Opin Struct Biol*, 18(6):756–764, Dec 2008.
- [176] Matt E Oates, Pedro Romero, Takashi Ishida, Mohamed Ghalwash, Marcin J Mizianty, Bin Xue, Zsuzsanna Dosztányi, Vladimir N Uversky, Zoran Obradovic, Lukasz Kurgan, A Keith Dunker, and Julian Gough. D²P²: database of disordered protein predictions. *Nucleic Acids Res*, 41(Database issue):D508–16, Jan 2013.
- [177] Sandro Bottaro and Kresten Lindorff-Larsen. Biophysical experiments and biomolecular simulations: A perfect match? *Science*, 361(6400):355–360, Jul 2018.
- [178] Andrea Sottini, Alessandro Borgia, Madeleine B. Borgia, Katrine Bugge, Daniel Nettels, Aritra Chowdhury, Pétur O. Heidarsson, Franziska Zosel, Robert B. Best, Birthe B. Kragelund, and Benjamin Schuler. Polyelectrolyte interactions enable rapid association and dissociation in high-affinity disordered protein complexes. *Nature Communications*, 11(1):5736, 2020.
- [179] Alex S. Holehouse and Rohit V. Pappu. Collapse transitions of proteins and the interplay among backbone, sidechain, and solvent interactions. *Annual Review of Biophysics*, 47(1):19–39, 2018. PMID: 29345991.
- [180] B A Shoemaker, J J Portman, and P G Wolynes. Speeding molecular recognition by using the folding funnel: the fly-casting mechanism. *Proc Natl Acad Sci U S A*, 97(16):8868–8873, Aug 2000.
- [181] Edward P O’Brien, Greg Morrison, Bernard R Brooks, and D Thirumalai. How accurate are polymer models in the analysis of förster resonance energy transfer experiments on proteins? *J Chem Phys*, 130(12):124903, Mar 2009.

- [182] Edward P. O’Brien, Guy Ziv, Gilad Haran, Bernard R. Brooks, and D. Thirumalai. Effects of denaturants and osmolytes on proteins are accurately predicted by the molecular transfer model. *Proceedings of the National Academy of Sciences*, 105(36):13403–13408, 2008.
- [183] Eilon Sherman and Gilad Haran. Coil-globule transition in the denatured state of a small protein. *Proc Natl Acad Sci U S A*, 103(31):11539–11543, Aug 2006.
- [184] Edward P. O’Brien, Greg Morrison, Bernard R. Brooks, and D. Thirumalai. How accurate are polymer models in the analysis of Förster resonance energy transfer experiments on proteins? *The Journal of Chemical Physics*, 130(12):124903, 03 2009.
- [185] Evan R McCarney, James H Werner, Summer L Bernstein, Ingo Ruczinski, Dmitrii E Makarov, Peter M Goodwin, and Kevin W Plaxco. Site-specific dimensions across a highly denatured protein; a single molecule study. *J Mol Biol*, 352(3):672–682, Sep 2005.
- [186] Benjamin Schuler, Everett A. Lipman, Peter J. Steinbach, Michael Kumke, and William A. Eaton. Polyproline and the “spectroscopic ruler” revisited with single-molecule fluorescence. *Proceedings of the National Academy of Sciences*, 102(8):2754–2759, 2005.
- [187] Daniel Nettels, Sonja Müller-Späth, Frank Küster, Hagen Hofmann, Dominik Haenni, Stefan Rügger, Luc Reymond, Armin Hoffmann, Jan Kubelka, Benjamin Heinz, Klaus Gast, Robert B Best, and Benjamin Schuler. Single-molecule spectroscopy of the temperature-induced collapse of unfolded proteins. *Proc Natl Acad Sci U S A*, 106(49):20740–20745, Dec 2009.
- [188] Andreas Vitalis and Rohit V. Pappu. Absinth: A new continuum solvation model for simulations of polypeptides in aqueous solutions. *Journal of Computational Chemistry*, 30(5):673–699, 2009.
- [189] René Wuttke, Hagen Hofmann, Daniel Nettels, Madeleine B Borgia, Jeetain Mittal, Robert B Best, and Benjamin Schuler. Temperature-dependent solvation modulates the dimensions of disordered proteins. *Proceedings of the National Academy of Sciences USA*, 111(14):5213–5218, Apr 2014.
- [190] Robert B. Best and Jeetain Mittal. Protein simulations with an optimized water model: Cooperative helix formation and temperature-induced unfolded state collapse. *The Journal of Physical Chemistry B*, 114(46):14916–14923, 11 2010.
- [191] Paul S. Nerenberg, Brian Jo, Clare So, Ajay Tripathy, and Teresa Head-Gordon. Optimizing solute–water van der waals interactions to reproduce solvation free energies. *The Journal of Physical Chemistry B*, 116(15):4524–4534, 04 2012.

- [192] Stefano Piana, Alexander G. Donchev, Paul Robustelli, and David E. Shaw. Water dispersion interactions strongly influence simulated structural properties of disordered protein states. *The Journal of Physical Chemistry B*, 119(16):5113–5123, 04 2015.
- [193] Robert B. Best, Wenwei Zheng, and Jeetain Mittal. Correction to balanced protein–water interactions improve properties of disordered proteins and non-specific protein association. *Journal of Chemical Theory and Computation*, 11(4):1978–1978, 04 2015.
- [194] Abhinav Nath, Maria Sammalkorpi, David C DeWitt, Adam J Trexler, Shana Elbaum-Garfinkle, Corey S O’Hern, and Elizabeth Rhoades. The conformational ensembles of α -synuclein and tau: combining single-molecule fret and simulations. *Biophys J*, 103(9):1940–1949, Nov 2012.
- [195] Nicola Galvanetto, Miloš T. Ivanović, Aritra Chowdhury, Andrea Sottini, Mark F. Nüesch, Daniel Nettels, Robert B. Best, and Benjamin Schuler. Extreme dynamics in a biomolecular condensate. *Nature*, 619(7971):876–883, 2023.
- [196] AlphaFold Data Copyright (2022) DeepMind Technologies Limited. Prothymosin alpha. <https://alphafold.ebi.ac.uk/entry/P06454>, Last access: 2023-06-03.
- [197] F Segade and J Gómez-Márquez. Prothymosin alpha. *Int J Biochem Cell Biol*, 31(11):1243–1248, Nov 1999.
- [198] Uversky, Vladimir N. and Gillespie, Joel R. and Millett, Ian S. and Khodyakova, Anna V. and Vasiliev, Anatoly M. and Chernovskaya, Tatyana V. and Vasilenko, Raisa N. and Kozlovskaya, Galina D. and Dolgikh, Dmitry A. and Fink, Anthony L. and Doniach, Sebastian and Abramov, Vyacheslav M. Natively unfolded human prothymosin α adopts partially folded collapsed conformation at acidic pH. *Biochemistry*, 38(45):15009–15016, 11 1999.
- [199] A A Haritos, G J Goodall, and B L Horecker. Prothymosin alpha: isolation and properties of the major immunoreactive form of thymosin alpha 1 in rat thymus. *Proceedings of the National Academy of Sciences*, 81(4):1008–1011, 1984.
- [200] The Universal Protein Resource. P06454 · ptma_human. <https://www.uniprot.org/uniprotkb/P06454/entry#sequences>, Last access: 2023-06-03.
- [201] K Gast, H Damaschun, K Eckert, K Schulze-Forster, H R Maurer, M Müller-Frohne, D Zirwer, J Czarnecki, and G Damaschun. Prothymosin alpha: a biologically active protein with random coil conformation. *Biochemistry*, 34(40):13211–13218, Oct 1995.

- [202] V N Uversky, J R Gillespie, and A L Fink. Why are "natively unfolded" proteins unstructured under physiologic conditions? *Proteins*, 41(3):415–427, Nov 2000.
- [203] Benjamin Schuler, Alessandro Borgia, Madeleine B Borgia, Pétur O Heidars-son, Erik D Holmstrom, Daniel Nettels, and Andrea Sottini. Binding without folding – the biomolecular function of disordered polyelectrolyte complexes. *Current Opinion in Structural Biology*, 60:66–76, 2020.
- [204] A Piñeiro, O J Cordero, and M Nogueira. Fifteen years of prothymosin alpha: contradictory past and new horizons. *Peptides*, 21(9):1433–1446, Sep 2000.
- [205] J Gomez-Marquez and P Rodríguez. Prothymosin alpha is a chromatin-remodelling protein in mammalian cells. *Biochem J*, 333 (Pt 1)(Pt 1):1–3, Jul 1998.
- [206] Arevik Mosoian. Intracellular and extracellular cytokine-like functions of prothymosin α : implications for the development of immunotherapies. *Future Med Chem*, 3(9):1199–1208, Jul 2011.
- [207] Eric M George and David T Brown. Prothymosin alpha is a component of a linker histone chaperone. *FEBS Lett*, 584(13):2833–2836, Jul 2010.
- [208] T Papamarcaki and O Tsolas. Prothymosin alpha binds to histone h1 in vitro. *FEBS Lett*, 345(1):71–75, May 1994.
- [209] Ken A. Dill and Hue Sun Chan. From levinthal to pathways to funnels. *Nature Structural Biology*, 4(1):10–19, 1997.
- [210] Levinthal, Cyrus. How to fold graciously, Mösbauer spectroscopy in biological Systems. *University of Illinois Press*, 67:22–24, 1969.
- [211] Robert F Service. Problem solved* (*sort of). *Science*, 321(5890):784–786, Aug 2008.
- [212] George D. Rose, Patrick J. Fleming, Jayanth R. Banavar, and Amos Maritan. A backbone-based theory of protein folding. *Proceedings of the National Academy of Sciences*, 103(45):16623–16633, 2006.
- [213] Jean Marc Kwasigroch Christophe Biot Marianne Rooman, Yves Dehouck and Dimitri Gilis. What is paradoxical about levinthal paradox? *Journal of Biomolecular Structure and Dynamics*, 20(3):327–329, 2002. PMID: 12437370.
- [214] K A Dill. Theory for the folding and stability of globular proteins. *Biochemistry*, 24(6):1501–1509, Mar 1985.
- [215] J D Bryngelson and P G Wolynes. Spin glasses and the statistical mechanics of protein folding. *Proceedings of the National Academy of Sciences*, 84(21):7524–7528, 1987.

- [216] P G Wolynes, J N Onuchic, and D Thirumalai. Navigating the folding routes. *Science*, 267(5204):1619–1620, Mar 1995.
- [217] Frauenfelder, H and Sligar, S G and Wolynes, P G. The energy landscapes and motions of proteins. *Science*, 254(5038):1598–1603, Dec 1991.
- [218] J N Onuchic, P G Wolynes, Z Luthey-Schulten, and N D Socci. Toward an outline of the topography of a realistic protein-folding funnel. *Proceedings of the National Academy of Sciences*, 92(8):3626–3630, 1995.
- [219] A. Fersht. *Structure and Mechanism in Protein Science: A Guide to Enzyme Catalysis and Protein Folding*. W. H. Freeman, 1999.
- [220] LJ Lapidus. Protein unfolding mechanisms and their effects on folding experiments [version 1; peer review: 2 approved]. *F1000Research*, 6(1723), 2017.
- [221] Sridip Parui, Rabindra Nath Manna, and Biman Jana. Destabilization of hydrophobic core of chicken villin headpiece in guanidinium chloride induced denaturation: Hint of π -cation interaction. *J Phys Chem B*, 120(36):9599–9607, Sep 2016.
- [222] V V Mozhaev, K Heremans, J Frank, P Masson, and C Balny. High pressure effects on protein structure and function. *Proteins*, 24(1):81–91, Jan 1996.
- [223] Calvin R. Chen and George I. Makhatadze. Molecular determinant of the effects of hydrostatic pressure on protein folding stability. *Nature Communications*, 8(1):14561, 2017.
- [224] F M Richards. Areas, volumes, packing and protein structure. *Annu Rev Biophys Bioeng*, 6:151–176, 1977.
- [225] Julien Roche, Jose A. Caro, Douglas R. Norberto, Philippe Barthe, Christian Roumestand, Jamie L. Schlessman, Angel E. Garcia, Bertrand García-Moreno E., and Catherine A. Royer. Cavities determine the pressure unfolding of proteins. *Proceedings of the National Academy of Sciences*, 109(18):6945–6950, 2012.
- [226] K J Frye and C A Royer. Probing the contribution of internal cavities to the volume change of protein unfolding under pressure. *Protein Sci*, 7(10):2217–2222, Oct 1998.
- [227] Jean-Baptiste Rouget, Tural Aksel, Julien Roche, Jean-Louis Saldana, Angel E Garcia, Doug Barrick, and Catherine A Royer. Size and sequence and the volume change of protein folding. *J Am Chem Soc*, 133(15):6020–6027, Apr 2011.
- [228] Andrea Arsiccio and Joan-Emma Shea. Pressure unfolding of proteins: New insights into the role of bound water. *J Phys Chem B*, 125(30):8431–8442, Aug 2021.

- [229] R.H. Pain. *Mechanisms of Protein Folding*. Frontiers in molecular biology. Oxford University Press, 2000.
- [230] C N Pace. The stability of globular proteins. *CRC Crit Rev Biochem*, 3(1):1–43, May 1975.
- [231] C Tanford. Protein denaturation. *Adv Protein Chem*, 23:121–282, 1968.
- [232] C Tanford. Protein denaturation. c. theoretical models for the mechanism of denaturation. *Adv Protein Chem*, 24:1–95, 1970.
- [233] J E Rothman and R D Kornberg. Cell biology. an unfolding story of protein translocation. *Nature*, 322(6076):209–210, Jul 1986.
- [234] K Verner and G Schatz. Import of an incompletely folded precursor protein into isolated mitochondria requires an energized inner membrane, but no added atp. *EMBO J*, 6(8):2449–2456, Aug 1987.
- [235] R J Deshaies, B D Koch, and R Schekman. The role of stress proteins in membrane biogenesis. *Trends Biochem Sci*, 13(10):384–388, Oct 1988.
- [236] Balasubramanian Harish, Richard E. Gillilan, Junjie Zou, Jinqiu Wang, Daniel P. Raleigh, and Catherine A. Royer. Protein unfolded states populated at high and ambient pressure are similarly compact. *Biophysical Journal*, 120(12):2592–2598, 2024/10/20 2021.
- [237] S E Jackson. How do small single-domain proteins fold? *Fold Des*, 3(4):R81–91, 1998.
- [238] Nölting, B. *Protein Folding Kinetics*. Springer, 2 edition, 2006.
- [239] N. D. Socci, J. N. Onuchic, and P. G. Wolynes. Diffusive dynamics of the reaction coordinate for protein folding funnels. *The Journal of Chemical Physics*, 104(15):5860–5868, 04 1996.
- [240] Marco Buscaglia, Benjamin Schuler, Lisa J Lapidus, William A Eaton, and James Hofrichter. Kinetics of intramolecular contact formation in a denatured protein. *J Mol Biol*, 332(1):9–12, Sep 2003.
- [241] Lisa J. Lapidus, William A. Eaton, and James Hofrichter. Measuring the rate of intramolecular contact formation in polypeptides. *Proceedings of the National Academy of Sciences*, 97(13):7220–7225, 2000.
- [242] William A Eaton. Modern kinetics and mechanism of protein folding: A retrospective. *J Phys Chem B*, 125(14):3452–3467, Apr 2021.
- [243] Oliver Bieri, Jakob Wirz, Bruno Hellrung, Mike Schutkowski, Mario Drewello, and Thomas Kiefhaber. The speed limit for protein folding measured by triplet–triplet energy transfer. *Proceedings of the National Academy of Sciences*, 96(17):9597–9601, 1999.

- [244] Florian Krieger, Beat Fierz, Oliver Bieri, Mario Drewello, and Thomas Kiefhaber. Dynamics of unfolded polypeptide chains as model for the earliest steps in protein folding. *J Mol Biol*, 332(1):265–274, Sep 2003.
- [245] G J Vidugiris, J L Markley, and C A Royer. Evidence for a molten globule-like transition state in protein folding from determination of activation volumes. *Biochemistry*, 34(15):4909–4912, Apr 1995.
- [246] National Instruments Corporation. LabVIEW. <https://www.ni.com/de/shop/labview.html>, Last URL access: 10.10.2023.
- [247] Kodosky, Jeffrey. Labview. *Proc. ACM Program. Lang.*, 4, 2020.
- [248] PerkinElmer. *Single Photon Counting Module SPCM-AQR Series Datasheet*, 2004.
- [249] Hamamatsu. *SPAD modules C11202 series Datasheet*, 2022.
- [250] molx. *Polymicro Technologies™ Polyimide Coated Polyimide Coated Fused Silica Capillary Tubing Datasheet*. molx, 2016.
- [251] Irving H. Malitson. Interspecimen comparison of the refractive index of fused silica. *Journal of the Optical Society of America*, 55:1205–1209, 1965.
- [252] (Partially) created with BioRender.com.
- [253] Cargille Laboratories. *Fused-Silica-Matching-Liquid-Code-50350 Datasheet*, 11 2017.
- [254] Aleš Benda, Martin Hof, Michael Wahl, Matthias Patting, Rainer Erdmann, and Peter Kapusta. Tcspc upgrade of a confocal fcs microscope. *Review of Scientific Instruments*, 76(3):033106, 2005.
- [255] PicoQuant GmbH. *User’s Manual and Technical Data*, 2004.
- [256] Becker & Hickl GmbH. *The bh TCSPC Handbook*, 5 edition, 2012.
- [257] Dr. Pasqual Bernhard. *USB2.0-TDC CS Manual*. Surface Concept, Am Sägewerk 23a, 55124 Mainz, 6, 2010.
- [258] Suren Felekyan, Hugo Sanabria, Stanislav Kalinin, Ralf Kühnemuth, and Claus A.M. Seidel. Chapter two - analyzing förster resonance energy transfer with fluctuation algorithms. In Sergey Y. Tetin, editor, *Fluorescence Fluctuation Spectroscopy (FFS), Part B*, volume 519 of *Methods in Enzymology*, pages 39–85. Academic Press, 2013.
- [259] Lauren Ann Metskas and Elizabeth Rhoades. Single-molecule fret of intrinsically disordered proteins. *Annu Rev Phys Chem*, 71:391–414, Apr 2020.

- [260] Cytiva. Cy5 Maleimide Mono-Reactive Dye 5-Pack - Product specifications. <https://www.cytivalifesciences.com/en/de/shop/molecular-and-immunodiagnosics/genomic-consumables/cy3-and-cy5-maleimide-mono-reactive-dye-5-packs-p-06157#order>, Last URL access: 21.12.2023.
- [261] ThermoFisher Scientific. The Molecular Probes Handbook - A Guide to Fluorescent Probes and Labeling Technologies, 11th Edition. <https://www.thermofisher.com/de/de/home/references/molecular-probes-the-handbook/mp-handbook-download.html>, 2010.
- [262] ATTO-TEC. Product Information: ATTO 488. https://www.attotec.com/fileadmin/user_upload/Katalog_Flyer_Support/ATTO_488.pdf, 2022.
- [263] ATTO-TEC. Product Information: ATTO 647N. https://www.attotec.com/fileadmin/user_upload/Katalog_Flyer_Support/ATTO_647N.pdf, 2022.
- [264] Molecular Probes, Inc. *TetraSpeckTM Fluorescent Microsphere Standards - Manual*. Molecular Probes, Inc., 2006.
- [265] M C Lin and R B Jr Macgregor. The activation volume of a dna helix-coil transition. *Biochemistry*, 35(36):11846–11851, Sep 1996.
- [266] Robert B Macgregor. The interactions of nucleic acids at elevated hydrostatic pressure. *Biochim Biophys Acta*, 1595(1-2):266–276, Mar 2002.
- [267] Thomas W Lynch, Dorina Kosztin, Mark A McLean, Klaus Schulten, and Stephen G Sligar. Dissecting the molecular origins of specific protein-nucleic acid recognition: hydrostatic pressure and molecular dynamics. *Biophys J*, 82(1 Pt 1):93–98, Jan 2002.
- [268] T.W. Lynch and S.G. Sligar. Experimental and theoretical high pressure strategies for investigating protein–nucleic acid assemblies. *Biochimica et Biophysica Acta (BBA) - Protein Structure and Molecular Enzymology*, 1595(1):277–282, 2002.
- [269] Tang, Y., Schneider W.M., Shen, Y., Raman, S., Inouye, M., Baker, D., Roth M.J., and Montelione, G.T. Solution Structure of Cold Shock Protein CspA Using Combined NMR and CS-Rosetta method - PDB entry 2L15, Last access: 2023-11-29 2010.
- [270] H Schindelin, W Jiang, M Inouye, and U Heinemann. Crystal structure of cspa, the major cold shock protein of escherichia coli. *Proceedings of the National Academy of Sciences*, 91(11):5119–5123, 1994.

- [271] Yuefeng Tang, William M. Schneider, Yang Shen, Srivatsan Raman, Masayori Inouye, David Baker, Monica J. Roth, and Gaetano T. Montelione. Fully automated high-quality nmr structure determination of small 2h-enriched proteins. *Journal of Structural and Functional Genomics*, 11(4):223–232, 2010.
- [272] Andrea Sottini, Alessandro Borgia, Madeleine Borgia, Katrine Bugge, Daniel Nettels, Aritra Chowdhury, Pétur Heidarsson, Franziska Zosel, Robert Best, Birthe B. Kragelund, and Benjamin Schuler. Polyelectrolyte interactions enable rapid association and dissociation in high-affinity disordered protein complexes. *Nature Communications*, 11, 11 2020.
- [273] Martin Steinegger and Johannes Söding. Clustering huge protein sequence sets in linear time. *Nature Communications*, 9(1):2542, 2018.
- [274] WaveMetrics Inc. Igor Pro, Version: 9.01. <https://www.wavemetrics.com/products/igorpro>, Last URL access: 05.07.2023.
- [275] WaveMetrics, Inc. *Igor Pro Manual, Version 9.05*. WaveMetrics, Inc., 2022.
- [276] Henri P. Gavin. The levenberg-marquardt method for nonlinear least squares curve-fitting problems c ©. 2013.
- [277] Ted A. Laurence, Samantha Fore, and Thomas Huser. Fast, flexible algorithm for calculating photon correlations. *Opt. Lett.*, 31(6):829–831, Mar 2006.
- [278] Wei Liu, Jin Shen, and Xianming Sun. Design of multiple-tau photon correlation system implemented by fpga. pages 410 – 414, 08 2008.
- [279] G. Lanzani. *Photophysics of Molecular Materials: From Single Molecules to Single Crystals*. Wiley, 2006.
- [280] Y Chen, J D Müller, P T So, and E Gratton. The photon counting histogram in fluorescence fluctuation spectroscopy. *Biophys J*, 77(1):553–567, Jul 1999.
- [281] Jan Pavlita. *Einzelmoleküluntersuchungen des Leuchtverhaltens organischer Farbstoffmoleküle*. PhD thesis, Universität zu Lübeck, 2019.
- [282] Schönle, Andreas and Von Middendorff, Claas and Ringemann, Christian and Hell, Stefan W. and Eggeling, Christian. Monitoring triplet state dynamics with fluorescence correlation spectroscopy: Bias and correction. *Microscopy Research and Technique*, 77(7):528–536, 2014.
- [283] Ingo Gregor, Digambara Patra, and Jörg Enderlein. Optical saturation in fluorescence correlation spectroscopy under continuous-wave and pulsed excitation. *ChemPhysChem*, 6(1):164–170, 2005.
- [284] Jörg Enderlein, Ingo Gregor, Digambara Patra, and Jörg Fitter. Art and artefacts of fluorescence correlation spectroscopy. *Current pharmaceutical biotechnology*, 5:155–61, 05 2004.

- [285] Visscher, K. and Brakenhoff, G. J. and Visser, T. D. Fluorescence saturation in confocal microscopy. *Journal of Microscopy*, 175(2):162–165, 1994.
- [286] Goro Nishimura and Masataka Kinjo. Systematic error in fluorescence correlation measurements identified by a simple saturation model of fluorescence. *Analytical Chemistry*, 76(7):1963–1970, 04 2004.
- [287] Arjun Sharma, Jörg Enderlein, and Manoj Kumbhakar. Photon antibunching in complex intermolecular fluorescence quenching kinetics. *The Journal of Physical Chemistry Letters*, 7(16):3137–3141, 08 2016.
- [288] Ülo Mets, Jerker Widengren, and Rudolf Rigler. Application of the antibunching in dye fluorescence: measuring the excitation rates in solution. *Chemical Physics*, 218(1):191–198, 1997.
- [289] T Basché, WE Moerner, M Orrit, and H Talon. Photon antibunching in the fluorescence of a single dye molecule trapped in a solid. *Phys Rev Lett*, 69(10):1516–1519, Sep 1992.
- [290] R. Rigler and E.S. Elson. *Fluorescence Correlation Spectroscopy: Theory and Applications*. Springer Series in Chemical Physics. Springer Berlin Heidelberg, 2001.
- [291] Daniel Nettels, Dominik Haenni, Sacha Maillot, Moussa Gueye, Anders Barth, Verena Hirschfeld, Christian G. Hübner, Jérémie Léonard, and Benjamin Schuler. Excited-state annihilation reduces power dependence of single-molecule fret experiments. *Phys. Chem. Chem. Phys.*, 17:32304–32315, 2015.
- [292] Simon Sindbert, Stanislav Kalinin, Hien Nguyen, Andrea Kienzler, Lilia Clima, Willi Bannwarth, Bettina Appel, Sabine Müller, and Claus A. M. Seidel. Accurate distance determination of nucleic acids via Förster resonance energy transfer: Implications of dye linker length and rigidity. *Journal of the American Chemical Society*, 133(8):2463–2480, 03 2011.
- [293] Thomas Heinlein, Jens-Peter Knemeyer, Oliver Piestert, and Markus Sauer. Photoinduced electron transfer between fluorescent dyes and guanosine residues in dna-hairpins. *The Journal of Physical Chemistry B*, 107(31):7957–7964, 08 2003.
- [294] Masaki Torimura, Shinya Kurata, Kazutaka Yamada, Toyokazu Yokomaku, Yoichi Kamagata, Takahiro Kanagawa, and Ryuichiro Kurane. Fluorescence-quenching phenomenon by photoinduced electron transfer between a fluorescent dye and a nucleotide base. *Analytical Sciences*, 17(1):155–160, 2001.
- [295] Jerker Widengren and Petra Schwille. Characterization of photoinduced isomerization and back-isomerization of the cyanine dye cy5 by fluorescence correlation spectroscopy. *The Journal of Physical Chemistry A*, 104(27):6416–6428, 07 2000.

- [296] Akira Kitamura, Johan Tornmalm, Baris Demirbay, Joachim Piguet, Masataka Kinjo, and Jerker Widengren. Trans-cis isomerization kinetics of cyanine dyes reports on the folding states of exogeneous RNA G-quadruplexes in live cells. *Nucleic Acids Research*, 51(5):e27–e27, 01 2023.
- [297] Iwo König, Arash Zarrine-Afsar, Mikayel Aznauryan, Andrea Soranno, Bengt Wunderlich, Fabian Dingfelder, Jakob C Stüber, Andreas Plückthun, Daniel Nettels, and Benjamin Schuler. Single-molecule spectroscopy of protein conformational dynamics in live eukaryotic cells. *Nature Methods*, 12(8):773–779, 2015.
- [298] Dana Kahra. *Die Energielandschaft von Proteinen: Von der Faltung zur Katalyse - Einzelmolekül-FRET-Studien an einem Zwei-Domänen-Protein*. PhD thesis, Universität zu Lübeck, 2012.
- [299] Christian Eggeling, Jerker Widengren, Leif Brand, Jörg Schaffer, Suren Felekyan, and Claus A M Seidel. Analysis of photobleaching in single-molecule multicolor excitation and förster resonance energy transfer measurements. *J Phys Chem A*, 110(9):2979–2995, Mar 2006.
- [300] Luis A Campos, Jianwei Liu, Xiang Wang, Ravishankar Ramanathan, Douglas S English, and Victor Muñoz. A photoprotection strategy for microsecond-resolution single-molecule fluorescence spectroscopy. *Nature Methods*, 8(2):143–146, 2011.
- [301] Gregory-Neal W. Gomes, Mickaël Krzeminski, Ashley Namini, Erik W. Martin, Tanja Mittag, Teresa Head-Gordon, Julie D. Forman-Kay, and Claudiu C. Gradinaru. Conformational ensembles of an intrinsically disordered protein consistent with nmr, saxs, and single-molecule fret. *Journal of the American Chemical Society*, 142(37):15697–15710, 09 2020.
- [302] Jaby Jacob, Robin S Dothager, P Thiyagarajan, and Tobin R Sosnick. Fully reduced ribonuclease a does not expand at high denaturant concentration or temperature. *J Mol Biol*, 367(3):609–615, Mar 2007.
- [303] Uversky, Vladimir N. What does it mean to be natively unfolded? *European Journal of Biochemistry*, 269(1):2–12, Jan 2002.
- [304] Andrea Soranno and Iwo Koenig and Madeleine B. Borgia and Hagen Hofmann and Franziska Zosel and Daniel Nettels and Benjamin Schuler. Single-molecule spectroscopy reveals polymer effects of disordered proteins in crowded environments. *Proceedings of the National Academy of Sciences*, 111(13):4874–4879, 2014.
- [305] P.G. de Gennes and P.P.G. Gennes. *Scaling Concepts in Polymer Physics*. Cornell University Press, 1979.

- [306] John Portman, Shoji Takada, and Peter Wolynes. Microscopic theory of protein folding rates. ii. local reaction coordinates and chain dynamics. *Chemical Physics - CHEM PHYS*, 114:5082–5096, 03 2001.
- [307] Nian-Sheng Cheng. Formula for the viscosity of a glycerolwater mixture. *Industrial & Engineering Chemistry Research - IND ENG CHEM RES*, 47:3285–3288, 05 2008.
- [308] Andreas Volk and Christian J. Kähler. Density model for aqueous glycerol solutions. *Experiments in Fluids*, 59(5):75, 2018.
- [309] Ted A Laurence, Xiangxu Kong, Marcus Jäger, and Shimon Weiss. Probing structural heterogeneities and fluctuations of nucleic acids and denatured proteins. *Proc Natl Acad Sci U S A*, 102(48):17348–17353, Nov 2005.
- [310] Fang Huang, Satoshi Sato, Timothy D Sharpe, Liming Ying, and Alan R Fersht. Distinguishing between cooperative and unimodal downhill protein folding. *Proc Natl Acad Sci U S A*, 104(1):123–127, Jan 2007.
- [311] Kusai A Merchant, Robert B Best, John M Louis, Irina V Gopich, and William A Eaton. Characterizing the unfolded states of proteins using single-molecule fret spectroscopy and molecular simulations. *Proc Natl Acad Sci U S A*, 104(5):1528–1533, Jan 2007.
- [312] Vincent A Voelz, Marcus Jäger, Shuhuai Yao, Yujie Chen, Li Zhu, Steven A Waldauer, Gregory R Bowman, Mark Friedrichs, Olgica Bakajin, Lisa J Lapidus, Shimon Weiss, and Vijay S Pande. Slow unfolded-state structuring in acyl-coa binding protein folding revealed by simulation and experiment. *J Am Chem Soc*, 134(30):12565–12577, Aug 2012.
- [313] Elza V Kuzmenkina, Colin D Heyes, and G Ulrich Nienhaus. Single-molecule fret study of denaturant induced unfolding of rnae h. *J Mol Biol*, 357(1):313–324, Mar 2006.
- [314] Kuzmenkina, Elza V, Heyes, Colin D, and Nienhaus, G Ulrich. Single-molecule forster resonance energy transfer study of protein dynamics under denaturing conditions. *Proceedings of the National Academy of Sciences*, 102(43):15471–15476, 2005.
- [315] microfluidic ChipShop GmbH. mcs-foil-146. <https://www.microfluidic-chipshop.com/catalogue/polymer-substrates-foils/foils/>, Last access: 2024-02-26.
- [316] Jeremy L. England and Gilad Haran. To fold or expand—a charged question. *Proceedings of the National Academy of Sciences*, 107(33):14519–14520, 2010.

Acknowledgement

An erster Stelle möchte ich mich bei meinem Doktorvater, Herrn Prof. Dr. Christian Hübner bedanken. Er hat mir nicht nur die Möglichkeit gegeben, diese Doktorarbeit an seinem Institut durchzuführen, sondern stand mir auch zu jeder Zeit mit seiner unerschöpflichen Begeisterung und seinem Optimismus zur Seite – selbst in schwierigen Momenten. Besonders schätze ich, dass er jederzeit ein offenes Ohr für meine Fragen und Anliegen hatte, sowie seine wertvollen fachlichen Anregungen.

Mein Dank gilt auch Dr. Verena Hirschfeld für das Korrekturlesen meiner Arbeit und ihre Hilfe bei Fragen zum Versuchsaufbau. Ich danke Dr. Sven Schneider für die angenehme Zusammenarbeit und die Einführung in die Welt der Druckmessungen, die meine Forschung maßgeblich bereichert hat.

Ein besonderer Dank geht auch an meine Bachelor- und Masterstudentinnen, die durch ihre Abschlussarbeiten einen wertvollen Beitrag zu dieser Dissertation geleistet haben, Joana Weiler, Carla Neitzke, Rieke Meyer und Jessica Rückert.

Auch möchte ich Reinhard Schulz meinen Dank aussprechen, der durch seine Unterstützung und die Anfertigung zahlreicher Teile zur kontinuierlichen Weiterentwicklung des Versuchsaufbaus beigetragen hat.

Christian Rönau danke ich für seine tatkräftige Unterstützung bei der Proben- und Pufferherstellung sowie bei den Justagearbeiten im Versuchsaufbau, aber auch für die stets gute Stimmung im Büro und seine Hilfe bei vielen anderen Aufgaben.

Joana Weiler danke ich sehr, da sie mich nicht nur in wissenschaftlicher Hinsicht sondern auch privat tatkräftig unterstützt hat und immer ein offenes Ohr hatte.

Ich möchte mich außerdem bei allen noch nicht genannten Mitarbeitern des Instituts für das freundliche Miteinander und die angenehme Arbeitsatmosphäre bedanken.

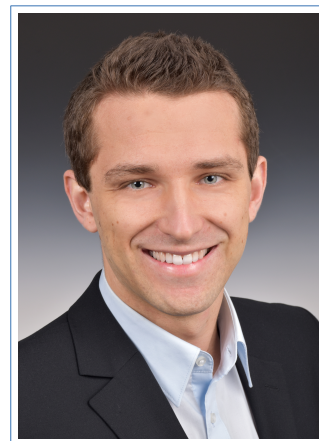
Mein größter Dank gilt meiner Familie, besonders meiner Mama Andrea, meinem Papa Jan und meiner Schwester Sina. Sie haben mir in all den Jahren den notwendigen Rückhalt und die Sicherheit gegeben und waren auch in schwierigen Zeiten für mich da. Das werde ich nie vergessen und weiß es sehr zu schätzen. Außerdem bin ich für ihre Geduld dankbar und ihren Glauben daran, dass auch diese Arbeit irgendwann einmal ein Ende findet.

Abschließend danke ich meiner Frau Rieke für den Glauben an mich und ihre tatkräftige Unterstützung und Ermutigung.

Kim Colin Reiter

Curriculum Vitae

✉ kim.c.reiter@gmail.com



Studies and Doctorate

- since 02/17 **Scientific researcher and PhD student**
Institute of Physics, University of Lübeck
- 10/14 – 01/17 **Master of Science**
Medical Engineering Science, University of Lübeck
Final grade: 1.1
- 10/15 – 04/16 **Student assistant**
Institute of Physics, University of Lübeck
- 10/11 – 03/15 **Bachelor of Science**
Medical Engineering Science, University of Lübeck
Final grade: 2.8

School

- 2002 – 2011 **Allgemeine Hochschulreife**
Thomas-Mann-Schule, Lübeck
Grade: 2.5

Scholarship

- 02/17 – 07/18 Graduate School for Computing in Medicine & Life Sciences, University of Lübeck

Publication

- Sven Schneider, Kim Colin Reiter, Erik Hinze, Cordelia Schiene-Fischer, Christian G. Hübner: *Single molecule FRET investigation of pressure-driven unfolding of cold shock protein A*, Journal of Chemical Physics, Volume 148, 2018